168

BULLETIN OF THE MINERAL RESEARCH AND EXPLORATION

2022

Phone : +90 (312) 201 10 00
Fax : +90 (312) 287 91 88
Adress : MTA 06530 - Ankara - TURKEY
www.mta.gov.tr

BULLETIN OF THE MINERAL RESEARCH AND EXPLORATION

2022 168 ISSN : 0026-4563
E-ISSN : 2651-3048

CONTENTS

Research Articles

Short Note

BULLETIN OF THE MINERAL RESEARCH AND EXPLORATION

2022 168 ISSN : 0026-4563
E-ISSN : 2651-3048

CONTENTS

Research Articles

Short Note

LOCATION OF MANAGEMENT
Bilimsel Dokümantasyon ve Tanıtma Dairesi Başkanlığı
Maden Tetkik ve Arama Genel Müdürlüğü
Çukurambar Mahallesi
Dumlupınar Bulvarı No: 11 06530
Çankaya/ANKARA
e-mail: bilimsel_dairesi@mta.gov.tr

TRANSLATIONS
The translation of Kara et al. was made by the authors. The translations of Özcan, Erdem et al. were made by Department of International Relations in MTA. The translation of Sönmez et al. was made by Mustafa Selman ARSAY. The translation of Msumange et al. was made by Buğra ÇAVDAR, The translation of Göçmengil et al. was made of Tuğba ISIK. The translations of Ilgar et al., Toka were made by Kerem Mustafa AVCI. The translations of Özsöz and Toker, Alkan and Bayrak were made by Sevda DEMİR. The translation of Boğazkesen and Karslı was made by Dilek YENER.

Bull. Min. Res. Exp. is indexed and abstracted in TR Dizin, Emerging Source Citation Index (ESCI), Scopus, The ICI Journals Master List (Copernicus), Directory of Open Access Journals (DOAJ), Open Academic Journals Index (OAJI), Georef, MIAR, EBSCO and Zoological Record.

The Bulletin of the Mineral Research and Exploration is published in three issues in a year. Each volume is published in Turkish and English in pdf format on the website of Bulletin of the Mineral Research and Exploration and English issue published in print. The English volume of the "Bulletin of the Mineral Research and Exploration" can be obtained from "BDT Department" free of charge, either directly or ordered by adding postage fee from the correspondence address. Typesetting and printing operations are carried out and followed by the Publication Service of the Scientific Documentation and Publicity Department.

The section of "notes to the authors", format, copyright and other information can be obtained from www.mta.gov.tr as PDF files.

Printed Date:
Printing House: Kuban Matbaacılık - İvedik Organize Sanayi Matbaacılar Sitesi 1514. Sokak No: 20 • Phone: 0312 395 2070 • Fax: 0312 395 3723 • www.kubanmatbaa.com
Periodical
ISSN: 0026-4563
E-ISSN: 2651-3048

Bulletin of the Mineral Research and Exploration

http://bulletin.mta.gov.tr

A graph method for interpretation of magnetic anomalies over 2D dikes and vertical faults

İbrahim KARA[a], Oya TARHAN BAL[a*] and Anisya B.TEKKELİ[a]

[a]*İstanbul University-Cerrahpaşa, Engineering Faculty, Department of Geophysical Engineering, İstanbul, Türkiye*

Research Article

Keywords:
Magnetic Interpretation, 2D Dike, Vertical Fault, Graph Method.

ABSTRACT

Simple geometric assumptions for dikes and faults are often used for interpreting the parameters of these structures from magnetic anomalies. The magnetic anomaly of a 2D dike or a vertical fault consists of two components; one with even and the other with odd symmetries. The function resulting from the ratio of the even and odd components is independent from the amplitude coefficient. The abscissa of the half-maximum of the even component and the maximum of the odd component of a dike or a vertical fault is related to its depth and its half-width. Incorporating this relation into the corresponding equations for dikes and vertical faults, the half-width value can be eliminated from the equations. Thus, the resulting ratio can be used for determining the model parameters. Using the ratio of the even component to the odd component for given distances, curves can be obtained for different depth-index parameter pairs, and from the graph of these curves, parameters of 2D dikes and vertical faults can be determined. The validity of the method is tested using synthetic models for dike and vertical fault cases. The method is also implemented on two different field data, and the results obtained are compared to previous studies.

Received Date: 02.01.2021
Accepted Date: 16.04.2021

1. Introduction

Dike and vertical fault models are used often in magnetic interpretation. Many researchers have interpreted the anomalies of these structures by decomposing the anomalies into their origin-symmetric even and odd components. Hutchison (1958) uses a logarithmic curve fitting method, Bhimasankaram et al. (1978) use Fourier transforms, in Kara et al. (1996) and Kara (1997) a method using correlation factors and integration nomograms is presented, in Rao et al. (1973) two methods are presented using the horizontal derivative of the anomaly, and in Atchuta Rao and Ram Babu (1981) a method using nomograms is presented.

Even though, nowadays 2D and 3D inversions are widely used for recovering subsurface structures, they often result within misleading results due to non-uniqueness of the solutions. For these reasons, calculations by assuming simple source geometries are still implemented for recovering model parameters for such structures. Some recent examples of methods developed to interpret anomalies of dikes and other simple geometries can be given as follows; Abdelrahman and Essa (2015) employed second derivative anomalies to obtain depth and shape properties of simple geological models, Abo-Ezz and Essa (2016) used linearized magnetic anomaly formula for simple geometries applied least-squares method. Essa and Elhussein (2017) recovered model

Citation Info: Kara, İ., Tarhan Bal, O., Tekkeli, B. A. 2022. A graph method for interpretation of magnetic anomalies over 2D dikes and vertical faults. Bulletin of the Mineral Research and Exploration 168, 1-10. https://doi.org/10.19111/bulletinofmre.928467

**Corresponding author: Oya TARHAN BAL, tarhan@istanbul.edu.tr*

parameters of a dipping dike using second horizontal gradient anomalies.

In this study, a method is proposed to recover model parameters of dipping dikes and vertical faults from magnetic field anomalies. For such simple structures assumptions, implementing least-squares inversion or global optimization methods do not provide much advantage since the calculations are fast. Hence, applying a graph method is preferred due to its simplicity in code development and implementation.

In the method, depth and index parameters of are delineated from the intersection point of a set of curves, which are obtained from the ratio of the even component to the odd component. Half-width of the structure is determined from its relation to the half-maximum of the even component and the abscissa of the maximum of the odd component. The method presented in this study is tested on synthetic models for both dike and vertical fault cases, and then, implemented on field data.

2. Method

In the method presented in this study, developed in order to interpret magnetic anomalies due to dikes and vertical faults, following notations and assumptions are made.

On a Cartesian coordinate system, the axis Y is assumed to be aligned with the strike direction of the 2D anomalous structure and the X axis showing the direction of the measurement profile (Figure 1a, b and c). i is the geomagnetic inclination in the survey area, the azimuth of the profile according to the magnetic north is denoted with α, dipping angle of the dike or fault is shown with d, k is the susceptibility contrast, T is the nominal value of the total field intensity, R=sinθ for dikes, and R=cosθ for vertical faults.

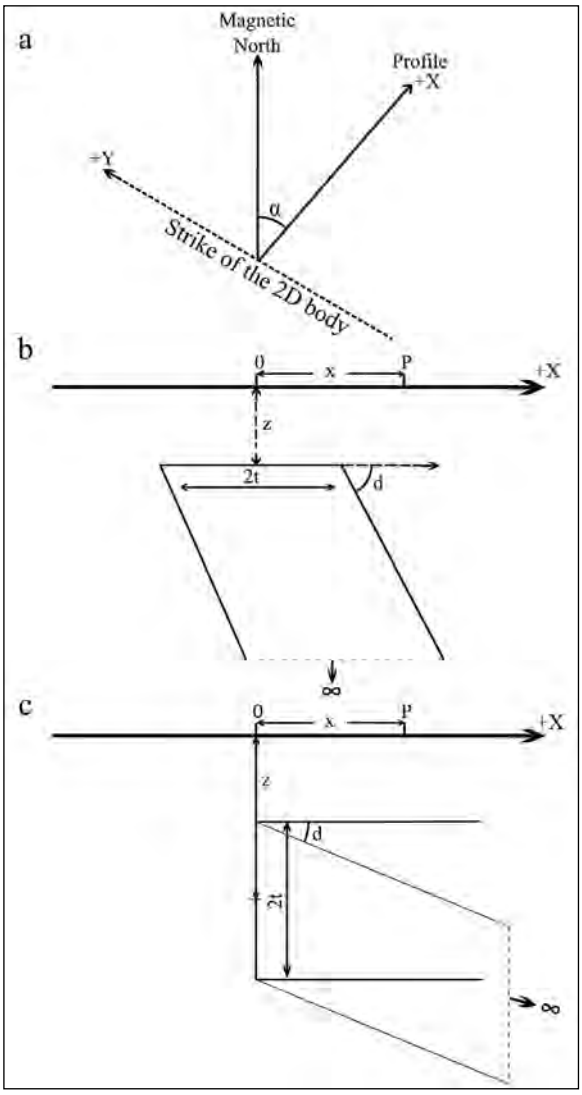

Figure 1- Generalized presentation of 2D dikes and vertical faults; a) view from top, showing magnetic north, the profile and the strike of the 2D body, b) cross-section of a dike and c) cross-section of a vertical fault.

According to the notations defined above, variation of the amplitude coefficient and the index parameter may be given as in Table 1 for total, vertical, and horizontal magnetic anomaly components respectively. In the table, $I=\tan^{-1}(\tan(i) / \cos(\alpha))$.

Table 1- Amplitude coefficient and index parameters for different magnetic field components.

Anomaly in	Amplitude Coefficient (M)	Index Parameter (θ)
Total field	$2kTS\ (1-\cos^2 i-\sin^2\alpha)$	2I-d-90°
Vertical field	$2kTS\ (1-\cos^2 i\ \sin^2\alpha)^{1/2}$	I-d
Horizontal field	$2kTS\ \sin\alpha\ (1-\cos^2 i\ \sin^2\alpha)^{1/2}$	I-d-90°

2.1. Implementation of the Method for Dipping Dikes

The magnetic anomaly (ΔF) due to a dipping dike (Figure1b) at any point P(x) is given as below,

$$\Delta F = M\left\{cos\theta\left[tan^{-1}\left(\frac{x+t}{z}\right)-tan^{-1}\left(\frac{x-t}{z}\right)\right]+\frac{1}{2}sinQ.ln\left[\frac{(x+t)^2+z^2}{(x-t)^2+z^2}\right]\right\} \quad (1)$$

(Parker, 1963). In the equation, x is the distance of the observation point to the origin, z is the depth to the top of the dike, and t is the half-width. The Equation 1 may be expressed as the sum of the even (E) and the odd (F) components and given below,

$$\Delta F(x)= E(x)+F(x) \quad (2)$$

where,

$$E(x) = M.cos\theta\left[tan^{-1}\left(\frac{x+t}{z}\right)-tan^{-1}\left(\frac{x-t}{z}\right)\right](even) \quad (3a)$$

$$F(x) = \frac{1}{2}M.sin\theta.ln\left[\frac{(x+t)^2+z^2}{(x-t)^2+z^2}\right](odd) \quad (3b)$$

If we denote the abscissa corresponding to the half-maximum of E(x) and to the maximum of F(x) with s, the relation between them is given as: $s=(z^2+t^2)^{1/2}$ and solving this equation for t yields to

$$t=(s^2-h^2)^{1/2} \quad (4)$$

If the value of the even component at any distance x is divided to the odd component for the same distance x, and denote the left-hand side using C_1 and right-hand side with C_2, following expressions can be written,

$$C_1 = \frac{E(x)}{F(x)} \quad (5a)$$

$$C_2 = \frac{cos\theta\left[tan^{-1}\left(\frac{x+t}{z}\right)-tan^{-1}\left(\frac{x-t}{z}\right)\right]}{0.5\,sin\theta\,ln\left[\frac{(x+t)^2+z^2}{(x-t)^2+z^2}\right]} \quad (5b)$$

Since, t may be given as product of z and s, if the value of z is obtained, the value of t can be calculated using the Equation 4.

In the presented method, using Equation 5a, C_1 is calculated from the values of the even and the odd components obtained from the observed field anomaly and the C_2 is obtained by varying theoretical [θ , z] pairs. One should notice that the C_1/C_2 ratio is independent of the amplitude coefficient.

Each set of C_2 values are calculated using Equation 5b for a value of z by varying θ between 0°-90° , 90°-180°, 180°-270° or 270°-360° according to the Table 2. This process must be repeated by varying z to scan trough all possible values. For each z, the value of θ minimizing the difference between the observed and theoretical ratios, C_1 and C_2, is determined and these z-θ pairs are plotted on a graph (z values against θ) as a curve. It's clear that the C_1-C_2 difference should be minimized for all distance values for the true values of the model parameters, θ and z. Thus, when the curves for different distances are plotted together, the intersection point of these curves yields to the actual values of z and θ. Once value of z is clear, t can be calculated using Equation 4. The flowchart of the process is given in Figure 2.

Table 2- Variation of θ according to the extremum of the anomaly.

Extremum	θ
Major positive anomaly towards	positive x axis $0° \leq \theta \leq 90°$
Major negative anomaly towards	negative x axis $90° \leq \theta \leq 180°$
Major negative anomaly towards	positive x axis $180° \leq \theta \leq 270°$
Major positive anomaly towards	negative x axis $270° \leq \theta \leq 360°$

2.2. Implementation of the Method for Vertical Faults

Similar to the case in dikes, the magnetic anomaly (ΔF) at any point P(x) on the profile due to a vertical fault may be given as,

$$\Delta F = M\left\{Cos\theta\ ln\ ln\left[\frac{x^2+(z+t)^2}{x^2+(z-t)^2}\right]^{1/2}+Sin\theta\left[tan^{-1}\frac{x}{z-t}-tan^{-1}\frac{x}{z+t}\right]\right\} \quad (6)$$

(Atchuta Rao and Ram Babu, 1981). Where, x is the distance of the observation point to the origin, z is the depth from surface to the half-thickness of the fault and t is the half-width of the fault. The Equation 6 may also be expressed using even (E) and odd (F) components,

$$\Delta F(x)= E(x)+F(x) \quad (7)$$

where,

$$E(x) = M\,Cos\theta\ ln\left[\frac{x^2+(z+t)^2}{x^2+(z-t)^2}\right]^{1/2} \quad (8a)$$

$$F(x) = M\,Sin\theta\,\left[tan^{-1}\frac{x}{z-t} - tan^{-1}\frac{x}{z+t}\right] \quad (8b)$$

If the abscissa of the half-maximum of the E(x) and the maximum of F(x) is denoted with s, it's known that $s=(z^2 - t^2)^{½}$ and hence,

$$t=(z^2 - s^2)^{½} \quad (9)$$

If the value of the even component at any distance x is divided to the odd component for the same distance x, following expressions can be written, where the left-hand side of the division is denoted using C_1 and right-hand side with C_2,

$$C_1 = \frac{E(x)}{F(x)} \quad (10a)$$

$$C_2 = \frac{Cos\theta\ ln\ \left[\frac{x^2+(z+t)^2}{x^2+(z-t)^2}\right]^{1/2}}{Sin\theta\ \left[tan^{-1}\frac{x}{z-t} - tan^{-1}\frac{x}{z+t}\right]} \quad (10b)$$

Since the value of the t may be given in terms of z and s, the unknowns remaining in the Equation 10b are θ and z. Once the value of z is obtained, t can be calculated using Equation 9. To obtain θ and z for vertical faults, the same process given for the dike is applied (Figure 2).

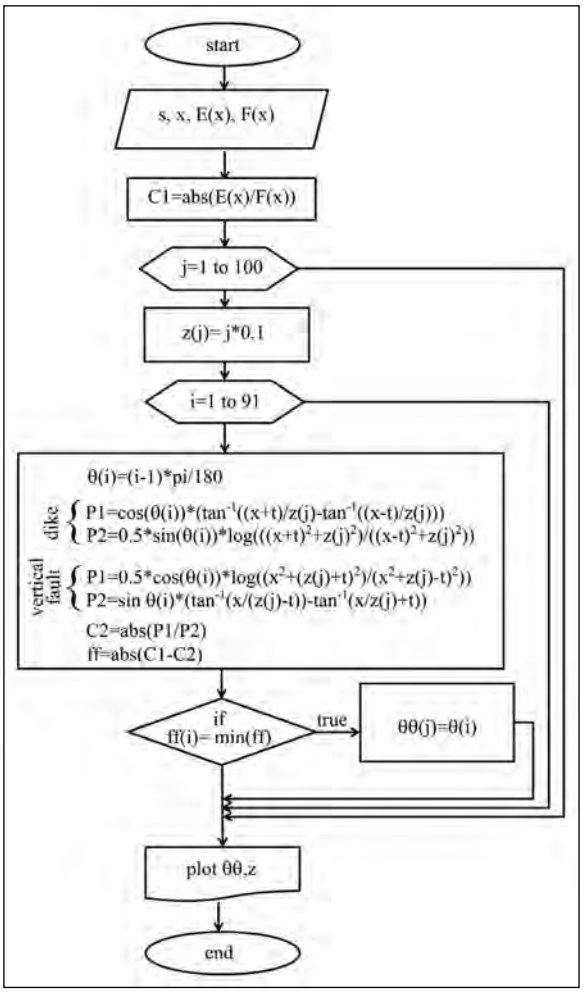

Figure 2- Flowchart to obtain a single curve.

3. Findings

3.1. Theoretical Implementation on a Dike Anomaly

In this synthetic test, the following model parameters are employed; z=8 m, t=4 m, and θ=50°. The anomaly, obtained from the given model parameters, is shown in Figure 3a, and its even and odd components are shown in Figure 3b.

The proposed method is implemented using the values of the even and odd components between x=[1, 12] m. The set of curves obtained for these values are presented in Figure 4. The intersection point of these curves yields to the actual depth (z) and index parameter (θ) values.

From the Figure 4, it's easy to note that the value of z=8m and θ=50°. The value of s=8.95m is also obtained from the Figure 3b. Using the obtained z and s values in Equation 4, the half-width value is obtained as t=4m. These values are the same of the actual values, justifying the proposed method to recover the model parameters.

In order to demostrate the applicability of the method for noisy datasets, 5% Gaussian noise is applied on the data and the results of the algorithm are compared. 1000 realizations are performed for the described experiment. For the automated selection of θ and z values, outliers are eliminated using 70% trimmed mean and thereafter the best intersection point is determined.

A sample noisy data and its even and odd components for x>0 are shown in Figure 5; the set of curves obtained for the given noisy data is shown in Figure 6a. Each [θ , z] pair, which are recovered from the 1000 realizations of the experiment, are shown in Figure 6b as a scatterplot; the value recovered for the sample noisy data is also marked in the figure. For the

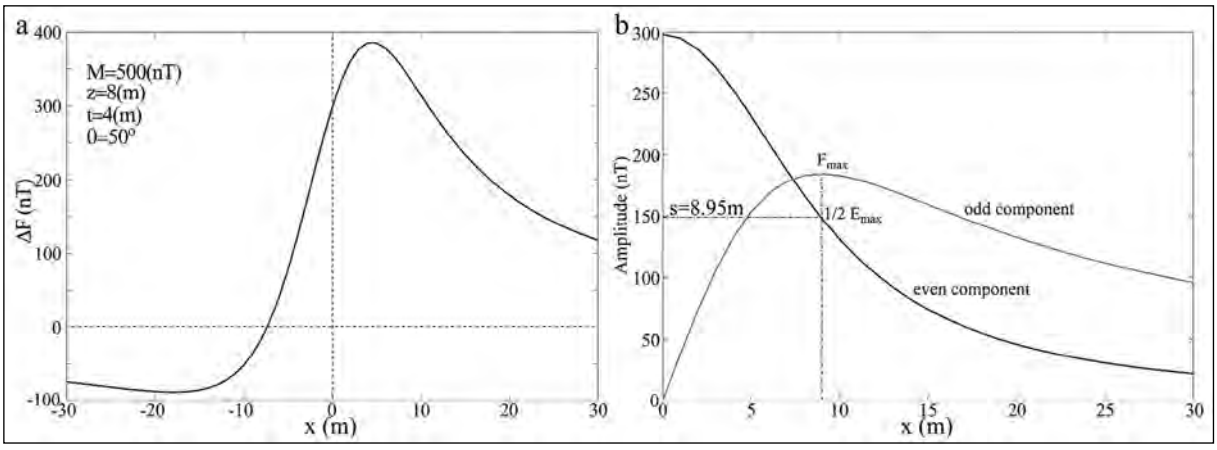

Figure 3- a) Calculated magnetic anomaly of the theoretical dike model and b) calculated even and odd components of the magnetic anomaly of the theoretical dike model.

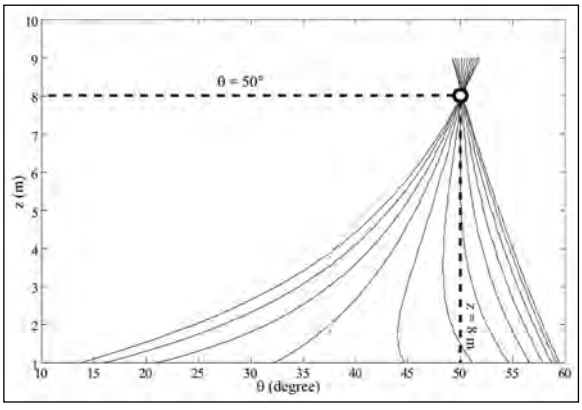

Figure 4- The set of curves obtained by the implementation of the method on the even and odd components due to the theoretical model.

introduced noise level, the experiment shows that the θ values are scattered between [49, 51] degrees, and z values are varying between [7, 9] m. The experiment shows that the method can also be applied successfully to noisy datasets.

3.2. Implementation on Field Data of a Dike

For the implementation on field data, the data collected on a diabase dike located in Durham Triassic Basin in North Carolina, USA, previously interpreted by Won (1981) is sampled (Figure 7a, solid line). Thereafter the presented method is implemented by the decomposition of the data into its even and odd components (Figure 7b).

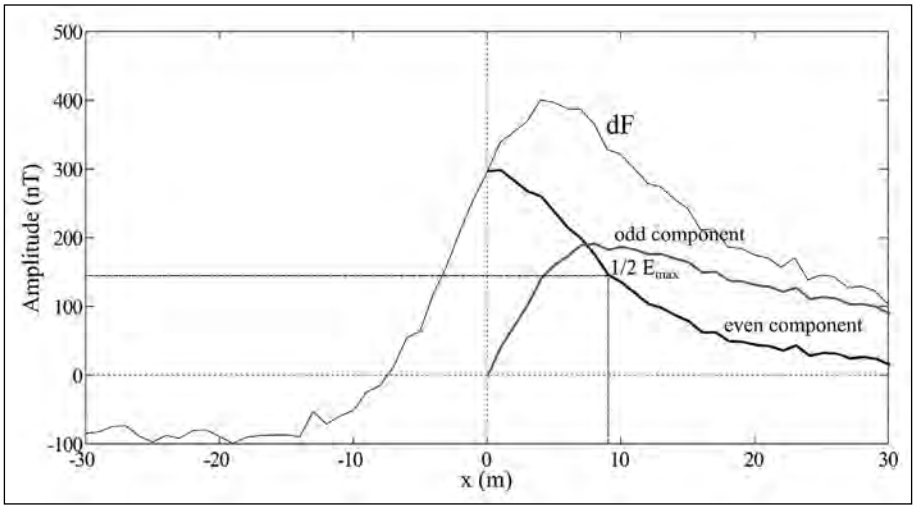

Figure 5- Magnetic anomaly of a theoretical dike model with 5% Gaussian noise (dF), and its even and odd components for x>0.

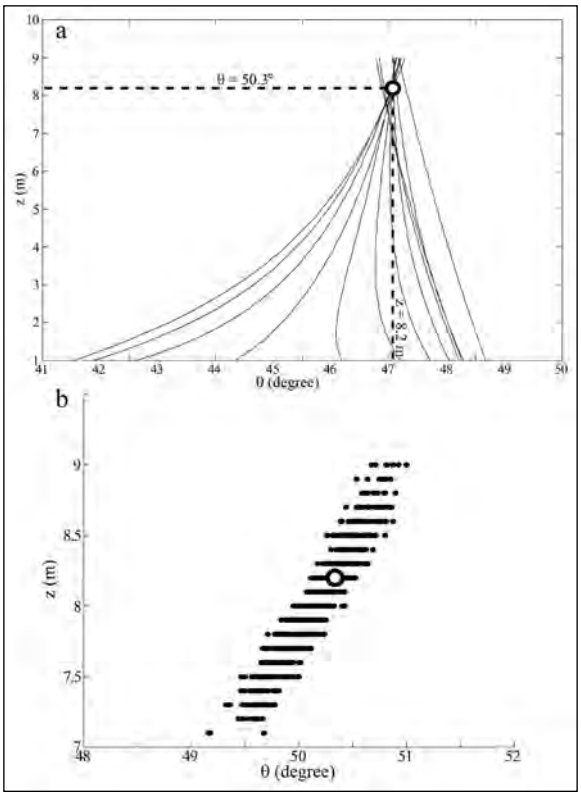

Figure 6- a) The set of curves obtained from the implementation of the method on data with 5% Gaussian noise and b) distribution of the [θ , z] pairs obtained by the application of the method on noisy anomaly [for 1000 realizations]. The [θ, z] pair obtained for the sample noisy data is shown with circle.

In the Figure 7b, the abscissa of the half-maximum of the even component yields to s=21.34m. When the proposed method is applied using the even and odd component values at x=10, 20, 30, and 40m the curves given in Figure 8 are obtained. From their intersection point z=8.4m and θ=329° values are determined. Using these values, t=19.62m is calculated using Equation 4.

At this stage, all the parameters except the amplitude coefficient (M) are obtained. The value of M=346.1 can be computed using Equation 3a and the synthetic anomaly can be plotted as seen in Figure 7a (dots) by using the recovered parameters. As seen in Figure 7a, the calculated and the observed anomalies are noticeably similar. These values are also similar to the results (z= 7.97 m, t= 19.7 m, θ=292.6°) given by Won (1981).

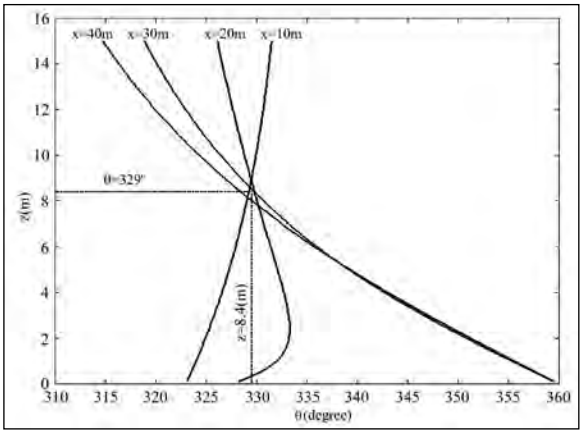

Figure 8- The set of curves obtained by the implementation of the proposed method using the even and odd components of the field anomaly.

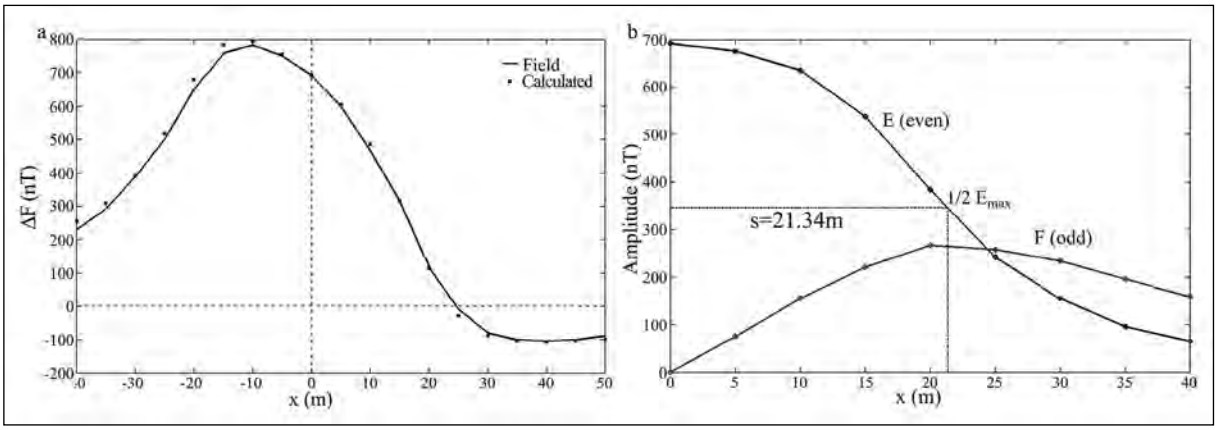

Figure 7- a) The vertical magnetic field anomaly (solid line) over a diabase dyke (Won, 1981), and the anomaly obtained from the model parameters recovered using the proposed method (dots) and b) even and odd component anomalies of the field data.

3.3. Theoretical Implementation on a Vertical Fault Anomaly

For this example, the anomaly for a vertical fault is calculated using following model parameters; M=500 nT, z=10 m, t=6 m, and θ=45° and shown in Figure 9a. The even and the odd components calculated for this model are presented in Figure 9b.

The set of curves given in Figure 10 are obtained by the implementation of the proposed method employing the even and odd component anomalies for x= [1 , 12] m interval. The intersection point of these curves should yield to the depth (z) and index parameters (θ).

From the Figure 10, the intersection point of the curves yields to z= 10 m and θ=45°, and s=8 m is obtained from Figure 9b. Incorporating these values in Equation 9, the half-width is calculated as t=6 m. The values recovered by the proposed method are the same of the defined model parameters.

In order to show that the method is also valid for noisy data vertical faults, the results of the algorithm are tested after adding 5% Gaussian noise to the data due to the theoretical vertical fault. For the vertical fault case, the experiment is also performed with 1000 realizations. In the Figure 11, a sample noisy data and its even and odd components for x>0 are shown; the set of curves obtained for the given data is given in Figure 12a. The [θ , z] pairs obtained after performing 1000 realizations are presented as a scatterplot in the Figure 12b; the value obtained for the sample noisy data is also marked on the plot. For the introduced noise level, the experiment shows that the θ values are scattered between [43.75, 46] degrees, and z values

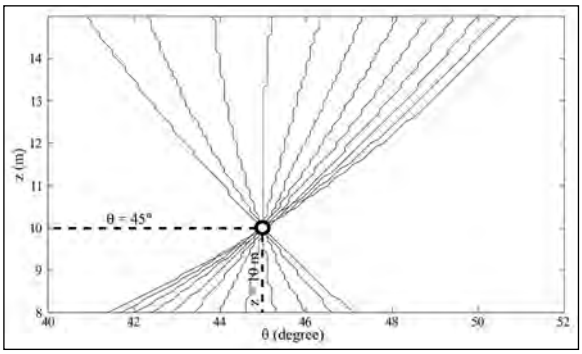

Figure 10- The set of curves, obtained by the implementation of the proposed method on the theoretical even and odd component anomalies due to the vertical fault.

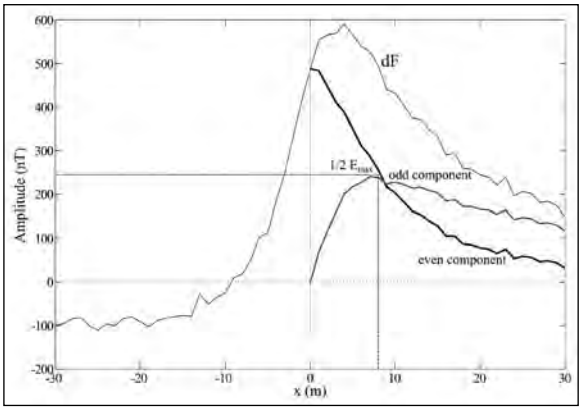

Figure 11- Magnetic anomaly of a theoretical fault model with 5% Gaussian noise (dF), and its even and odd components for x>0.

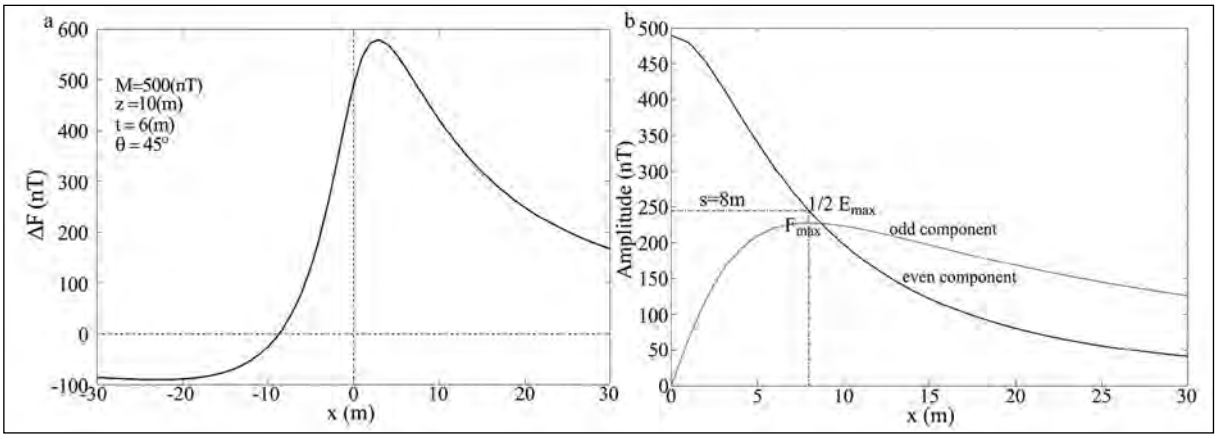

Figure 9- a) Calculated magnetic anomaly due to the theoretical vertical fault and b) even and odd components calculated using the theoretical vertical fault anomaly.

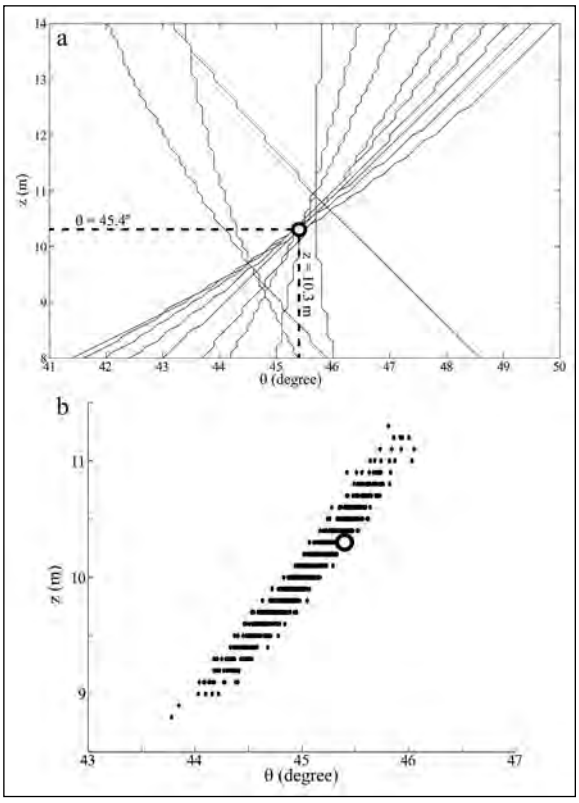

Figure 12- a) The set of curves obtained from the implementation of the method on data with 5% Gaussian noise and b) distribution of the [θ , z] pairs obtained by the application of the method on noisy anomaly [for 1000 realizations]. The [θ , z] pair obtained for the sample noisy data is shown with circle.

vary [8.7, 11.3] m. The experiment shows that the method can also be applied successfully on noisy datasets of vertical faults.

3.4. Implementation on Field Data of a Vertical Fault

For the implementation on the field data, the total magnetic field anomaly collected over the western margin of Perth Basin (Atchuta Rao and Ram Babu, 1981) is sampled with 2 km intervals (Figure 13, solid line) and the sampled anomaly is decomposed into its even and odd components (Figure 13b).

By the decomposition of this anomaly into its even and odd components, s=10.3 km is delineated from the abscissa of the half-maximum of the even component and the maximum of the odd component (Figure 13b). When the proposed method is applied using the even and the odd components at x=2, 4, 6, and 8 km the set of curves given in Figure 14 are obtained. From the intersection point z=11 km and θ=33° values are recovered, and using Equation 9 t=4.12 is calculated. The anomaly calculated using the recovered parameters is given in Figure 13a with dots.

In the Figure 13a, the agreement between the observed and the calculated anomalies is good, and the recovered model parameters are similar to the values estimated in the previous studies of Qureshi and Nalaye (1978), Atchuta Rao and Ram Babu (1981).

4. Discussion

Although multi-dimensional inversion methods, based on geometric discretion of the subsurface, are widely implemented using modern software and

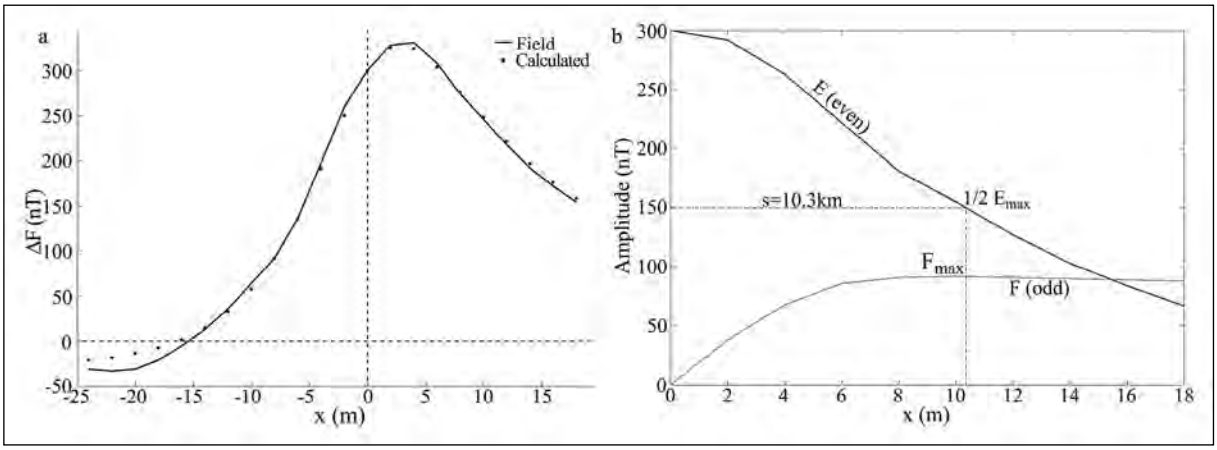

Figure 13- a) The total magnetic field anomaly over the western margin of Perth Basin (Atchuta Rao and Ram Babu, 1981; solid line) and the anomaly calculated using the model parameters recovered by the implementation of the proposed method (dots) and b) the even and odd component of the field anomaly for the vertical fault.

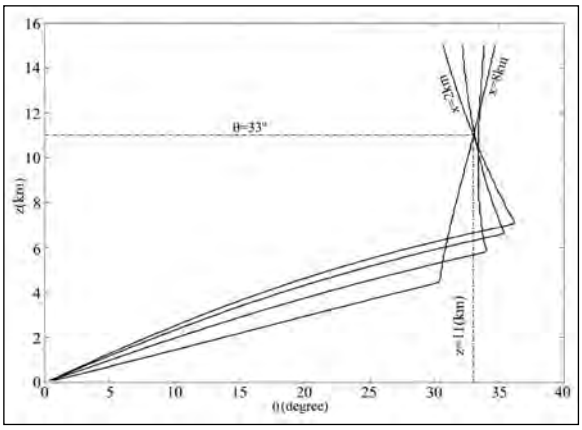

Figure 14- The set of curves obtained by the implementation of the proposed method.

methods, recovering dips and depths of structures correctly is rather difficult due to the lack of inherent depth resolution of the magnetic field data. Thus, graph and inversion methods, using simple structure geometries, are still implemented in recovering the parameters of the assumed structures.

The method implemented in this study, uses a graph based approach to recover model parameters from even and odd components of the measured data. Even though, the same approach can also be implemented using least-squares inversion, employing search via graphs method is equally effective since the calculations are fast and the non-uniqueness is rather low due to the assumed geometries.

The method estimates, depth, half-width and index parameters of dikes and vertical faults. The method is applied using even and odd components of the observed magnetic field anomaly. The method uses the ratio of the even component to the odd component for any distance x; this ratio becomes independent of the amplitude coefficient. The aim of the algorithm is to minimize the difference between the values obtained at several x distances for the observed data and the theoretical values calculated for different [θ , z] pairs. Since the true parameters are expected to minimize this difference for all distance values, parameters can be determined from the intersection of the curves obtained for different x distances. Then, half-width value (t) is calculated using Equation 4. The proposed graph method is found to be effective on both dipping dike and vertical fault models for the calculated synthetic datasets.

The implementation of the presented interpretation method on field data for vertical fault anomalies proved to be successful in recovering the model parameters very similar to the previous interpretations of the same data by Qureshi and Nalaye (1978), Atchuta Rao and Ram Babu (1981). For the vertical fault data, the recovered parameters are compared to the mentioned previous studies in Table 3.

When the parameters recovered for the dike anomaly, provided in Won (1981), are compared, all parameters except the dip angle are found to be very close. However, the similarity of the observed and the calculated anomalies (Figure 7), suggests that the discrepancy in the recovered dip angle is in acceptable limits.

5. Results

In this study, a graph method to recover parameters from magnetic field anomalies due to dipping dikes and vertical faults is presented. The noise-free and noisy theoretical data examples have shown that the proposed method can determine the related model parameters, justifying the method.

Table 3- The recovered model parameters of the vertical fault, recovered by the method proposed in this study, and the results of the previous studies.

Parameter	Qureshi and Nalaye (1978)	Achuta Rao and Ram Babu (1981)	Present Method
Depth (z) to top in km	6.85	7.2	6.88
Depth (z) to top in km	6.30	7.9	
Depth (H) to bottom in km	11.55	14.4	15.12
Depth (H) to bottom in km	16.50	15.7	
θ in degrees	-330	-315	-327 (33)

Since the true parameters are unknown, the field data examples are selected from previously interpreted data. Accordingly, data due to a diabase dike located in Durham Triassic Basin in North Carolina, USA, given in Won (1981), and data from a vertical fault in the western margin of Perth Basin, given in Atchuta Rao and Ram Babu (1981) are investigated, respectively.

The results have shown that the graph method described in this study is able to recover model parameters with values close to that of the previous studies. The only exception is determined for the dip angle of the diabase dike, the result of which was calculated to carry a 36.4° difference from the results given in Won (1981). However, the similarity between the observed and the calculated data shows that the given difference is within acceptable limits. The other parameters of the dike are obtained with values, which are very similar to that of Won (1981). For the data, collected over vertical fault, a more detailed comparison is realized since this data is interpreted in numerous studies. The comparison of results has shown that the method is able to recover all parameters of the given vertical fault successfully.

Considering synthetic and field data examples, the proposed graph method is found to be successful for recovering model parameters of dipping dikes and vertical faults from their magnetic anomalies.

Acknowledgements

This paper is dedicated by his co-authors to the memory of Prof. Dr. İbrahim KARA. From the moment we stepped into the university, he guided and treated us as his own children, and inspired us as educators and researchers.

References

Abdelrahman, E. M., Essa, K. S. 2015. A new method for depth and shape determinations from magnetic data. Pure and Applied Geophysics 172(2), 439-460.

Abo-Ezz, E. R., Essa, K. S. 2016. A least-squares minimization approach for model parameters estimate by using a new magnetic anomaly formula. Pure and Applied Geophysics 173(4), 1265–1278.

Atchuta Rao, D., Ram Babu, H. V. 1981. Nomograms for rapid evaluation of magnetic anomalies over long tabular bodies. Pure and Applied Geophysics 119(5), 1037-1050.

Bhimasankaram, V. L. S., Mohan, N. L., Seshagiri Rao, S. V. 1978. Interpretation of magnetic anomalies of dikes using Fourier transforms. Geoexploration 16(4), 259-266.

Essa, K. S., Elhussein, M. 2017. A new approach for the interpretation of magnetic data by a 2-D dipping dike. Journal of Applied Geophysics 136, 431–433.

Hutchison, R. D. 1958. Magnetic analysis by logarithmic curves. Geophysics 23(4), 749-769.

Kara, İ. 1997. Magnetic interpretation of two-dimensional dikes using integration- nomograms. Journal of Applied Geophysics 36(4), 175-180.

Kara, İ., Özdemir, M., Yüksel, F. A. 1996. Interpretation of magnetic anomalies of dikes using correlation factors. Pure and Applied Geophysics 147(4), 777-788.

Parker Gay, S. 1963. Standard curves for interpretation of magnetic anomalies over long tabular bodies. Geophysics 28(2), 161-200.

Qureshi, I. R., Nalaye, A. M. 1978. A method for the direct interpretation of magnetic anomalies caused by two-dimensional vertical faults. Geophysics 43, 179-188.

Rao, B. S. R., Murthy, I. V. R., Visweswara Rao, C. 1973. Two methods for computer interpretation of magnetic anomalies of dikes. Geophysics 38(4), 710-718.

Won, I. J. 1981. Application of Gauss's method to magnetic anomalies of dipping dikes. Geophysics 46(2), 211-215.

Bulletin of the Mineral Research and Exploration

http://bulletin.mta.gov.tr

Efficiency of singularity and PCA mapping of mineralization-related geochemical anomalies: a comparative study using BLEG and <180µm stream sediment geochemical data

Fatma Nuran SÖNMEZ[a*], Simay KOÇKAR[a] and Hüseyin YILMAZ[a]

[a]*Dokuz Eylül University, Faculty of Engineering, Department of Geological Engineering, Tınaztepe, Buca, 35160, İzmir, Türkiye*

Research Article

Keywords:
Singularity Mapping, C-A, N-S, PCA, Multi-Fractal Models, Eskişehir.

ABSTRACT

In gold (Au) exploration, the analysis of both bulk leach extractable gold (BLEG) and acid-extractable Au in the <180µm stream sediment fraction are the two most common approaches. The Eskişehir-Sivrihisar region in Western Türkiye hosts several orogenic type mineral deposits. The purpose of this study is to delineate geochemical anomalies of ore-related elements and track their dispersion, which may lead to discovery of unknown ore deposits. This research also compares the capability of conventional statistical and principal component analysis (PCA), with concentration area (C-A) and number-size/concentration (N-S/C) fractal methods as well as singularity index method to differentiate anomalous and background Au distributions. Known Au mineralization in the region of interest is strongly reflected in stream sediment BLEG Au patterns, which have robust singularity indices with C-A and N-S multifractal modeling and PCA. A hundred % of the Au deposits were detected using either BLEG Au and Ag singularity index mapping with C-A fractal analysis whereas the factor analysis of which revealed 85% efficiency. Several strong Au-Ag anomalies defined by the singularity index and factor analysis in this study requires further follow up for the discovery of new deposits.

Received Date: 03.02.2021
Accepted Date: 15.06.2021

1. Introduction

Identification of significant mineralization-related geochemical patterns or anomalies is of great importance in ore deposit exploration. Several statistical methods have been investigated for generating robust geochemical anomaly maps and models from geochemical exploration data. These include conventional parametric and non-parametric methods (Sinclair, 1991; Govett et al., 1975), and alternative techniques that are not dependent on data distribution types or affected by the presence of outlying populations including fractal modelling (Mandelbrot, 1983; Cheng et al., 1996; Afzal et al., 2011; Zuo, 2011; Sadeghi et al., 2015) and catchment basin analysis (Bonham-Carter et al., 1987; Carranza, 2010*a*). In recent years there has been a move towards latter as a more robust approach in the recognition of significant geochemical anomalies (Cheng et al., 1994; Grunsky, 2007, 2010; Carranza, 2010*b*; Zuo and Wang, 2016). In relation, there is also the need to consider spatial patterns and other processes that can lead to complexity in defining geochemically anomalous behavior (Zuo et al., 2013; Parsa et al., 2017*a*; Yılmaz et al., 2019). Explatory Data Analysis (EDA) methods are not as robust as fractal modelling

Citation Info: Sönmez, N. F., Koçkar, S., Yılmaz, H. 2022. Efficiency of singularity and PCA mapping of mineralization-related geochemical anomalies: a comparative study using BLEG and <180mm stream sediment geochemical data. Bulletin of the Mineral Research and Exploration 168, 11-33. https://doi.org/10.19111/bulletinofmre.955280

**Corresponding author: Fatma Nuran SÖNMEZ, nuran.sonmez@deu.edu.tr*

in case of sparse geochemical data. Most EDA methods ignore spatial relations between geochemical data whereas fractal modelling can be designed so as to consider spatial relationships between regolith geochemistry and known mineral deposits (Agterberg et al., 1990).

Fractal modelling uses the complete geochemical data set without the necessity of transformations to meet assumptions about data distribution and effects of outliers (Luz et al., 2014). Fractal modelling is predicted on power-law distribution, which means that some statistical characteristics of the data are invariant (self-similar) at different scales (Mandelbrot, 1983; Shen and Cohen 2005). Fractal models that have gained a considerable application in delineating geochemical anomalies are the number-size (N-S) concentration-area (C-A), singularity indexes (SI) and concentration-volume (C-V) (Mandelbrot, 1983; Cheng et al., 1996, 2000; Cheng, 2007; Afzal et al., 2010; Daneshvar, 2017; Yasrebi and Hezarkhani, 2019; Zadmehr and Shahrokhi, 2019; Aliyari et al., 2020; Mirzaie et al., 2020; Ahmadi et al., 2021). Afzal et al. (2013) delineated different Au mineralized zones in the Qolqoleh orogenic gold deposit by the C–V fractal model. They emphasized that extremely highly mineralized Au zones identified by the C–V fractal model had a positive correlation with meta-volcanic rocks whereas moderately mineralized zones correlate with sericite schist in the Qolqoeh (Iran) deposit. Similarly, Mirzaie et al. (2020) determined the zones based on ores and gangues by using a combination of fractal and factor analysis in the Chah Gaz iron ore (Central Iran). They successfully differentiated waste material from ore zones for proper exploitation. In other words, the C-V fractal modeling, which has been used for the classification of different populations including parameters such as regionalized variables of environment and economy used to identify zones of mineralization in various ores (Mirzaie et al., 2020). Zadmehr and Shahrokhi (2019) has re-discovered Qolqoleh, Kervian and Qabaghloujeh (Iran) Au deposits using concentration-area (C-A) and concentration-number (C-N)-categorized Au, As, Hg and Bi anomalies. They showed that C-A and C-N fractal-modeled anomalous results had a very strong correlation with rock units including highly deformed acidic and basic metavolcanic and sericite schists. Shuguang et al. (2015) has classified fractal or multifractal approaches employed in geochemical anomaly definition into hard- and soft-threshold techniques. The hard-threshold group includes N-S and C-A fractal models with clear-cut thresholds to define population breaks and identify anomalies but fails to identify more subtle changes in fractal behavior typical of complicated or composite geological environments (Zuo et al., 2013). The soft-threshold methods include S-A and SI multifractal techniques. These filtering methods improve the reliability in setting thresholds for geochemically anomalous populations but are unable to determine thresholds for the separation of geochemical populations (Zuo and Wang, 2016). Thus, geochemical signatures generated by the S-A and singularity mapping methods essentially require additional calibration of geochemical values to adjust for potential dilution effects following the concepts of Hawkes (1976). For stream sediment geochemistry sediment dilution in drainage must also be taken into account as a potential factor in setting thresholds to background Au distributions. The typical approach is to use catchment area weighting This study compares the results of selected conventional and fractal methods to define anomalous catchments based on both raw and catchment-weighted BLEG Au and Ag values well as <180µm Au, Ag, Cu, Pb, Zn, As and Sb values. Verification of the results attained can be employed utilizing geochemical properties of already discovered gold deposits and prospects along with the rock chip samples in the area.

2. Study Area and Data

2.1. Regional Geology and Tectonic Setting

The study area of ~2.662 km^2 is situated in the Eskisehir region of Western Türkiye. It is underlain by three major ore-hosting tectono-stratigraphic units (Figure 1). These are: a) the Precambrian to Lower Paleozoic undifferentiated high-grade unit consisting of gneiss, metagranite, schist, amphibolite and marble, which are cut by Upper Paleozoic granitoids; b) the Triassic Karakaya Complex containing low-grade schists and marbles with meta-sandstone, meta-mudstone, and meta-volcanic/volcanic intercalations (Altıner et al., 1991; Okay et al., 1996) and c) Jurassic-Cretaceous ophiolites or accretionary meta-clastic rocks intruded by Cenozoic magmatic units (Okay and Satır, 2000; Yılmaz, 2003). The low-grade schists and

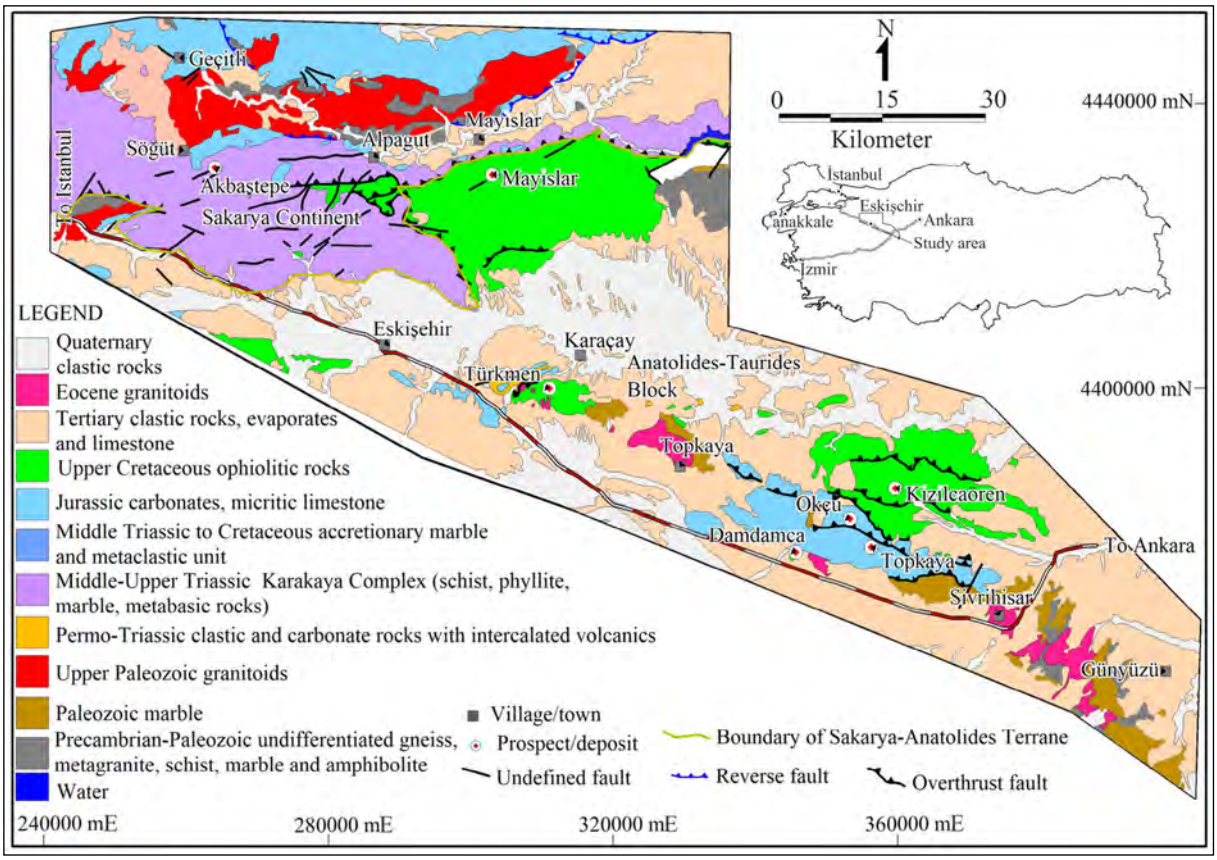

Figure 1- Simplified geological map of the Karakaya Formation, Cenozoic volcano- plutonic field and sedimentary cover rocks in Eskişehir-Sivrihisar region, location of the study area and significant mineralizations (after Okay et al., 1996; Okay and Satır, 2000; MTA, 2002; Yılmaz, 2003 and this study).

marbles are considered parts of the Karakaya Complex (Okay et al., 1996). The Karakaya Complex contains metamorphosed mafic rocks, which are intercalated with phyllite and marble, and was strongly affected by Alpine north-south-trending compressional tectonics during the Upper Cretaceous-Eocene.

2.2. Local Geology and Mineralization

The Karakaya Complex hosts the probable orogenic-type Akbaştepe Au-As-Sb-W deposit (SE of Söğüt; MTA, 1965, 1970; Yılmaz, 2003), as well as the epithermal-style Damdamca and Topkaya Au-Ag deposits to the NW of Sivrihisar, and the Mayıslar and Türkmen deposits (Table 1). In the Akbaştepe deposit, Au mineralization is contained in quartz veins, with peak grades of 20 g/t Au over a 220 m strike length and width of 2 m (Eurogold, 1996) in low- grade schists and marbles. The Damdamca and Topkaya Au-Ag-As deposits have a combined indicated resource of 1.454 Mt at 4.07 g/t Au, and a resource of 1.950 Mt at 4.9 g/t Au (Koza Gold, 2013). The Damdamca deposit is hosted in a serpentinite block, being sandwiched between the Damdamca granite and meta-clastic rocks whereas the Topkaya deposit is hosted in marble and meta-clastic rocks. Both deposits occur in the footwall of a south-verging thrust (Yılmaz, 2003).

The sub-economic Mayıslar polymetallic Cu-Pb-Zn-As-Mo is hosted in Eocene andesite and tectonically emplaced Cretaceous ophiolites (Parlak and Sayılı, 2012). In the deposit, altered (silicified, seriticized, argillized) andesites, which are enriched in tourmaline, are intersected by quartz and calcite veins. According to Parlak and Sayılı (2012), the alteration mineralogy is characterized by the presence of high temperature quartz and sericite forming between 270 and 370 °C and, sericite. The ore mineralogy and the presence of tourmaline suggest the possibility of a buried granitoid intrusion somewhere at depth (Parlak and Sayılı, 2012).

Table 1- Characteristics of and reserve or resource data for orogenic precious/base metal deposits and prospects in Eskişehir-Sivrihisar region, Western Türkiye.

Name	Commodity	Tectonic belt	Host rock	Deposit Type	Age of host rock	Ore body and Structure	Mineral reserve/resources	Status	Reference
Türkmen	Pb, Zn, Ag, Cu, As, Mo	Anatolid-Taurid	Granodiorite, monzodirite porphyry	Epithermal (Orogenic)	Eocene	Not known	Very significant Cu, Pb, Zn, Ag, Mo, As in soil	Prospect	Yılmaz, 2003
Mayıslar	Pb, Zn, Ag, Cu, As, Mo, Sb	Karakaya	Diorite porphyry, microdiorite	Porphyry (intrusion-related)	Eocene	Quartz veinlet	0.5 g/t Au (grab sample)	Prospect	Parlak and Sayılı, 2012
Kızılcaören	REE, Th, Ag	Anatolid-Taurid	Metasandstones, pyroclastics, trachytic porphyry, phonolites	Epithermal (volcanogenic)	Oligo-Miocene	Infilling of radial circular and funnel shaped fractures and five breccia pipes with fluorite, barite and REE	30 Mt@3.14% REE, 37.44% CaF2,31.04% BaSO4; 0.384 Mt@0.212% ThO2 in bastnasite	Prospect	Özgenç, 1993
Okcu	Ag	Anatolid-Taurid	Marble, metaclastic, metacarbonate	Epithermal (Orogenic)	Mesozoic	Silicified carbonates, metacarbonate	Rockchip (max): 11 g/t Ag	Prospect	Eurogold, 1996
Damdamca	Au, Ag, As	Anatolid-Taurid	Marble, metaclastic, metacarbonate	Epithermal (Orogenic Listwanite)	Mesozoic	Quartz vein/veinlet, breccia and replacement in silica-carbonate altered ophiolitic rocks associated with EW-trending thrust faults and shearings	Resource indicated: 1.454 Mt@ 4.07 g/t Au, 4.98 g/t Ag; Resource indicated and inferred: 1.950 Mt@ 4.9 g/t Au, 4.49 g/t Ag	Operating Mine	Koza Gold, 2013
Topkaya	Au, Ag, As	Anatolid-Taurid	Marble, metaclastic, metacarbonate	Epithermal (Orogenic Listwanite)	Mesozoic	Quartz vein/veinlet, breccia and replacement in silica-carbonate altered ophiolitic rocks associated with EW-trending thrust faults and shearings	Included in the above resource	Operating Mine	Koza Gold, 2014
Akbaştepe	Au, As, Sb, W	Upper Paleozoic metamorphic schists and marble	Sakarya continent	Mesothermal (Orogenic)	Permo-Triassic	Quartz vein/veinlet, breccia and replacement in carbonate rocks associated with EW-trending thrust faults and shearings	Resource indicated: 1.943 Mt@ 12.5 g/t Au; Resource inferred: 2.788 Mt@ 10.5 g/t Au, with 1.5 Moz contained Au	Developing Mine	Koza Gold, 2016; AK yatırım report, 2018

The Türkmen deposit is located 6 km north of Türkmentokat village and is underlain by Upper Cretaceous ophiolites intruded by Eocene granodiorite porphyries. Altered serpentinite hosts quartz stockwork containing abundant sphalerite, galena and pyrite, and minor chalcopyrite and arsenopyrite (Eurogold, 1996; Yılmaz, 2003). An Fe-oxide-altered silica cap overlies the intrusive rocks. The Türkmen mineralization has similarities with porphyry intrusive-related skarn systems containing a proximal Pb-Zn-Ag-Cu±Au-Mo-W), peripheral Au-Zn-Pb-As, and distal Pb-Zn-Ag-Au skarn replacements (Yılmaz, 2003). However, proximal or distal skarn alteration and metal-bearing stockwork quartz veins/veinlets in the porphyry intrusions or serpentinites has not been recognized yet.

3. Sampling and Chemical Analysis

A total of 258 BLEG, 612 - <180µm stream sediment and 65 rock chip samples were obtained from the Sivrihisar-Eskişehir region. BLEG sampling was conducted at a density of ~1 sample per 10 km^2 depending on stream system morphology, with sites selection designed to exclude sediment input from higher order streams (Figure 2). The BLEG results were followed up by collecting -180um stream sediment samples from higher order streams at a density of 4 samples per square km. Sampling and analytical techniques as well as precision set by Eurogold according to Howarth (1983) for BLEG and 180µm stream sediment were discussed in detail by Yılmaz et al. (2019) and therefore, the reader is referred to the article cited hereby. Digital geology was provided by MTA (2002). Singularity mapping was carried out by using A MATLAB-based code. C-A and N-S calculations were completed in Excel and PCA using SPSS. Interpolation data for rastering was carried out using ArcMap10.5.

4. Multifractal Modeling Methods

The C-A and N-S fractial models were used to separate populations in the geochemical data. Although such hard methods are used in the separation of geochemical populations, they are inefficient in recognizing settled and composite anomalies (Zuo and Wang, 2016). As for the soft threshold techniques, they applied spectrum-area (S-A) model and singularity mapping (SM). However, SM method has been widely used while returning robust meaningful results during statistical treatment of geochemical data (Zuo et al., 2013). On the other hand, the soft techniques are filtering methods and unearth the weak and complex geochemical signatures camouflaged by extreme values in the area under investigation (Parsa et al., 2017*b*). It is suggested that the soft-threshold techniques may first be used to increase ability of anticipating the

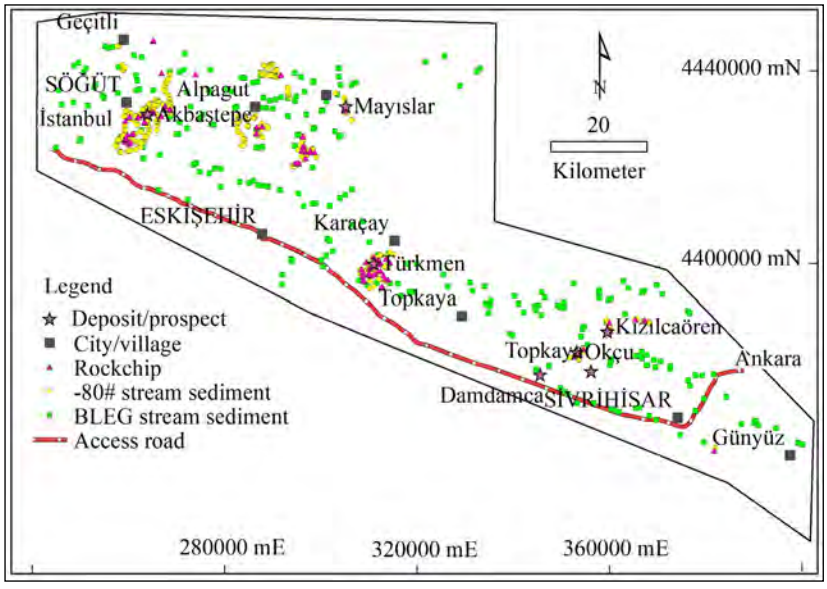

Figure 2- Location of major mineral deposits and prospects along with sampling sites for BLEG stream sediments, <180µm stream sediments and rock chips.

geochemical signatures and thereafter, hard-threshold techniques are used for the separation of multifractal geochemical anomalies. The singularity processes related to mineralizing events are, by definition, associated with accumulation of highly elevated metal concentrations within a narrow spatial-temporal interval (Halsey et al., 1986). More specifically, weak anomalies, which were not recognized because of the influences of strong background deviations or deep burial (Wang et al., 2018) can be robustly delineated. Cheng (2007) also strongly emphasized that the concept of singularity and the singularity technique are useful in delineating anomalies stemmed from mineralization and thereby predicting the locations of undiscovered ore deposits. Theory and concept of the SI (Singularity index) fractal method are described by numerous authors (Halsey et al., 1986; Cheng, 2007; Zuo and Wang, 2016; Parsa et al., 2017*a*; Yılmaz et al., 2019) and therefore, it is not necessary to repeat them in hereat.

5. Results

5.1. Delineation of BLEG and <180µm Stream Sediment Geochemical Anomalies

5.1.1. Descriptive Statistics

Histograms and Q-Q plots of BLEG Au and Ag in BLEG and Au, Ag, Cu, Pb, Zn, As and Sb in the <180µm stream sediment, along with key statistical parameters are presented in the Supplement (Supplementary Table 1 and Figures 1, 2 and 3).

5.1.2. Concentration-Area (C-A) Fractal Statistics

If the study area is treated as one mineral district without considering the effects of changing geology on geochemical background weak geochemical anomalies would not be recognized by means of Inverse Distance Weighting (IDW) because they will be camouflaged within the background variance (Arias et al., 2012). Based on log-log plots of element concentrations versus cell area with values greater than a concentration value (Figure 3) C-A plots for

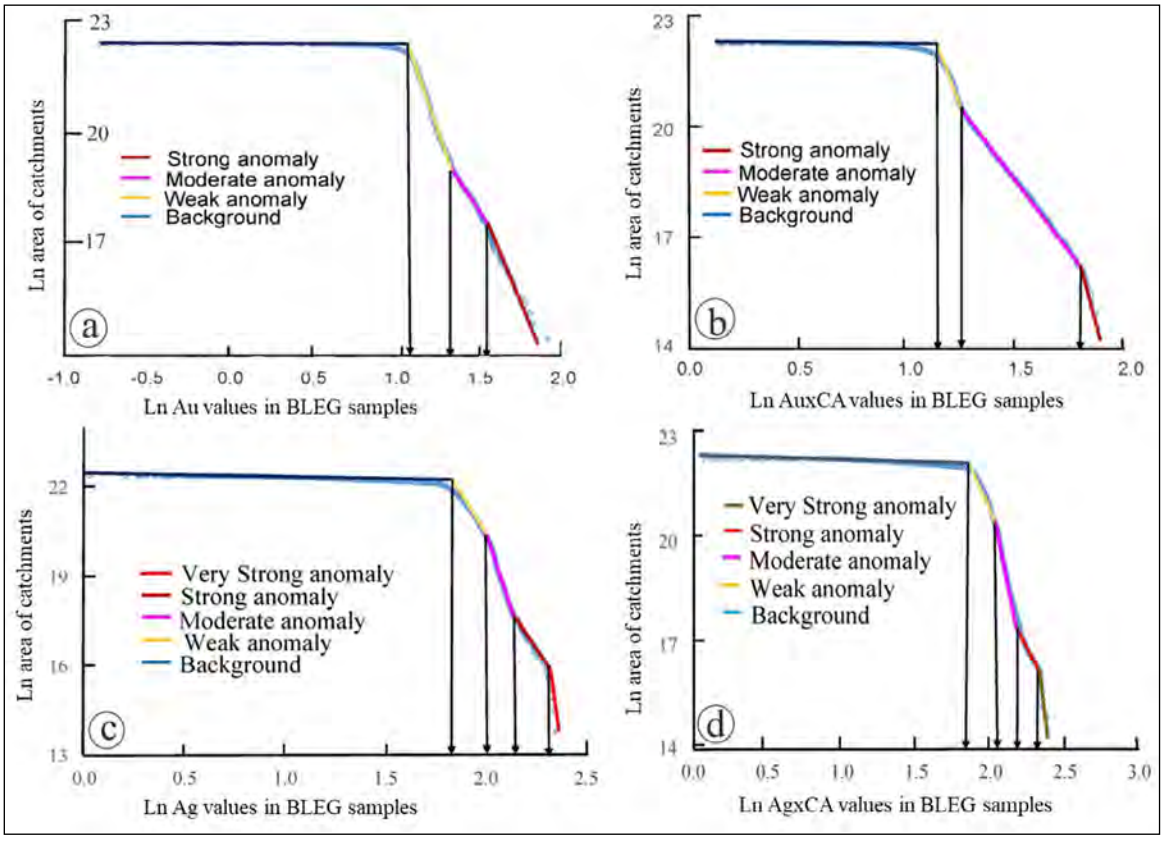

Figure 3- Ln-transformed C-A fractal model of ; a) Au, b) AuxCA; c) Ag and, d) AgxCA in BLEG samples.

BLEG Au and AuxCA may be modeled with four (4) straight lines segments whereas C-A plots for BLEG Ag and AgxCA can be modeled with five (5) straight lines segments. For Au and AuxCA (Figure 3a, b) the left-hand line segment represents backgrounds whereas the two middle line segments represent low to moderate anomalies and the right-hand line segments represent strong anomalies (Figure 3a, b). For Ag and AgxCA (Figure 3c, d) the left-hand line segment represents backgrounds whereas the three middle line segments (Figure 3c, d) represent low to strong anomalies and the right-hand line segments represents very strong anomalies. Figure 4 shows spatial distribution of BLEG Au, AuxCA, Ag and AgxCA background, weak, moderate, strong and very strong anomalies defined by C-A fractal modeling (Figure 3) and their relationship to already known deposits/prospects. As is shown in Figure 4, moderate Au and AuxCA anomalies encompass whole deposits/prospects (Figure 4c, d) whereas strong and very strong Ag and AgxCA anomalies (Figure 4c, d) cover 85% of the deposits/prospects.

5.1.3. Spatial Patterns of Multi-Element Geochemical Signatures Using C-A Statistics Model

In this study in order to extract enhanced multi-element geochemical signatures, ordinary PC as a multivariate analysis tool was applied to log-transformed data of 7 elements including Au, Ag, As, Sb, Cu, Pb and Zn from <180µm stream sediments. Geochemical associations related to different deposit types and geochemical processes in stream systems may be obtained using PC, some of which may be interpreted as pathfinders for the deposit type including Au, Ag, As, Sb, Cu, Pb and Zn from <180µm stream sediments. Geochemical associations related to different deposit types and geochemical processes in stream systems may be obtained using PC, some of which may be interpreted as pathfinders for the deposit type sought. As illustrated in Table 2, three components were extracted based on the significant eigenvalues (>0.9). The PCA results demonstrated that the log-transformed <180µm stream sediments data were classified into the following two

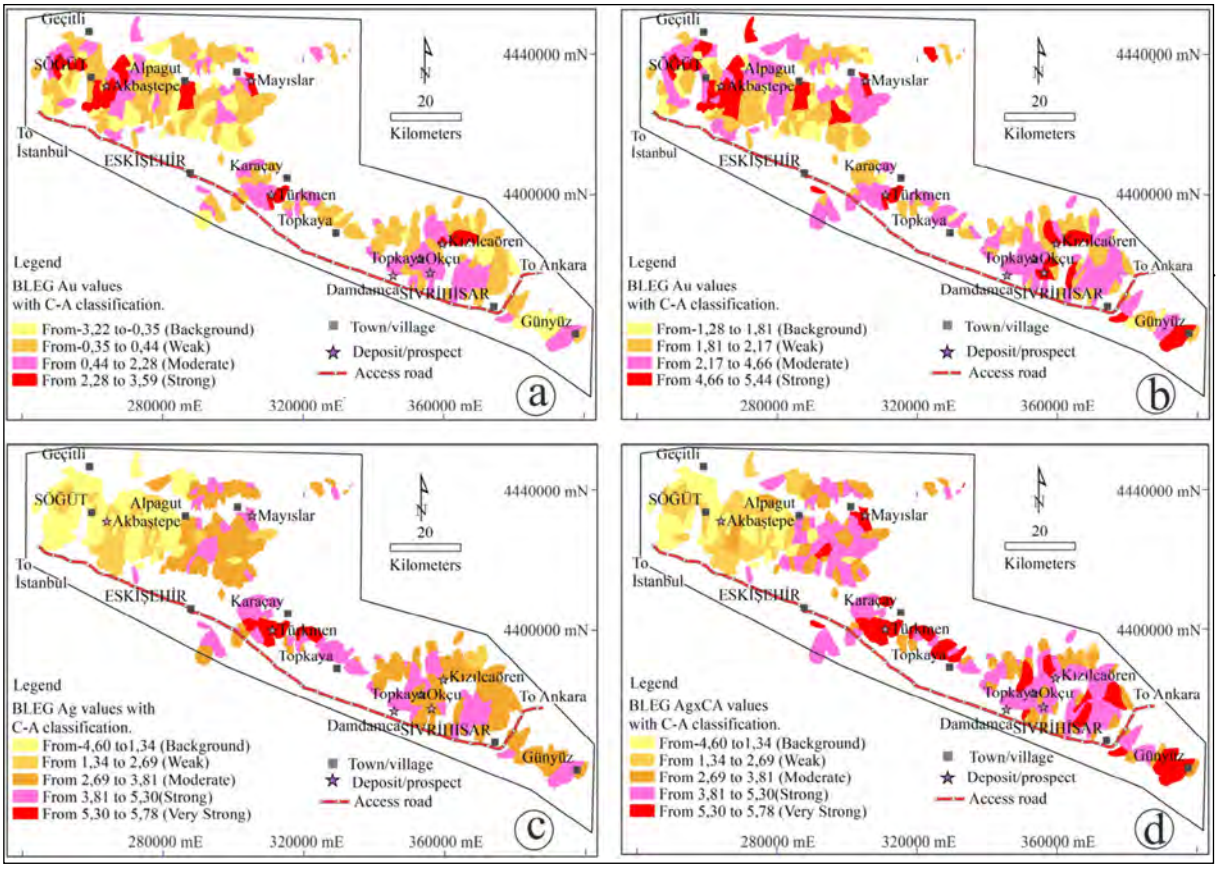

Figure 4- Geochemical maps of Ln-transformed BLEG; a) Au, b) AuxCA, c) Ag and, d) AgxCA obtained from C-A multifractal modeling.

PC2 account for ~30% and ~28% of total variability, respectively. Gold, Cu, Pb, Zn and As have significant positive PCA1 loadings and represents the effects of a mixture of orogenic, porphyry and skarn-related mineralization- in the study area. PC2 is representative of Ag and Sb mineralization. C-A and N-S fractal models were applied to the PCA scores (Figure 8) for comparison with the BLEG and BLEG Au-AgxCA and BLEGxCA Au-Ag models. The C-A fractal model indicated four BLEG Au-Ag or BLEGxCA Au-Ag populations (Figure 5). The N-S fractal model of PC1 returned 5 distinct geochemical populations of strong, moderate and weak anomalies plus background and low background for Au in <180µm data (Figure 5e, f) whereas PC2 of the <180µm stream sediment data was classified into 3 populations. Gold deposits/prospects of the area are mainly confined to the moderate to strong anomalous zones of PC1 BLEG data whereas the Akbaştepe deposit is located in the background zone of PC1 of BLEGxCA data with others occurring mostly in moderately anomalous zones (Figure 5b, d). The efficiency of PCA method is evaluated using five mineral deposits/prospects. Four of these deposits/prospects of the study area fall over the moderate to strongly anomalous zones of PC1 with positive Au-Cu-Pb-Zn-As loadings ≥ 0.5 (80% efficiency) whereas PC2 has 40% efficiency (Figure 5e-h). From geological index point of view both principal components represent Au mineralization in the area and anomalous contents of these components coincide with metamorphic (i.e. Akbaştepe) and ophiolitic rock (i.e. Mayıslar, Türkmen) types that host Au deposits and base metal prospects, respectively.

5.1.4. Spatial Patterns of Mono-Element Geochemical Signatures Using C-A and N-S Statistics Model in BLEG and <180µm Stream Sediment Data.

To augment the geochemical characteristics, the singularity mapping has been implemented to the geochemical results of BLEG and <180µm stream sediment samples. Five window sizes with minimum size of ri = 500 m and an interval of 500 m were used to determine singularity indices in the study area and the singularity index (α values) specific to each catchment basins obtained (Yılmaz et al., 2019). Gold and AuxCA α values ranged from 1.13 to 2.66 and 1.17 to 3.26, respectively whereas for Ag and AgxCA ranged from 1.17 to 3.27 and 0.95 to 3.62, respectively. The C-A fractal model of singularity indexes (Figure 6) indicated four distinct Au geochemical populations for BLEG Au data (Figure 6a). Likewise, the c-a fractal model has identified 5 geochemical groups ranging from strong through moderate to weak anomalies as well as background and low backgrounds for AuxCA, Ag and AgxCA (Figure 6b, c, d). Figure 6e, f, g, h also illustrates the areal dispersal of identified geochemical groups. Known gold mineralizations in the study area are confined to the strong and moderate Au and AuxCA BLEG anomaly zones (Figure 6e, f). Singularity anomaly patterns coincide much on pointing to mineralization and carbonate-mica altered metamorphic rocks in the western part (Akbaştepe/Söğüt), argillic-chlorite-talc-altered ophilites in the central part (Türkmen) and argillic-altered high-pressure metamorphic rocks in the eastern part (Topkaya, Damdamca, Okçu, Kızılören) of the study area.

Table 2- Rotated component matrix PCA on Ln-logarithmically transformed data. Loadings in bold exhibit significant geochemical indicators.

Element	PC1	PC2	PC3
Au	0.501	–0.398	0.448
Ag	–0.11	0.752	0.228
Cu	0.683	0.039	0.381
Pb	0.522	–0.654	–0.24
Zn	0.810	0.242	0.094
As	0.603	0.259	–0.651
Sb	0.290	0.813	–0.023
Eigenvalue	2.206	1.338	0.901
Var.%	29.725	27.711	12.705
Var.% cum.	29.725	57.435	70.141

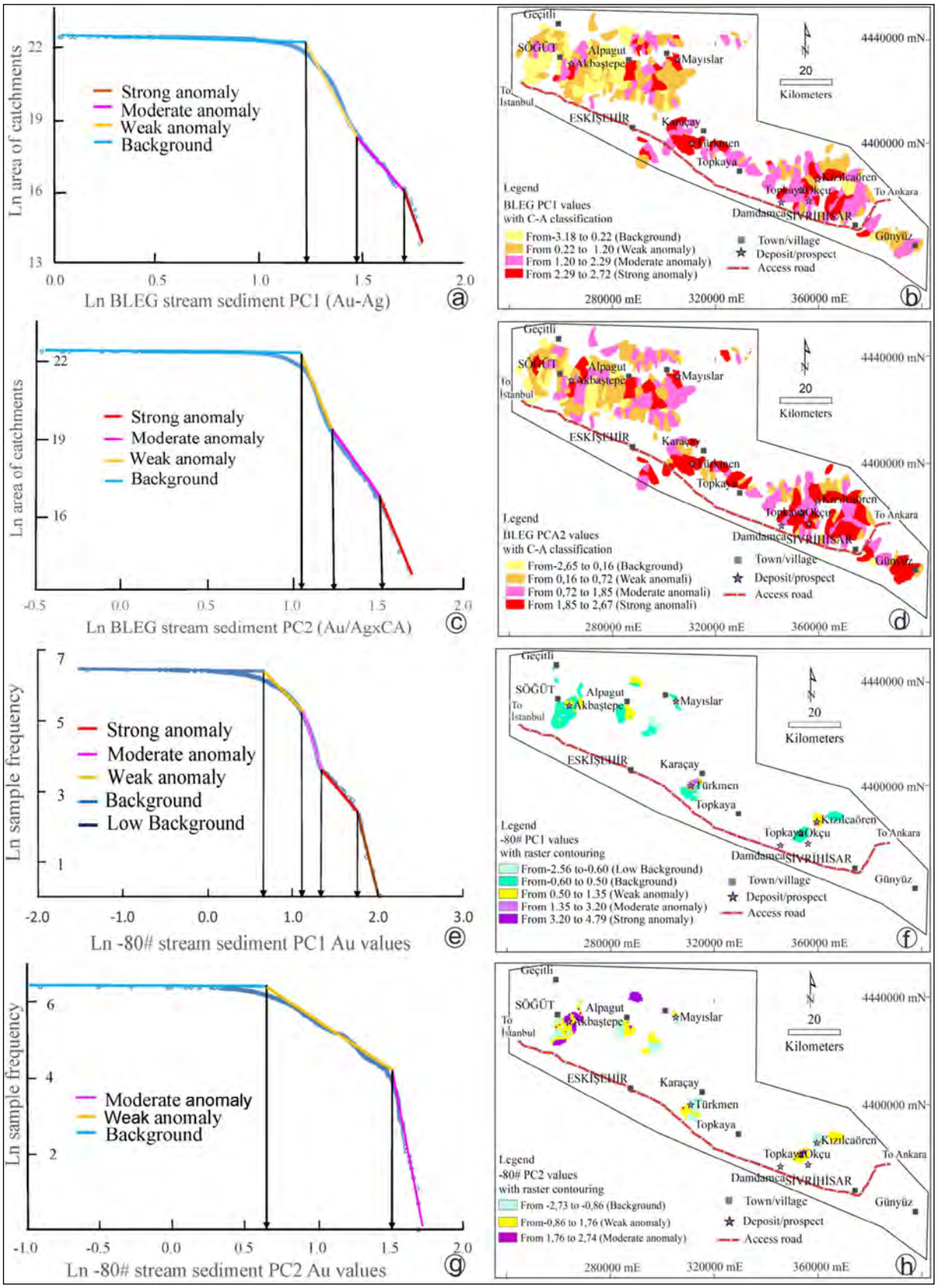

Figure 5- a), b) PC1 with fractal models and delineated geochemical anomaly population maps of Au, c), d) AuxCA in BLEG samples, e), f) PC1 and PCA2 with fractal models and delineated geochemical anomaly population maps of loaded Au+Cu+Pb+Zn+As and, g), h) Ag+Sb in <180µm stream sediment samples.

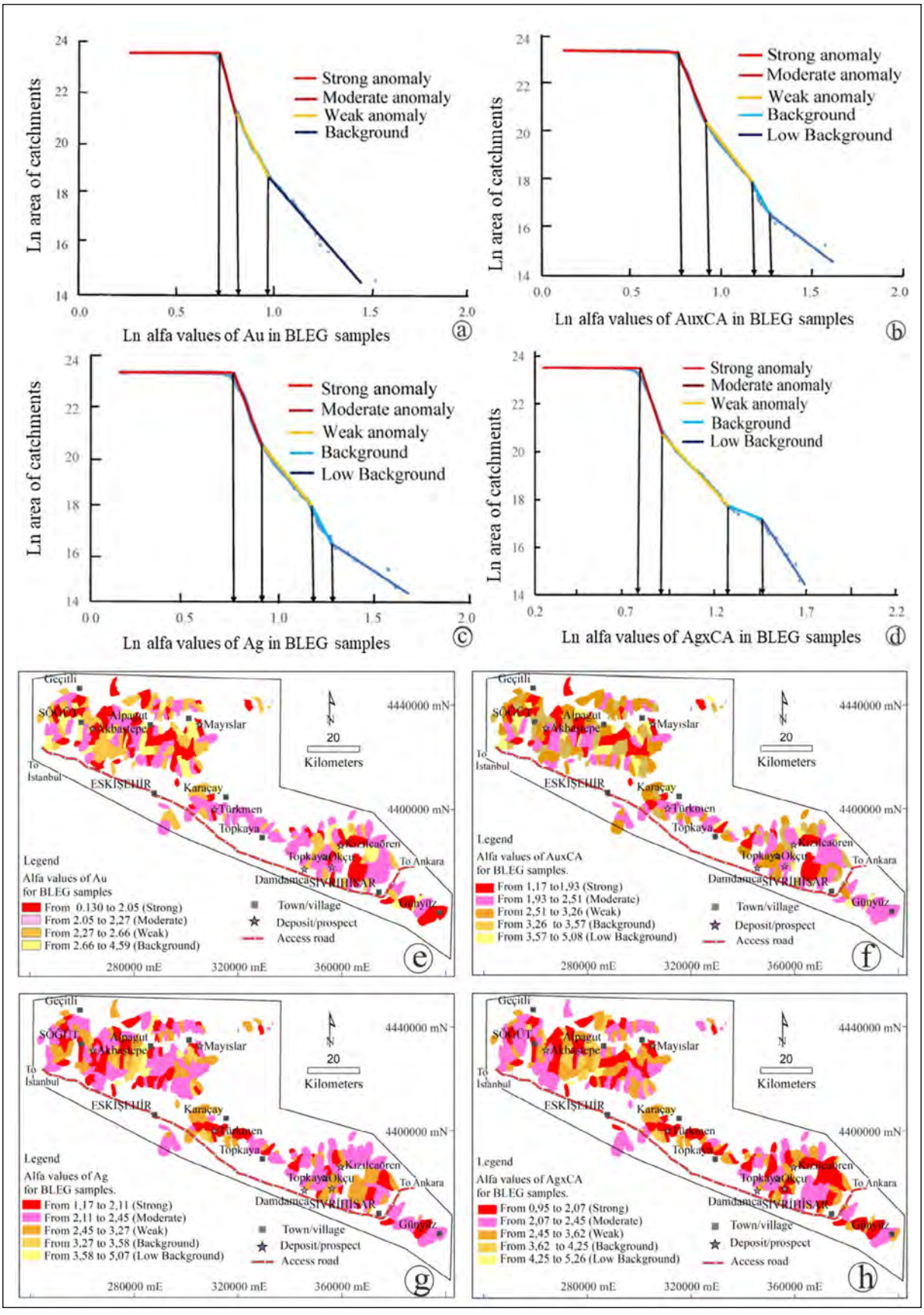

Figure 6- C-A fractal model applied to singularity indexes of; a) Au, b) AuxCA, c) Ag, d) AgxCA, e) delineated geochemical anomaly population of Au, f) AuxCA, g) Ag and h) AgxCA in BLEG samples.

5.1.5. Delineation of <180µm Stream Sediment Geochemical Anomalies

<180 um stream sediment samples were analyzed for Au, Cu, Pb, Zn As and Sb. The descriptive statistics of these elements has shown that they have positively skewed distributions (Supplementary Table 1) and thus they likely contain multiple populations. Therefore, multifractal analysis was implemented to delineate geochemical populations of these elements, which are related to mineralization. The procedure as applied to BLEG data, the results of geochemical analyses of <180µm stream sediments were initially subjected to singularity multifractal technique, with the window and interval size similar to procedure as applied to the BLEG data. To model the areal dispersion of the SI α values, a square window-based singularity mapping technique was applied as individual samples cannot be directly linked to unique catchment basins. Hence the N-S fractal model was used for the <180µm data. Four different classes of geochemical signatures of Au, As, Sb were obtained using N-S fractal model (Figure 7a, f, g) whereas the 5 geochemical populations were received for the geochemical signature of Ag, Cu, Pb and Zn in stream sediment data (Figure 7b c, d, e). The geographical dispersion maps of <180µm stream sediment α-Au, α-Cu, α-Ag, α-Pb, α-Zn, α-As and α-Sb shows the anomalies with low singularity values (Figure 8). Akbaştepe, Mayıslar, Türkmen, Okçu and Kızılcaören deposits fall over the areas with low α-Au, α-Ag, α-Zn singularity values whereas Türkmen base metal deposit is defined by high α-Au, α-Cu, α-Ag, α-Pb, α-Zn, α-As and α-Sb singularity values. To quantitatively measure the geographical correlation between areas with α and the locality of known Au deposits, the singularity maps of Au, Ag, Cu, Pb, Zn, As and Sb (Figure 8a-g), and the α values were recategorized implementing the N-S fractal model. The known gold deposits were nearly related to the lower α values (mostly less<2.2) of Au, Ag, Cu, Pb, Zn, As and Sb (Figure 8) despite of the slightly differing geographic distribution of Au, Cu, Pb, Zn, As and Sb anomalies. Besides, 100% (5), 100% (5), 60% (3), 80% (4), 100% (5), 100% (5), 60% (3) of known deposits coincide with the moderate to strong anomalies of Au, Ag, Cu, Pb, Zn, As and Sb, respectively (Figure 9). This suggests that Au, Ag, Pb, Zn and As are suitable pathfinder elements in the study area as the singularity mapping technique may recognize precious/base metal deposits/prospects.

5.1.6. Verification of the Anomalies Delineated

Figure 9 shows the efficiency assessment of the delineated BLEG and <180µm stream sediment geochemical anomalies regarding the known gold prospects and deposits of the study area. According to Figures 3-8, >85% of known gold and base metal deposits are located within the Au, AuxCA, Ag and AgxCA based on the singularity index, C-A fractal analysis and PCA. However, these values are highly variable for <180µm stream sediment data. 100% of the known deposits are located within the anomalous zones of <180µm stream sediment Zn, As and Sb based on singularity and log-transformed data with N-S fractal modeling (Figure 9). Besides, singularity index and log-transformed data of <180µm Ag and Cu with N-S fractal modeling also returned moderate to strong anomalies encompassing 100% of the deposits and prospects. Interpretation of rock sample results verify the power of the BLEG and <180µm stream sediment sampling in accurate detection of orogenic Au-As-Sb-W (Akbaştepe), Cu-Pb-Zn-As-Mo (Mayıslar), Cu-Pb-Zn-Ag-As-Sb-Au (Türkmen) and Au-Ag deposits (west of Sivrihisar Town). The anomalous zones (strong-moderate anomaly) of BLEG Au suggest that these areas deserve additional exploration campaigns. The BLEG and <180µm stream sediment geochemical Au and Ag as well as base metal anomalies recognized are encompassed by illite-sericite-silica-bearing rocks, and therefore, are of high-priority targets for supplementary exploration in addition to the already discovered occurrences (Figures 3-8).

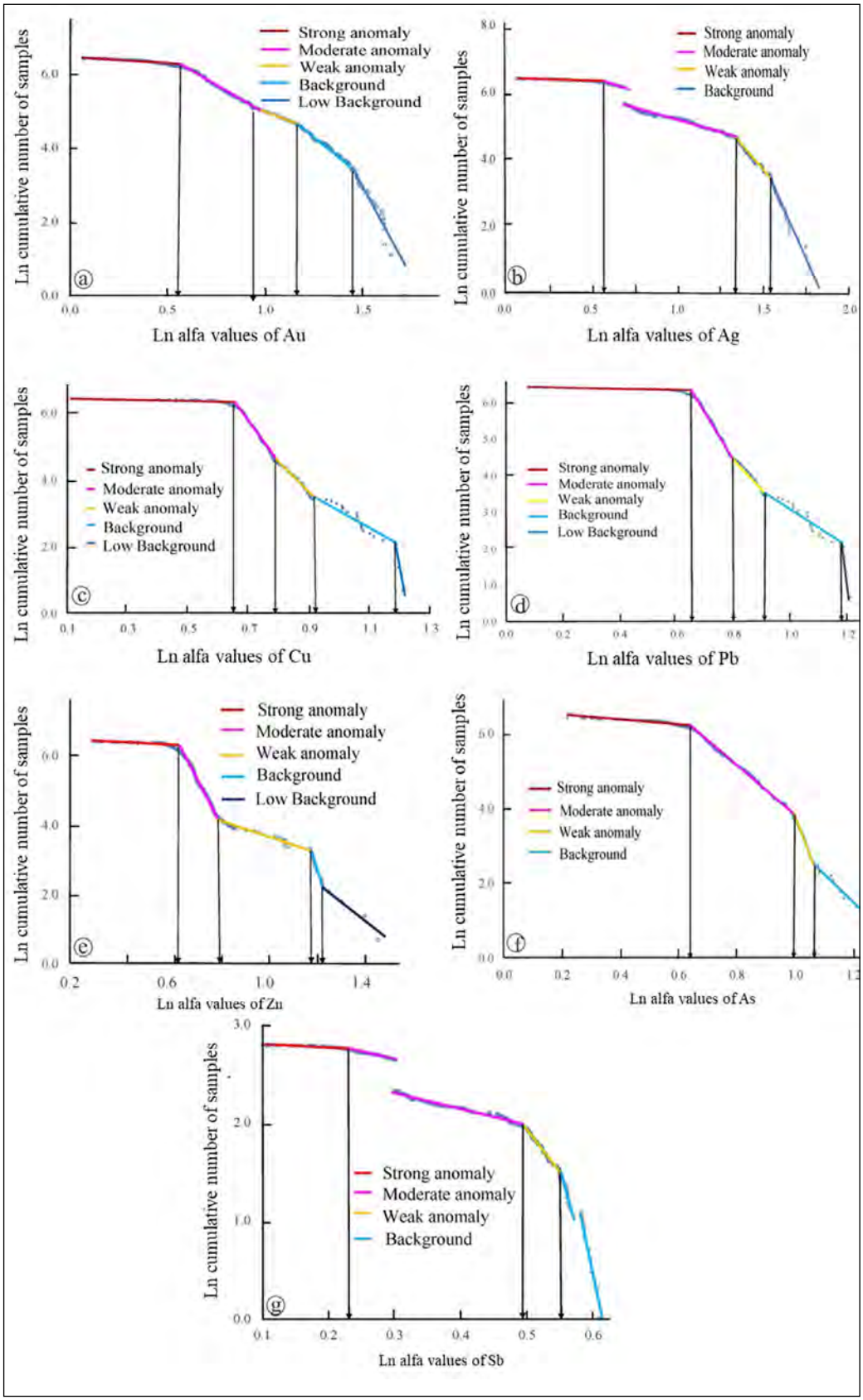

Figure 7- N-S fractal model applied to singularity indexes of; a) Au, b) Ag, c) Cu, d) Pb, e) Zn, f) As and, g) Sb in <180µm stream sediment samples.

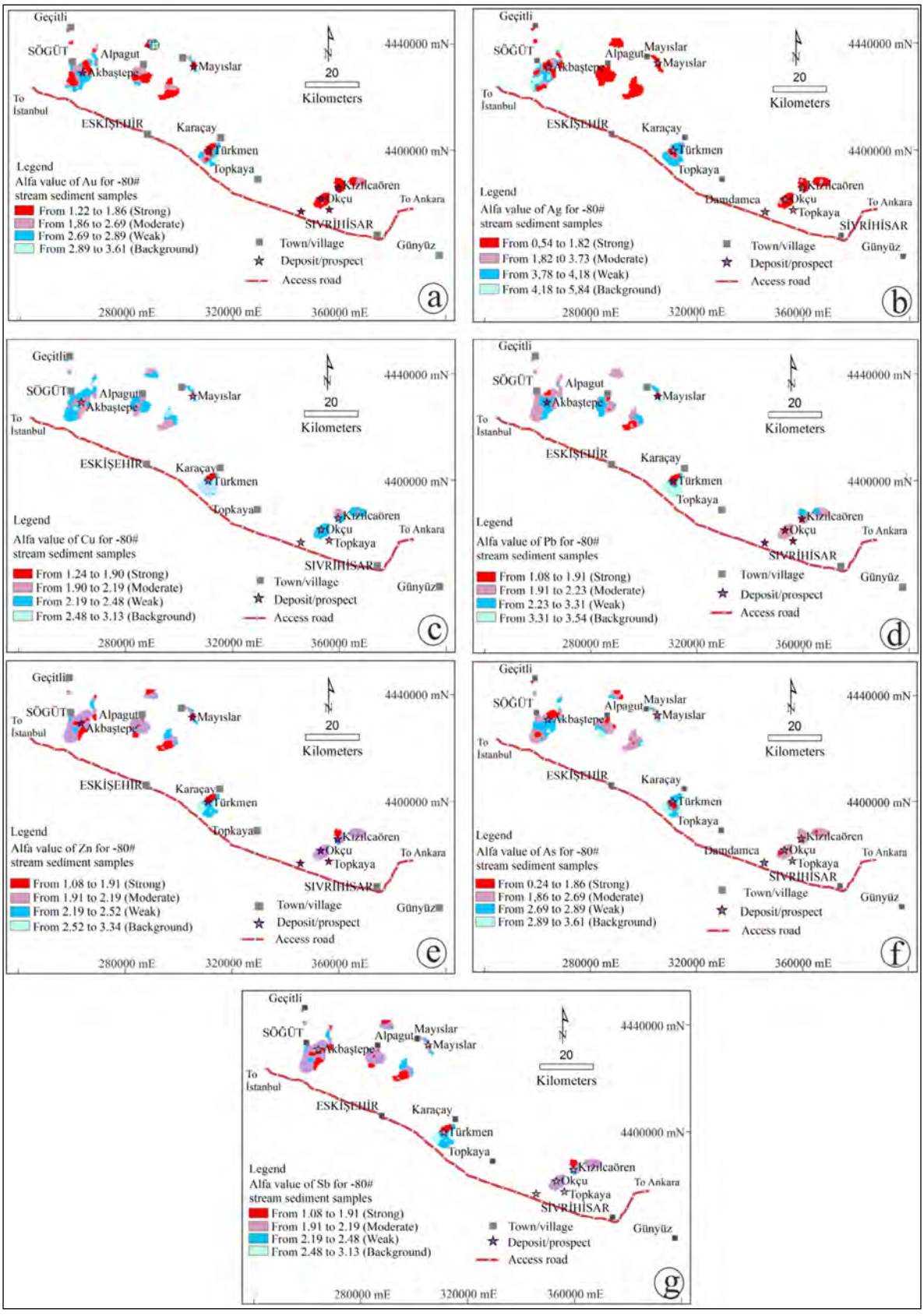

Figure 8- Raster map showing α-values of the stream sediment; a) Au, b) Ag, c) Cu, d) Pb, e) Zn, f) As and, g) Sb concentrations estimated using the window-based method.

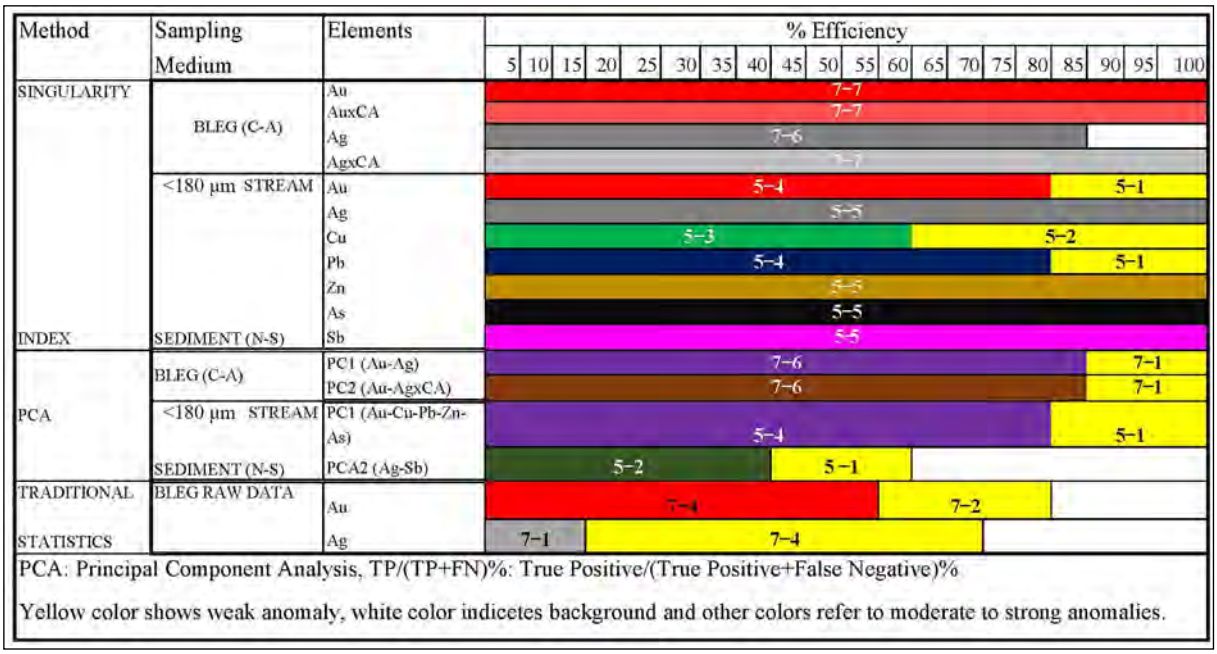

Figure 9- Agreement between geochemical anomaly classification and presence/absence of known mineral deposits or anomalous rock chip geochemistry in catchment. 7/7: number of deposits detected by stream sediment survey/Au deposits being discovered, 100%: efficiency percentage of the geochemical anomalies of stream sediment data in regard to the known gold prospects and deposits.

6. Discussion

The strength of stream sediments geochemical anomalies typically diminishes downstream due to dilution of element abundances (Parsa et al., 2017*a, b*; Yılmaz et al., 2019) in addition to errors induced by sampling and analytical errors (Parsa et al., 2016) coupled with smoothing effect by common moving average interpolation techniques (Yuan et al., 2015; Yousefi, 2017*a, b*). Nevertheless, multifractal interpolation methods (e.g., MIDW and multifractal Kriging) may use singularity and moving average interpolation to simultaneously measure local singularities and the spatial correlation between data, thereby also overcoming the smoothing effect of applying a moving average interpolation method (Cheng et al, 1999). These methods simplify the distinction of geochemical populations by enhancing geochemical anomalies and segregation from geochemical background values (Cheng et al., 2000; Yuan et al., 2015). Hard threshold techniques are not always able to identify weak anomalies (e.g., traditional statistical techniques and C-A fractal modeling), particularly in intensely altered lateritic covers (Shuguang et al., 2015). Nevertheless, when window-based contrast filtering methods, e.g., singularity mapping (Cheng et al., 1999; Cheng, 2007) are implemented as soft threshold techniques, numerous discoveries of weak geochemical anomalies have been encountered quite often (Zuo et al., 2015; Yuan et al., 2015; Yousefi, 2017*a, b*). Once the local singularity indexes (α values) are integrated in multifractal moving average interpolation, as in this study, the MIDW-interpolated geochemical data represents enhanced geochemical models, allowing for the recognition of weak anomalies. BLEG Au and Ag anomalies highly correlates with those of <180 µm stream sediment abnormalities showing the dependability of the results of sampling and analytical techniques. In addition to these, high-grade rock-chip assays as well as the discovery of mineralizations in the recognized zones of BLEG and <180µm stream sediment anomalies suggested that these BLEG and <180µm stream sediment anomaly zones without undetected mineralizations deserve further exploration. BLEG Au and Ag geochemical signatures derived from SI, C-A, N-S and PCA multifractal techniques can justify gold deposition in the study area due to the affiliation of BLEG geochemical signatures with gold mineralization (Figures 3-9). Besides, <180µm stream sediments singularity index Au and Ag geochemical anomalies have strong geographic correlation with

gold mineralization over the areas with argillic and silicic alterations. Moreover, the singularity index-based geochemical signatures of the Pb-Zn-As-Sb and C-A fractal values of Cu-Pb-Zn-As elements in <180μm stream sediment samples show strong association with gold mineralization (Figure 9). Even, <180μm stream sediments with PCA1 loadings ≥ 0.5 (Au-Cu-Pb-Zn-As) display strong association with known ore deposits at 80% efficiency level. Au and Ag geochemical anomalies, which were derived from the traditional statistical analysis of raw BLEG data had associations with known deposits with 57% and 15% underlain by moderate to weak anomalies, respectively (Supplementary Figure 3 and Figure 9). However, Log-transformed BLEG Au and Ag signatures display association with the known deposits at 100% and 30 efficiency level, respectively. It was demonstrated that IDW interpolation of Log-transformed Au anomalies derived from median +2σ, 3σ and 4σ detected all the deposits/prospects. However, multifractal analysis also generates additional moderate to strong, even weak, BLEG Au and Ag anomalies, which may be targets for discovering additional significant Au deposits (Supplementary Figure 3c, d and Figures 4-6). This shows that multifractal analysis is robust and very efficient in identifying ore-related geochemical anomalies, which have been probably missed by traditional statistical analysis. The geochemical anomalies derived from SI coupled with C-A and N-S fractal/multifractal models should be accompanied by further prospecting and structural mapping. This would probably give way to the identification of new mineralization sites encompassed by low α values <2.

Acknowledgements

We would like to express our appreciation to Eurogold Madencilik/Normandy Mining Ltd., Türkiye for generous financial support to the project during Hüseyin YILMAZ's presence in Eurogold as Exploration Manager. Anonymous reviewers are thanked for their invaluable comments in improving the quality of this paper.

References

Afzal, P., Khakzad, A., Moarefvand, P., Omran, N. R., Esfandiari, B., Alghalandis, Y. F. 2010. Geochemical anomaly separation by multifractal modeling in Kahang (GorGor) porphyry system, Central Iran. Journal of Geochemical Exploration 104, 34–46.

Afzal, P., Alghalandis, Y. F., Khakzad, A., Moarefvand, P., Omran, N. R. 2011. Delineation of mineralization zones in porphyry Cu deposits by fractal concentration–volume modeling. Journal of Geochemical Exploration 108, 220–232.

Afzal, P., Ahari H. D, Omran, N. R, Aliyari F. 2013. Delineation of gold mineralized zones using concentration–volume fractal model in Qolqoleh gold deposit, NW Iran. Ore Geology Reviews 55, 125–133.

Agterberg, F. P., Bonham-Carter, G. F., Wright, D. F. 1990. Statistical pattern integration for mineral exploration. Computer applications in resource exploration and assessment for minerals and petroleum. Pergamon, Elmsford.

Ahmadi, N. R, Afzal, P., Yasrebi, A. B. 2021. Delineation of gas content zones using N-S fractal model in coking coal deposits. Journal of Mining and Environment 12, 181-189.

Ak Yatırım. 2018. Ak Yatırım Madencilik şirket raporu, 4 (unpublished).

Aliyari, F. P., Afzal, P., Lotfi, M., Shokri, S. H., Feizi, H. 2020. Delineation of geochemical haloes using the developed zonality index model by multivariate and fractal analysis in the Cu–Mo porphyry deposits. Applied Geochemistry 121, 104694.

Altıner, D., Koçyiğit, A., Farinacci, A., Nicossia, U., Conti, M. A. 1991. Jurassic, Lower Cretaceous stratigraphy and paleogeographic evolution of the southern part of north-western Anatolia. Geologica Romana 28, 13-80.

Arias, M., Gumiel, P., Martín-Izard, A. 2012. Multifractal analysis of geochemical anomalies: a tool for assessing prospectivity at the SE border of the Ossa Morena Zone, Variscan Massif (Spain). Journal of Geochemical Exploration 122, 101-112.

Bonham-Carter, G. F., Rogers, P. J., Ellwood, D. J. 1987. Catchment basin analysis applied to surficial geochemical data, Cobequid Highlands, Nova Scotia. Journal of Geochemical Exploration 29, 259-278.

Carranza, E. J. M. 2010*a*. Catchment basin modelling of stream sediment anomalies re-visited: incorporation of EDA and fractal analysis. Geochemistry: Exploration, Environment, Analysis 10, 365-381.

Carranza, E. J. M. 2010*b*. Mapping of anomalies in continuous and discrete fields of stream sediment geochemical landscapes. Geochemistry: Exploration, Environment, Analysis 10, 171–187.

Cheng, Q. 2007. Mapping singularities with stream sediment geochemical data for prediction of undiscovered mineral deposits in Gejiu, Yunnan Province, China. Ore Geology Reviews 32, 314-324.

Cheng, Q., Agterberg, F. P., Ballantyne, S. B. 1994. The separation of geochemical anomalies from background by fractal methods. Journal of Geochemical Exploration 51, 109-130.

Cheng, Q., Agterberg, F. P., Bonham-Carter, G. F. 1996. A spatial analysis method for geochemical anomaly separation. Journal of Geochemical Exploration 56, 183–195.

Cheng, Q., Xu, Y., Grunsky, E. 1999. Integrated spatial and spectral analysis for geochemical anomaly separation. Proceeding of the Fifth Annual Conference of the International Association for Mathematical Geology, Trondheim, Norway 6–11th August.

Cheng, Q., Xu, Y., Grunsky, E. C. 2000. Integrated spatial and spectrum method for geochemical anomaly separation. Natural Resources Research 9, 43–52.

Daneshvar, S. L. 2017. Delineation of enriched zones of Mo, Cu and Re by concentration volume fractal model in Nowchun Mo-Cu porphyry deposit, SE Iran. Iranian Journal of Earth Sciences 9, 64- 72.

Eurogold, 1996. Review report on gold anomalies and prospects generated between 1991 and 1996 in western Turkey, Unpublished Company Report, 200.

Govett, G. J. S., Goodfellow, W. D., Chapman, A., Chor, C. Y. 1975. Exploration geochemistry-distribution of elements and recognition of anomalies. Mathematical Geology 7, 415–446.

Grunsky, E. C. 2007. The interpretation of regional geochemical survey data. Advances in Regional-Scale Geochemical Methods 8, 139–182.

Grunsky, E. 2010. The interpretation of geochemical survey data. Geochemistry: Exploration, Environment, Analysis 10, 27–74.

Halsey, T. C., Jensen, M. H., Kadanoff, L. P., Procaccia, I., Shraiman, B. I. 1986. Fractal measures and their singularities: the characterization of strange sets. Physics Review 33, 1141–1151.

Hawkes, H. E. 1976. The downstream dilution of stream sediment anomalies. Journal of Geochemical Exploration 6, 345–358.

Howarth, R. J. 1983. Mapping. Statistics and Data Analysis I Geochemical Prospecting, Handbook of Exploration Geochemistry 2. Elsevier, Amsterdam, 111–205.

Koza Gold. 2013. Koza Gold Company activity report, 54 (unpublished).

Koza Gold. 2014. Koza Gold Company activity report, 63 (unpublished)

Koza Gold. 2016. Koza Gold Company activity report, 97 (unpublished)

Luz, F., Mateus, A., Matos, J. X., Gonçalves, M. A. 2014. Cu-and Zn-soil anomalies in the NE border of the South Portuguese Meier Zone (Iberian Variscides, Portugal) identified by multifractal and geostatistical analyses. Natural Resources Research 23, 195-215.

Mandelbrot, B. B. 1983. The Fractal Geometry of Nature. Freeman, New York, 495.

Mirzaie, M., Afzal, P., Adib, A., Rahimi, E., Mohammadi, G. 2020. Detection of zones based on ore and gangue using fractal and multivariate analysis in Chah Gaz iron ore deposit, Central Iran. Journal of Mining and Environment 11, 453-466.

MTA. 1965. Tungsten and molybdenum deposits of Turkey. General Directorate of Mineral Research and Exploration Publications No. 128, Ankara, Turkey.

MTA. 1970. Arsenic, mercury, antimony and gold deposits of Turkey. General Directorate of Mineral Research and Exploration Publication No. 129, Ankara, Turkey.

MTA. 2002. 1:500000 Geological map of Turkey. General Directorate of Mineral Research and Exploration, Ankara, Turkey.

Okay, A. I., Satır, M. 2000. Coeval plutonism and metamorphism in a latest Oligocene metamorphic core complex in northwest Turkey. Geological Magazine 137, 495–516.

Okay, A. I., Satır, M., Maluski, H., Siyako, M., Monie, P., Metzger, R., Akyüz, S. 1996. Paleo- and Neo-Tethyan events in northwest Turkey: geological and geochronological constraints. Tectonics of Asia. Cambridge University Press, 420–441.

Özgenç, I. 1993. Kızılcaören (Sivrihisar-Eskişehir) karbotermal bastneazit-fluorit-barit yatağının jeolojisi ve nadir toprak element jeokimyası. Geological Bulletin of Turkey 36, 1–11.

Parlak, B., Sayılı, S. 2012. Fluid inclusion data on quartz and calcite in alteration zones of polymetallic mineralizations at Mayıslar Area (Sarıcakaya-Eskişehir, Turkey). Geological Bulletin of Turkey 55, 111−132.

Parsa, M., Maghsoudi, A., Ghezelbash, R. 2016. Decomposition of anomaly patterns of multi-element geochemical signatures in Ahar area, NW Iran: a comparison of U-spatial statistics and fractal models. Arabian Journal of Geosciences 9, 1-16.

Parsa, M., Maghsoudi, A., Yousefi, M., Sadeghi, M. 2017*a*. Multifractal analysis of stream sediment geochemical data: implications for hydrothermal nickel prospection in an arid terrain, eastern Iran. Journal of Geochemical Exploration 18, 305-317.

Parsa, M., Maghsoudi, A., Yousefi, M., Carranza, E. J. M. 2017*b*. Multifractal interpolation and spectrum–area fractal modeling of stream sediment geochemical data: implications for mapping exploration targets. Journal of African Earth Sciences 128, 5-15.

Ren, L., Cohen, D. R., Rutherford, N. F., Zissimos, A. M., Morisseau, E. G. 2015. Reflections of the geological characteristics of Cyprus in soil rare earth element patterns. Applied Geochemistry 56, 80–93.

Sadeghi, B., Madani, N., Carranza, E. J. M. 2015. Combination of geostatistical simulation and fractal modeling for mineral resource classification. Journal Geochemical of Exploration 149, 59–73.

Shen, W., Cohen, D. R. 2005. Fractally invariant distributions and an application in geochemical exploration. Mathematical Geology 37, 895–909.

Shuguang, Z., Kefa, Z., Yao, C., Jinlin, W., Jianli, D. 2015. Exploratory data analysis and singularity mapping in geochemical anomaly identification in Karamay, Xinjiang, China. Journal of Geochemical Exploration 154, 171-179.

Sinclair, A. J. 1991. A fundamental approach to threshold estimation in exploration geochemistry: Probability plots revisited. Journal of Geochemical Exploration 41, 1–22.

Wang, W., Cheng, Q., Zhang, S., Zhao, J. 2018. Anisotropic singularity: A novel way to characterize controlling effects of geological processes on mineralization. Journal of Geochemical Exploration 189, 32–41

Yasrebi, A. B., Hezarkhani, A. 2019. Resources classification using fractal modelling in Eastern Kahang Cu-Mo porphyry deposit, Central Iran. Iranian Journal of Earth Sciences 11, 56-67.

Yılmaz, H. 2003. Geochemical exploration for gold in western Turkey: success and failure. Journal of Geochemical Exploration 80, 117-135.

Yılmaz, H., Mahyar, Y., Parsa, M., Sonmez, F. N., Maghsoodi, A. 2019. Singularity mapping of bulk leach extractable gold and -80# < 180µm stream sediment geochemical data in recognition of gold and base metal mineralization footprints in Biga Peninsula South, Turkey. Journal of African Earth Sciences 153, 156-172.

Yousefi, M. 2017*a*. Analysis of zoning pattern of geochemical indicators for targeting of porphyry Cu mineralization: A pixel-based mapping approach. Natural Resources Research 26, 429–441.

Yousefi, M. 2017*b*. Recognition of an enhanced multi-element geochemical signature of porphyry copper deposits for vectoring into mineralized zones and delimiting exploration targets in Jiroft area, SE Iran. Ore Geology Reviews 83, 200-214.

Yuan, F., Li, X., Zhou, T., Deng, Y., Zhang, D., Xu, C., Zhang, R., Jia, C., Jowitt, S. M. 2015. Multifractal modeling-based mapping and identification of geochemical anomalies associated with Cu and Au mineralization in the NW Junggar area of northern Xinjiang Province, Gangdese Belt, Tibet (China). Journal of Geochemical Exploration 154, 252-264.

Zadmehr, F., Shahrokhi, S. V. 2019. Separation of geochemical anomalies by concentration-area and concentration-number methods in the Saqez 1/100.000 sheet. Iranian Journal of Earth Sciences 11, 196-204.

Zuo, R. 2011. Identifying geochemical anomalies associated with Cu and Pb–Zn skarn mineralization using principal component analysis and spectrum–area fractal modeling in the Gangdese Belt, Tibet (China). Journal of Geochemical Exploration 111, 13–22.

Zuo, R., Wang, J. 2016. Fractal/multifractal modeling of geochemical data: a review. Journal of Geochemical Exploration 164, 33-41.

Zuo, R., Xia, Q., Wang, H. 2013. Compositional data analysis in the study of integrated geochemical anomalies associated with mineralization. Applied Geochemistry 28, 202-211.

Zuo, R., Xia, Q., Wang, H. 2015. Compositional data analysis in the study of integrated geochemical anomalies associated with mineralization. Applied. Geochemistry 28, 202–211.

Supplementary Material

1. Descriptive Statistics

The skewness and kurtosis of the raw Au and Ag concentrations in the BLEG stream sediments are 8.9 and 10.3, and 102 and 122 whereas these are 4.9 and 7.4, and 28.4 and 58.8, respectively for AuxCA and AgxCA (Figure 1). The skewness and kurtosis of the Ln Au and Ln Ag concentrations in the BLEG are 0.3 and -0.6 and, 1.8 and -0.6 respectively, indicating that the BLEG Au have slightly negative skewness and low kurtosis whereas the BLEG Ag have negative skewness and low kurtosis. Again, Ln-transformed Au and Ag data do not fully follow a normal distribution (as shown by Table 1) and histograms, and Q-Q plots in Figure 1. In addition, the histogram of the logarithmic Ag concentrations has a multimodal pattern for the BLEG (Figure 1h). These statistical characteristics may suggest that the Eskişehir-Sivrihisar region have had multiple geochemical framework and has undergone multi-geological processes, thereby displaying a complex Ag ore-formation during Eocene time. The skewness of the raw Au, Ag, Cu, Pb, Zn, As and Sb concentrations in the <180µm stream sediment data are 6.9, 5.6, 4.8, 11.1, 7.2, 7.5 and 2.7, respectively (Table 1 and Figure 1). This indicates that the data are positively skewed containing large positive tailing values with very excessive kurtosis (Au: 66.8, Ag: 43.7, Cu: 31.7, Pb: 148.1, Zn: 61, As: 84.7 and Sb: 9.1) and the data do not follow a normal distribution (as shown in the Table 1 and histograms in Figure 2 a-g). Ln Cu, Pb and Zn histograms display moderately normal and leptokurtic distributions (Figure 2h, q) with Ln Cu and As displaying negative skewness. However, Ln-transformed Au, Ag, As and Sb data do not fully follow a normal distribution (as shown in Figure 2. In and addition, the histograms of the Ln Au, Ag, Cu, Pb, Zn, As and Sb concentrations have weak to strong multimodal patterns for the <180µm stream sediments (Figure 2). These statistical characteristics as in the BLEG data imply that the Eskişehir-Sivrihisar region have had multiple geochemical framework and has undergone multi-geological processes, thereby complex ore-formations during Eocene time. As is typical for trace element geochemical data, the distributions are skewed with an overall tendency towards right, but significant deviations from ln-normality due to the complex interplay of factors such as parent lithology controlling element distributions (Reimann and Filzmoser, 2000; Ren et al., 2015). The size of BLEG Au- and Ag-anomalous areas above background generated by traditional statistics using median+2S.D (Table 1) was calculated using IDW interpolation by ArcGis 10.5 version. Maximum anomalous areas above the background for raw Au and Ag data are 266 km^2 (Figure 3a) and 31 km^2 (Figure 3b) whereas these are 2895 km^2 (Figure 3c) for Ln Au and 683 km^2 (Figure 3d) for Ln Ag, which are derived from 3580 km^2 BLEG-sampled area. The ratio of raw Au and Ag anomalous areas to that of BLEG-sampling is 1/15 and 1/115, respectively whereas these are 1/1.25 for LnAu and 1/1.4 for LnAg. However, these ratios may be decreased to 1/5 and 1/3.7 of BLEG-sampled area for LnAu and for LnAg, respectively, at median+3SD (Red highlighted areas in Figure 3c, d). Number of deposits/prospects detected by raw Au and raw Ag anomalies are 3 (45%) and 1 (15%) out of 7, respectively whereas percentage of discoveries of deposits/prospects by weak to strong LnAu and LnAg anomalies are 100 and 85%, respectively, with the majority of mineralizations covered by strong LnAu anomalies.

References

Reimann, C., Filzmoser, P. 2000. Normal and lognormal data distribution in geochemistry: death of a myth, consequences for the statistical treatment of geochemical and environmental data. Environmental Geology 39, 1001–1014.

Ren, L., Cohen, D. R., Rutherford, N. F., Zissimos, A. M., Morisseau, E. G. 2015. Reflections of the geological characteristics of Cyprus in soil rare earth element patterns. Applied Geochemistry 56, 80–93.

Table 1- Summary statistics for BLEG Au and Ag, and <180 µm Stream sediment Au, Ag, Cu, Pb, Zn, As and Sb.

BLEG							
	Au (ppb)	AuxCA	Ag (ppb)	AgxCA			
Mean	1.4	15.2	12.72	122.1			
Std. Deviation	2.9	29.2	44.64	382.5			
Skewness	8.9	4.9	10.28	7.4			
Kurtosis	101.9	28.4	121.81	58.8			
Minimum or DL	0.0	0.3	0.01	0.1			
Maximum	38.1	252.8	595.51	3763.6			
N	258	258	258	258			
<180 µm stream sediment							
	Au (ppb)	Ag (ppm)	Cu (ppm)	Pb (ppm)	Zn (ppm)	As (ppm)	Sb (ppm)
Mean	15.2	1.2	49.7	95.2	92.5	41.2	5.4
Std. Deviation	42.9	3.5	51.6	386.1	202.3	70.3	8.7
Skewness	6.9	5.6	4.8	11.1	7.2	7.5	2.7
Kurtosis	66.8	43.7	31.7	148.1	61.0	84.7	9.1
Minimum or DL	0.3	0.0	3.0	1.0	5.0	1.0	1.0
Maximum	587.0	40.1	539.2	6292.5	2441.2	1056.6	61.7
N	612	612	612	612	612	612	612

BLG: Bulk Leach Extractable Gold, CA: Concentration times area in square km, N: Number of samples, DL: Detection limit

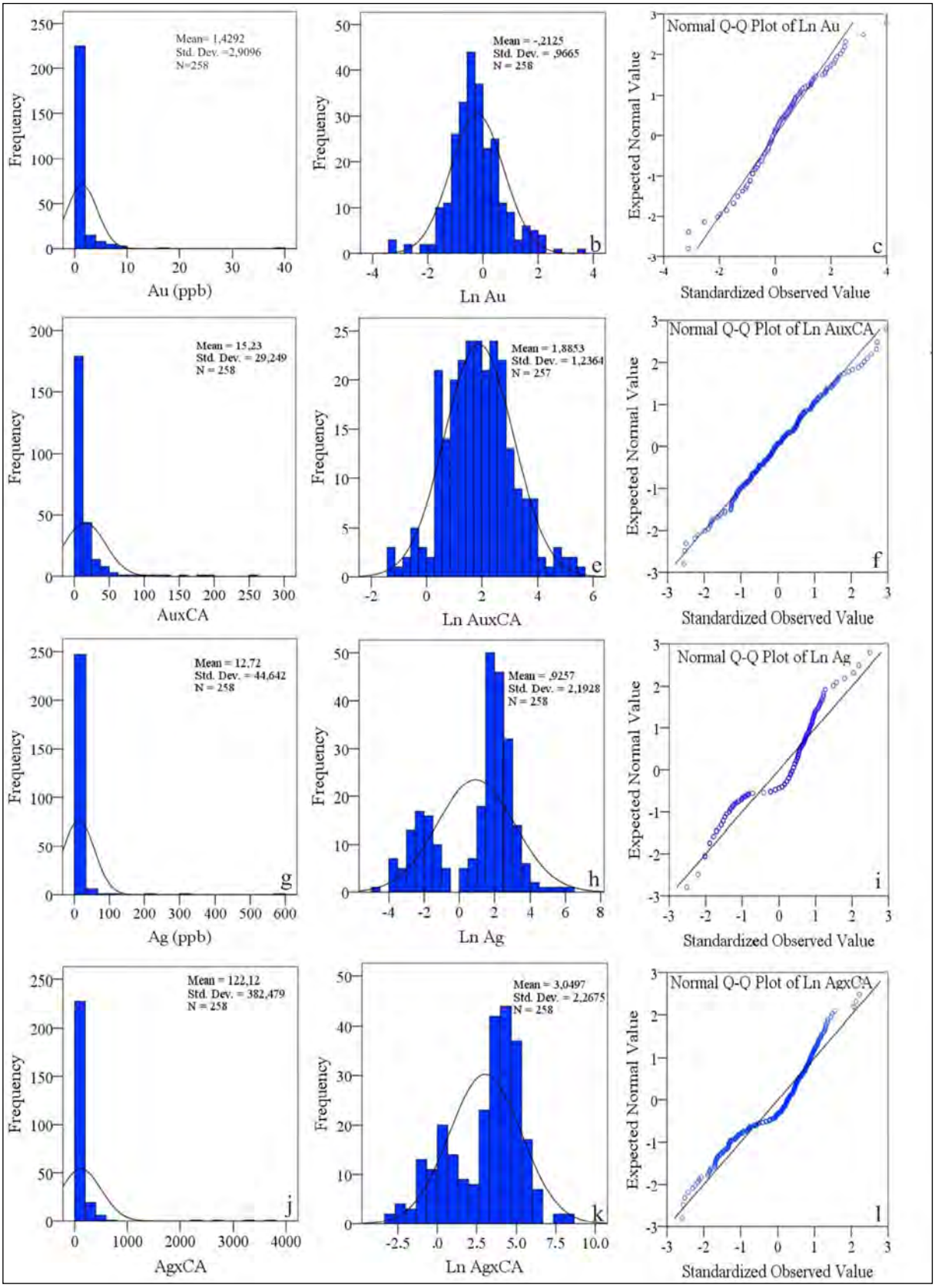

Figure 1- The Au-Ag statistical charts from the BLEG stream sediment samples in the Eskişehir-Sivrihisar region; a) the raw Au, b) Ln Au, c) Q-Q Au, d) Raw AuxCA, e) Ln AuxCA, f) Q-Q Ln Au, g) the raw Ag, h) Ln Ag, i) Q-Q Ag, j) Raw AgxCA, k) Ln AgxCA, l) Q-Q Ln AgxCA.

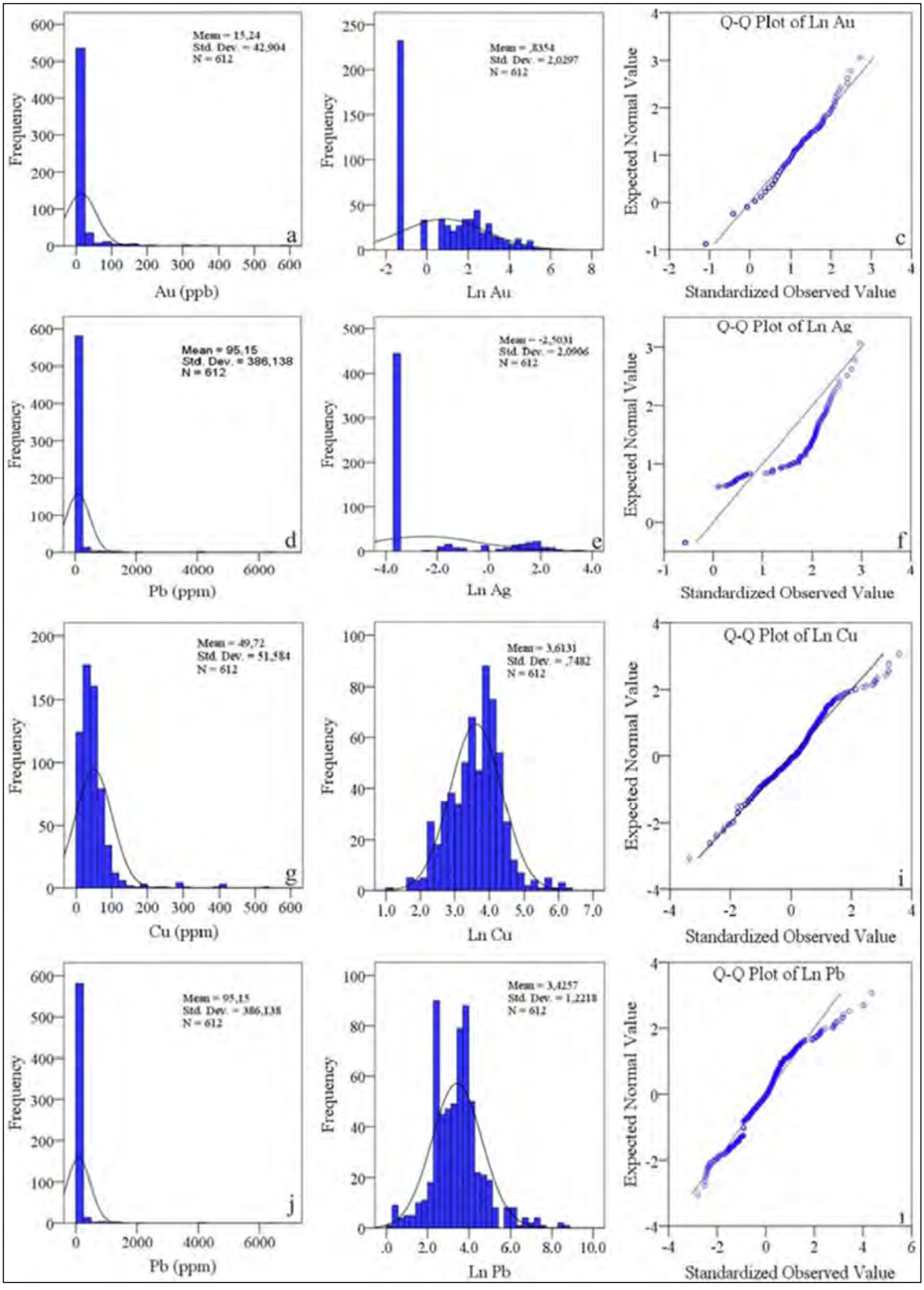

Figure 2- The Au, Ag, Cu, Pb, Zn, As and Sb statistical charts from the<180µm stream sediment samples in the Eskişehir-Sivrihisar region; a) the raw Au, b) Ln Au, c) Q-Q Au, d) Raw Ag, e) Ln Ag, f) Q-Q Ln Ag, g) the raw Cu, h) Ln Cu, i) Q-Q Cu, j) Raw Pb, k) Ln Pb, l) Q-Q Ln Pb, m) Raw Zn, n) Ln Zn, o) Q-Q Ln Zn, p) Raw As, q) Ln As, r) Q-Q Ln As, s) Raw Sb, t) Ln Sb, u) Q-Q Ln Sb.

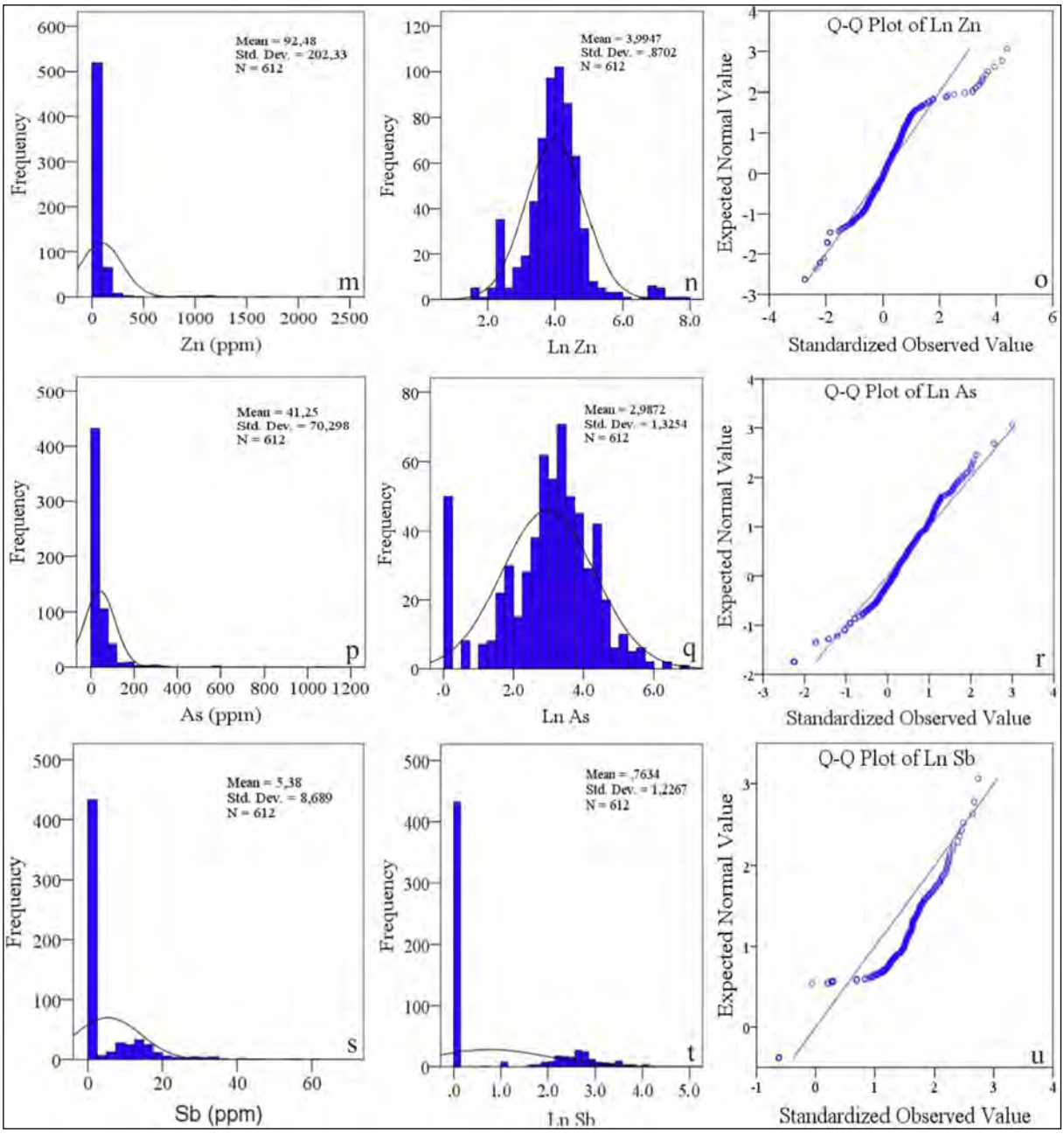

Figure 2- Continued.

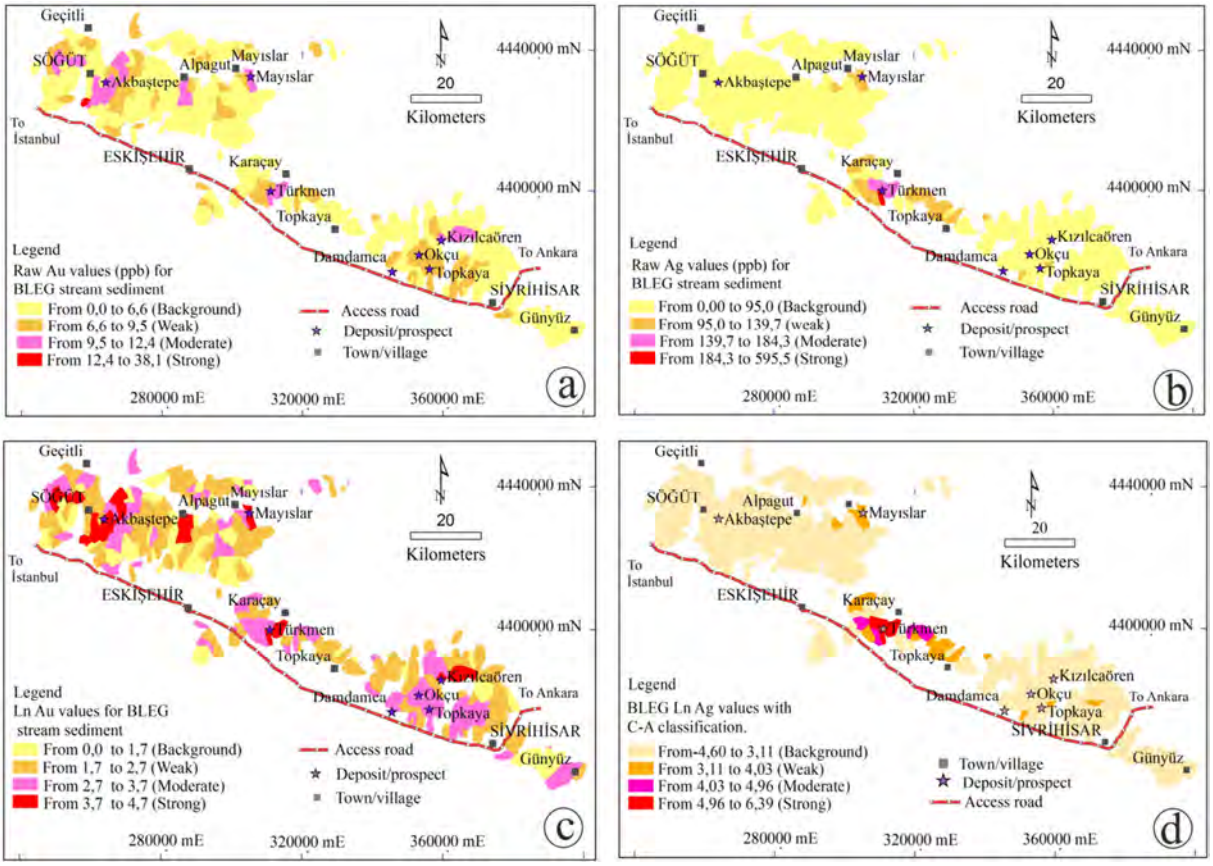

Figure 3- Areal extent of raw; a) Au-anomalous, b) Ag-anomalous areas generated by median+2S.D, and c), d) Ln-transformed Au-Ag-anomalous fields derived from median+2SD, 3SD and 4SD in the Eskişehir-Sivrihisar area. Median+1SD refers to background.

Bulletin of the Mineral Research and Exploration

http://bulletin.mta.gov.tr

A comparison of ion-exchange resins and activated carbon in recovering gold from cyanide leach solutions with low levels of copper

Deus Albert MSUMANGE[a*], Ersin Yener YAZICI[a], Oktay CELEP[a] and Hacı DEVECİ[a]

[a]*Karadeniz Technical University, Department of Mining Engineering, Division of Mineral and Coal Processing, Hydromet B & PM Research Group, Trabzon, Türkiye*

Research Article

Keywords:
Copper-Rich Gold Ore, Gold Adsorption, Activated Carbon, Resin, Selectivity.

ABSTRACT

This study was conducted to determine the effectiveness of three different adsorbents for the adsorption of gold from a real cyanide leach liquor. An activated carbon (NORIT GAC 1240), strong base (Purogold A194), and weak base (Purogold S992) resins were tested as the adsorbents. The pregnant leach solution (PLS) was derived from cyanide leaching (1.5 g/L NaCN, 25% w/w solids ratio, 1.5 L/min air flow rate, pH 10.5 – 11. 24 h) of the roasted copper-rich refractory gold ore pretreated with H_2SO_4. Gold and copper concentrations in the PLS were analysed to be 26.1 mg/L Au and 62.4 mg/L Cu, respectively. Activated carbon was found to be the best performing adsorbent as it achieved the highest gold loading. Purogold A194 loaded the highest amount of copper amongst the adsorbents tested. Despite the fact that activated carbon loaded a high amount of gold, it was less selective than Purogold S992. Purogold A194 exhibited the lowest selectivity, which was defined as the distribution ratio of gold to copper, compared with Purogold S992 and activated carbon. Therefore, the order of selectivity of the adsorbents tested was as follows: Purogold S992 > Activated carbon > Purogold A194.

Received Date: 05.02.2021
Accepted Date: 16.06.2021

1. Introduction

Some gold ores can contain high levels of copper, which presents specific difficulties during the extraction of gold via cyanidation. Due to the rapid exhaustion of free milling ores, the world has now turned to refractory ores including Cu-Au ores. This group was formerly deemed economically unappealing. Fleming et al. (2011) pointed out that as of 2009, more than 20% of the global gold production was from copper - gold ores. The process of gold recovery from these ores is often associated with different problems ascribed to the ready dissolution of most copper minerals in cyanide solutions (Sceresini, 2005; Bas et al., 2012; Bas et al., 2015; Msumange et al., 2020). The dissolution of copper minerals essentially leads to high cyanide consumption and low gold recoveries (Marsden and House, 2006).

Several factors can contribute to the refractory character of the ore. These include inorganic / organic carbon present in the ore and gold locked in sulfides such as arsenopyrite and pyrite. The presence of cyanides such as copper is another reason for refractory behavior (Habashi, 1999; Marsden and House, 2006; Adams, 2016; Chryssoulis and McMullen, 2016). Sulfide in gold ores not only consumes cyanide and oxygen but also forms a coating on grains of gold. This

Citation Info: Msumange, D. A., Yazıcı, E. Y., Celep, O., Deveci, H. 2022. A comparison of ion-exchange resins and activated carbon in recovering gold from cyanide leach solutions with low levels of copper. Bulletin of the Mineral Research and Exploration 168, 35-41. https://doi.org/10.19111/bulletinofmre.955403

**Corresponding author: Deus Albert MSUMANGE, msudeak8@gmail.com*

passive layer interferes with gold leaching (Marsden and House, 2006; Bas et al., 2012). A previous study (Yen and Aghamirian, 2002) suggested that sulfide minerals could affect the leaching of gold. Stibnite, chalcocite, and pyrrhotite have often negative effects. But pyrite, chalcopyrite, arsenopyrite, and sphalerite neither seriously reduce nor greatly improve gold leaching. Galena may enhance gold leaching (Yen and Aghamirian, 2002).

The recovery of gold from cyanide leach solutions is widely carried out by adsorption on activated carbon (Dai et al., 2012; Van Deventer et al., 2014). There are three industrial activated carbon adsorption processes used for gold recovery; namely, carbon in leach (CIL), carbon in pulp (CIP), or carbon in column (CIC). However, copper, if present in the cyanide leach liquor competes with gold during the adsorption process (Van Deventer, 2014; Msumange, 2019; Msumange et al., 2021). High copper concentration may severely affect gold adsorption (Van Deventer et al., 2014). In this respect, the formation of $Cu(CN)_2^-$ complex should be controlled to minimize copper loading onto the activated carbon since $Cu(CN)_2^-$ competes with $Au(CN)_2^-$ directly. This may be achieved by maintaining excess free cyanide or elevating pH (Van Deventer, 2014). Some researchers focused on the removal of copper in alkaline (Bas et al., 2012 and 2015) or acid solutions (Yazıcı et al., 2015; Msumange, 2019) before cyanide leaching to eliminate the copper interference during leaching and adsorption stages.

Various investigators (Kotze et al., 2005, Kotze, 2010; Van Deventer et al., 2012, Van Deventer, 2014) have mooted that ion exchange resins have some advantages over activated carbon for the recovery of gold from leach solutions. These include better selectivity for gold over copper, enhanced gold recoveries from preg - robbing ores, and no requirement for thermal regeneration. The main drawback of ion exchange resins is that they are more expensive than activated carbon (Van Deventer, 2014).

The objective of this study is to compare the effectiveness of activated carbon and different types of resins (Purogold A194 and Purogold S992) in the recovery of gold from a cyanide liquor with low copper concentration (62.4 ppm Cu). Gold selectivity over copper (Au / Cu), distribution ratio, and the loading capacity of Au and Cu of adsorbents were evaluated.

2. Experimental Studies

A copper-rich refractory gold ore sample (108 g/t Au, 1.6% Cu), mainly composed of quartz (67.3%), cordially supplied by Koza Gold Co. (Gümüşhane / Mastra, Türkiye), was used to produce the leach solution. The ore can be categorized as refractory due to its low response to direct cyanide leaching (1.5 g/L NaCN, 25% w/w solids ratio, air flow rate: 1.5 L/min, pH 10.5 - 11) under typical cyanidation conditions i.e., 18.4% Au extraction over 24 h. Different pretreatment routes were tested and roasting was found to be an auspicious route for high gold extractions from the ore (Msumange, 2019).

Adsorption tests were carried out using the pregnant leach solution produced from cyanide leaching (1.5 g/L NaCN) of the roasted ore (at 650 °C for 8 h), which was firstly pretreated by acid leaching (1 M H_2SO_4, Leaching time: 2 h) to remove reactive copper. Cyanide leaching of the roasted ore was carried out under the conditions of 1.5 g/L NaCN, 25% w/w solids ratio, 1.5 L/min air flow rate, pH 10.5-11, and 24 h leaching time. Gold and copper concentrations in PLSs were analysed to be 26.1 mg/L Au and 62.4 mg/L Cu, respectively. The PLSs were used in the adsorption tests.

The effectiveness of strong base (Purogold A194) and weak base (Purogold S992) resins for gold recovery from the cyanide leach solution generated was evaluated in comparison with an activated carbon (NORIT GAC 1240). These resins were claimed to be particularly developed for adsorption of gold - cyanide complexes from cyanide liquors. Gold selectivity over copper and loading capacity of adsorbents were evaluated. The distribution ratio of Au and Cu was also studied. The activated carbon sample used (NORIT GAC 1240) is 0.65 mm in size (NORIT, 2003). The technical properties of the resins, used in the study, are presented in Table 1.

The PLSs were prepared in 50 mL Erlenmeyer flasks, which were then placed onto an orbital shaker (Wiggen Hauser). Prior to the addition of adsorbents,

Table 1- Technical properties of the ion exchange resins used in the tests (PUROLITE, 2015; 2016*a*, *b*; 2020).

Name/brand of the resin	Matrix / Type	Functional Group	Ionic Form	Capacity	Moisture retention (%)	Effective Size
Purogold A194	Macroporous / Strong base anion	Quaternary Amines	Cl^-	3 eq/kg	44 - 52	710 - 1300 µm
Purogold S992	Macroporous Polystyrene - divinylbenzene / Weak base, Chelating	Mixed Amines	Free Base	4.4 eq/kg	47 - 55	800 - 1300 µm

these flasks with PLSs were aerated at 1.5 L/min, and pH of PLSs was adjusted at 10.5 - 11 by using 1 M NaOH, if required. pH was maintained at 10 - 10.5 where the weak - base resin, Purogold S992, was employed due to its sensitivity to the high alkalinity (>pH 10.5). To avoid evaporation of the leach solution, the top of the flasks was kept covered by a sponge. The adsorption tests were carried out using the adsorbents (5 g/L) under the conditions of 25 °C at 170 rpm agitating speed over the period of 4 h. The sampling of each flask was carried out at 0.5, 1, 2, and 4 hours by removing a 1 - mL solution. Metal concentrations (Au and Cu) in solutions were analysed by atomic absorption spectroscopy (AAS, Perkin Elmer AAnalyst 400).

The weak base resin (Purogold S992) was initially transformed into the form of sulphate before its use in the adsorption tests. It was contacted with two - bed volumes (BVs) of a 0.5 M $Na_2SO_4.10H_2O$ solution in a column at a flow rate of 2 - bed volumes per hour. Thereafter, the resin was treated with 4 BVs of water to remove the excess reagent from the resin (Van Deventer et al., 2014).

The selectivity (µ) and adsorbent loading capacity (A) were calculated using the equations below:

$$\mu = \frac{D_{Au}}{D_{Cu}} = \frac{[Au]_{adsorbent} x [Cu]_{solution}}{[Au]_{solution} x [Cu]_{adsorbent}} \quad (1)$$

where D_{Au} and D_{Cu} are the distribution ratio for Au and Cu, respectively.

$$A = (C_o - C_f) \times V \times m^{-1} \quad (2)$$

Where, C_o: Initial concentration of the adsorbate in solution (mg/L), C_f: Equilibrium concentration of the adsorbate in solution (mg/L), A: Adsorbent loading (mg/g), V: Volume of solution (L), m: Adsorbent mass (g).

3. Findings

The pH - dependent distribution of Cu(I) - cyanide species in the pregnant leach solution (PLS) was plotted using MEDUSA (2009) software (Figure 1a). This plot shows that the dominant Cu(I) - cyanide species in the pregnant leach solution used in the adsorption tests are $Cu(CN)_4^{3-}$ with ≈70% followed by $Cu(CN)_3^{2-}$ with ≈30 % over the pH range of 10 - 11. Figure 1b also illustrates the speciation of cyanide (CN^-) as a function of pH in the PLSs produced. At pH 10 - 11, 78 - 88% of cyanide is present in the free cyanide (CN^-) form.

In the adsorption tests, the selectivity of gold over copper and metal loadings are shown in Table 2.

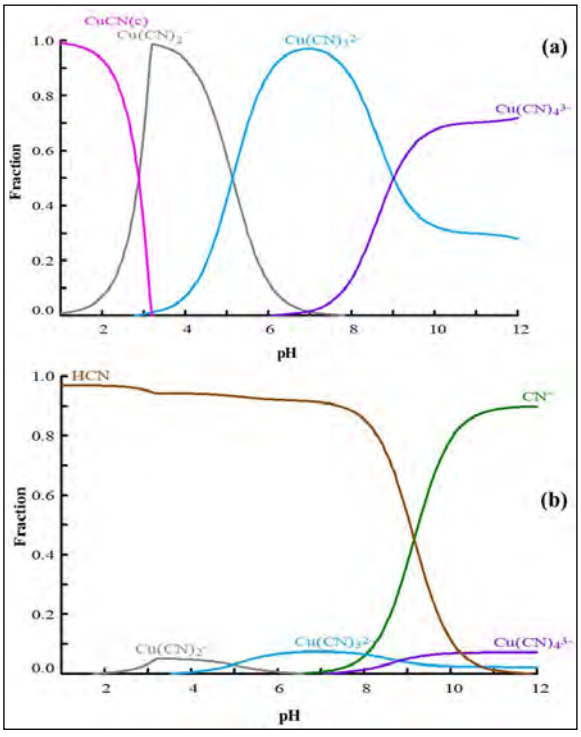

Figure 1- Speciation of ; a) Cu(I) species vs. pH, b) cyanide (CN^-) species vs. pH (CN_{Total}= 38.8 mM (1.90 g/L NaCN), Cu(I)= 62.4 mg/L, Au(I)= 26.1 mg/L) reflecting the conditions of PLSs produced (MEDUSA, 2009).

Figures 2 - 4 demonstrate the kinetics of gold/copper loading onto adsorbents and the change in the solution metal concentration at pH 10.5 - 11 (for Purogold A194) or 10 - 10.5 (for Purogold S992). It was found that 25 kg of gold was loaded per ton of activated carbon within 4 hours (Figure 3). During the first hour of adsorption, approximately half of the amount of gold initially present in the solution was observed to load onto Purogold S992 resin with 12 kg/ton. At the same time interval, 20 kg of gold were loaded per ton of activated carbon, while the gold loading for Purogold A194 was 16 kg/ton.

At the first hour of adsorption, 80% of the total gold loaded onto the activated carbon was achieved. This suggested the trend of the adsorption process since only 20% of the total loaded gold was attained within the 3 remaining hours of adsorption. For the case of Purogold A194, 70% gold loading was attained during the first hour. These data (Figure 3) show that the activated carbon has fast kinetics and a high capacity for gold adsorption compared with the tested resins. When it comes to copper, Purogold S992 loaded only 5 kg copper per ton of the resin over 4 hours. There was a remarkable change in the amount of copper loaded onto this adsorbent from the second to fourth hour (i.e., only 0.3 kg/ton was loaded). In comparison,

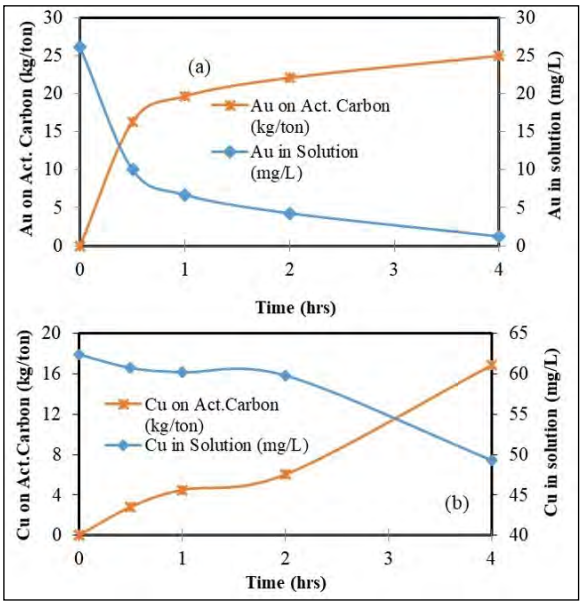

Figure 3- a) Kinetics of gold and b) copper loading onto activated carbon and concentrations (concentration of adsorbent: 5 g/L, pH 10.5 - 11.25 °C).

17 kg/ton of copper was loaded onto activated carbon over the same time interval. The extent of adsorption onto the strong base anion resin (Purogold A194) was also high as it loaded 23 kg/ton of Cu over a time frame of 4 hours. When compared to the Purogold S992, the activated carbon loaded 11 kg/ton of copper

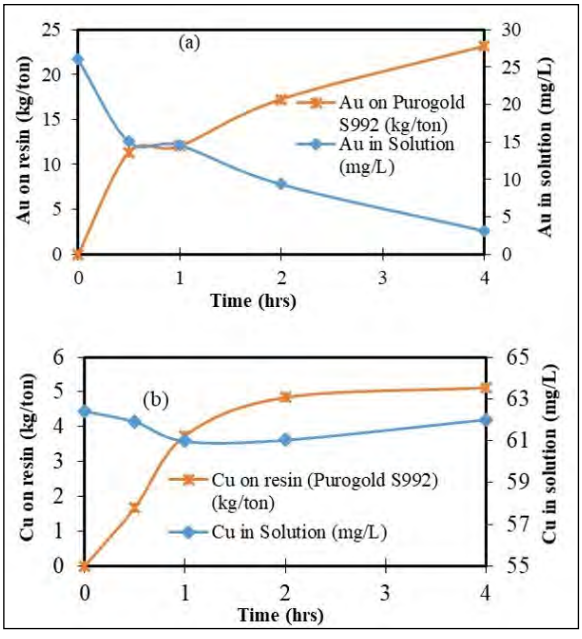

Figure 2- a) Kinetics of gold and b) copper loading onto Purogold S992 and metal concentrations (concentration of adsorbent: 5 g/L, pH 10 - 10.5, 25 °C).

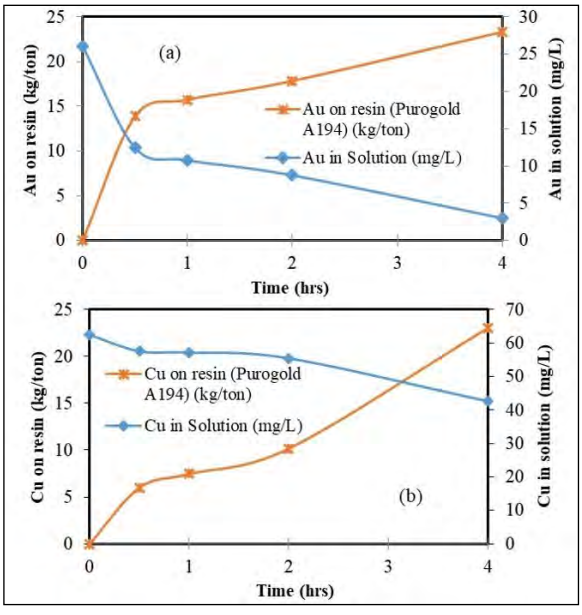

Figure 4- a) Kinetics of gold and b) copper loading onto Purogold A194 and metal concentrations (concentration of adsorbent: 5 g/L, pH 10.5 - 11.25 °C).

from the second hour to the fourth hour whilst the Purogold A194 loaded 13 kg/ton from the second hour to the fourth hour of adsorption (Figure 4). Despite the fact that the gold loading capacity attained by the activated carbon was high compared to the resin - type adsorbents tested, yet it was less selective for gold over copper compared to the Purogold S992. The amount of copper loaded onto activated carbon was higher by 11.7 kg/ton than that on to Purogold S992. These results indicate that the Purogold S992 is more a selective adsorbent than the activated carbon and the Purogold A194. Figure 5 shows the percent recovery of metals (Au and Cu) from the leach solution by the activated carbon and resins. The results showed that 96% of gold and only 27% of copper were adsorbed onto activated carbon.

The distribution ratios of gold and copper were 20027 and 342, respectively. This gave a selectivity of 59 for the activated carbon. Similar findings (i.e. 89% Au and 37% Cu) were also observed for Purogold A194 for which the distribution ratio for gold and copper was determined to be 7757 and 540, respectively. The selectivity was 14. For Purogold S992, 89% of gold and 9% of copper were observed to occur (Figure 5). The distribution ratio of gold was found to be substantially larger than that of copper indicating the high selectivity of S992 resin as the most selective adsorbent tested for gold (Table 2). In this respect, the Purogold S992 appeared to be 1.5 and 6 times more selective than the activated carbon and the Purogold A194 as shown in Table 2, respectively. There appears to be a relatively limited number of studies on the recovery of gold from refractory ores by ion exchange resins compared with activated carbon. The current findings seem to be consistent with the previous studies. A previous study conducted by Van Deventer (2014) also showed that Purogold S992 was a selective adsorbent. The investigator employed a synthetic cyanide liquor with 9 mg/L Au, 13.6 mg/L Cu, 1 mg/L Zn, and 10.4 mg/L Ni in solution.

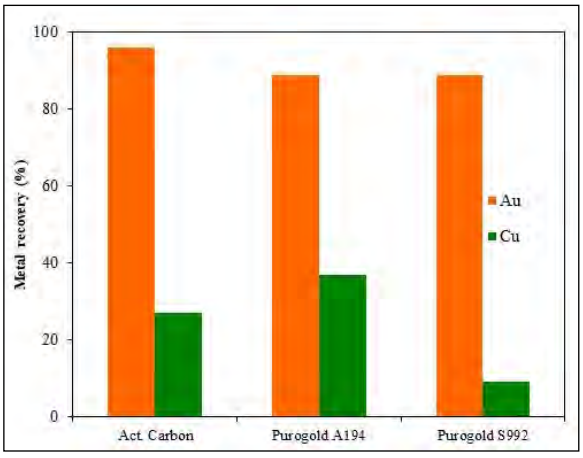

Figure 5- The percentage of metals recovered by adsorbents (concentration of adsorbent: 5 g/L, pH 10.5 – 11. 25 °C, 4 hours).

Gold loadings onto carbon and Purogold S992 were 16450 mg/kg and 4183 mg/kg, respectively. The loading of copper onto the activated carbon was 105 mg/kg whilst no copper loading onto Purogold S992 was recorded by the researcher. It was concluded from these findings that Purogold S992 has high selectivity for gold over copper. Other researchers (Fleming and Cromberge, 1984; Van Deventer et al., 2012) also found that the selectivity of weak/medium base resins for gold over copper is higher than strong base resins. Voiloshnikova et al. (2014*a*) studied the adsorption of metals from cyanide solutions using Purogold S992 and showed that the selectivity for gold is higher than zinc, silver, iron(III), and copper. Ahlatcı et al. (2018) also indicated that the adsorption of copper onto Purogold S992 was low, limited to 2.2% from a waste cyanide solution (1.5 g/L NaCN, pH 10.5) containing 135 mg/L Cu, 196 mg/L Zn and 5.3 mg/L Fe.

Table 2- The comparison of the activated carbon with IX resins used for the adsorption of Au and Cu from a real cyanide leach solution (26.1 mg/L Au, 62.4 mg/L Cu, concentration of adsorbent: 5 g/L, pH 10.5 - 11.25 °C, 4 hours).

Adsorbent	**D (Au)**	**D (Cu)**	**μ (Selectivity)**	**Au on Adsorbent (kg/ton)**	**Cu on Adsorbent (kg/ton)**
Activated Carbon	20.027	342	59	25	17
Purogold A194	7.757	540	14	23	23
Purogold S992*	7.353	83	89	23	5

*pH for Purogold S992 was maintained at 10 - 10.5.

4. Conclusions

Three adsorbents i.e. activated carbon, Purogold S992, and Purogold A194 were employed to compare their efficiency for the recovery of gold and copper from a pregnant cyanide leach solution (PLS) with a low level of copper. The PLS had 26.1 ppm of gold and 62.4 ppm of copper. Activated carbon had high loadings of gold (25 kg/ton) compared to other adsorbents tested (23 kg/ton) whilst Purogold S992 had the lowest copper loadings of about 5 kg/ton. This compared to 17 kg/ton for the activated carbon and 23 kg/ton for Purogold A194. The selectivity was found to be 14, 59, and 89 for Purogold A194, activated carbon, and Purogold S992, respectively. The latter seems to have the highest selectivity for gold over copper. These findings suggest that Purogold S99 can be used as the selective adsorbent for the selective recovery of gold from copper - laden cyanide leach solutions.

Acknowledgements

The authors would like to express their sincere thanks to the Scientific Research Foundation of Karadeniz Technical University for the financial support (Project no: FBA-2018-7399), to PUROLITE for kindly providing resin samples and to Koza Gold Co. (Gümüşhane / Mastra, Türkiye) for kindly providing copper - rich gold ore samples.

References

Adams, M. D. 2016. Gold Ore Processing: Project Development and Operations. Elsevier, 15(2).

Ahlatcı, F., Koç, E., Yazıcı, E., Celep, O., Deveci, H. 2018. Adsorption of heavy metals from waste cyanide solutions with anionic resins, Scientific Mining Journal 57, 17-22.

Bas, A. D., Yazıcı, E. Y., Deveci, H. 2012. Treatment of copper - rich gold ores by ammonia assisted cyanide leaching. Proceedings of the XXVI International Mineral Processing Congress (IMPC), New Delhi, India, 356−365.

Bas, A. D., Koç, E., Yazıcı, E. Y., Deveci, H. 2015. Treatment of copper - rich gold ore by cyanide leaching, ammonia pretreatment, and ammoniacal cyanide leaching. Transactions of Nonferrous Metals Society of China 25 (2), 597-607.

Chryssoulis, S. L., Mcmullen, J. 2016. Mineralogical Investigation of Gold Ores: Gold Ore Processing - Project Development and Operations. Elsevier, 57-93.

Dai, X., Simons, A., Breuer, P. 2012. A Review of copper cyanide recovery technologies for the cyanidation of copper containing gold ores. Minerals Engineering 25, 1-13.

Fleming, C. A., Cromberge, G. 1984. The elution of aurocyanide from strong- and weak- base resins. Journal of the South African Institute of Mining and Metallurgy 84(9), 269-280.

Fleming, C. A., Mezei, A., Bourricaudy, E., Canizares, M., Ashbury, M. 2011. Factors influencing the rate of gold cyanide leaching and adsorption on activated carbon, and their impact on the design of CIL and CIP circuits. Minerals Engineering 24(6), 484–494.

Habashi, F. 1999. A Textbook of Hydrometallurgy. Metallurgie Extractive Quebec Publications, Canada, 220-223.

Kotze, M. 2010. Gold ion exchange. ALTA 2010 Gold Conference. ALTA Metallurgical Services, Melbourne, Australia.

Kotze, M., Green, B., Mackenzie, M., Virnig, M. 2005. Resin - in - Pulp and Resin – in - Solution.: Advances in Gold Ore Processing. Elsevier Science, 15.

Marsden, J., House, I. 2006. The Chemistry of Gold Extraction. The Society for Mining Metallurgy and Exploration Incorporated, USA 2, 318-392.

Medusa, 2009. Software for chemical equilibrium diagrams, 32 bit version. Royal Institute of Technology, Sweden.

Msumange, D. A. 2019. Recovery of gold from copper -rich ores using ion exchange resins. Master Thesis, Karadeniz Technical University, The Graduate School of Natural and Applied Sciences, Department of Mining Engineering, Trabzon.

Msumange, D. A., Yazıcı, E. Y., Celep, O., Deveci, H. 2020. Investigation of the amenability of a copper - rich refractory gold ore to cyanide leaching. Scientific Mining Journal 59(4), 225-234.

Msumange, D. A., Yazıcı, E. Y., Celep, O., Deveci, H. 2021. The effectiveness of the adsorbents for selective recovery of gold from copper - bearing cyanide leach solutions. Scientific Mining Journal 60(1), 21-30.

NORIT. 2003. Data sheet. NORIT GAC 1240, Granular Activated Carbon, Report No: 2201, 2.

PUROLITE. 2015. Purogold ion exchange resins for metals recovery applications: P - 000033 - 250PP - 0515 - PCO, 2.

PUROLITE. 2016*a*. Product data sheet. Purogold A193, 1 August, 1.

PUROLITE. 2016*b*. Product data sheet. Purogold S992, 1 August, 1.

PUROLITE. 2020. Product information. Purolite product guide: P-000023-NPOLD-0120-R2-ENG-PCO, 25.

Sceresini, B. 2005. Gold - Copper Ores. Advances in Gold Ore Processing Developments in Mineral Processing. Elsevier, Amsterdam, 89-824.

Van Deventer, J. 2014. New developments in ion exchange resins for the recovery of gold from complex ores: Hydrometallurgy. Canadian Institute of Mining, Metallurgy and Petroleum, Montreal, Canada, 677-687.

Van Deventer, J., Kotze, M., Yahorava, V. 2012. Gold recovery from copper - rich ores employing the Purolite S992 gold - selective ion exchange resin. ALTA 2012 Gold Conference. ALTA Metallurgical Services, Melbourne, Australia, 8.

Van Deventer, J., Bazhko, V., Yahorava, V. 2014. Comparison of gold - selective ion exchange resins and activated carbon for the recovery of gold from copper gold leach liquors. ALTA 2014 Gold - Precious Metals Conference, ALTA Metallurgical Service, Melbourne, Australia, 18.

Voiloshnikova, N., Deementyev, V., Voiloshnikov, G., Grigoryeva, I., Moskaeva, N. 2014*a*. Comparison of anion exchange resins for adsorption processes in the gold industry. XXVII International Mineral Processing Congress, Santiago - Chile, 1-10.

Yazıcı, E. Y., Ahlatcı, F., Koc, E., Celep, O., Deveci, H. 2015. Pre - treatment of a copper - rich gold ore for elimination of copper interference. 8th European Metallurgical Conference (EMC), Duesseldorf, 2, 601-613.

Yen, W. T., Aghamirian, M. M. 2002. Effect of sulfide minerals and dissolved ions on gold dissolution. Canadian Institute of Mining, Metallurgy and Petroleum, Montreal, 79-86.

Bulletin of the Mineral Research and Exploration

http://bulletin.mta.gov.tr

Sedimentology and Miocene-Pliocene depositional evolution of the stream-dominated alluvial fan deposits at circum-Sultandağları region

Ayhan ILGAR[a*], Ali ERGEN[a], Alper BOZKURT[a] and Ercan TUNCAY[a]

[a]*General Directorate of Mineral Research and Exploration, Deptartment of Geological Researches, Ankara, Türkiye*

Research Article

Keywords:
Yalvaç Basin, Ilgın Basin, Braided River, Meandering River, Forced Regression.

ABSTRACT

Yalvaç and Ilgın basins surrounding Sultandağları were opened due to the orogenic collapse in the early Miocene. The NW-SE trending Çakırçal and Akşehir fault zones, forming boundaries with these basins, caused both the opening of the basins and uplifting of Sultandağları. During the Miocene-Pliocene period, the alluvial fans fed from Sultandağları developed on the basin margins, while the lacustrine carbonate and clastic depositions formed in the basin's interior. The alluvial fan deposits are laterally and vertically transitional with lacustrine sediments and alternate several times in the sequence. The alluvial fans, widespread in the region, consist of debris flow, hyperconsantrated stream flood, braided river and meandering river deposits. Fan deposits that pass from high-energy fluvial facies at the basin margin to the low-energy fluvial facies towards the basin interior have been interpreted as stream-dominated alluvial fan deposits. The age data obtained from the fan deposits of the Yalvaç and the Ilgın basins show that Sultandağları concurrently feeds the alluvial fans on both flanks. Alluvial fan deposition around Sultandağları formed under the control of tectonic and climatic processes. The tectonism led to the formation of basins and source areas. Simultaneously, the climate maintained the streams to be perennial by precipitation, thus proving a continuous sediment supply to the basins. Tectonism and climate-controlled base-level changes determined the quantity of sediments carried to the basin from the source area, causing regressive or transgressive developments.

Received Date: 19.02.2021
Accepted Date: 15.04.2021

1. Introduction

Many studies have been published in the last 50 years on the stratigraphic significance, sedimentological and geomorphological features of the alluvial fan deposits, and their identification criteria (Bull, 1977; Leeder et al., 1988; Nemec and Postma, 1993; Ridgway and DeCelles, 1993; Blair and McPherson, 1994; Harvey et al., 2005; Ghinassi and Ielpi, 2016). Such high interest in researching alluvial fans may be attributed to the fact that they are sensitive recorders of allogenic processes such as tectonism, climate and the base level changes ongoing in a basin (Blair and Bilodeau, 1988; Leeder et al., 1988; Colella and Prior, 1990; Gawthorpe and Colella, 1990; Paola et al., 1992; Nemec and Postma, 1993; Sarıkaya et al., 2015*a, b*; Yıldırım et al., 2016). The alluvial fans, which are the basin margin systems, contain traces of many processes that a basin undergoes throughout its development since its opening. Defining these processes that have developed in the basin allows obtaining main data in basin analysis and establishing the basin evolution (Miall, 1996).

Citation Info: Ilgar, A., Ergen, A., Bozkurt, A., Tuncay, E. 2022. Sedimentology and Miocene-Pliocene depositional evolution of the stream-dominated alluvial fan deposits at circum-Sultandağları region. Bulletin of the Mineral Research and Exploration 168, 43-66. https://doi.org/10.19111/bulletinofmre.928456

**Corresponding author: Ayhan ILGAR, ayhan.ilgar@mta.gov.tr*

Syn-sedimentary tectonic activity is one of the most important processes controlling the basin evolution. The tectonism while on one hand provides the formation of the accommodation space by causing subsidence in the basin and the deposited fan sediments to be protected; it determines on the other hand the amount sediment supply to the basin by controlling the emergence of the source area surrounding the basin, the extent and the capacity of the drainage area, and the fluvial erosion occurring in this area. The syn-sedimentary tectonic activity thus shapes the facies types deposited at the basin margin and the depositional evolution in active extensional basins (Leeder and Gawthorpe, 1987; Alexander and Leeder, 1987). Depending on the climatic processes, the amount of precipitation falling on a basin and the evaporation occurring in the basin also control the deposition in the basin. The quantity, size and continuity of the drainage systems developed in the source area due to the precipitation are determinant on the sediment supply into the basins. The intensity of the evaporation occurring in hydrologically closed basins such as the lacustrine basins directly affects the chemical sedimentation developing in the basin.

The Yalvaç Basin in the west and the Ilgın Basin in the east of Sultandağları located on the NE edge of Isparta Angle (Figure 1) started to open in the early Miocene depending on the extensional tectonic regime (Koçyiğit and Deveci, 2007; Koçyiğit et al., 2013; Koç et al., 2014; Ilgar et al., 2021). The alluvial fan and lacustrine depositions occurred in these basins in the Miocene-Pliocene period (Demirkol et al., 1977; Demirkol, 1982; Demirkol and Yetiş, 1983, 1984; Yağmurlu, 1991; Tuncer, 2020; Ilgar et al., 2021). The alluvial fan deposits constitute the first sedimentary products of Yalvaç and Ilgın basins. The alluvial fans deposited around Sultandağları with a wide spatial distribution consist of many facies and facies associations. The alluvial fans and the accompanying lacustrine carbonate and clastics deposited in basin interior alternate several times in the stratigraphic sequence. The alternation of these sediments reflects the rate and recurrence interval of tectonic subsidence-basin margin uplift and precipitation changes due to climatic processes (Alexander and Leeder, 1987; Kazancı, 1988; Astin, 1990; Carroll and Bohacs, 1999; Gawthorpe and Leeder, 2000; Changsong et al., 2001; Ilgar and Nemec, 2005; Akıska and Varol, 2020).

In this study, the sedimentary facies of the alluvial fan deposits around Sultandağları were studied in detail. The facies changes of the fan deposits from the basin margin towards the basin interior were determined, and the Miocene-Pliocene tectono-stratigraphic evolutions of the Yalvaç and Ilgın basins surrounding Sultandağları were revealed. In addition to the sedimentary processes prevailing in the basin, the control of the tectonism- and the climate-controlled water level changes and sediment supply over the sedimentological and paleogeographic development of basin margin sedimentation systems were also discussed.

2. Regional Geological Setting and Stratigraphy

The Yalvaç and Ilgın basins are intramontane molasse basins and it is considered that these basins were opened due to the orogenic collapse in the early Miocene after nappe emplacements in the Central Taurides (Koçyiğit and Deveci, 2007; Koçyiğit et al., 2013; Koç et al., 2014; Ilgar et al., 2021). The pre-Miocene units forming Sultandağları extend in NW–SE direction between the Yalvaç and Ilgın basins and constitute the bedrock of both basins (Figure 1b). The activities of the NW–SE trending Çakırçal and Akşehir fault zones (Figure 1b) which restrict Sultandağları caused the opening of the Yalvaç and Ilgın basins, while at the same time resulting in Sultandağları to rise as a horst structure. These faults have controlled both the tectono-sedimentary development of the basins and the geomorphology of Sultandağları.

The bedrock of the Yalvaç Basin within the study area is consisted by Sultandağları Sequence, the Beyşehir-Hoyran Nappes and their common-cover Celeptaş formation (Figure 1b). Sultandağları Sequence consists of Sultandağı Unit comprising early Cambrian-Late Cretaceous sedimentary and volcanic metamorphic rocks and the overlying Çay Unit, which is constituted by Late Devonian-Late Cretaceous metasedimentary rocks (Özgül et al., 1991; Göncüoğlu et al., 2007; Güngör, 2013; Ergen et al., 2016, 2017, 2021). The Beyşehir-Hoyran Nappes, tectonically overlying Sultandağı Unit, consist of nappes represented by Mesozoic aged ophiolite, ophiolitic mélange, neritic-pelagic carbonate and clastic rocks (Gutnic et al., 1968; Brunn et al., 1971;

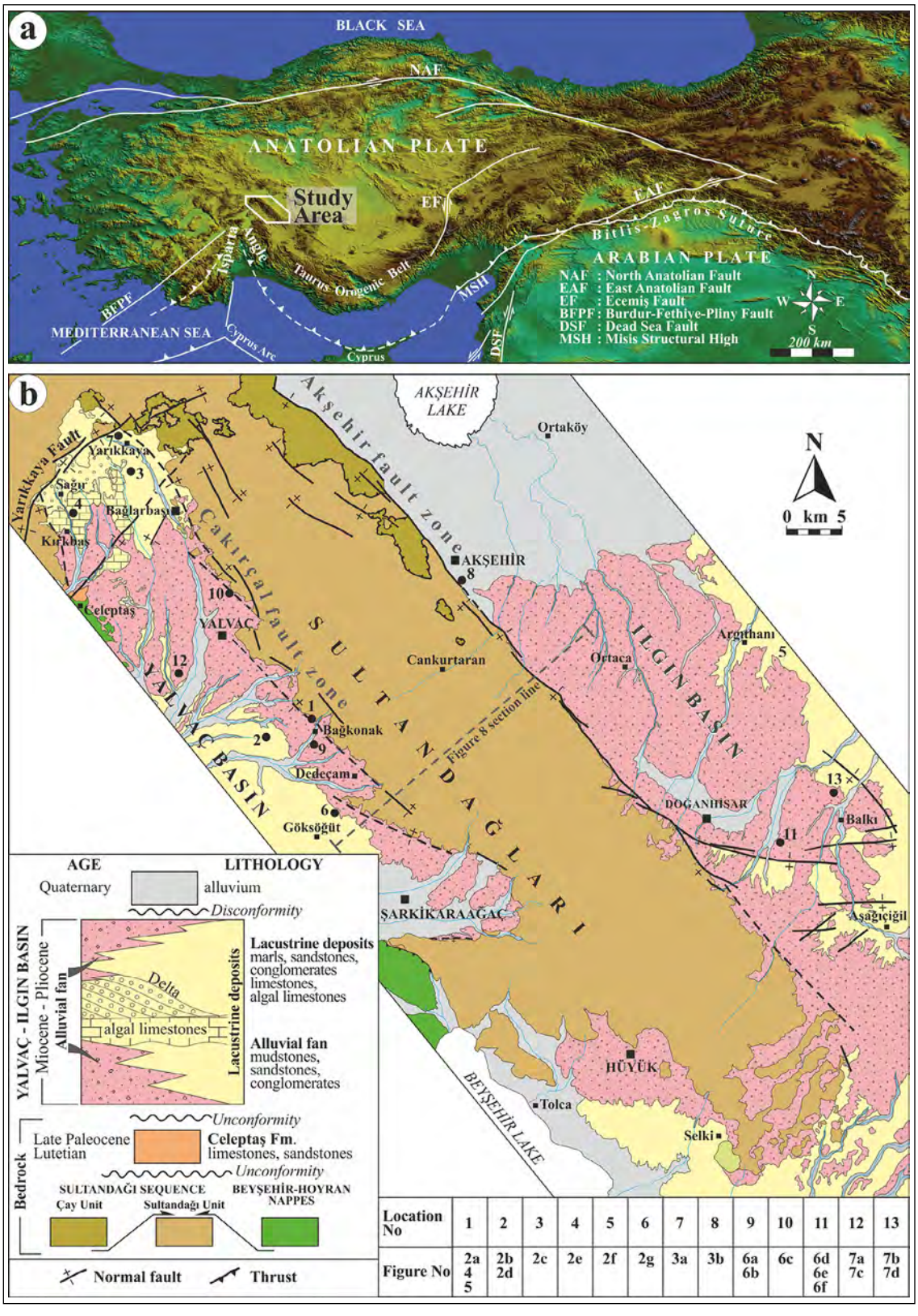

Figure 1- Location map of the study area; a) the location of Yalvaç and Ilgın basins and main tectonic lines on the topographic view of Anatolia (SRTM image with 90 m resolution; after Jarvis et al., 2008) and b) geological map of Yalvaç and Ilgın basins around Sultandağları (simplified from Ergen et al., 2021). The numbers on the map indicate outcrop locations to which other figures of the article refer.

Özgül, 1976; Monod, 1977). The Celeptaş Formation consists of late Paleocene-Lutetian turbidites. The bedrocks belonging to Sultandağları Sequence form the bedrocks of the Ilgın Basin within the study area. Sultandağları has undergone polyphase deformation during its tectonic evolution (Demirkol et al., 1977; Eren, 1987, 1990; Özgül et al., 1991; Ergen et al., 2021).

In Yalvaç and Ilgın basins, the alluvial fans were initially deposited unconformably on the pre-Miocene rocks of Sultandağları (Figure 2a). The alluvial fan deposits mainly consist of red-brick colored conglomerate, sandstone, siltstone and mudstone in both basins. The alluvial fan sediments deposited in the Yalvaç Basin were named as Bağkonak and Kırkbaş formations (Demirkol et al., 1977; Demirkol, 1982; Demirkol and Yetiş, 1983, 1984; Yağmurlu, 1991), and the alluvial fan sediments of the Ilgın Basin were defined as Ayaslar, Belekler and Doğanhisar formations by Umut et al. (1987). Since all alluvial fan deposits around Sultandağları, defined as different formations, are parts of a common depositional process, they have been investigated under the title alluvial fan deposits circum-Sultandağları region in this study.

The alluvial fans are transgressively overlain by lacustrine carbonate and clastic rocks in both basins. The lacustrine sediments mainly consist of mudstone, marl, clayey limestone, algal limestone (Figures 2b, c, d, e), sandstone, conglomerate and coal. These units were deposited in offshore, offshore-transition, shoreface, beach, Gilbert-type delta, shoal-water delta and swamp sub-environments within the basin (Ergen et al., 2021; Ilgar et al., 2021). The facies assemblages reflecting these environments in the Yalvaç Basin were studied under the name of Göksöğüt, Madenli and Yarıkkaya formations by previous researchers (Demirkol et al., 1977; Demirkol, 1982; Yağmurlu, 1991) while the lacustrine sediments deposited in the Ilgın Basin were named as Aşağıçiğil and Derviş formations (Umut et al., 1987). However, these facies associations reflecting the sub-environments, have been defined as lacustrine deposits in this study, since they are laterally and vertically transitional and alternate several times in the sequence.

The alluvial fans and the lacustrine sediments deposited in the Yalvaç and Ilgın basins are in alternation in the stratigraphic sequence (Figure 2f) which ends with alluvial fan deposits (Figure 2g).

3. Structural Geology of Circum-Sultandağları Region

The Çakırçal fault zone and the Akşehir fault zone, respectively (Figure 1b), bound the western and eastern edges of Sultandağları. The Çakırçal fault zone forms the boundary of the bedrock units of Sultandağları and the Neogene sediments of the Yalvaç Basin (Figure 3a). This fault zone has a length of approximately 65 km in N40°-50°W direction and consists of four fault segments (Figure 1b). These segments, which extend in a parallel to sub-parallel direction with respect to the main direction, make a stepped structure by displacing in NE or SW directions. There are relay ramps between the fault segments. The plunge of slickenlines measured on faults are generally between 80°-90°. The slickenlines, vertical or almost vertical corrugation axes and chatter marks indicate normal faulting. The alluvial fan deposits around Yalvaç and the lacustrine carbonate deposits around Yarıkkaya were deposited on the footwall blocks of the Çakırçal fault zone (Figure 1b). These deposits present an onlapping geometry on fault planes and indicate that the normal faulting occurred prior to the deposition. The Çakırçal fault zone, which is one of the most important fracture systems causing the opening of the Yalvaç Basin to the southwest of Sultandağları, consists of steeply inclined faults. Pre- and syn-depositional activities of these faults caused the development of a consistent steep basin margin morphology to the north of the basin. Syn-sedimentary activities of the faults also provided with the preservation of accommodation space on the northern margin of the basin, thus giving rise to deposition of a thick sequence of lacustrine carbonates and alluvial fan deposits. The activity of the Çakırçal fault zone has also continued after the deposition. Depending on this activity, travertines were deposited on the alluvial fans through the waters from the fault zone.

The Akşehir fault zone, which is almost parallel to the Çakırçal fault zone, forms a boundary between the basement units of Sultandağları and the Ilgın Basin in the east (Figures 1b and 3b). The Akşehir fault zone, approximately 90 km long, extends in N40°W

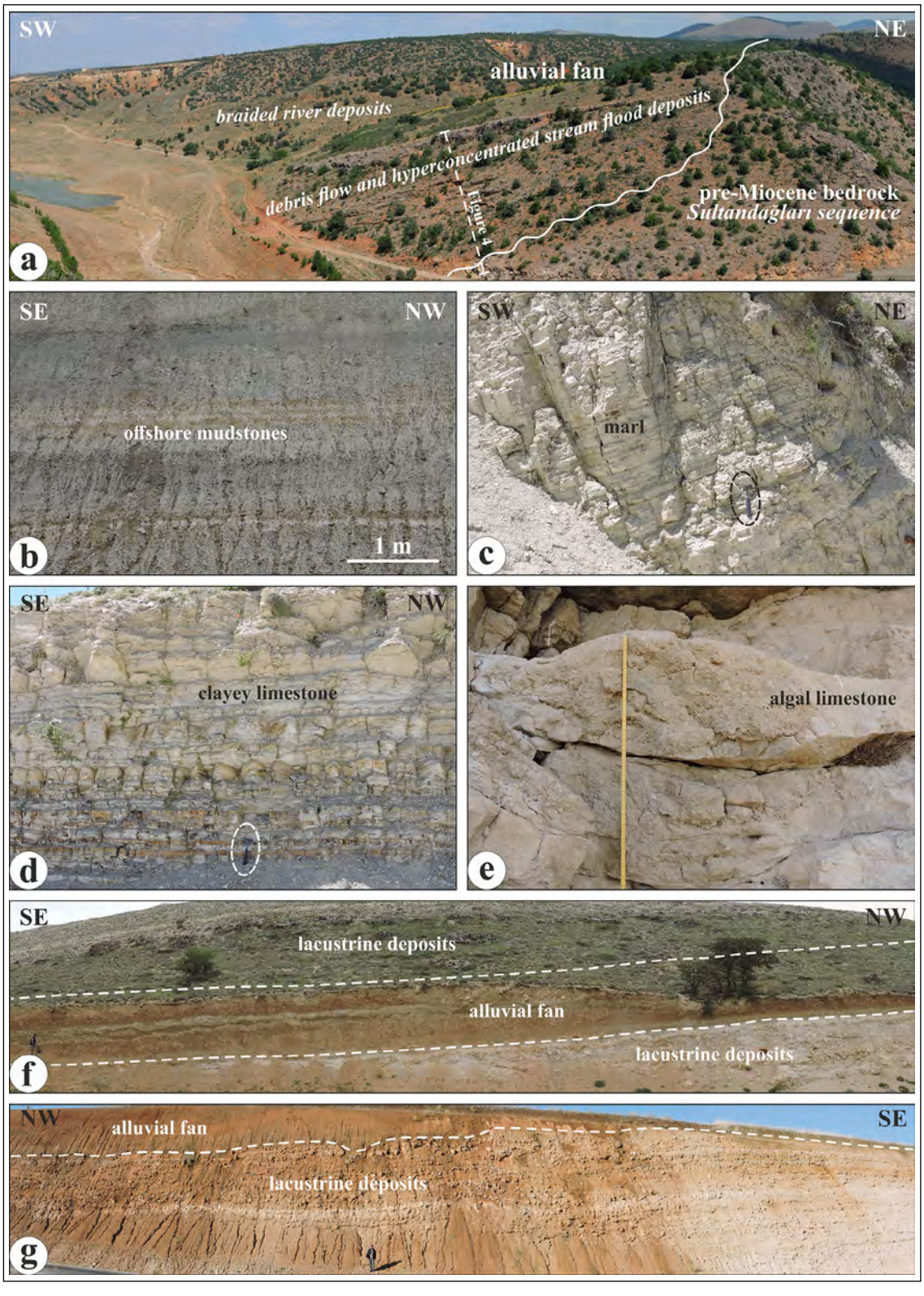

Figure 2- a) Facies belonging to alluvial fan deposits unconformably overlying pre-Miocene bedrocks of Sultandağları in the Yalvaç Basin. The section line of Figure 4 is seen on this figure. b, c, d, e) Facies belonging to lacustrine sediments transgressively overlying alluvial fan deposits, f) a repetitive view of the alluvial fan and the lacustrine sediments deposited in Yalvaç and Ilgın basins within the succession and g) alluvial fan deposits overlying the lacustrine sediments during the closure of the basins. Numbers in Figure 1b indicates the locations of the figures in the basin.

Figure 3 - A view of; a) Çakırçal fault zone forming the boundary between the bedrock units of Sultandağları and the Neogene sediments of the Yalvaç Basin in the west and b) a Google Earth view of the Akşehir fault zone forming the border of the Neogene sediments of the Ilgın Basin in the east. A photograph illustrating some parts of the Akşehir fault zone is placed in this figure. Numbers in Figure 1b indicates the locations of the figures in the basin.

direction. The Akşehir fault zone is an active normal fault and its last activity with a magnitude of Mw = 6.5 occurred on February 3, 2002 (Emre et al., 2003; Kalafat et al., 2020). With this activity, a surface rupture of approximately 26 km was formed and a vertical displacement of 30 cm occurred on this fracture (Kalafat et al., 2020). Depending on the activity of the Akşehir fault zone, the Ilgın Basin began to open. The alluvial fan sediments were deposited in front of the fault scarps within this basin. The slickenlines, vertical or almost vertical corrugation axes and chatter marks observed on the Akşehir fault zone indicate normal faulting. The onlapping geometry on the Akşehir fault zone, which has a steep basin margin morphology, indicates that the normal faulting occurred prior to the deposition, as well as the Çakırçal fault zone. With the activity of the fault in the Miocene-Pliocene period, the accommodation space on the basin margin basin was continuously preserved and a thick alluvial fan sequence and lacustrine carbonates were deposited in the Ilgın Basin.

4. Alluvial Fan Deposits

4.1. General Characteristics

The alluvial fan deposits limited by Sultandağları crop out in very large areas in the Yalvaç and Ilgın basins. The alluvial fan deposits are distributed between Bağlarbaşı and Şarkikaraağaç in the Yalvaç Basin and crop out around Hüyük in the south. In the east, these deposits crop out along Akşehir, Argıthanı, Doğanhisar and Aşağıçiğil in the Ilgın Basin. Thus, the fan deposits surround Sultandağları (Figure 1b). The fan deposits have a width of 1-7 km in the Yalvaç Basin and 3-18 km in the Ilgın Basin. While the alluvial fan deposits have an apparent thickness of approximately 300 m at their contact with Sultandağları, this thickness gradually decreases in basinward direction. The

Paleozoic-Mesozoic rocks of Sultandağları form the source areas of the alluvial fans. The drainage systems developed on Sultandağları eroded Sultandağları sequence and provided clastic material to the fan sediments. Today, the extension of the deep valleys on Sultandağları towards the basin is in compatible with the main distributary channel systems of the Miocene-Pliocene alluvial fans. The alluvial fans deposited in the Dedeçam village and around Yalvaç in the Yalvaç Basin are the best examples of this relationship (Figure 1b). This situation has been interpreted as some of the current drainage systems used the old river beds. The average difference between the recent heights of Sultandağları and the surrounding basins is over 1000 m. Since a thick delta package with Gilbert-type delta architecture was deposited on the northern margin of the Yalvaç Basin during the Miocene period (Ilgar et al., 2021), it is considered that a similar height difference between the source area and the basin floor could have also existed in the Miocene-Pliocene period as well.

4.2. Facies Assemblages

Alluvial fan deposits, which present different facies characteristics from the basin margin to the basin interior, consist of many facies and facies associations. In this study, four facies associations were defined as debris flow deposits, hyperconsantrated stream flood deposits, braided river deposits and meandering river deposits. Debris flow and hyperconsantrated stream flood deposits are observed in a narrow area in the Yalvaç Basin just in front of the fault plane that limits the basin. Although there is no outcrops, these facies are thought to have been deposited in the Ilgın Basin according to the grain size distribution of the fan deposits on the basin margin. These facies gradually pass into braided river and then to meandering river deposits in the basinward direction. The dominant facies assemblage of alluvial fan sediments deposited in the Yalvaç and Ilgın basins consists of braided river and meandering river deposits, which have similar facies characteristics in both basins. The facies assemblages were described below in detail without making any basin discrimination. The facies assemblages were defined under their interpretive genetic labels in this study as they reflect the transport-deposition environment and conditions. But their descriptions are separated from interpretations in the text.

4.2.1. Debris Flow Deposits

This facies assemblage consisting entirely of conglomerates is found together with hyperconsantrated stream flood deposits in conglomeratic sequence outcropping at the basin margin and alternates with those sediments (Figure 4). These conglomerates are generally thick bedded (120-250 cm) and the beds are planar or mound-shaped (Figure 4). The lower boundaries of the beds are nonerosional. The conglomerates, which are generally composed of medium to coarse pebbles and cobbles, have a clast-supported texture (Figures 4, 5a, b). Boulders with a size of up to 115 cm are also commonly observed (Figure 4). The spaces between the gravels are filled with sands, granules and fine pebbles. No stratification is observed within the poorly sorted conglomerates, consisting of angular, sub-angular grains, they are massive or roughly inversely graded (Figures 4, 5a, b). The pebbles that make up this facies assemblage are mostly derived from the Jurassic-Cretaceous dolomitic limestones of Sultandağları (Figure 5b).

Massive or inversely graded, clast-supported, planar or mound-shaped conglomerates have been interpreted as noncohesive debris flow deposits (Nemec and Steel, 1984; Nemec, 1990). The deposition of alluvium carried by debris flow processes, which is a dense, viscous flow, occurred due to en masse freezing (Johnson, 1984; Nemec and Steel, 1984; Kim et al., 1995).

4.2.2. Hyperconsantrated Stream Flood Deposits

This facies assemblage, which is found together with the debris flow deposits in the sequence, consists entirely of conglomerates (Figures 4, 5c, d, e). The conglomerates are generally thick-bedded (50-150 cm), and to a lesser extent thin to medium-bedded (Figures 4, 5c, d, e). The basal surfaces of the conglomerate beds are sharp and erosional with an erosion rate reaching up to 50 cm (Figures 4, 5c). It shows lenticular geometries in the parts where basal erosion is high (Figure 5e). These clast-supported conglomerates consist of fine pebble to boulder-sized grains (Figures 4a, b). The blocks with a grain size of up to 70 cm are also commonly observed in the

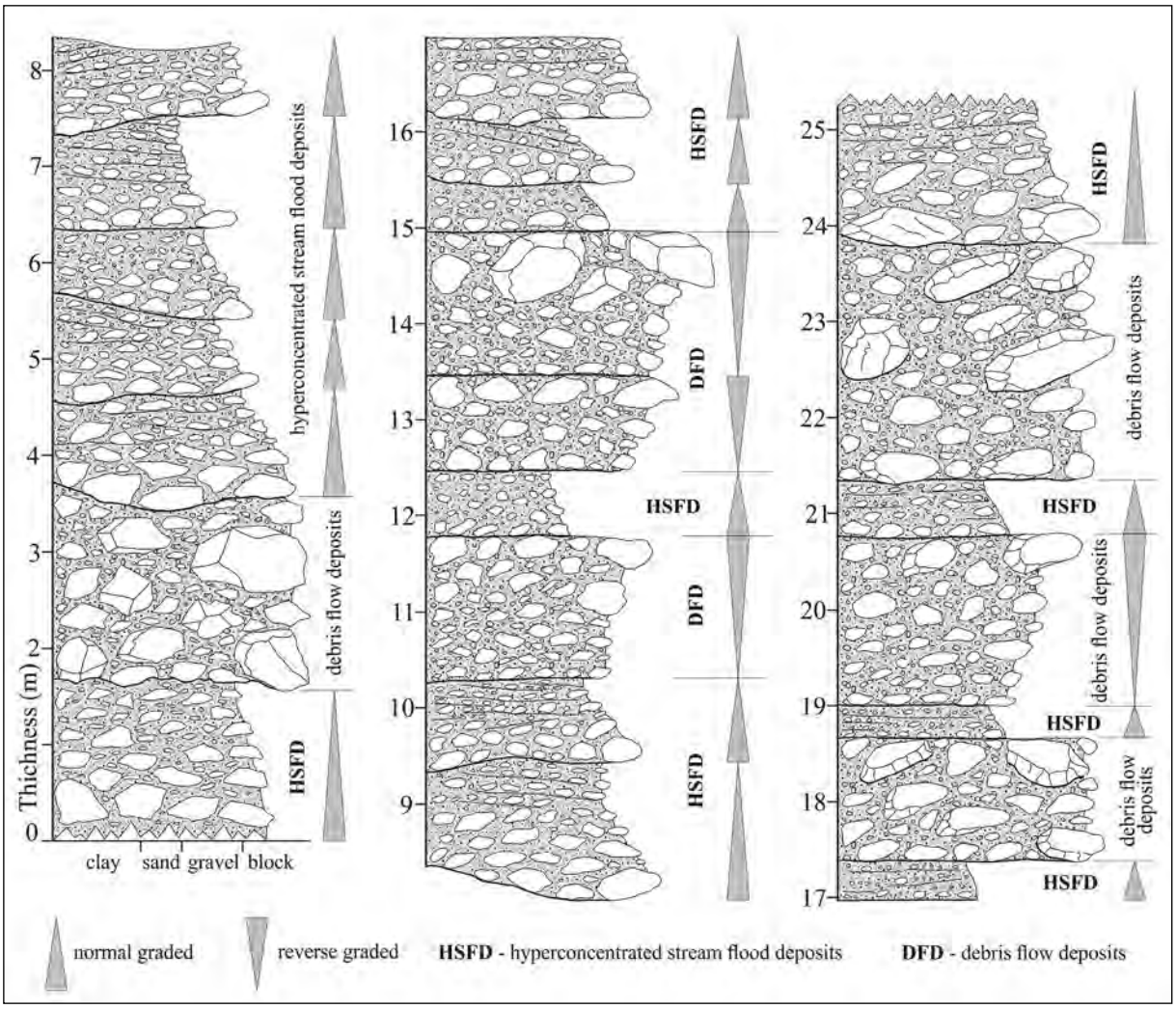

Figure 4- Sedimentological log of alluvial fan deposits outcropping in a limited area just in front of the fault plane at the basin margin of the Yalvaç Basin and consisting of debris flow and hyperconsantrated stream flood deposits. This section is taken from location 1 in Figure 1b.

rocks. The interstitial spaces between the pebbles are filled by sands and granules. The conglomerates defined within this facies assemblage consist of angular, sub-angular and slightly subrounded grains, and are generally poorly sorted. No stratification is observed in thick-bedded conglomerates, however; it has a weak or well-developed normal grading (Figures 4, 5c, d, e). Particularly in the uppermost parts of the normal graded conglomerates, a significant reduction in grain size is observed (Figure 5e). The thinner bedded conglomerates, generally normal-graded, consist of fine to coarse pebbles (Figures 4, 5e). These conglomerates, a generally normal-graded, starting with cobble-sized gravels on erosional bottom surfaces and the grain size passes into granule to fine pebble upwards (Figure 5e). In the middle-upper parts of the conglomerates, planar parallel- and planar cross-stratifications are observed. The gravels forming this facies association are mostly derived from the Jurassic-Cretaceous dolomitic limestones of Sultandağları in the Yalvaç Basin, and from the Paleozoic-Mesozoic quartzite, marble and schists in the Ilgın Basin.

It is thought that since the thick-bedded and clast-supported conglomerates described within this facies assemblage have lenticular geometries, erosional bottom surfaces and normal grading, they indicate very strong fluvial bedload deposits that can cause erosion. These thick-bedded conglomerates have been interpreted as hyperconsantrated stream flood deposits

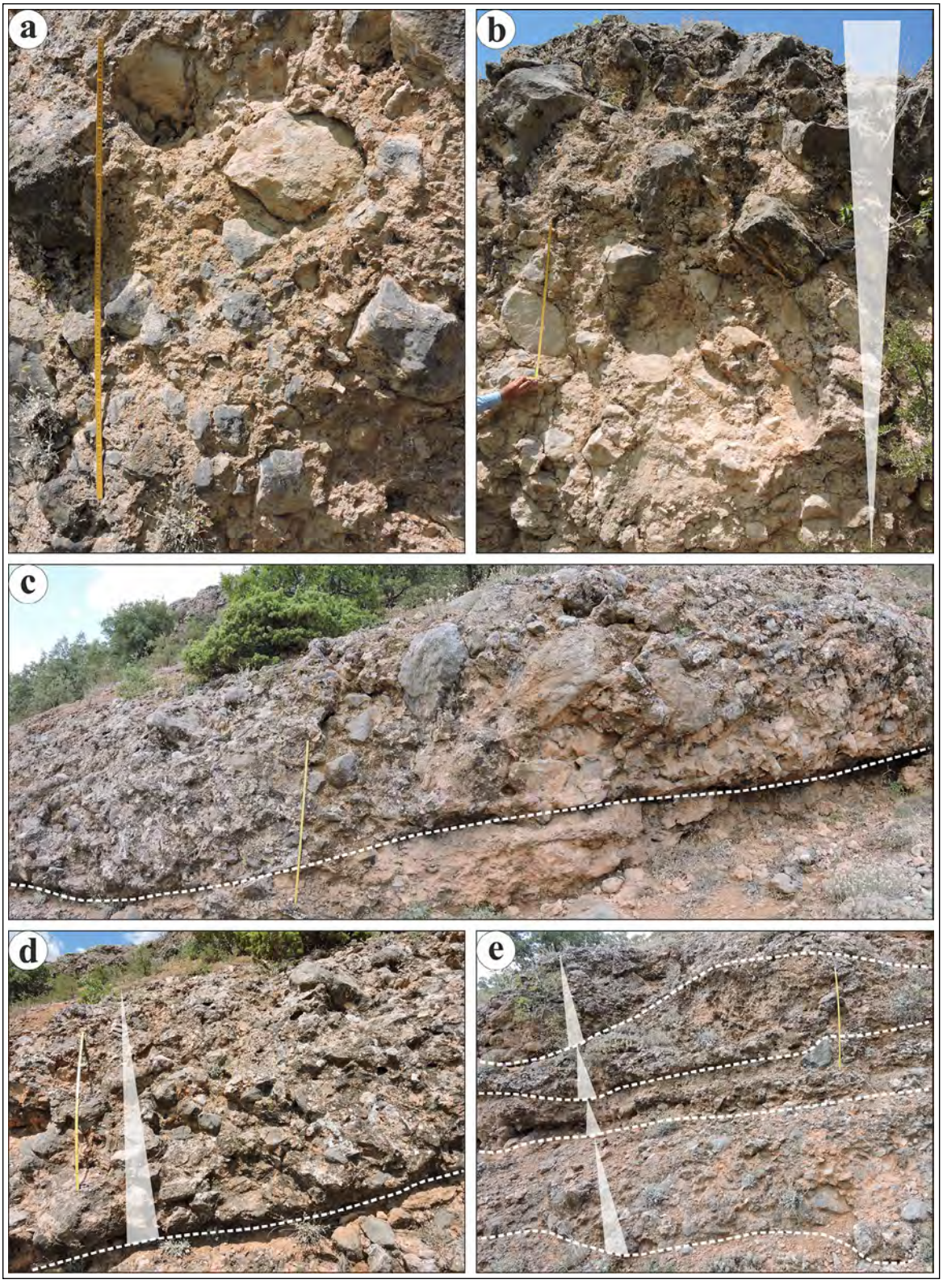

Figure 5- a), b) Debris flow deposits consisting of medium-coarse pebble to boulder conglomerates deposited at the basin margin just in front of the fault plane. The conglomerates are a) massive or b) inversely graded. Thick bedded hyperconsantrated stream flood deposits found in the sequence with debris flow deposits have, c) erosional bottom surfaces and d, e) normal grading, e) erosional lenticular geometries are observed in fine to medium pebble, thin to medium-bedded conglomerates. Numbers in Figure 1b indicates the locations of the figures in the basin.

(Nemec and Muszyński, 1982; Ballance, 1984; Wells, 1984; Todd, 1989; Sohn et al., 1999). The flows forming these deposits have a high viscosity flow rheology between Newtonian fluid and Bingham plastic (Nemec and Muszyński, 1982). Hyperconsantrated stream flood deposits have a rheology between debris flows and river flows and represent a transitional facies between these flows (Nemec and Muszyński. 1982; Ballance, 1984; Nemec and Steel, 1984; Wells, 1984; Todd, 1989; Sohn et al., 1999). Therefore, massive or inverse graded deposition reflecting debris flow processes or well-developed parallel cross-stratification reflecting grainflows in rivers has not been developed in these deposits. The fact that thin- to medium-bedded conglomerates found together with thick-bedded conglomerates having erosional bottom surfaces, normal grading, planar parallel and planar cross-stratification in the uppermost parts of the beds indicate a transport in river channels as bedload and a deposition (Todd, 1989; Collinson, 1996; Miall, 1996). Planar parallel- and planar cross-stratified conglomerates defined in the upper parts of these deposits form bar deposits (Smith, 1974; Boothroyd and Ashley, 1975; Miall, 1985; Nemec and Postma, 1993). The thin-bedded planar parallel cross-stratified conglomerates were deposited at the uppermost parts of thick-bedded conglomerates due to the decrease in the grain concentration in the flow due to the deposition from hyperconsantrated stream flood flows.

4.2.3. Braided River Deposits

This facies assemblage is observed in the sequence as multistorey fluvial channel deposits (Figures 6a, b). The channel deposits possess a large scale erosional bottom surface and lenticular geometry in sections parallel to the basin margin (Figure 6a). In sections perpendicular to the basin margin, it is observed as planar-bedded with basinward inclination (Figures 6c, d). The width of the channel deposits reaches 50 m and the erosion rate on the bottom surfaces reaches up to 5 m in places. In addition, the smaller scale channel deposits have also been identified within the sequence. The braided river facies assemblages consist of channel lag deposits and channel bar deposits.

Channel Lag Deposits: The channel lag deposits underlying the channel bar deposits on uneven erosional surfaces are observed as a single or as several rows of gravels (Figures 6b, e, f). These sediments, which are laterally discontinuous, consist of sub-rounded to rounded, coarse pebbles to cobbles and, in places, boulders. These clast-supported lag deposits lacks stratification and the interstitial spaces is filled by coarse sand, granule and fine pebbles.

The thin-bedded conglomerates located on erosional paleochannel bases have been interpreted as the channel lag deposits (Miall, 1985; Nemec and Postma, 1993).

Channel Bar Deposits: The channel bar deposits, predominating the alluvial fan sequence, are mainly composed of conglomerates and a lesser amount of and sandstone and pebbly-sandy mudstones (Figures 6a, b, e, f). The conglomerates consist of angular to sub-angular, mostly bladed, to a lesser extent rod- and spherical-shaped, fine to coarse pebbles, which are mostly derived from metamorphic rocks and limestones. The conglomerates have a clast-supported texture and are moderately sorted. The interstitial spaces between the gravels is filled with coarse sand and gravel. Conglomerates have a bedding thickness of 15-45 cm and are planar parallel stratified or planar cross-stratified (Figures 6a, b, e, f). The stratifications within the beds are recognizable by differences in grain size, sorting and matrix. Conglomerates pass upwards into brick-colored, granule to fine pebbly, medium to coarse grained sandstones (Figures 6e, f). These low-angle planar cross-stratified sandstones have a thickness of 10-30 cm and are laterally discontinuous due to the erosion of the overlying new channel deposits. Conglomerates and sandstones form fining-upward bedsets which are bounded by the erosional surfaces at the top and the bottom, by being deposited upon one another (Figures 6a, b, e, f).

The fining-upward bedsets bounded by erosional surfaces were interpreted as the channel fill deposits of braided rivers (Collinson, 1996; Miall, 1996). These river channels form distributary channels on alluvial fans. The planar parallel-stratified and planar cross-stratified conglomerates within the channel deposits form longitudinal, transverse or oblique bar deposits in braided rivers (Smith, 1974; Boothroyd and Ashley, 1975; Miall, 1985; Nemec and Postma, 1993). The sandstones observed in the upper parts of bar deposits

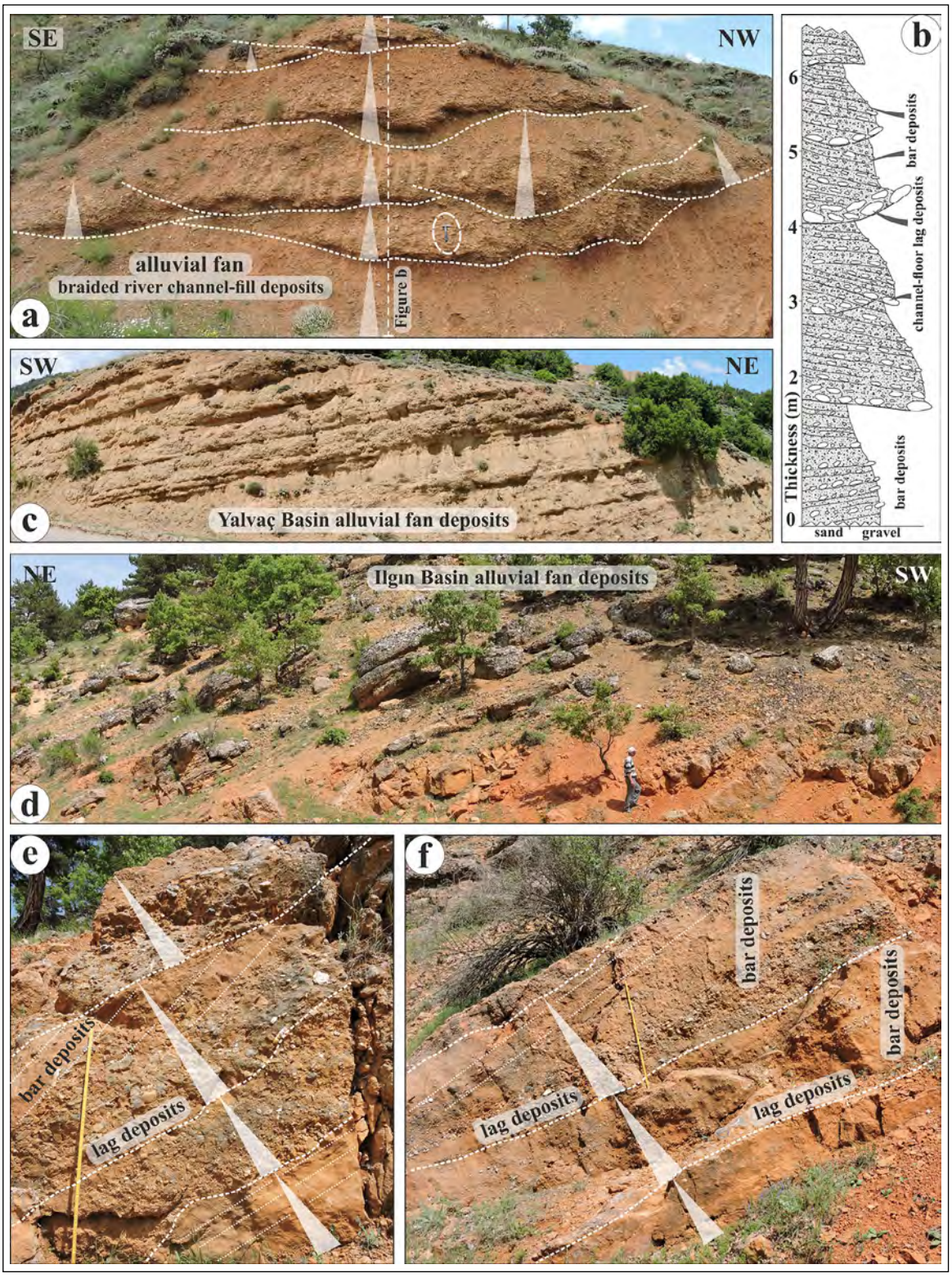

Figure 6- Braided river channel deposits of alluvial fans are deposited in the Yalvaç and Ilgın basins; a) these deposits have lenticular geometry in sections parallel to the basin margin, b) channel floor lag and bar deposits are seen on the sedimentological log of the braided river sediments. The section line is shown in Figure 6a. c), d) Braided river sediments consist of planar-bedded deposits with basinward inclination in the sections perpendicular to the basin margin and e), f) channel deposits, which are overlain by planar parallel or planar cross-stratified bar deposits, start with channel floor lag deposits in the form of a single or several rows of gravel on the erosional surfaces. Numbers in Figure 1b indicates the locations of the figures in the basin.

were interpreted as transverse bar sediments deposited due to small currents in periods when the alluvial fan distributary channels migrate laterally and hence their strength decreases (Miall, 1985).

4.2.4. Meandering River Deposits

The meandering river deposits defined in the distal part of the alluvial fan system consist of red-brick colored conglomerate, sandstone, siltstone and mudstone (Figure 7). Within this facies assemblage, the point bar deposits, chute deposits and flood plain deposits have been defined.

Point Bar Deposits: Point bar deposits, which are mainly composed of sandstones and conglomerates, have erosional bottom surfaces and the rate of erosion reaches 1.5 m in places (Figures 7a, b). Groove marks are often observed on erosional surfaces. Point bar deposits start with a laterally discontinuous isolated gravel beds on the uneven erosional surfaces. These

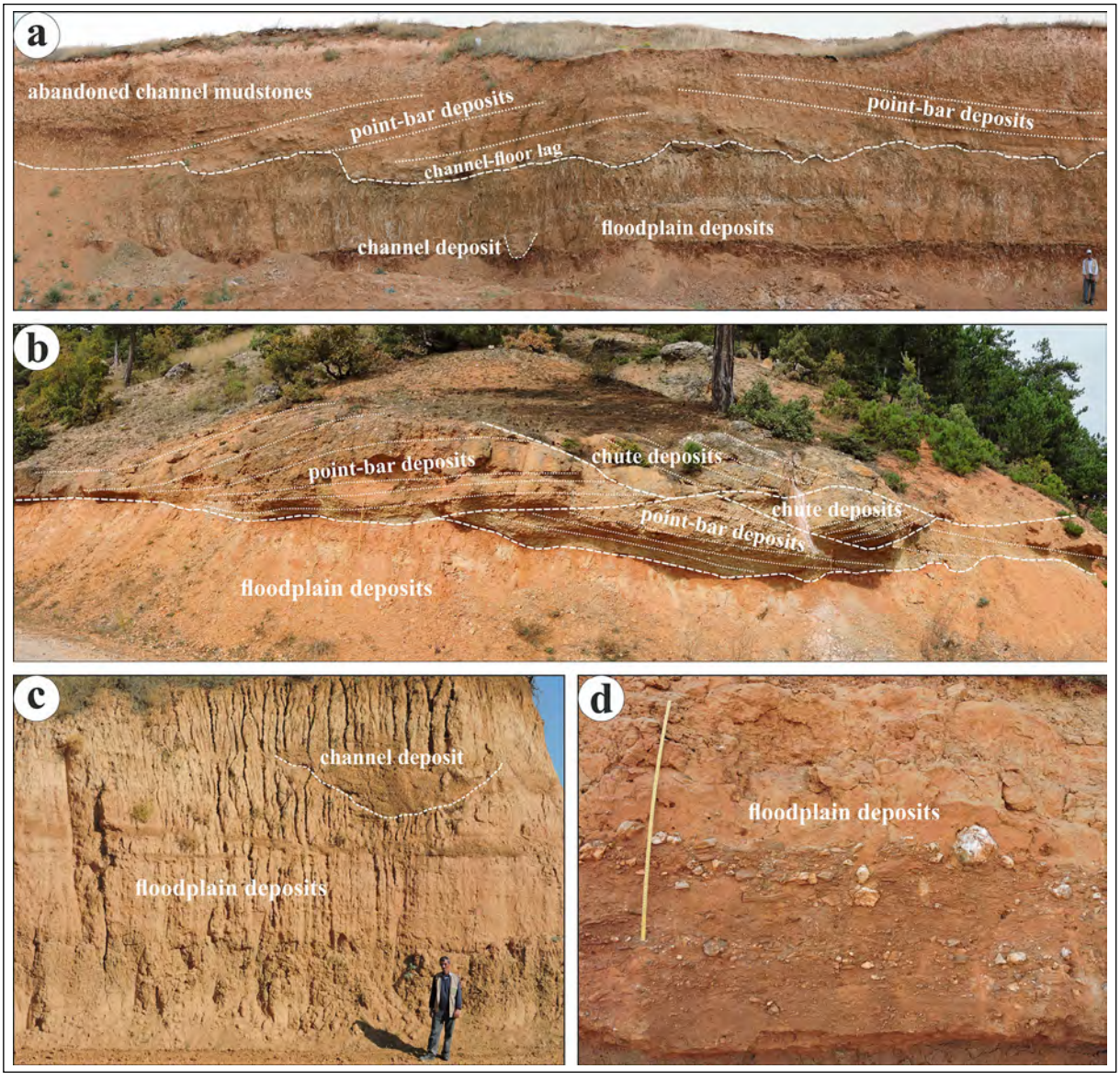

Figure 7- Meandering river sediments identified in the distal parts of alluvial fans are composed of red-brick colored conglomerate, sandstone, siltstone and mudstone. Point bar and floodplain deposits of the meandering rivers from; a) Yalvaç and, b) Ilgın basins. Chute deposits consisting of planar cross-stratified conglomerates can be seen upon the point bar deposits with a diagonal erosional surface, c), d) floodplain deposits consisting of alternation of planar horizontal bedded, light brown-brick mudstone, siltstone and sandstone above and below the point bar deposits. Numbers in Figure 1b indicates the locations of the figures in the basin.

sediments, which consist of medium to coarse pebbles and have a clast-supported texture, form the channel-floor lag deposits. These lag deposits lacks stratification and the interstitial spaces is filled by medium to coarse sand and granules. Point bar deposits placed on the channel-floor lag deposits consist of sandstones, pebbly sandstones and conglomerates (Figures 7a, b). Point bars observed as planarly inclined and sigmoidal geometry in cross sections have a bedset height reaching 2.5 m and inclination angles varying between 15°-25° (Figures 7a, b). As they have a sigmoidal geometry, the slope angles of the point bars decrease in the upward and downward directions and pass tangentially to the stream floor (Figure 7b). These beds are generally planar parallel and occasionally planar cross-stratified. Point bar deposits developed in different directions and separated from each other by erosional surfaces can be observed in the sequence (Figures 7a, b). The inclinations, bedding thickness and grain size of the point bar deposits gradually decrease in dip direction in the channel and these deposits pass into horizontal and very thin-bedded sandstone, siltstone and mudstone (Figure 7a).

Sigmoidal point bar deposits determined in the meandering river deposits have been interpreted as meandering belt deposits formed by lateral growth due to the lateral displacement of the meandering river channels (Jackson, 1976; Nanson, 1980; Brierley, 1991). The channel-floor lag deposits underlying the point bar deposits on an erosional surface are associated with laterally migrating channel bottoms (Ghinassi et al., 2014). The very thin and horizontally bedded sandstone, siltstone and mudstone covering the point bars are thought to be the sediments deposited in lakes formed due to the abandonment of the meandering channel.

Chute Deposits: There are channel deposits up to 1 m in depth and 3 m in width on the sigmoidal sandstones and conglomerates of point bar deposits (Figure 7b). These channel deposits with erosional bottom surfaces developed obliquely to the dip directions of the planarly inclined beds. Channel deposits consisting of fine pebbly conglomerates and coarse-grained sandstones are generally planar cross-stratified (Figure 7b).

The small channel sediments deposited on point bar deposits by eroding them in the oblique direction have been interpreted as the chute deposits. Chute deposits represent channel deposits that were eroded and filled during the flood periods of river (McGowen and Garner, 1970). The cross-stratified sandstones deposited in chute form the chute bars accumulated in the flow direction of the river (McGowen and Garner, 1970; Ghinassi et al., 2014).

Flood Plain Deposits: Flood plain deposits underlying and overlying the point bar deposits in the stratigraphic sequence consist mainly of light brown-brick colored mudstone, siltstone and sandstone alternation (Figure 7). The very thin planar beds of these deposits form laterally continuous sheet-like beds (Figures 7c, d). There are also very thin bedded (5-15 cm thick), fine pebbly conglomerates, which are laterally discontinuous in the sandstones and mudstones (Figure 7d). These conglomerates have a small scale erosional bottom contact. In several levels, the V shaped channel deposits with a depth of 1 m were defined in this sequence. The channel deposits are composed of slighltly inclined planar cross-stratified fine pebble conglomerates.

This facies assemblage is a product of deposits that occur in flood plain areas at the edges of river channel during flooding periods of meandering rivers (McGowen and Garner, 1970; Miall, 1985). The decrease in the energies of non-channelized sheetfloods caused mudstone deposition from the suspension (Collinson, 1996; Tooth, 1999). The V shaped channel conglomerates identified in flood plain deposits probably reflect small stream channel opened due to the rupture of meandering river channel and the sedimentation in this channel.

5. Age of the Alluvial Fan Sediments

The age of the alluvial fan sediments deposited on the bedrock around Sultandağları was determined by compiling the age data obtained in this study and the previous studies. Since the alluvial fan deposits in Yalvaç and Ilgın basins have lateral and vertical relationships with lacustrine deposits, the age data obtained from lacustrine deposits have also enabled the relative aging of fan deposits.

No age data could be obtained from the first fan deposits overlying the bedrock units in the Yalvaç

Basin. The lacustrine deposits transgressively overlying these alluvial fan sediments were dated as the mid-late Miocene by Yağmurlu (1991). Late early Miocene-early middle Miocene ages were obtained for the lower levels of the same deposits carried out in the same sediments by Tuncer (2020) based on ostracod, mammals and palynological dating, while the late Miocene-Pliocene ages were obtained for the upper levels of the lacustrine sequence (Table 1). In this study, the late Miocene-early Pliocene age was determined based on the ostracod assemblage of the mudstone and marl samples taken from the upper levels of the lacustrine sequence (Table 1). The age of alluvial fan deposits, which overlie the lacustrine deposits with a forced regression in the closure period of the Yalvaç Basin, was determined as the late Miocene based on mammals content (Table 1; Usta et al., 2019). According to all these studies, the age of the

Table 1- The fossil content and ages of the alluvial fan and lacustrine sediments outcropping in the Yalvaç Basin.

Sediments		**Fossil Assemblage and Age**
Yalvaç Basin	**Alluvial Fan**	**Upper levels of the alluvial fan sediments:** **Dedeçam village, Pamuklu locality:** Gompotheridae *Choerolophodon pentelici*, Equidae *Hipparion* cf. *philippus*, Equidae *Hipparion* sp. *(*small form*)*, Rhinocerotidae *Chilotherium* sp., Rhinocerotidae *Ceratotherium neumayri*, Bovidae *Prostrepsiceros syridisi*, Bovidae *Gazella* sp., Bovidae *Palaeoryx*, Giraffidae *Palaeotragus* sp. **Kuyucak village, İldere locality:** Gompotheridae *Choerolophodon pentelici*, Equidae *Hipparion* sp., Bovidae *Gazella* sp., Bovidae *Palaeoryx pallasi*, Giraffidae *Helladotherium duvernoyi*, Giraffidae *Palaeotragus rouenii* **Kuyucak village, South of Belez:** Hyaenidae *Adcrocuta eximia*, Gompotheridae *Choerolophodon pentelici*, Equidae *Hipparion* cf. *mediterraneum* Equidae *Mediterraneum*, Rhinocerotidae *Ceratotherium neumayri*, Bovidae *Gazella* sp. **Tokmacık village:** Hyaenidae *Adcrocuta eximia*, Mammutidae *Zygolophodon* sp., Equidae *Hipparion mediterraneum*, Equidae *Hipparion* sp. (small form), Rhinocerotidae *Chilotherium* sp., Rhinocerotidae *Ceratotherium neumayri*, Cervidae *Pliocervus* sp., Bovidae *Gazella* sp., Bovidae *Palaeoryx pallasi*, Giraffidae *Palaeotragus rouenii*, Giraffidae *Helladotherium duvernoyi* **Age:** Late Miocene, MN 11 mammals zone (Usta et al., 2019)
	Lacustrine Sediments	**Lower levels of the lacustrine sediments:** *Democricetodon franconicus* Fahlbusch, 1966 **Age:** MN 4 mammals zone, middle Orleanian (late Early Miocene) (Tuncer, 2020) *Herpetocyprella mongolica, Mediocypris candonaeformis, Fabaeformiscandona pokornyi, Cyclocypris ovum, Leucocythere sieberi, Herpetocyprella auriculata, Lineocypris lunata, Lineocypris inflexa* **Age:** late Early – Middle Miocene (Tuncer, 2020) **Upper levels of the lacustrine sediments:** *Arctocypris fuhrmanni, Candonopsis arida, Ilyocypris gibba, Potamocypris gracilis, Fabaeformiscandona pokornyi, Cyclocypris ovum, Leucocythere immigrata, Heterocypris steinheimensis, Zonocypris membranae, Neglecandona angulata decimai, Cypris pubera, Potamocypris zschokkei, Cypria ophtalmica, Pseudocandona marchica, Herpetocypris brevicaudata, Neglecandona altoides, Neglecandona angulata, Limnocythere inderica, Fabaeformiscandona acuminata, Tonnacypris convexa* **Age:** Late Miocene–Pliocene (Tuncer, 2020) **The uppermost levels of the lacustrine sediments:** *Heterocypris salina* (Brady), *Heterocypris salina salina* (Brady), *Heterocypris salina barneri* (Luttic), *Candona parallela pannonica* (Zalanyi), *Candona* aff. *parallela pannonica* (Zalanyi), *Candona* aff. *iliensis* Mandelstam, *Candona candida* (Koch), *Candona* aff. *candida* (Koch), *Cypridopsis* aff. *vidua* (O. F. Müller), *Candona (Candona)* cf. *churmensis* Freels, *Candona (Candona)* aff. *iliensis* Mandelstam, *Darwinula cylindrica* Straub, *Candona neglecta* Sars, *Darwinula stevensoni* (Brady ve Robertson), *Candona (Candona)* cf. *marchica marchica* Hartwaing, *Candona (Pseudocandona) compressa* (Koch), *Candona (Pseudocandona)* cf. *compressa* (Koch), *Ilyocypris gibba* (Ramdohr), *Cyclocypris ovum* (Jurine), *Ilyocypris bradyi* Sars, *Zonocypris membranae* Livantel, *Candona (Candona)* aff. *gracilis* Livental, *Cyclocypris ovum* (Jurine), *Ilyocypris* sp., *Candona* sp., *Candona (Caspiocypris)* sp., *Cypridopsis* sp., *Heterocypris* sp. **Age:** Late Miocene–Early Pliocene (this study)

alluvial fan and lacustrine sediments deposited in the Yalvaç Basin has been accepted as Miocene-Pliocene.

Similarly, there is no age data obtained from the first alluvial fan deposits in the Ilgın Basin. Umut et al. (1987) determined an age of latest Oligocene or the earliest Miocene with mammals dating from the lower levels of the lacustrine deposits which transgressively overlie the alluvial fan deposits (Table 2). An Early Miocene age was determined based on the ostracod content of marl samples taken from the lower levels of the sequence (Tuncer, 2020; Table 2). Tuncer (2020), determined a Late middle Miocene (Serravallian)-Early late Miocene (Tortonian) from the middle levels of the lacustrine sequence based on the ostracod assemblage. Umut et al. (1987) and Tuncer (2020) assigned a Late Miocene-Pliocene age to the middle-upper levels of the sequence; Umut et al. (1987), on

Table 2- The fossil content and ages of the alluvial fan and lacustrine sediments outcropping in the Ilgın Basin.

Sediments		**Fossil Assemblage and Age**
Ilgın Basin	**Alluvial Fan**	**Belekler village:** *Hipparion* sp., *Vertebrate* gen. et. sp. indet, *Testude* sp., *Gompotheridae* gen. et. sp. indet **Age:** Late Miocene (Umut et al., 1987) **2.5 km south of Argıthanı:** *Hipparion gracile, Rhinoceras* sp., *Gazella* sp., *Antilope* (*Carnasiere*), *Ruminantia* **Age:** late Miocene or Pontian (Yalçınlar, 1953) **2.5 km south of Argıthanı:** *Hipparion* sp. **Age:** Early Pliocene (Sickenberg et al., 1975)
	Lacustrine Sediments	**Lower levels of the lacustrine sediments:** *Mirabella intermedia, Eumyarion* aff. *bifidus*, *Eumyarion* sp. II, *Eumyarion* sp. III, *Eumyarion* sp. IV, *Paleosciurus* sp., *Brausatoglis* sp., Gliridae gen. et sp. indet **Age:** latest Oligocene or earliest Miocene (Umut et al., 1987) **Gölyaka village:** *Ilyocypris boehli, Cyprinotus turcica, Metacypris gokcenae, Moenocypris* cf. *francofurtana, Fabaeformiscandona* sp. A **Çeltek village:** *Virgatocypris virgata, Metacypris gokcenae, Heterocypris* aff. *parva, Stenocypris* sp. A, *Fabaeformiscandona* sp. B, *Fabaeformiscandona* sp. juv. ve *Pseudocandona* sp. juv. **Age:** Early Miocene (Tuncer, 2020) **Middle levels of the lacustrine sediments:** *Strandesia spinosa, Darwinula stevensoni, Vestalenula cylindrica, Candonopsis arida, Ilyocypris gibba, Paralimnocythere rostrata, Potamocypris gracilis, Pseudocandona compressa, Fabaeformiscandona pokornyi, Cyclocypris ovum, Cypris falki, Cyprinotus inaequalis, Leucocythere immigrata, Amnicythere nodigera, Heterocypris steinheimensis, Paracandona euplectella, Cavernocypris subterranea, Zonocypris membranae, Neglecandona angulata decimai, Cyprideis sublittoralis, Heterocypris glozaniensis, Cypria ophtalmica, Heterocypris rotundata, Herpetocypris* cf. *brevicaudata, Scottia pseudobrowniana* **Age:** Late-Early Miocene (Serravalian)?–Early-Late Miocene (Tortonian) (Tuncer, 2020) **Middle-upper levels of the lacustrine sediments:** *Arctocypris fuhrmanni, Paracandona euplectella, Ilyocypris bradyi, Vestalenula cylindrica, Candona* sp. C ve *Mixtacandona*? sp. A, *Bithynia glabra, Bithynia pseudemmericia* **Age:** Late Miocene–Pliocene (Tuncer, 2020) **Middle-upper levels of the lacustrine sediments:** *Cyprinotus salinur* BRADY, *Hydobia vitrella* STEF., *Hydrobia syrmica* NEUM., *Candona* sp., *Candoniella* sp., *Prionocypris* sp., *Zonocypris* sp., *Pseudamnicola* (*Andrussowiella*) *carasiensis* JEK., *Valvata* sp. **Age:** upper levels of the Miocene - Pliocene (Umut et al., 1987) **Upper layers of the lacustrine sediments:** *Heterocypris salina salina* (BRADY), *Ilyocypris* cf. *gibba* RHAMDOR, *Candona* cf. *altoides* PETKOVSKI, *Pseudocandona* sp., *Candona* sp., Gastrodlar, *Valvata (Valvata) cristata* MÜLLER, *Caecilioides* sp., *Opercule, Heterocypris salina salina* (BRADY), *Zonocypris* sp., *Candona* cf. *altoides, Candona* sp., *Chara, Hydrobia vitrella* STEF., *Techochora cilindrica* MÖD. **Age:** Pliocene (Umut et al., 1987)

the other hand, determined the Pliocene ages from the uppermost levels of the same sequence (Table 2). Late Miocene age assigned by Umut et al. (1987), Late Miocene or Pontian age by Yalçınlar (1953) and an Early Pliocene age by Sickenberg et al. (1975) to the alluvial fan deposits overlying the lacustrine deposits with a forced regression in the closure period of the Ilgın Basin (Table 2). According to all abovementioned studies, the age of the alluvial fan and lacustrine sediments deposited in the Ilgın Basin has been accepted as the Miocene-Pliocene in age.

6. Depositional Evolution and Discussion

Sultandağları, located on the NE edge of the Isparta Angle, and the surrounding Yalvaç and Ilgın basins are placed in a horst-graben system. These basins started to open in the Early Miocene under the control of an extensional tectonic regime (Koçyiğit et al., 2013; Koç et al., 2014). The formation of Yalvaç and Ilgın basins occurred due to the orogenic collapse (Koçyiğit and Deveci, 2007; Koçyiğit et al., 2013). The region, which had been subjected to compressional deformation during the Late Cretaceous-Eocene period, was subjected to orogenic collapse due to the disappearance of the regional force forming the compressional tectonism (Koçyiğit and Deveci, 2007; Koçyiğit et al., 2013). Thus, while on one hand Sultandağları were rising, on the other hand the normal fault controlled basins started to open on both sides of Sultandağları. The alluvial fan and lacustrine carbonates were deposited in these basins in the Miocene-Pliocene period (Figure 8).

With the opening of the Yalvaç and Ilgın basins, first the alluvial fans began to be deposited in these basins. The river systems flowing from the watershed boundary of Sultandağları towards SW and the drainage systems flowing towards the NE formed the alluvial fans of the Yalvaç and Ilgın basins, respectively (Figure 8a). These fan deposits show significant changes from the basin margin to the basin interior in terms of grain size, bedding thickness and sedimentary facies. Thick bedded debris flow and hyperconsantrated stream flood deposits, which are deposited at the basin margin and composed of coarse pebbles-boulders pass into conglomerates and sandstones formed by the braided river facies assemblage in the basinward direction. The proximal and medial parts of the alluvial fan are composed of mainly braided river facies assemblages. This facies assemblage has well preserved lenticular shaped stream channel geometries with erosional bottom surfaces in sections parallel to the basin margin. In these channel deposits that form the main distributary channels, there are braided river bar deposits accumulated on top of each other with lateral displacements. The braided river deposits gradually pass into the meandering river deposits towards the distal parts of the alluvial fans. The meandering river deposits consist of point bars and widespread flood plain deposits.

These facies assemblages from the basin margin towards the basin interior display changes ranging; a) from high energy fluvial facies to lower energy fluvial facies; b) from thick bedded and laterally discontinuous rocks to thin bedded and laterally continuous rocks and c) from coarse grained sediments to fine grained sediments. The river deposits having these facies changes from the basin margin towards the basin interior were interpreted as stream dominated alluvial fan deposits (Nemec and Postma, 1993; Ridgway and DeCelles, 1993). In stream dominated alluvial fans, perennial streams are the dominant sediment transport agents on the fan surface (Collinson, 1996). Rapid and frequent displacements are observed in the stream channels that form these alluvial fans. With the decrease seen in the river bed slopes in the basinward direction, the braided rivers pass into the meandering rivers (Leeder, 1999).

The alluvial fan deposits, which have a very wide spatial distribution around Sultandağları, are not the product of a single fan, but reflect a combination of many fans (Figure 8a). The combination of fan deposits that have developed side by side in the stream dominated alluvial fans and the covering of one fan the other are common features (Mukherji, 1990). The presence of concurrent alluvial fans, independent from each other, indicates that many drainage systems have developed on Sultandağları. These drainage systems also indicate that the region received abundant precipitation during the Miocene-Pliocene period. The development of stream dominated alluvial fans due to the many drainage systems feeding the basin and the coal formation in the basins reflect the presence of humid climatic conditions in the Miocene-Pliocene period. In the palynology study conducted by Akgün

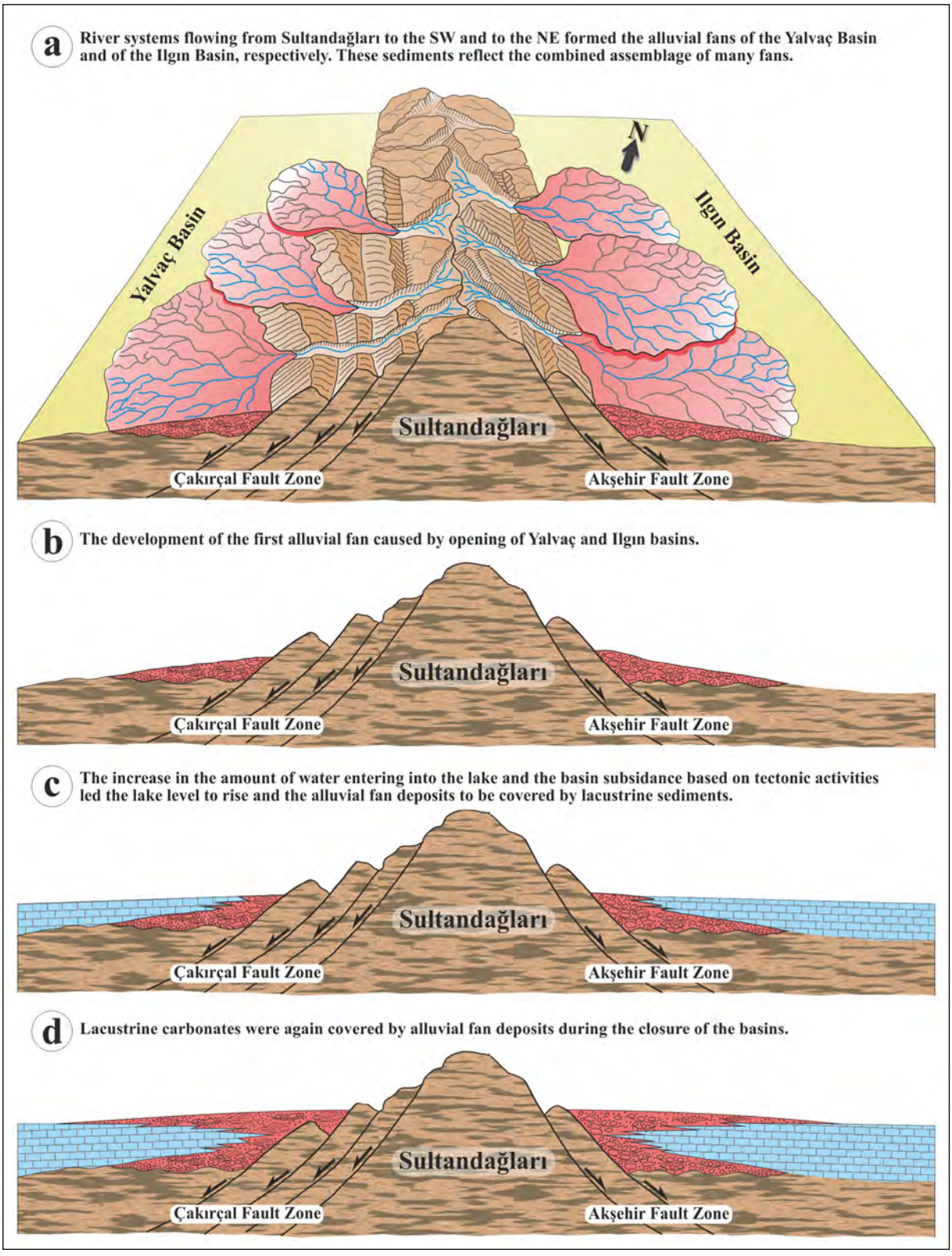

Figure 8- a) Block diagram showing alluvial fans deposited in Yalvaç and Ilgın basins around Sultandağları. The cross-section line of the block diagram is given in Figure 1b. b, c, d) The schematic illustration of the development of alluvial fans and lacustrine depositions depending on the tectonism and climate in the Miocene-Pliocene period in these basins (not to scale).

and Akyol (1992) in the region, the temperate and humid climatic conditions were determined for the Miocene period.

Debris flow and hyperconsantrated stream flood deposits deposited just in front of the basement rocks and fault scarp in the Yalvaç Basin form the proximal facies of alluvial fans. The clastic sediments derived from the source areas were transported to the basin as floods during flooding periods due to the steep slope caused by the fault scarps and gravity effect. These floods accumulated the sediments they dragged, increased the amount and density of sediments and deposited them in front of fault planes by hyperconsantrated stream flood flows (Figure 8b). Hyperconsantrated stream flood deposits are characteristic for tectonically active, alluvial fan sediments deposited on steep slope basin margins (Nemec and Muszyński, 1982; Ballance, 1984). According to Blair (1987), the deposition of hyperconsantrated stream flood deposits at the contact with the bedrock at the basin margin constitutes the first records of the subsidence in the basin. Since these flows have a high viscosity flow rheology, they show a limited lateral distribution in front of the fault scarps (Nemec and Muszyński, 1982).

Hyperconsantrated stream flood deposits pass into the braided river sediments both in the basinward direction and in the vertical sequence. The braided river facies assemblage shows that the sediment supply from Sultandağları into the basin occurred with well-channelized flows. Thus, the alluvium transported to the basin were deposited as well-organized channel sediments. It is estimated that the transport distance of the alluviums derived from Sultandağları is approximately 10-20 km. Since it is not very long distances, the conglomerates are not well rounded. However, the fluvial processes enabled the sediments to have relatively better sorting, the development of sedimentary structures such as planar parallel and planar cross-bedding, and better organized depositional architectures such as the fining upward sequence. During the occasional flooding periods, the alluviums overflowing from braided river caused the deposition of thin bedded, sandstone, siltstone and mudstone flood sediments. Thus, significant part of the alluviums transported by the streams from Sultandağları are deposited in the proximal and medial parts of the fan.

The braided river facies decreases towards the inner parts of the Yalvaç and Ilgın basins. Thus, the point bar and flood plain deposits of the meandering rivers become the predominant facies in the inner parts of the basin, reflecting that the energy and sediment carrying capacities of rivers with high energy flowing in the proximal and medial parts of the basins begin to decrease towards the basin interior.

The age data obtained from alluvial fan sediments of Yalvaç and Ilgın basins show that Sultandağları concurrently fed these alluvial fan deposits. This also reveals that Çakırçal and Akşehir fault zones, which limit Sultandağları and open the Yalvaç-Ilgın basins, are most likely contemporaneous. The ongoing activities of these fault zones enabled the subsidence of the basins and the creation of a continuous accommodation space (Figure 8b). Thus, while new erosional areas were formed with the uplift of Sultandağları, the subsidence of the basins enabled the deposition of clastic materials derived from these erosional areas and the protection of the deposited sediments (Figure 8).

The relay ramps developed within the fault zones also controlled the position and development direction of the alluvial fans in the basin by directing the flow direction of the drainage systems fed from Sultandağları. The relay ramps developed especially in the east of Yalvaç and the south of Dedeçam in the Yalvaç Basin caused the development of alluvial fans in the N-NW direction with morphological control (Figure 1b).

The fact that an alluvial fan sequences with a thickness of approximately 300 m were deposited in the Yalvaç and Ilgın basins during the Miocene-Pliocene period indicates a thin sedimentary sequence deposition in a large geological time. The probable reasons for this situation were interpreted as; 1) that the deposition did not always occur in the same locality, that there were lateral displacements within the same fan and between different fans; 2) there might be partial erosions on fan surfaces where the active deposition did not occur; 3) there were changes in the amount of sediment supply over time. The changes in

sediment supply and the reasons and consequences of these changes are discussed in detail below.

Drainage systems developed on Sultandağları both fed the alluvial fans on one hand and enabled the formation of lacustrine basins in front of the fans on the other hand. Thus, clastic and carbonate rocks started to be deposited in lacustrine basins. The increase in lake level due to both the increase in the amount of water entering the lake and the subsidence of the basin caused by the activities of the Çakırçal and Akşehir fault zones led the alluvial fan sediments to be covered with lacustrine sediments (Figure 8c). However, there is a significant decrease in the amount of clastic material transported to Yalvaç and Ilgın basins during trangressive periods. During this period, carbonate deposition prevailed in the basins and no clastic deposition except for a few small localities occurred. Only foreshore, shoreface and shoal water deltas as clastic facies were deposited in a narrow belt on the basin margins of these basins. These deltas with low set height and small spatial distribution rapidly pass into the carbonate sediments towards the basin. In the periods when the lake level reached its maximum height, there is almost no detrital supply occurred into the basin.

It is thought that the absence of a significant progradation in clastic shoreline at the basin margin during maximum transgression periods is associated with decrease in the sediment supply into the basin. The decrease in the sediment supply did not allow a progradation in clastic shoreline and a significant regression. Despite the fact that clastic material can be transported to the basin to a large extent and to form thick alluvial fans around Sultandağları, the reason for the sudden decrease in the amount of clastic material during the development of lacustrine transgressions can be explained by different processes and mechanisms such as; a) decrease in precipitation over Sultandağları due to climatic changes, b) displacement of drainage systems due to catchment in river drainage systems, c) increase in the base level due to the transgression seen at the basin margin, and thus reduction in the erosion in the source area. Among these mechanisms, the rise in the lake level and the lacustrine transgression seen in the basin are incompatible with the decrease in precipitation due to the climate. In case of displacement of the river bed systems due to the catchment, it is expected that the abundant clastic material was transported to different parts of the basin. The absence of this situation also eliminates the possibility of catchment. It is thought that the most probable mechanism could be the decrease in the clastic sediment supply to the basin due to the base-level rise. The base level, which is an imaginary and dynamic equilibrium surface between the erosion and deposition, is theoretically accepted as the sea or lake level and controlled by the changes in this level (Catuneanu, 2006). Below and above the base level, the deposition and erosion occurs, respectively. The drainage systems discharging into the basin especially during the periods when tectonism paused or slowed down (assuming that there is no change in the amount of rainfall in the basin) caused the drowning of alluvial fans by increasing the lake water level (Figure 8c). The increase in the lake level also caused the base level rise, thus reducing the erosion at the basin margin and accordingly the sediment supply to the basin. During the periods when the lake level increased, with the decrease in the amount of detritus entering the basin, clastic deposition at the basin margin either occurred in very limited areas or did not occur. Thus, deposition of the carbonate rock were dominated instead of clastics in Yalvaç and Ilgın basins. The algae in the lake also significantly contributed to the carbonate-dominated sedimentation.

In cases when the lake level relatively decreases, it was seen that alluvial fan sediments were deposited with sharp contact on the lacustrine deposits and prograde towards the basin (Figure 8d). The forced regressive periods in which the alluvial fan deposits prograde on the lacustrine carbonates were repeated several times, especially in the Ilgın Basin. This clearly reveals that the base level change controls the amount of clastic material entering the basin. The decrease of the lake water level due to the climatic processes or the displacement of the lake shoreline by tectonic reasons led to the fall in the base level, and thus an abundant sediment supply to the basin due to erosion on the basement units. The increase in the lake level on the other hand caused a decrease in the amount of sediment entering the basin with the rise of the base level. Periodic changes and alternations observed in alluvial fans and lacustrine deposits have also been described in different basins (Heward, 1978; Wilson,

1980; Mack and Rasmussen, 1984; Ilgar and Nemec, 2005). During the closure of the lacustrine basins around Sultandağları, the repetition of this process one more time and the fall in the base level due to tectonic-climatic origin caused the lacustrine carbonates to be covered with alluvial fan sediments due to intense erosion at the basin margin and the abundant clastic input into the basin (Figure 8d).

7. Results

Yalvaç and Ilgın basins, which are located on the NE edge of the Isparta Angle and surround Sultandağları, are intramontane molasse basins that were opened due to the orogenic collapse under the extensional tectonic regime in Neogene period. Activities of NW-SE trending Çakırçal and Akşehir fault zones provide the opening of the Yalvaç and Ilgın basins, restrict Sultandağları and uplift it as a horst structure as well.

The lacustrine carbonates and the alluvial fans fed from Sultandağları during the Miocene-Pliocene period were deposited in these basins.

The age data obtained from lacustrine deposits and alluvial fans in both basins show that Sultandağları concurrently fed these alluvial fans.

In this study, the debris flow, hyperconcentrated stream flood, braided river and meandering river deposits have been defined in the alluvial fan deposits around Sultandağları. The braided river and meandering river deposits constitute the dominant facies assemblages of the alluvial fans. These facies assemblages from the basin margin towards the basin interior display changes ranging; a) from high energy fluvial facies to lower energy fluvial facies; b) from thick bedded and laterally discontinuous rocks to thin bedded and laterally continuous rocks and c) from coarse grained sediments to fine grained sediments.

The alluvial fan deposits surrounding Sultandağları have been interpreted as the stream dominated alluvial fan deposits according to these facies characteristics. These alluvial fans are not the product of a single fan, but reflect a combined assemblage of many fans. The presence of coeval alluvial fans indicates that many drainage systems were developed on Sultandağları and that the region received abundant precipitation during the Miocene-Pliocene period.

This study, in addition to the sedimentary processes prevailing in the basin throughout the basin evolution, contributes in comprehending the issue of the tectonism- and climate-controlled water level changes and the rate of sediment supply on the control of sedimentological and paleogeographic development of basin margin deposition systems. While the tectonic-climatic- origin base level fall causes intense erosion at the basin margin and the transportation of abundant clastics into the basin, the rise of the base level causes a decrease both in the erosion rate at the basin margin and accordingly the amount of sediment supply to the basin, in the fields examined in this study. As a result normal or forced regression or transgression developed at the basin margin depending on the amount of clastic sediment supply.

Acknowledgements

This study was carried out within the scope of Sultandağları'nın Jeolojisi ve Jeodinamik Evrimi (Geology and Geodynamic Evolution of Sultandağları) project conducted between 2015-2016 by the Department of Geological Researches of the General Directorate of Mineral Research and Exploration (MTA), Türkiye. The determination of ostracod fossils was made by Dr. Gönül ÇULHA. We would like to acknowledge Dr. Oktay PARLAK and Tolga ESİRTGEN who reviewed the earlier version of the manuscript and provided valuable contributions. We are also thankful to Prof. Dr. Attila ÇİNER and the other anonymous referee.

References

Akgün, F., Akyol, E. 1992. Yukarıkaşıkara ve Yarıkkaya (Isparta) kömürlerinin karşılaştırmalı palinostratigrafisi ve paleoekolojisi. Türkiye Petrol Jeologları Derneği Bülteni 4(1), 129–139.

Akıska, E., Varol, B. E. 2020. Alluvial-lacustrine sedimentation and volcaniclastic deposition in an intracontinental tectonic graben: paleoenvironmental evolution of the Neogene Sinanpaşa Basin, West-central Turkey. Turkish Journal of Earth Sciences 29, 295–324.

Alexander, J., Leeder, M. R. 1987. Active tectonic control on alluvial architecture. Recent Developments in Fluvial Sedimentology. Society of Economic Paleontologists and Mineralogists Special Publications 39, 243–252.

Astin, T. R. 1990. The Devonian lacustrine sediments of Orkney, Scotland: implications for climate cyclicity, basin structure and maturation history. Geological Society of London. Special Publication 147, 141–151.

Ballance, P. F. 1984. Sheet-flow-dominated gravel fans of the non-marine Middle Cenozoic Simmler Formation, central California. Sedimentary Geology 38, 337–359.

Blair, T. C. 1987. Sedimentary processes, vertical stratification sequences, and geomorphology of the Roaring River alluvial fan, Rocky Mountain National Park, Colorado. Journal of Sedimentary Petrology 57, 1–18.

Blair, T. C., Bilodeau, W. L. 1988. Development of tectonic cyclothems in rift, pull-apart, and foreland basins: sedimentary response to episodic tectonism. Geology 16, 517–520.

Blair, T. C., McPherson, J. C. 1994. Alluvial fans and their natural distinction from rivers based on morphology, hydraulic processes, sedimentary structures and facies assemblage. Journal of Sedimentary Research 64, 450–489.

Boothroyd, J. C., Ashley, G. M. 1975. Process, bar morphology and sedimentary structures on braided outwash fans, Northeastern Gulf of Alaska. Glaciofluvial and Glaciolacustrine Sedimentation. Society of Economic Paleontologists and Mineralogists Special Publication 23, 193–222.

Brierley, G. J. 1991. Bar sedimentology of the Squamish River, British Columbia: definition and application of morphostratigraphic units. Journal of Sedimentary Petrology 61, 211–225.

Brunn, J. H., Dumont, J. F., Graciansky, P. C., Gutnic, M., Juteau, T., Marcoux, J., Monod, O., Poisson, A. 1971. Outline of the geology of the Western Taurides. Geology and History of the Turkey. Guidebook for the 13th field session os PESL, Tripoli, 225–255.

Bull, W. B. 1977. The alluvial fan environment. Progress in Physical Geography 1, 222–270.

Carroll, A. R., Bohacs, K. M. 1999. Stratigraphic classification of ancient lakes: balancing tectonic and climatic control. Geology 27, 99–102.

Catuneanu, O. 2006. Principles of Sequence Stratigraphy. Elsevier, Amsterdam, 375.

Changsong, L., Eriksson, K., Sitian, L., Yongxian, W., Jianye, R., Yanmei, Z. 2001. Sequence architecture, depositional systems, and controls on development of lacustrine basin fills in part of the Erlian Basin, northeast China. American Association of Petroleum Geologists Bulletin 85, 2017–2043.

Colella, A., Prior, D. B. 1990. Coarse-grained deltas. International Association of Sedimentologists Special Publications 10.

Collinson, J. D. 1996. Alluvial sediments. Sedimentary Environments: Processes, Facies and Stratigraphy. Blackwell Science, Oxford, 37–82.

Demirkol, C. 1982. Yalvaç-Akşehir dolayının stratigrafisi ve Batı Toroslarla deneştirimi. Türk Mühendis ve Mimar Odaları Birliği Jeoloji Mühendisliği Dergisi 14, 3-14.

Demirkol, C., Yetiş, C. 1983. Hoyran Gölü kuzeyinin stratigrafisi. Bulletin of the Mineral Research and Exploration 101- 102, 1–13.

Demirkol, C., Yetiş, C. 1984. Hoyran Gölü kuzeyinin stratigrafisi. Bulletin of the Mineral Research and Exploration 101- 102, 1-13.

Demirkol, C., Sipahi, H., Barka, A., Sönmez, Ş., Çiçek, S. 1977. Sultandağı'nın stratigrafisi ve jeolojik evrimi. Maden Tetkik ve Arama Genel Müdürlüğü, Report No: 6305, 86, Ankara (unpublished).

Emre, Ö., Duman, T. Y., Doğan, A., Özalp, S., Tokay, F., Kuşçu, İ. 2003. Surface faulting associated with the Sultandağı earthquake (Mw 6.5) of 3 February 2002, Southwestern Turkey. Seismological Research Letters 74(4), 382–392.

Eren, Y. 1987. Sultandağları Masifi'nin stratigrafisi ve mesoskopik tektoniği. Yüksek Lisans Tezi, Selçuk Üniversitesi, 80 (unpublished).

Eren, Y. 1990. Engilli (Akşehir) ve Bağkonak (Yalvaç) köyleri arasında Sultandağları Masifi'nin tektonik özellikleri. Türkiye Jeoloji Bülteni 33, 39–50.

Ergen, A., Bozkurt, A., Tuncay, E., Doğan, A., Ilgar, A. 2016. Çay-Akşehir arası Sultan Dağları'nın tektono-stratigrafisi: yeni bulgular. 69. Türkiye Jeoloji Kurultayı Bildiri Özleri, 11-15 Nisan 2016, Ankara.

Ergen, A., Tuncay, E., Bozkurt, A., Doğan, A., Ilgar, A. 2017. Sultan Dağları güneydoğusunun tektonostratigrafisi: Paleozoyik volkanik aktivitelerinin bölgesel jeolojik olaylarla ilişkisi. 70. Türkiye Jeoloji Kurultayı Bildiri Özleri, 10-14 Nisan 2017, Ankara.

Ergen, A., Bozkurt, A., Ilgar, A., Tuncay, E., Doğan, A. 2021. Sultandağları'nın jeolojisi ve jeodinamik evrimi. Maden Tetkik ve Arama Genel Müdürlüğü, Report No: 13958, 241, Ankara (unpublished).

Gawthorpe, R. L., Colella, A. 1990. Tectonic controls on coarse-grained delta depositional systems in rift basins. Coarse-Grained Deltas. International Association of Sedimentologists Special Publications 10, 113-128.

Gawthorpe, R. L., Leeder, M. R. 2000. Tectono-sedimentary evolution of active extensional basins. Basin Research 12, 195-218.

Ghinassi, M., Ielpi, A. 2016. Morphodynamics and facies architecture of stream-dominated, sand-rich alluvial fans, Pleistocene Upper Valdarno Basin, Italy. Geology and geomorphology of alluvial and fluvial fans: terrestrial and planetary perpectives. Geological Society of London Special Publications 440, 175-200.

Ghinassi, M., Nemec, W., Aldinucci, M., Nehyba, S., Özaksoy, V., Fidolini, F. 2014. Plan-form evolution of ancient meandering rivers reconstructed from longitudinal outcrop sections. Sedimentology 61(4), 952-977.

Göncüoğlu, M. C., Çapkınoğlu, Ş., Gürsu, S., Noble, P., Turhan, N., Tekin, U. K., Okuyucu, C., Göncüoğlu, Y. 2007. The Mississipian in the Central and Eastern Taurides (Turkey): constraints on the tectonic setting of the Tauride-Anatolide Platform. Geologica Carpathica 58(5), 427-442.

Gutnic, M., Keller, D., Monod, O. 1968. Decouverte de Nappes de charriage dans de nord du Taurus occidental (Turquie meridionale). Comptes rendus de l'Académie des Sciences 226, 998-991.

Güngör, T. 2013. Kinematics of the Central Taurides during Neotethys closure and collision, the nappes in the Sultan Mountains, Turkey. International Journal Earth Science 102, 1381-1402.

Harvey, A. M., Mather, A. E., Stokes, M. 2005. Alluvial fans: geomorphology, sedimentology, dynamics–introduction. A review of alluvial-fan research. Alluvial fans: geomorphology, sedimentology, dynamics. Geological Society of London Special Publications 251, 1-8.

Heward, A. P. 1978. Alluvial fan and lacustrine sediments from the Stephanian A and B (La Magdalena, Cinera-Matallana and Sabero) coalfields, northern Spain. Sedimentology 25, 451-488.

Ilgar, A., Nemec, W. 2005. Early Miocene lacustrine deposits and sequence stratigraphy of the Ermenek Basin, Central Taurides, Turkey. Sedimentary Geology 173, 217–249.

Ilgar, A., Ergen, A., Tuncay, E., Bozkurt, A. 2021. Basin margin tectonics and morphology as controls of delta type and architecture: examples from the Mio-Pliocene Yalvaç Basin (SW Turkey). Turkish Journal of Earth Sciences 30, 516–535.

Jackson, R. G. 1976. Depositional model of point bars in the Lower Wabash River. Journal of Sedimentary Petrology 46, 579-594.

Jarvis, A., Reuter, H. I., Nelson, A., Guevara, E. 2008. Hole-filled SRTM for the Globe, Version 4. CGIAR-CSI SRTM 90m Database.

Johnson, A. M. 1984. Debris Flow. Slope Instability. Wiley, Chichester, 257-361.

Kalafat, D., Güneş, Y., Kara, M., Kekovalı, K. 2020. Sultandağı Fay Zonu'nun (Afyonkarahisar-Konya) güncel depremselliğine bir bakış. Bulletin of the Mineral Research and Exploration 163, 195-218.

Kazancı, N. 1988. Repetitive deposition of alluvial fan and fan-delta wedges at a fault-controlled margin of the Pleistocene-Holocene Burdur Lake graben, Southwestern Anatolia, Turkey. Nemec, W., Steel, R. J. (Ed.). Fan Deltas-Sedimentology and Tectonic Settings. Blackie, London, 185-196.

Kim, S. B., Chough, S. K., Chun, S. S. 1995. Bouldery deposits in the lowermost part of the Cretaceous Kyokpori Formation, SW Korea: cohesionless debris flows and debris falls on a steep-gradient delta slope. Sedimentary Geology 98, 97-119.

Koç, A., Kaymakci, N., van Hinsbergen D. J. J., Vissers, R. L. M. 2014. A Miocene onset of the modern extensional regime in the Isparta angle: constraints from the Yalvaç Basin (Southwest Turkey). International Journal of Earth Sciences 105, 369-398.

Koçyiğit, A., Deveci, Ş. 2007. A N-S-trending active extensional structure, the Şuhut (Afyon) Graben: commencement age of the extensional neotectonic period in the Isparta Angle, SW Turkey. Turkish Journal of Earth Sciences 16, 391-416.

Koçyiğit, A., Gürboğa, Ş., Kalafat, D. 2013. Nature and onset of neotectonic regime in the northern core of Isparta angle, SW Turkey. Geodinamica Acta 25(1-2), 52-85.

Leeder, M. 1999. Sedimentology and Sedimentary Basins. Blackwell Scientific, Oxford, 592.

Leeder, M. R., Gawthorpe, R. L. 1987. Sedimentary models for extensional tilt-block/half-graben basins. Continental extensional tectonics. Geological Society of London Special Publication 28, 139–152.

Leeder, M. R. Ord, D. M., Collier, R. 1988. Development of alluvial fans and fan deltas in neotectonic

extensional settings: implications for the interpretation of basin fills. Nemec, W., Steel, R. J. (Ed.). Fan Deltas: Sedimentology and Tectonic Settings. Blackie and Son, Glasgow, 173-185.

Mack, G. H., Rasmussen, D. L. 1984. Alluvial fan sedimentation of the Cutler Formation (Permo-Pennsylvanian) near Gateway, Colorado. Geological Society of America Bulletin 95, 109–116.

McGowen, J. H., Garner, L. E. 1970. Physiographic features and stratification types of coarse-grained point bars: modern and ancient examples. Sedimentology 14, 77–111.

Miall, A. D. 1985. Architectural-element analysis: a new method of facies analysis applied to fluvial deposits. Earth-Science Reviews 22, 261–308.

Miall, A. D. 1996. The Geology of Fluvial Deposits. Springer-Verlag, Heidelberg, 582.

Monod, O. 1977. Recherches Geologique Mineralogique et Geochimegue des Bouxites de la Region d'Akseki Seydişehir (Taurus Occidental-Turquie). These Université Pierre-et-Marie-Curie, Paris.

Mukherji, A. B. 1990. The Chandigarh Dun Alluvial Fans: An Analysis of the Process-Form relationship. Alluvial Fans: A Field Approach. John Wiley and Sons, 131-149.

Nanson, G. C. 1980. Point bar and floodplain formation of the meandering Beatton River, northeastern British Columbia, Canada. Sedimentology 27, 3-29.

Nemec, W. 1990. Aspects of sediment movement on steep delta slopes. Coarse-Grained Deltas. International Association of Sedimentologists Special Publications 10, 29–73.

Nemec, W., Muszyński, A. 1982. Volcaniclastic alluvial aprons in the Tertiary of Sofia district (Bulgaria). Annales Societatis Geologorum Poloniae 52, 239–303.

Nemec, W., Postma, G. 1993. Quaternary alluvial fans in southwestern Crete: sedimentation processes and geomorphic evolution. Alluvial Sedimentation. International Association of Sedimentologists Special Publication 17, 235-276.

Nemec, W., Steel, R. J. 1984. Alluvial and coastal conglomerates: their significant features and some comments on gravelly mass-flow deposits. Sedimentology of Gravels and Conglomerates. Canadian Society of Petroleum Geologists, Memoir 10, 1-31.

Özgül, N. 1976. Torosların bazı temel jeolojik özellikleri. Türkiye Jeoloji Kurumu Bülteni 19(1), 65-67.

Özgül, N., Bölükbaşı, S., Alkan, H., Öztaş, Y., Korucu, M. 1991. Sultandağları-Sandıklı-Homa-Akdağ yöresinin jeolojisi. Türkiye Petrolleri (TPAO) Anonim Ortaklığı, Rapor No: 3028, Ankara, Türkiye.

Paola, C., Heller, P. L., Angevine, C. L. 1992. The large-scale dynamics of grain-size variation in alluvial basins, 1: theory. Basin Research 4, 73–90.

Ridgway, K. D., DeCelles, P. G. 1993. Stream-dominated alluvial fan and lacustrine depositional systems in Cenozoic strike-slip basins, Denali fault system, Yukon Territory, Canada. Sedimentology 40(4), 645-666.

Sarıkaya, M. A., Yıldırım, C., Çiner, A. 2015*a*. Late Quaternary alluvial fans of Emli Valley in the Ecemiş Fault Zone, south central Turkey: insights from cosmogenic nuclides. Geomorphology 228, 512-525.

Sarıkaya, M. A., Yıldırım, C., Çiner, A. 2015*b*. No surface breaking on Ecemiş Fault, central Turkey, since Late Pleistocene (64.5 ka); new geomorphic and geochronologic data from cosmogenic dating of offset alluvial fans. Tectonophysics 649, 33-46.

Sickenberg, O., Becker Platen, J. D., Benda, L., Berg, D., Engesser, B., Gaziry, W., Heissiğ, K., Alban, H. K., Sondarr, P. Y., Schmidt Kittler, N., Staesche, K., Staesche, N., Steffens, P., Tobien, H. 1975. Die Gliederung des Höheren Jungtertiars und Alguartersinder Türkei nach Vertebraten und ihre Bedeutung für die internationale Neogen-Stratigraphie Geologisches Jahrbuch Reihe B Heft 15.

Smith, N. D. 1974. Sedimentology and bar formation in the Upper Kicking Horse River, a braided outwash stream. The Journal of Geology 82(2), 205–224.

Sohn, Y. K., Rhee, C. W., Kim, B. C. 1999. Debris flow and hyperconcentrated flood-flow deposits in an alluvial fan, Northwestern part of the Cretaceous Yongdong Basin, Central Korea. The Journal of Geology 107, 111–132.

Todd, S. P. 1989. Stream-driven, high-density gravelly traction carpets: possible deposits in the Trabeg Conglomerate Formation, SW Ireland and some theoretical considerations of their origin. Sedimentology 36, 513-530.

Tooth, S. 1999. Downstream changes in floodplain character on the Northern Plains of arid Central Australia. Fluvial Sedimentology VI. International

Association of Sedimentologists Special Publication 28, 93-112.

Tuncer, A. 2020. Yalvaç ve Ilgın karasal Neojen havzalarında (Güneybatı Anadolu) Ostracoda taksonomisi ve biyostratigrafisi: Ostrakodlara dayalı eskiortamsal-eskiiklimsel yaklaşımlar. Doktora Tezi, Hacettepe Üniversitesi, Ankara, Türkiye.

Umut, M., Karabıyıkoğlu, M., Saraç, G., Bulut, V., Demirci, A. R., Erkan, M., Kurt, Z., Metin, S., Özgönül, E. 1987. Tuzlukçu-Ilgın-Doğanhisar-Doğanbey (Konya ili) ve dolayının jeolojisi. Maden Tetkik ve Arama Genel Müdürlüğü, Report No: 8246, 38 (unpublished).

Usta, N. D. Y., Mayda, S., Kaya, T. T. 2019. Yeni buluntular ışığında Yalvaç (Isparta / Türkiye) Neojen devir omurgalı fosil yatakları. Süleyman Demirel Üniversitesi Fen-Edebiyat Fakültesi Sosyal Bilimler Dergisi 47(2), 79–96.

Wells, N. A. 1984. Sheet debris flow and sheetflood conglomerates in Cretaceous Cool-Maritime alluvial fans, South Orkney Islands, Antarctica. Sedimentology of Gravels and Conglomerates. Canadian Society of Petroleum Geologists, Memoir 10, 133–145.

Wilson, A. C. 1980. The Devonian sedimentation and tectonism of a rapidly subsiding semi-arid fluvial basin in the Midland Valley of Scotland. Scottish Journal of Geology 16, 291–313.

Yağmurlu, F. 1991. Yalvaç-Yarıkkaya Neojen Havzası'nın stratigrafisi ve depolanma ortamları. Türkiye Jeoloji Bülteni 34, 9–19.

Yalçınlar, İ. 1953. Sultan Dağları eteklerinde omurgalılar ihtiva eden Neojen tabakaları. Türkiye Jeoloji Kurumu Bülteni 4(1), 118–121.

Yıldırım, C., Sarıkaya, M. A., Çiner, A. 2016. Late Pleistocene intraplate extension of the Central Anatolian Plateau, Turkey: inferences from cosmogenic exposure dating of alluvial fan, landslide and moraine surfaces along the Ecemiş Fault Zone. Tectonics 35, 1446-1464.

Bulletin of the Mineral Research and Exploration

http://bulletin.mta.gov.tr

Mud systems applied to problematic formations in core drilling rigs

Bülent TOKA[a*]

[a]*General Directorate of Mineral Research and Exploration, Department of Drilling, Ankara, Türkiye*

Research Article

Keywords:
Diamond Drilling, Drilling Mud, Problematic Formations, In-pipe Caking.

ABSTRACT

The two most important features of drilling rigs based on the core drilling principles are the drill set rotating at high speeds and the very precise spacing between the pipe and the well wall. Formation pieces that swell, flow into the well, spill or collapse during the drilling of problematic formations mix into the mud or narrow the annulus and cause well problems by restraining the rotation of the drill string and circulation. The spilled formation pieces cause an excessive solid material increase in the mud structure and due to the effect of centrifugal force, the solids adhere to the inner wall of the pipes near the surface and form a cake. Excessive cake thickness in the pipes obstruct the descent of the core barrel inner tube catcher into the well. During the removal of the inner tube, a vacuum occurs in the well due to the mud discharged from the rod and the problematic formations are poured into the annulus and block the core between the core barrel and the well wall. In this study, the performance of mud systems determined by trial and error method against the problems encountered in unconsolidated claystone, mudstone (shale), siltstone and sand - pebble stones in core coal exploration drillings in Çorum - Amasya region were evaluated. Monitoring and regular improvement of the rheological values of the mud compositions, changing the mud composition according to the well conditions, keeping the gel strength high and increasing its density with salt was found to play an important role in keeping the unconsolidated formations physically balanced. Salt mud also minimized the formation of cake in the pipe.

Received Date: 02.03.2021
Accepted Date: 10.07.2021

1. Introduction

Diamond (core) drilling is based on the principle of taking a cylindrical original sample (core) that demonstrates the ground structure along the progression using a diamond drill bit (cutting tip). This method, which works with a rotary drilling system, is generally referred to as diamond drilling as diamond drill bits are used as the cutting tips.

The difference of diamond drilling rigs from the drilling rigs based on the principle of cuttings drilling are the drill string rotating at high speeds (500 - 2.500 rpm) and a very precise gap between the pipe and the well wall (approximately 2 - 4 mm). The rotation of the drill string at high speeds creates a centrifugal effect on the circulating mud coming out of the water swivel.

Depending on the bearing capacity of the diamond drill rigs and the drawworks power, in order to reach the targeted depth, the drill string of PQ (114.3 mm), HQ (89.9 mm), NQ (69.9 mm) and BQ (55.5 mm) diameters are usually used (Özbayoğlu, 1983) and the design of the well is made according to the depth to which the casings will be lowered. In deep and problematic formations, the upper levels of the well are usually drilled with a PQ (or HQ) drill string,

Citation Info: Toka, B. 2022. Mud systems applied to problematic formations in core drilling rigs. Bulletin of the Mineral Research and Exploration 168, 67-75. https://doi.org/10.19111/bulletinofmre.970177

**Corresponding author: Bülent TOKA, tokabulent@yahoo.com*

and PW (outer diameter - 139.7 mm) or HW (outer diameter - 114.3 mm) diameter pipes are lowered to this range when the planned depth is reached. In order to lower PW pipes, the well is enlarged with a drill, usually in the diameter range of 6 ¼″ (158.7 mm) or 6 ¾″ (171.4 mm). In the event of certain drilling related problems (mud leakage, collapse and spillage) occuring in the formations such as alluvium and sandstone at the upper levels of the deep wells to be drilled, it is recommended to lower $6^{5/8}$″ (168.3 mm) diameter protection pipes before the PW pipe. Following the PW pipes, HW, NW(88.9 mm), BW (73.0 mm), and AW (57.1 mm) casings are lowered into the well, in the order mentioned and according to the design plan or encountered problems related to the well. In case the well cannot be finished with BQ rods at the planned depth because of drilling problems, the drilling is tried to be completed at the desired depth with the AQ (44.5 mm) drill string.

In drilling works, it is desirable to have high core efficiency and penetration rates. While having knowledge related to the lithology of the area affects the core efficiency, high penetration rates allow for a more economically viable drilling activity. Choosing the suitable drilling mud composition for lithology increases the core efficiency and minimizes the drilling problems related to the formation that affect the penetration rates.

Since solid control equipment is not generally used in diamond drilling, the formation pieces are mixed into the mud and negatively affect the quality of the fluid. Therefore, it becomes difficult to control the properties of the mud which leads to the occurance of problems related to the well. Negative changes in mud properties decrease the penetration rates and core efficiency, cause collapses in the well, narrowing between the drill pipes and the well wall, and ineffective cleaning of the well inside. In addition, solid-contaminated mud causes cake formation (solid material deposition) that narrows the inner surface of the drill pipes under the water swivel. In this case, sometimes the whole entire drill string needs to be pulled up, as the inner tube catcher (sampler) cap cannot be lowered into the well or the core barrel cannot be taken out. For all these reasons, it is important to prepare and control the drilling mud suitable for the formation.

The most important of the main problems swelling, flow into the welll and spilling of active formations (water sensitive) such as clay and shale, poses to be the most important problem encountered in core drilling. Moreover, the unconsolidated formations such as claystone, siltstone, sandstone, conglomerate show the characteristic of flowing into the well with the deterioration of the physical balance in the well. In the clay types contained in clay and shale formations, sodium montmorillonite (smectite) is the most sensitive to water. Among the clays, sodium montmorillonite has the highest cation exchange and water-bearing capacity (Luckham and Rossi, 1999). The API non-treated bentonite, which provides viscosity and filtration control in drilling mud preparation, is also sodium montmorillonite. The chemical and physical properties of mud are used to control problematic formations (Toka, 2017). While the chemical balance is set up between the mud and the formation in drilling of active clays that swell with water, the physical balance has an important role in formations that tend to spill and flow. Inhibited or petroleum-based muds are used to provide chemical stability. The balancing mud density is also needed to provide a mechanical balance between the formation and the mud.

In the mud design of core drillings, the mud systems containing low solid (polymerized) are generally selected instead of bentonite muds. For this reason, the solid materials contained in bentonite increase the rate of in-pipe caking in bentonite-based mud systems. Therefore, high molecular weighted carboxymethyl cellulose (HV CMC), high molecular weighted polyanionic cellulose (PAC R), xantham gum (known as XCD in the market), and partially hydrolyzed polyacrylamide (PHPA) are added to the fluid system to increase the viscosity of the drilling fluid as bentonite amount is reduced in drill fluid compositions to decrease the in-pipe caking ratio. At the same time, the synthetic PHPA and semi-synthetic polyanionic cellulose (PAC) having the property of cutting encapsulation are also used to prevent swelling of active clay formations with water (Cario and Bagshaw, 1978; MI Drilling Fluids Engineering Manual, 1998). In order to hold in the water loss of the fluid, the low molecular weighted carboxymethyl cellulose (LV CMC), low molecular weighted

polyanionic cellulose (PAC LV), and modified starch are added to the system. The compatible work of modified starch with xantham gum, which is a branched polymer, improves the dynamic carrying capacity (yield point) of the mud and the ability to suspend cuttings (gel strength) in the static state (Darley and Gray, 1988).

2. Geological Structure and Formation Characteristics of Çorum - Amasya Fields

Borehole drilling activities for coal exploration were carried out in Sungurlu (Terziköy and Mecitözü) of Çorum province and Suluova region of Amasya province. While the Terziköy and Mecitözü formations are composed of brittle mudstone (shale) (Figure 1a), claystone, siltstone, and sandstone, the Suluova formation consists of unconsolidated claystone, siltstone, sandstone, and conglomerate (Figure 1b). In some wells, the acidic gas intrusions into the drilling mud were observed and the mud showed the characteristics of pH buffer solution. In addition, the mud leaks at different depths were observed in Suluova boreholes, followed by increases in pump pressure, and when the pressure relief line was opened to reduce the pressure, the mud that escaped from the drill pipes came back to the mud pools.

3. Material and Method

Drilling works were carried out with METASON with a drilling capacity of 2.000 m and SONMAK diamond drilling rigs with a capacity of 1.000 m.

Non-treated bentonite, HV CMC, XCD, PAC LV, LV CMC, modified starch, NaCl (density increasing water-soluble salt), and caustic soda (pH regulator) were used as mud additives.

For the physical measurement of the mud, the 6-speed viscometer, marsh funnel, filter press, and mud balance were used. For the chemical properties of the mud, the total hardness, P_f/M_f, and chlorine contents were continuously monitored (P_f: phenolphthalein alkalinity of the mud filtrate, M_f: methyl orange alkalinity end point of mud filtrate). The rheological values of the fluid (TS EN ISO 13500, 2010) were calculated according to the formulas given below.

$$AV = \frac{\theta_{600}}{2} \quad (1)$$

$$PV = \theta_{600} - \theta_{300} \quad (2)$$

$$YP = \theta_{300} - PV \quad (3)$$

where AV (apparent viscosity, cP), θ_{600} (value read at 600 rpm in the viscometer), θ_{300} (value read at 300 rpm in the viscometer), PV (plastic viscosity, cP) and YP (yield point, lb/100 ft^2).

Some of the mud compositions (Toka et al., 2016) selected according to the laboratory test results to determine rheological and filtration properties of the drilling fluid within the scope of the drilling mud research and development project of the Department of Drilling of the General Directorate of Mineral Research and Exploration were tested in this field (Table 1).

The most important reason for choosing the bentonite + CMC composition for this drilling is its low cost, suitable rheological and filtration values for the core drilling works as seen in Figure 2. This mud with its high gel strength value of 10' (17 lb/100 ft2) is expected to infiltrate into the voids of unconsolidated sandstones and conglomerates, provide reinforcement and prevent the flow of the formation into the well.

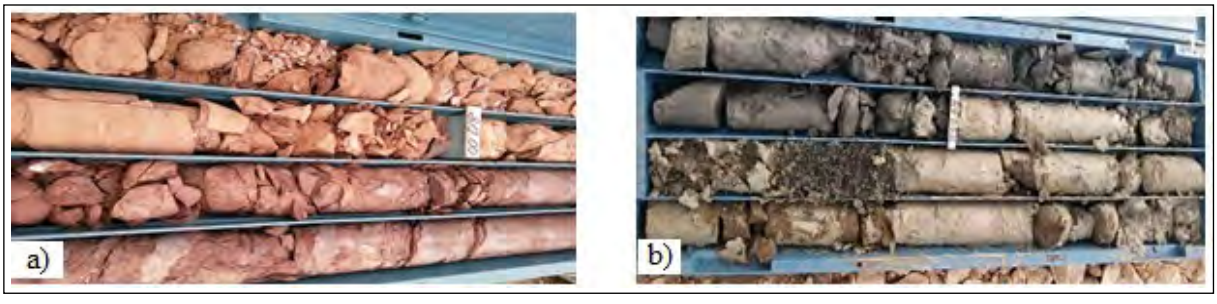

Figure 1- a) Brittle mudstones encountered in the Terzili and Yörüklü areas and b) unconsolidated sandstones, claystones and siltstones in the Suluova field.

Table 1- Mud compositions selected according to the laboratory test results to determine rheological and filtration properties of drilling fluid within the scope of drilling mud research and development project.

Mud Composition	Composition Additives
Bentonite + CMC composition	10 ppb (28.5 kg/m^3) Non-treated bentonite + 0.7 ppb (2 kg/m^3) LV CMC + 0.6 ppb (1.7 kg/m^3) HV CMC
Bentonite + Modified (M.) starch + XCD composition	10 ppb (28.5 kg/m^3) Non-treated bentonite + 0.9 ppb (2.6 kg/m^3) M. starch + 0.7 ppb (2 kg/m^3) XCD
Salt composition	NaCl saturated drill fluid preparation water + 2 ppb (5.7 kg/m^3) M. starch + 1 ppb (2.85 kg/m^3) PAC L + 1 ppb (2.85 kg/m^3) XCD

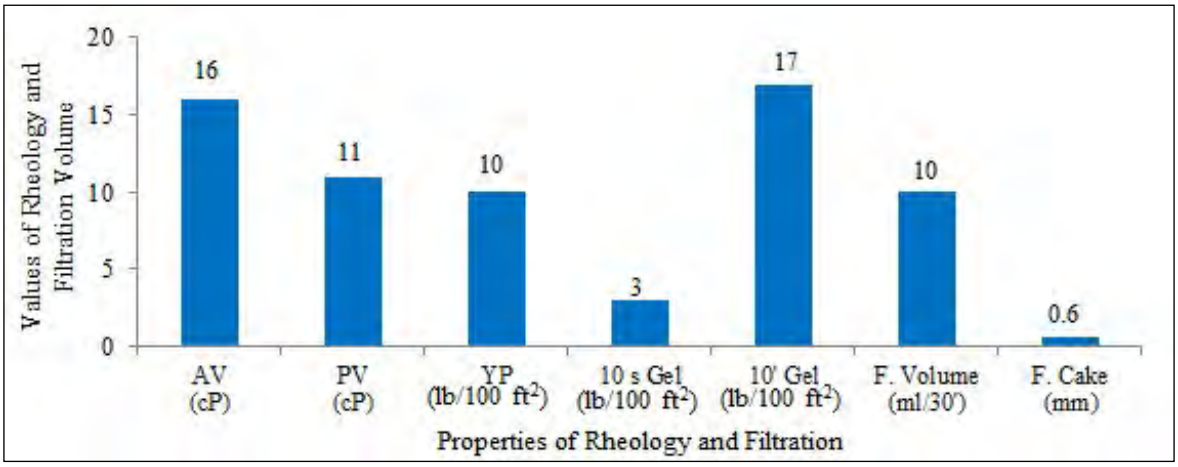

Figure 2- Rheological and filtration properties of bentonite + HV CMC + LV CMC based drilling fluid.

The mud composition consisting of modified starch, XCD, and non-treated bentonite was tested instead of this mud due to the viscosity decrease in the some zones where bentonite + CMC mud was used. Since 10 s and 10' gel strength (4 - 8.5 lb/100 ft^2) of this composition determined in the laboratory were close to each other and the YP value, which provides the dynamic carrying capacity, is higher than PV, this mud type was also tested in the drilling (Figure 3).

When the mechanical balance between the drilling fluid and the well wall was spoiled (when there were debris and spills in the well) the salt mud system, as one of the protected fluid types, was adopted in

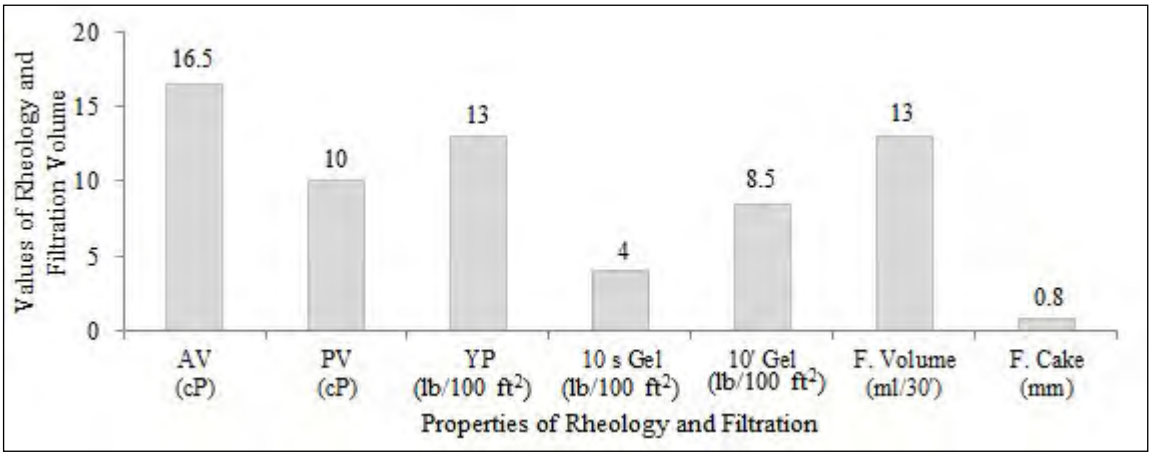

Figure 3- Rheological and filtration properties of bentonite + modified starch + XCD based drilling fluid.

order to increase the physical force (density) that the mud would exert on the well wall and provide extra inhibition. According to the observations on the field, since the cutting formations do not swell with water, the NaCl, which is more economical than KCl, was selected to prepare salt mud. The rheological properties of salt (NaCl saturated drilling fluid preparation water) + XCD + PAC L + modified starch composition according to laboratory tests are given in Figure 4. This mud type was also used as the yield point and gel strength, which express the carrying capacity of the cuttings under dynamic and static conditions, are at appropriate values, and increase the density of the fluid up to approximately 1.2 g/cm^3.

4. Field Studies and Evaluations

Since lithology, geological and tectonic structures, and formation behaviors of the field are not fully known, great difficulties are experienced in determining the mud composition and design of the well. Since the formation behavior of coal exploration drillings in Çorum - Sungurlu and Amasya - Suluova regions is not known, well problems were encountered during drilling. Problems related to the well increased, the mud compositions were changed according to the behavior of the well and efforts were put forward in order to achieve in-hole balance. In cases where it was not possible to balance the well with mud and the risk of jamming of the drill string increased, the well was brought under control by lowering the casing pipes into the problematic zones. Due to the variable depth of the well in deep exploration, the design of the well was started with the largest diameter pipes (PW).

Borehole processes which has the lowest cost were initiated with the bentonite + CMC mud composition as given in Table 1. The rheological and filtration properties of the mud were rearranged by reducing the amount of bentonite to 8 - 15 kg per 1 m^3 of mud and increasing the amount of polymer (Table 2) depending on the in-pipe caking (Figure 5). Efforts were put into keeping the viscosity of the circulating mud at around 13 - 20 (Table 3). Observations showed that between the aforementioned values, working with a pump flow rate of approximately 40-45 l/min for the HQ drill sing provided effective well cleaning. Since the increase in rheological values will also increase the pump fuel consumption (Toka and Şahin, 2006), the water + LV CMC was added to the mud depending on the water loss value, the cuttings accumulated in the channels were regularly discarded, the fresh mud was added to the mud system and solid control was carried out by adding desilter in order to prevent rheological values of the mud from increasing further. The rheological and filtration properties of the fresh mud added to the

Table 2- Bentonite + HV CMC + LV CMC mud composition.

Mud Additives	Concentration (kg/m^3)
Non-treated Bentonite	8 - 15
LV CMC	2 - 3
HV CMC	1.5 - 2
Caustic Soda	0.25 – 0.50

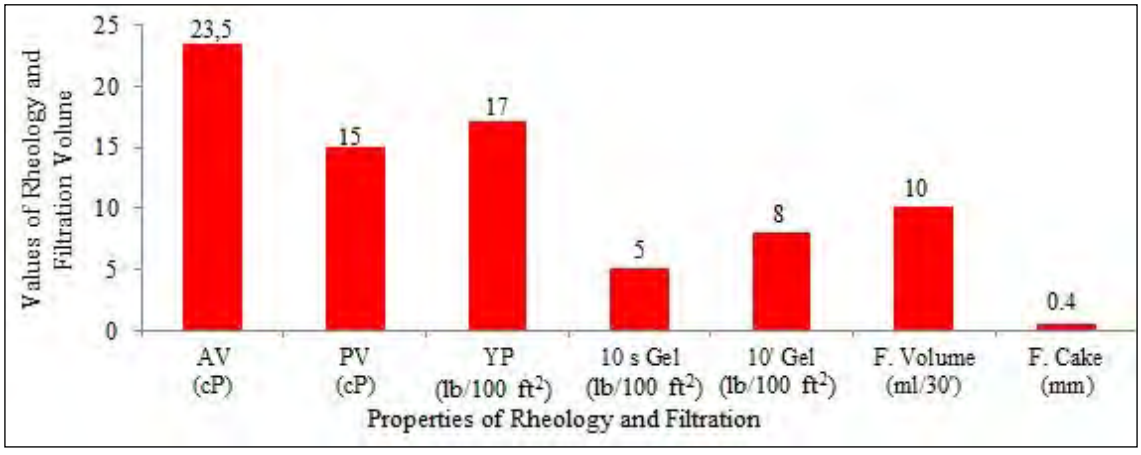

Figure 4- Rheological and filtration properties of drilling fluid containing NaCl saturated drilling fluid preparation water + XCD + PAC L + modified starch (F. Cake: filtrate cake).

Figure 5- The in-pipe caking and the rate of caking seen during the cleaning of the inside of the pipe.

system were kept at low values in order to reduce the rheological and filtration properties of the circulating mud and to remedy the mud. The AV value of the fresh mud added to the circulating mud was 11 - 12 cP and the water loss rate was adjusted between 10 - 15 ml/30′ (Table 3).

Table 3- Bentonite + HV CMC + LV CMC mud composition; average values of circulating and fresh mud.

Mud Properties	Circulating Mud	Fresh Mud
Mud Density (g/cm^3)	1.08 - 1.15	1.01- 1.02
Funnel Viscosity	36 - 42	32 - 35
AV (cP)	15 - 20	12 - 15
PV (cP)	9 - 12	10 - 12
YP (lb/100 ft^2)	10 - 13	5 - 6
10 s -10′ Gel Strength (lb/100 ft^2)	3 - 17 / 7 - 20	0 - 2
Water Loss (ml/30′)	8 - 12	10 - 12
Filtrate Cake Thickness (mm)	0.5 - 1.5	0.3 - 0.4
Ca (mg/l))	80 - 100	-
Pf/Mf	0.2 - 0.7	-
pH	9 - 10.5	-

The mud type containing bentonite + HV CMC + LV CMC showed an increase in rheological and gel strength when used in Terzili and Yörüklü areas, while it showed a decreasing trend in the formations in Suluova area. When it tended to decrease, the mud type was changed and the bentonite + modified starch and XCD composition determined in the laboratory (Table 4) was adopted. The composition of this mud is given in Table 4 and its physical and chemical properties are given in Table 5. This mud type provided very good rheological properties in such formations to carry the cuttings dynamically and keep them suspended in the static state.

Table 4- Bentonite + modified starch + XCD mud composition.

Mud Additives	Concentration (kg/m^3)
Non-treated Bentonite	8 - 15
Modified Starch	2 - 4
XCD	2 - 3
Caustic Soda	0.25 - 0.50

Table 5- Bentonite + modified starch + XCD mud composition; average values of circulating and fresh mud.

Mud Properties	Circulating Mud	Fresh Mud
Mud Density (g/cm^3)	1.07 - 1.10	1.01 - 1.02
Funnel Viscosity	40 - 48	34 - 40
AV (cP)	15 - 20	12 - 17
PV (cP)	14 - 16	8 - 10
YP (lb/100 ft^2)	11 - 14	8 - 14
10 s -10′ Gel Strength (lb/100 ft^2)	6 - 14 / 10 - 20	3 - 6
Water Loss (ml/30′)	8 - 12	10 - 12
Filtrate Cake Thickness (mm)	0.5 - 1	0.3 - 0.4
Ca (mg/l))	80 - 100	-
Pf/Mf	0.2 - 0.7	-
pH	9 - 10.5	-

In these two selected mud compositions, the density of mud was allowed to increase and the high-density value of mud was aimed to be preserved as long as the formation cuttings mixed into the system did not increase in-pipe caking. The reason for this is to provide the physical balance between the density of the mud and the well. Therefore, in order to maintain the physical balance in the well, complete removal and replacement of the old mud was avoided and the channels were consistently cleaned while adding fresh mud to the system to sustain the properties of the mud. By means of this method, the density of the mud was kept between 1.10 - 1.12 g/cm^3.

When the physical balance was spoiled in the well and the formation flowed and spilled into the well, in order to increase the density of the mud, the salt mud of which the composition is given in Table 6, was adopted in Terzili, Suluova, and Mecitözü areas. The other reasons for switching to salt mud, which is an inhibitory system, are that the water-insoluble thickening additives (barite, calcite) will increase in-pipe caking and the evaporates (gypsum, anhydrite) and acidic gases (H_2S) contained in the formation would adversely affect the performance of bentonite

Table 6- NaCl + modified starch + PAC L + XCD mud composition.

Mud Additives	Concentration (kg/m^3)
NaCl	140 - 160
PAC L	3 - 4
Modified Starch	6 - 8
XCD	2 - 3
Caustic Soda	0.50 - 1
Corrosion Inhibitor	as much as necessary

and negatively charged polymers. As can be seen in Table 7, the density of fresh mud was prepared to be between 1.08 - 1.11 g/cm^3 in Mecitözü drilling, and the density increased up to the range of 1.16 - 1.18 g/cm^3 with the clays and the cuttings mixed into the mud. It was planned to increase the mud density by adding more salt to the system and ensure the physical balance in the well in case of problems in the operation at this selected density. The reason for keeping the properties of the fresh mud added to the system low is to allow the mud to be improved by reducing the rheological properties of the circulating mud with rheological values increased.

Table 7- NaCl + modified starch + PAC L + XCD mud composition; average values of the circulating and the fresh mud.

Mud Properties	Circulating Mud	Fresh Mud
Mud Density (g/cm^3)	1.16 - 1.18	1.08 - 1.11
Funnel Viscosity	37 - 42	32 - 35
AV (cP)	15 - 20	10 - 15
PV (cP)	10 - 15	10 - 14
YP (lb/100 ft^2)	10 - 16	8 - 16
10 s -10′ Gel Strength (lb/100 ft^2)	4 - 7 / 8 - 15	3 - 5
Water Loss (ml/30′)	10 - 16	10 - 14
Filtrate Cake Thickness (mm)	0.75 - 1	0.5 - 0.8
Ca (mg/l))	800 - 1200	-
Cl (mg/l)	55000 - 60000	-
Pf/Mf	0 / 0.6	-
pH	7	10 - 11

The most important feature of all mud types used in these fields is their high gel strength. The reason for choosing a mud system with high gel strength is the opinion that the gelled mud penetrating into the formations (such as sandstone and conglomerate) on the well wall acts as reinforcement by filling the cracks and gaps. As can be seen in Figure 6, the gelled mud filling the voids by consolidating the formation obstructed the mud from flowing into the well together with the pressure exerted by the mud column on the formation.

Figure 6- Invasion of the unconsolidated formation by the high gel mud.

The decreases in pH values were experienced in some wells. Increasing the pH value by adding caustic soda to the system did not work, and since the pH value behaved like a buffer solution, the studies were carried out around pH 7. Since the bentonite content in the mud system is very low, it was observed that working at a low pH value did not have a significant effect on the rheological and filtration properties of the mud. The reason why the pH value of the mud decreased and could not be increased was due to the formation or the acidic gases contained therein.

During studies, the core samples representing the formation were kept in circulating mud, fresh mud, and water (Figure 7). Their behaviors were examined and the mud was altered according to the changes observed. While core samples did not show

Figure 7- Keeping the core samples in mud and water and observation of the properties such as dispersion and swelling.

any change in the mud samples used, some samples showed dispersion and fragmentation in water. Zones where samples dispersed in water were located by closely monitoring the water loss of the mud, aimed to preserve formation and cutting integrity.

In core drilling, the shale shakers are generally not used for solid control. Therefore, the silt separator (desilter) shown in Figure 8 was operated regularly according to the PV and sand content of the mud in order to remove the drilling cuttings from the mud and control mud properties. The cuttings accumulated in the channels were regularly ejected and approximately 2 - 3 m^3 of fresh mud was added to the system per day. When the proportion of sand in the mud reaches 1 - 1.5%, with these measures taken the percentage of sand in the mud system was kept to a maximum of 0.8 - 1.0%. Thus, the in-pipe caking close to the surface was minimized.

Figure 8- Desilter.

One of the important problems encountered in the Suluova field is that after the loss of complete circulation in a short interval, the pump pressure increased and when the pressure relief line was opened and the pressure was wanted to be reduced, the mud that escaped to the formation flowed out of the well through the rods and returned to the tanks. It was thought that this problem, which occurs at two different depths, may have two causes. The first is the clogging of the annulus with the collapse of unconsolidated formations due to the deterioration of the physical balance in the well during the removal of the inner tube from the well, and then the cracking of the weak formations by the drilling mud pumped into the well. The second is the presence of formation fluid (gas) traps at levels where the problem occurs, and the settlement of mud in the formation cavity after the gas is separated. The escape direction of the mud being from the pipe rather than the annulus indicates that the formation is settling and during this settlement, the formation closes the sensitive sized gap between the drill (or core barrel) and the well wall. Following the occurrence of this event, an observation was made for about two hours, during this process, the mud was re-pumped into the well and as there was no change in the return of the mud, the exit maneuver was performed to control the drill and drill string. Lowering of the drill string into the well resulted in an unrepeated, one time collapse of the well. Observations made raised the assumption that there was a high probability of fracture of the formation of a jammed formation fluid trap at these levels bas a result of unconsolidated formation collapsing and occluding the annulus.

5. Results

- Low cost bentonite + HV CMC + LV CMC composition with high 10′ gel strength demonstrated good core drilling performance in the first stage of the well and for unproblematic formations.

- Bentonite + modified starch + XCD composition with its capacity to form a good gel in a static state and carry cuttings in a dynamic state, provides well balancing in unconsolidated formations.

- Salt-based drilling mud, which is used to maintain the physical balance in the well and minimize the formation of in-pipe caking, exhibited a positive performance in the zones where spillage problems were faced.

- By using desilter in core drilling, keeping the percentage of sand in the mud between 0.8 - 1.0% maximum, regular cleaning of mud channels and adding fresh mud to the system daily ensured the preservation of the physical balance in the well and the control of the mud properties.

- Mud compositions with a yield point between 10 - 20 lb/100 ft^2 seems sufficient for core drilling at recommended circulation rates for cleaning of the pieces in the well.

● In an event of increasing pump pressure following a loss of circulation and fluid ejection through the set; ascending the drill string (or pulling into the casing pipe) and descending it again into the well until the circulation is achieved, would assist the re-establishment of the balance and lower the risk of drill string jamming.

Acknowledgements

Mud compositions that can be applied for core drilling, within the scope of drilling mud research and development project, in the Mud Laboratory of the Department of Drilling of the General Directorate of Mineral Research and Exploration (MTA) were determined by Oil and Natural Gas Engineer Nuray TOKA (MSc) and were consulted for new mud compositions applied.

The fieldwork was carried out together with the Mining Engineer Bülent TOSUN, Mining Engineer Hayati ÖZKAYA, the local staff trained for mud measurement and monitoring, and the permanent drilling technical staff.

References

Cario R. D., Bagshaw, F. R. 1978. Description and use of polymers used in drilling, workovers, and completion. The Society of Petroleum Engineers Production Technology Symposium, 30 October 1978, Hobbs, Mexico.

Darley, H. C. H., Gray, G. R. 1988. Composition and Properties of Drilling and Completion Fluids 5th Edition, Elsevier Inc., 643.

Luckham, P. F., Rossi, S. 1999. The Colloidal and rheological properties of bentonite suspensions, Advances in Colloid and Interface Science, 82, 43-92.

M-I Drilling Fluids, L. C. 1998. Drilling Fluids Engineering Manual.

Özbayoğlu, Y. 1983. Elmaslı Sondaj Tekniği El Kitabı. TMMOB Jeoloji Mühendisleri Odası, Ankara.

Toka, B. 2017. Sondaj Mühendisliği. TMMOB Maden Mühendisleri Odası, Ankara.

Toka, B., Şahin, M. 2006. Havza jeotermal sahasında yapılan SH - 5 ve diğer sondajların genel değerlendirmesi. Maden Mühendisleri Odası Madencilik Dergisi, 45(1), 3-14.

Toka, N., Tan, S., Çalışkan, O., Güngör, Y., Toka, B. 2016. Sondaj çamuru araştırma - geliştirme projesi laboratuvar çalışmaları. MTA Sondaj Dairesi, Ankara (unpublished).

TS EN ISO 13500. 2010. Petrol ve doğal gaz sanayi - sondaj akışkanı maddeleri - özellikler ve deneyler. Türkiye Standartları Enstitüsü, Ankara.

Bulletin of the Mineral Research and Exploration

http://bulletin.mta.gov.tr

Separation efficiency of different methods in treatment of a low-grade iron ore

Özgür ÖZCAN[a*]

[a]*Hacettepe University, Faculty of Engineering, Mining Engineering, Ankara, Türkiye*

Research Article

Keywords:
Separation Efficiency
Grade, Recovery,
Magnetic Separation,
Gravity Concentration.

ABSTRACT

In the present study, characterization and beneficiation tests were performed on an iron ore sample for the evaluation of separation efficiency (SE) of different methods. Results showed that the decrease in feed size fraction increases the SE irrespective of to beneficiation method. It was determined from the liberation analyses that the increase in SE values at finer size fractions is related with higher liberation. Calculated SE values revealed that operational parameters significantly affect the SE of all methods and the net forces acting on particles play an important role on SE of different size fractions. Mean SE of different size fractions showed that the separation efficiencies of gravity concentration and magnetic separation takes similar values above 1 mm, however, SE of magnetic separation is significantly higher than gravity concentration below 1 mm for the studied sample. For low grade ores, it is very crucial to develop a flow sheet to achieve the optimum grade and recovery while decreasing the cost likely by using optimum method. Therefore, SE calculations used in this research can be used as a basic method to compare the efficiency of different beneficiation methods. SE method has advantages as they provide fast evaluation of efficiency by using experimental results.

Received Date: 05.03.2021
Accepted Date: 07.09.2021

1. Introduction

The most important aim of different separation methods in minerals engineering has always been concentrating valuable minerals from gangue by using different properties of minerals. Separation methods produce different quality and quantity products (Drzymala, 2007). The quality of a concentrate or tailing is defined by the term grade. It can be defined as the valuable material in the final concentration. The recovery represents the ratio of concentration in weight of the total mineral or metal in an ore (Irannajad et al., 2018).

The grade and recovery are the most used performance evaluation parameters in beneficiation processes (Wills and Napier-Munn, 2006). To date, lots of parameters have been used by different researchers. Some of these parameters have been reported in the literature (Drzymala, 2006, 2007, 2008). Irannajad compared different indices and proposed a new approach in separation process evaluation. Authors reported that separation efficiency (SE), operation efficiency (OE) and selectivity index (SI) are the optimum parameter for assessment of mineral beneficiation methods (Irannajad et al., 2018). In addition, Mukherjee proposed an alternative method to SE evaluation of gravity concentration without the impact of feed properties (Mukherjee, 2009).

In iron ore beneficiation, efficiency determination of any concentration method is far more difficult, as heavy liquid tests for the materials are not possible

Citation Info: Özcan, Ö. 2022. Separation efficiency of different methods in treatment of a low-grade iron ore. Bulletin of the Mineral Research and Exploration 168, 77-92. https://doi.org/10.19111/bulletinofmre.992412

**Corresponding author: Özgür ÖZCAN, ozgurozcan@hacettepe.edu.tr*

due to higher specific gravities of the particles (Mukherjee, 2009). However, production of sinter/ pellet grade concentrates by developing suitable and low cost flowsheets is crucial (Özcan et al., 2021). The gangue and iron ore minerals have significant differences in magnetic susceptibility and density. As a result, gravity concentration and magnetic separation are possibly the two most effective methods in concentration of iron ores. However, the finer particle size distributions of the valuable and gangue minerals and their insufficient liberation are the main limitations that prevents its effective concentration at coarser size fractions (Makhija et al., 2013).

Different methods can be applied to iron ore concentrations. These methods can be listed as, gravity and centrifugal concentration, froth flotation, low and high intensity magnetic separation. Magnetic separation is the most effective between these methods. Froth flotation has higher selectivity, but magnetic separation has lower operational cost than froth flotation. Gravity concentration has also the potential of lower operational costs, but it can be performed in smaller scale than magnetic separation (Xiong et al., 2015). There have been some significant results published about the effectiveness of gravity and magnetic concentration techniques for the beneficiation of low-grade iron (Seifelnassr et al., 2012; Suthers et al., 2014; Amiri, 2019).

The following equation (Equation 1) for the separation efficiency (SE) can be used in expressing the technical excellence of any separation that occurs in mineral concentration processes or processes of any nature that consist of two matter that are physically separated from one another:

$$SE = W(Cm(c-f))/f(Cm-f)) \quad (1)$$

where, W is the percent amount of feed that reports to the concentrate, m is the maximum grade of valuable mineral (72.36% Fe in Fe_3O_4), f is the percentage of metal in the feed, and c is the percent metal in the concentrate (Schulz, 1979; Barari et al., 1979). Mukherjee studied various methods used in calculation of the SE. The author discussed 25 different equations and proposed a new method for calculation. In addition, the author reported that each of these 25 calculation method can be used with minor changes in the coal cleaning and gravity concentration plants (Mukherjee, 2009).

SE calculation is a useful method to identify various operating parameters. In addition, it can be used to compare performances of various concentration methods used in existing plants (Shivakumar et al., 2017). The values of SE vary between 0 and 100. SE index has been often used in technical evaluation of concentration methods (Irannajad et al., 2018).

Wills and Finch, (2016) have expressed that although separation efficiency can be useful in comparing the performance of different operating conditions, it does not take into account the economic factors, and is sometimes referred to as the technical separation efficiency. As discussed in the following chapters of this study, a high value of separation efficiency does not necessarily lead to the most economic return. Nevertheless, it remains a widely used measure to differentiate alternatives prior to the economic assessment. Sousa (2020) has also stated that, a plotted grade/recovery curve does not allow to distinguish the liberation efficiency (El) from the technical efficiency (Et). It is difficult to determine whether lower efficiency values are related to operational conditions or are a result of insufficient liberation. For this reason, the detailed material characterization can aid in understanding the process.

In the present, processing of low grade iron ore deposits has become high importance for economic and environmental preservation. Recovery of iron by using optimum separation method and operational conditions has grown in importance. In this study, detailed laboratory scale beneficiation studies were performed to determine the optimum beneficiation conditions of a typical low grade iron ore sample. For this purpose, separation efficiency values of various concentration methods were calculated by using chemical analysis of the test products. In literature, a significant amount of studies are found on iron ore beneficiation processes whereas studies on the evaluation and comparison of SE obtained from different methods are very limited. Therefore, the objective of this investigation is to find the fundamental effects of different operational parameters in dry and low magnetic separation, jigging and shaking table, on separation efficiency of a low grade iron ore and find out optimum method and operational parameters. In the present study, the author emphasizes the grade/

recovery curves and separation efficiency values in evaluation of beneficiation possibilities of a low grade iron ore.

2. Material and Method

The representative core samples were supplied from an ore potential area. The area is located in Kuluncak, one of the important areas having underground resources of iron and chromium stratum in the surrounding area of Hekimhan and Kuluncak towns in Malatya, located at Eastern Anatolia region of Türkiye. The sample acquired for this study was subjected to detailed characterization and laboratory scale testing. The core samples supplied from area were crushed below 30 mm and split into small amounts of representative samples for chemical, mineralogical and liberation analyzes, heavy liquid tests and beneficiation studies.

According to the material characterization, gravity concentration and magnetic separation studies were performed on different size fraction of run of mine ore. Grade/recovery curves for all methods were constructed and compared. The effects of material properties and operational parameters were evaluated.

For this aim, methods of jigging, flowing film concentration (shaking table), dry low intensity magnetic separation (DLIMS) and wet low intensity magnetic separation (WLIMS), were tested. Operational variables that may affect the performance of equipment, such as, magnetic field intensity in magnetic separation, tilt angle in shaking table, water velocity in jigging were taken into consideration in determining SE values. An explanatory diagram regarding the experimental procedure is given in Figure 1.

3. Material Characterization

Material characterization which gives information about the mineralogical, chemical and liberational attributes of the ore, is of crucial importance in studies of low grade ore deposits as it helps determining the most suitable method. The selection of suitable beneficiation method depends on the physical and textural properties of iron minerals and gangues. For this reason, the ROM sample and specific size fractions were subjected to various characterization studies such as determination of specific gravity, x-ray diffraction (XRD), Satmagan analysis, chemical analysis, liberation analysis and heavy liquid test. Specific size fractions have been chosen to be suitable for both coarse and fine fraction sized beneficiation tests.

3.1. Qualitative Mineralogical Analysis and Ore Microscopy

The mineral phases in the iron ore sample were determined by using XRD method. Diffractograms

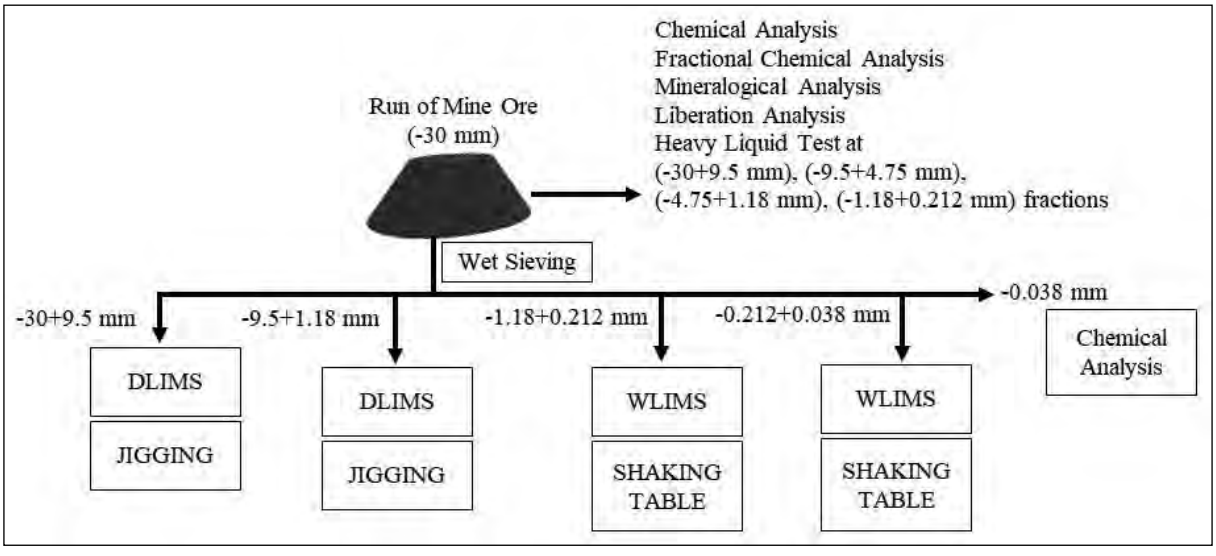

Figure 1- Simplified flowsheet of experimental studies.

were obtained from a Rigaku D/Max 2200 Powder X-ray Diffractometer, using a chrome anode. The Rigaku D/Max 2200 Powder X-ray Diffractometer is equipped with a horizontal goniometer capable of performing typical theta-2 theta scans. According to the results, the sample contains magnetite (Fe_3O_4). Additionally, the ore contains hematite (Fe_2O_3) and goethite $Fe^{3+}O(OH)$. Silicates, carbonates and clay minerals occur as the major gangue phases. The XRD pattern of the sample is given in Figure 2.

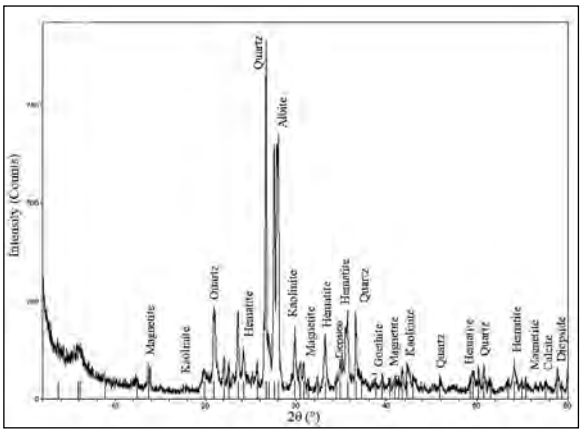

Figure 2- X-ray diffraction pattern of run of mine ore.

3.2. Fractional Chemical Analysis

The specific size fractions were analyzed for their major element composition by XRF (Table 1). It is indicated in Table 1 that iron ore contains 31.78% of total iron is low grade in nature, 17.52% silica as a major impurity, 14.26% CaO, 4.37% MgO, 0.56% Al_2O_3 with an LOI (Loss on Ignition) of 16.59%. Fractional analysis indicates that as the particle size decreased, iron content increased up to 38 µm, and below that, it decreased significantly. The -212+38 µm size fraction of feed has the highest total iron grade and lowest silica grade. Approximately 96% of total iron and 97% of silica are in the fraction are coarser than 0.212 mm. According to Table 1, -38 µm size fraction has highest alumina content (3.08%). Higher alumina and lower iron content (6.57%) of this fraction can be a marker of clay presence. XRD pattern shows the kaolinite presence in the ore.

3.3. Determination of Magnetite Content

Satmagan analyses have been performed by using Rapiscan Systems Satmagan 135 (Saturation Magnetization Analyzer) in order to determine the amount of iron originated from magnetite mineral.

Table 1- Fractional chemical analysis of iron ore sample.

Size (mm)	Weight (%)	Grade (%)				
		Fe	SiO_2	CaO	MgO	Al_2O_3
-30+9.5	48.47	30.54	18.73	15.14	4.37	0.51
-9.5+4.75	24.57	31.32	17.27	14.51	4.37	0.50
-4.75+1.18	12.54	34.55	16.06	13.26	4.55	0.53
-1.18+0.212	10.57	35.87	15.66	11.50	4.01	0.68
-0.212+0.038	2.82	38.66	9.50	9.96	3.62	0.75
-0.038	1.03	6.57	25.43	19.18	8.15	3.08
Head Sample	100.00	31.78	17.52	14.26	4.37	0.56
Size (mm)	Weight (%)	Distribution (%)				
		Fe	SiO_2	CaO	MgO	Al_2O_3
-30+9.5	48.47	46.58	51.82	51.46	48.43	43.90
-9.5+4.75	24.57	24.21	24.21	25.00	24.55	21.88
-4.75+1.18	12.54	13.63	11.49	11.66	13.06	11.92
-1.18+0.212	10.57	11.93	9.45	8.52	9.70	12.86
-0.212+0.038	2.82	3.43	1.53	1.97	2.33	3.76
-0.038	1.03	0.21	1.50	1.39	1.92	5.66
Head Sample	100.00	100.00	100.00	100.00	100.00	100.00

The Satmagan was designed specially to measure magnetite in iron ore concentrations. The principle behind the Satmagan 135 is to measure the force acting on the sample in a magnetic field with a spatial gradient. The magnetic field is strong enough to saturate the magnetic component in a sample. In this case all the magnetite in the sample gets measured regardless whether it can be separated by a magnet or not. Previous studies showed that particle size does not affect Satmagan measurements as it was expected (Amikiya, 2014). Therefore, representative samples were ground to -53 µm and analyses were performed. Magnetite content of the size fractions are tabulated in Table 2.

It is observed from Table 2 that magnetite is the main iron bearing mineral (98% wt) in the sample. Beside this ore consist minor amount of hematite (Fe_2O_3) and goethite $Fe^{3+}O(OH)$. Hematite and goethite contains only 2% of the total iron in the ore. These results are beneficial for determining the behavior of the ore in low intensity magnetic separators.

Figure 3- Stereo microscope and image analysis software.

3.4. Liberation Analysis

Liberation analysis was performed below 1 mm by using a Nikon SMZ 1500 Stereo Microscope and Clemex Vision PE 3.5.025 image analysis software (Figure 3). The size fractions were analyzed under the microscope using the reflected light mode.

The liberation degree of the magnetite particles was determined by the point counting technique. Approximately 600 grains was counted for each size fraction. Then, both free and locked magnetite particles in the images were counted and liberation degree of each size fractions was calculated. Liberation degree of size fractions are shown in Figure 4.

According to results, it is observed that the degree of liberation increases with a corresponding decrease in particle size. The liberation of magnetite particles are quite acceptable below 0.212 mm. Percentage of liberated particles increases from 49.18% to 89.05% in the -0.212+0.150 mm size fraction. The magnetite in the >95% liberated class can be regarded as free particles approximately. The magnetite in the

Table 2- Fractional magnetite content of size fractions.

Size (mm)	Weight (%)	Fe_3O_4 (%)	Fe from Analysis (%)	Fe from Satmagan (%)	Fe in Magnetite / Total Fe (%)
-30+9.5	48.47	41.15	30.54	29.78	0.975
-9.5+4.75	24.57	42.42	31.32	30.70	0.980
-4.75+1.18	12.54	47.07	34.55	34.06	0.986
-1.18+0.212	10.57	49.14	35.87	35.56	0.991
-0.212+0.038	2.82	52.35	38.66	37.88	0.980
-0.038	1.03	8.87	6.57	6.42	0.977
Head Sample	100.00	43.03	31.78	31.14	0.980

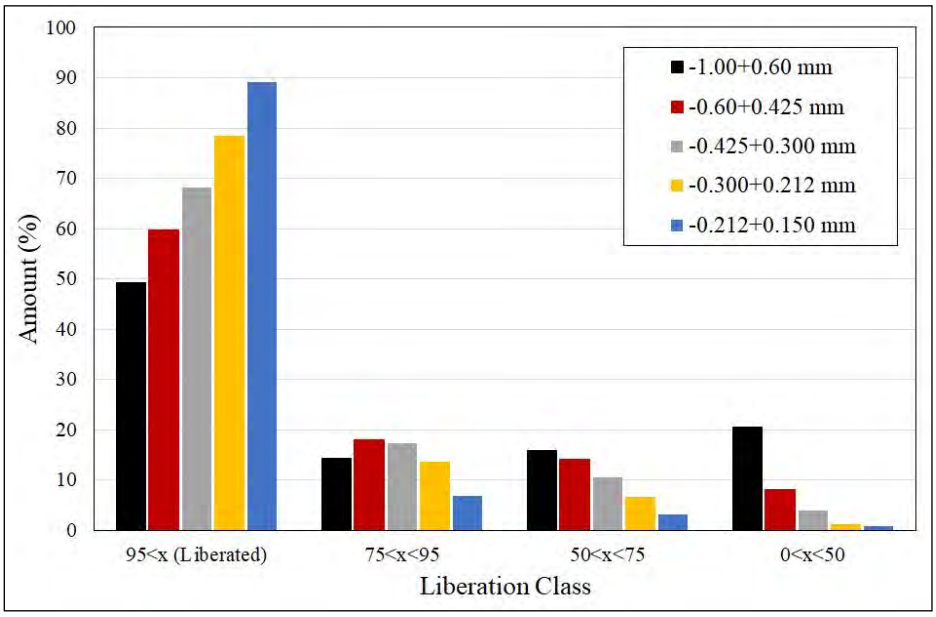

Figure 4- Liberation classes of magnetite mineral.

50>x>0% liberated (the magnetite in this class can be regarded as fully locked particles approximately) class is only 0.86% in 0.212+0.150 mm size fraction. This indicates that a grinding size finer than 212 µm is sufficient in separation of magnetite from gangue minerals.

3.5. Heavy Liquid Analysis

Heavy liquid analysis is an extremely useful tool in the determination of liberation characteristics of an ore. In this study, sized fractions of the ore were subjected to heavy liquid analysis. In a heavy liquid analysis theoretically, the liberated silicates and carbonates should concentrate in the float product, and iron minerals and locked particles (middling) of sufficient specific gravity should sink. In heavy liquid analysis, a tetrabromoethane (TBE) and acetone mixture was used to prepare the heavy liquids with densities of 2.70 g/cm^3 and 2.90 g/cm^3 separately. Then, each fraction was sunk into the 2.90 g/cm^3 heavy liquid. The float product was removed out, drained and sunk in the liquid of 2.70 g/cm^3 density. The all products were finally drained, washed, dried, weighed and analyzed. Heavy liquid analysis results are tabulated in Table 3.

It is indicated from Table 3 that the weight percentages of the sinks are increasing in finer size fractions. The total iron content in the sink product is higher than float products and varies between 51-55% Fe. Increase in fineness increases the total iron content and decreases the silica content in the sink product. The silica grade of float products is higher in the floats for all size fractions. The highest silica grade was observed at -30+9.5 mm size fraction. The results obtained from the heavy liquid test indicate that liberation of the iron and silica is insufficient. This observation was confirmed by visible and microscopic examination of heavy liquid analysis fractions. Heavy liquid test results also show that liberation degree of +4.75 mm is quite insufficient. These results mark that there are some locked gangue grains in the sink product.

4. Beneficiation Studies

A detailed test procedure was designed and performed in evaluation of separation efficiencies of magnetic separation and gravity concentration. Representative samples were taken during tests and chemical analyses of all samples were done to determine the performance of each test. Effect of feed size and some important operational parameters on separation efficiency were also evaluated. The grade/recovery curves of each test were constructed and evaluated. Details of experimental studies are discussed below.

Table 3- Heavy liquid analysis results.

Size Fraction (mm) / Product	(%)	Grade (%)				
	Weight	Fe	SiO_2	CaO	MgO	Al_2O_3
-30+9.5 / 2.7 Floats	30.09	9.95	24.44	18.93	5.75	0.53
-30+9.5 / 2.9 Floats	22.98	15.01	15.39	16.63	4.77	0.53
-30+9.5 / 2.9 Sinks	46.93	51.35	16.71	11.98	3.28	0.48
-30+9.5	100.00	30.54	18.73	15.14	4.37	0.51
-9.5+4.75 / 2.7 Floats	31.05	9.10	25.69	18.92	6.24	0.47
-9.5+4.75 / 2.9 Floats	19.59	15.06	19.92	17.74	4.44	0.66
-9.5+4.75 / 2.9 Sinks	49.36	51.74	10.91	10.45	3.16	0.45
-9.5+4.75	100.00	31.32	17.27	14.51	4.37	0.50
-4.75+1.18 / 2.7 Floats	24.76	6.71	30.75	22.99	7.42	0.69
-4.75+1.18 / 2.9 Floats	19.26	14.14	25.84	15.48	5.14	0.69
-4.75+1.18 / 2.9 Sinks	55.98	53.89	6.19	8.19	3.08	0.41
-4.75+1.18	100.00	34.55	16.06	13.26	4.55	0.53
Size Fraction (mm) / Product	(%)	Distribution (%)				
	Weight	Fe	SiO_2	CaO	MgO	Al_2O_3
-30+9.5 / 2.7 Floats	30.09	9.81	39.26	37.62	39.64	31.58
-30+9.5 / 2.9 Floats	22.98	11.29	18.88	25.24	25.10	24.01
-30+9.5 / 2.9 Sinks	46.93	78.90	41.86	37.13	35.25	44.41
-30+9.5	100.00	100.00	100.00	100.00	100.00	100.00
-9.5+4.75 / 2.7 Floats	31.05	9.02	46.20	40.50	44.37	29.55
-9.5+4.75 / 2.9 Floats	19.59	9.42	22.60	23.95	19.92	25.92
-9.5+4.75 / 2.9 Sinks	49.36	81.56	31.19	35.55	35.72	44.53
-9.5+4.75	100.00	100.00	100.00	100.00	100.00	100.00
-4.75+1.18 / 2.7 Floats	24.76	4.81	47.42	42.93	40.38	31.94
-4.75+1.18 / 2.9 Floats	19.26	7.88	31.00	22.49	21.75	24.96
-4.75+1.18 / 2.9 Sinks	55.98	87.31	21.58	34.58	37.87	43.10
-4.75+1.18	100.00	100.00	100.00	100.00	100.00	100.00

4.1. Magnetic Separation Studies

It is well known from the detailed characterization studies that the main mineral in the feed is magnetite. For this reason, low intensity magnetic separation tests were developed and conducted to investigate the effect of field intensity and feed size distribution on SE (Table 4). One stage low intensity magnetic separation was performed to different size fractions. A simplified schematic view of test procedure is shown in Figure 1. Magnetic separation tests were performed in a batch scale. Feed rate was adjusted manually to approximately 0.25 kg/min to generate a mono-particle layer on the surface of the type magnetic separator. The operational magnetic field intensity was measured by using a Gauss meter on the roller surface.

4.2. Gravity Concentration Studies

4.2.1. Jigging

Jigging tests were performed by using -30+9.5 and -9.5+1.18 mm size fractions to evaluate the effect of water velocity on SE. A laboratory scale Denver mineral jig was used which dimensions of 10.5x10.5 was used for the process. A constant duration of five minutes jigging was applied during each test (feeding 60 sec., jigging 240 sec.). All products (float and sink) were collected, and chemical analysis were performed.

Table 4- Low intensity magnetic separation test conditions.

Test No.	Feed Size (mm)	Test Type	Magnetic Intensity (Gauss)
1	-30+9.5	Dry	1000
2	-30+9.5	Dry	1200
3	-30+9.5	Dry	1400
4	-30+9.5	Dry	1600
5	-9.5+1.18	Dry	1000
6	-9.5+1.18	Dry	1200
7	-9.5+1.18	Dry	1400
8	-9.5+1.18	Dry	1600
9	-1.18+0.212	Wet	1000
10	-1.18+0.212	Wet	1200
11	-1.18+0.212	Wet	1400
12	-1.18+0.212	Wet	1600
13	-0.212+0.038	Wet	1000
14	-0.212+0.038	Wet	1200
15	-0.212+0.038	Wet	1400
16	-0.212+0.038	Wet	1600

It is reported in the literature that traditional jigging techniques become increasingly inefficient in finer size fractions (Dobbins et al., 2009). Therefore -1.18 mm fraction of iron ore sample was removed before jigging and WLIMS tests and shaking table test was conducted to this fraction. The jigging test conditions are tabulated in Table 5.

Table 5- Jigging test conditions.

Test No.	Feed Size (mm)	Water velocity (cm/sec)
17	-30+9.5	5
18	-30+9.5	10
19	-30+9.5	15
20	-30+9.5	20
21	-30+9.5	25
22	-9.5+1.18	3
23	-9.5+1.18	6
24	-9.5+1.18	9
25	-9.5+1.18	12
26	-9.5+1.18	15

4.2.2. Shaking Table Tests

Shaking table tests were performed on the -1.18+0.212 mm and -0.212+0.038 mm size fractions to evaluate the effect of feed size fraction and table tilt angle on separation efficiency (SE). During the tests a shaking table with dimensions 500×1200 mm was used. Wash water rate (10 lpm) and feed pulp density (25% solid) were kept constant during the tests. Concentrate, middling and tailing samples were collected by using a special design sampler during each test. Shaking table test conditions are tabulated in Table 6.

Table 6- Shaking table test conditions.

Test No.	Feed Size (mm)	Table tilt Angle (degrees)
27	-1.18+0.212	2
28	-1.18+0.212	4
29	-1.18+0.212	6
30	-1.18+0.212	8
31	-0.212+0.038	2
32	-0.212+0.038	4
33	-0.212+0.038	6
34	-0.212+0.038	8

5. Discussion

Grade/recovery curves of separation methods were compared for different feed size fractions (Figure 5).

It is indicated from Figure 5 that total iron recovery of gravity concentration method is higher than the magnetic separation coarser than 1 mm. In contrast, total iron recovery of gravity concentration method is lower than the magnetic separation finer than 1 mm. Grade/recovery values are lowest in the -30+9.5 mm size fraction. Recovery and grades

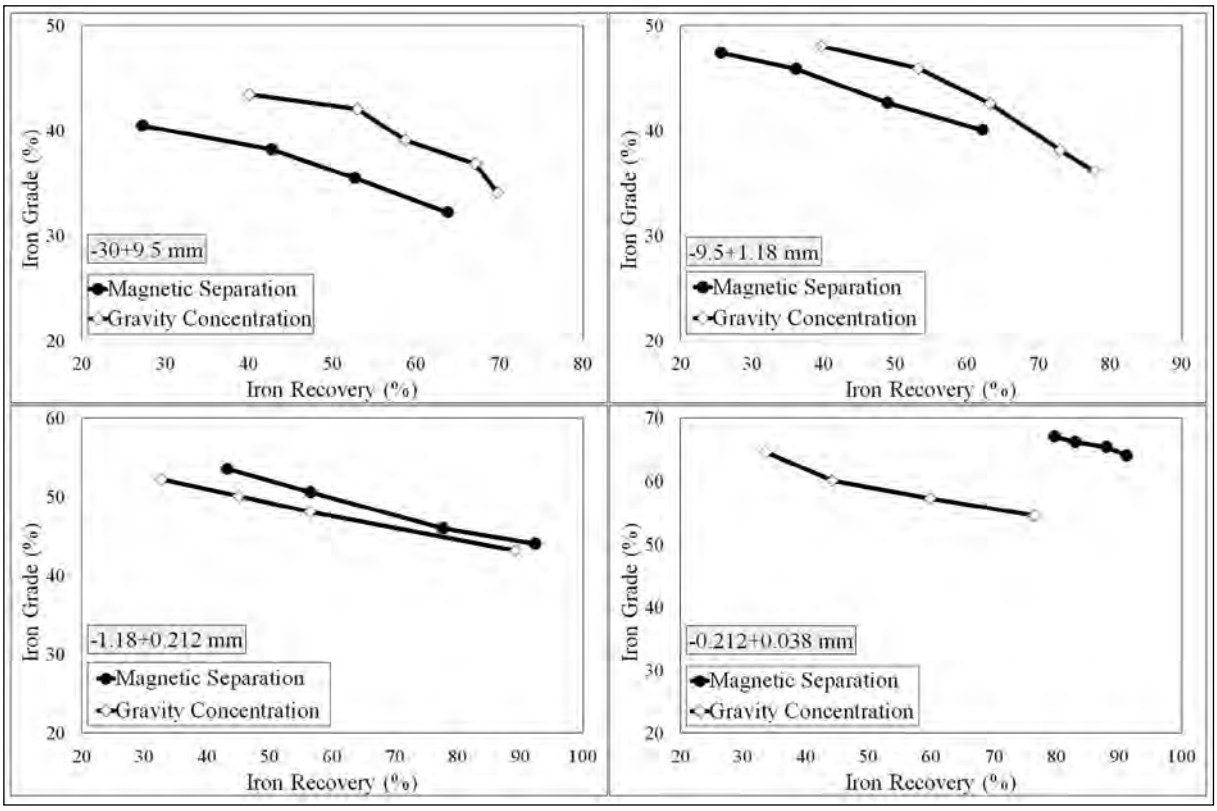

Figure 5- Grade/recovery curves of separation methods for different feed size fractions.

increase with decrease in feed size irrespective to separation method. The reason for lower recoveries of particles above 1 mm is mainly due to poor liberation of the magnetite mineral as discussed in heavy liquid analysis results.

In terms of process dynamics of jigging, concentration of coarser size fractions is relatively simpler than the finer size fractions (Mukherjee et al., 2006). However, in the current magnetic separation devices, an effective concentration occurs only when the magnetic forces exceed the gravitational forces, many folds (Lin et al., 1997). Hence, irrespective to the liberation of particles as the particle size increases, the gravity force will further increases and it may be also greater than the magnetic force. This can lead to a decrease in the recovery of coarse particles in magnetic separation. According to Figure 10 the jigging method can be beneficial as a pre concentrator above 1 mm. According to results, jig has a higher capability to treat coarser particles.

The liberation degree of magnetite increases significantly below 1 mm according to liberation analysis results. Therefore, an upwards and/or to the right shift of the curves shows an improvement in performance of shaking table and wet magnetic separator. Wet magnetic separation and shaking table gives a similar grade/recovery curve at feed size fraction -1.18+0.212 mm. However, magnetic separation produces a higher grade concentrate for the same recovery value. As a result of Satmagan analyses it is well described that the main iron bearing mineral is magnetite in the ore. The magnetite contains 98% of total iron. Magnetic susceptibility of these more liberated particles increases in finer size fractions. It is reported in the previous studies that magnetic forces become more dominant for the intermediate size ranges (Rayner and Napier-Munn, 2000; Vijayendra, 2001; Arol and Aydoğan, 2004; Mahmoud, 2010; Dworzanowski, 2012). Higher recovery of magnetic separation can be described with dominant magnetic forces on the intermediate size particles. However, similar grade/recovery curves of both wet magnetic separation and shaking table reveal that both method have the capability to treat intermediate particles with varying recovery values. In addition, neither magnetic

separation nor shaking table can produce a high grade concentrate with higher recoveries at intermediate size ranges of the sample studied.

Grade/recovery values of magnetic separation is significantly higher than shaking table below 0.212 mm. This fraction can be defined as fully liberated (Figure 4). Therefore, the difference of grade/recovery curves can be described by finer magnetite treatment capabilities of magnetic separation and gravity concentration. It is well known that the performance of conventional gravity equipment such as spiral and shaking table decreases significantly below 75 µm (Hearn, 2002). The particle movement in a fluid is affected by its specific gravity and particle diameter. The particles having larger diameter are affected more than the smaller diameter particles. Higher efficiency separation is more likely with coarser particles in gravity concentration. As a result, effect of magnetic forces on particles is higher than gravity and drag forces results a better recovery at feed size -0.212+0.038 mm (Chatterjee, 1998).

A SE based performance calculation is applied in the present study to determine the effect of operational parameters and feed size on magnetic separation, jigging and shaking table separately. The SE of each method calculated by using iron analysis in the feed and the products. SE of magnetic separation tests is figured in Figure 6. The SE of each feed size fraction is calculated by applying the Equation 1.

Figure 6 reveals that magnetic separation has lowest SE at the coarsest size. The separation efficiency gradually improves with increasing fineness for all magnetic field intensities. According to some authors, hydrodynamic forces, magnetic forces, gravity forces and drag forces are the main forces that lead the complete movement of particles in a magnetic separator (Arol and Aydoğan, 2004; Wills and Napier-Munn, 2006). Gravity and drag forces work against magnetic forces which attract magnetic particles. The magnitude of these forces is significantly affected by the size of particles. It is reported from the previous studies that; the hydrodynamic drag forces are proportional to the diameter of a particle. The magnetic forces and gravity forces are proportional to the second and third power of the particle diameter, respectively. Consequently, the gravity forces are effective on the coarse particles while the hydrodynamic drag forces are more effective on the fine particles (-38 µm), and magnetic forces are more effective on the intermediate particle sizes. Because the attraction is directly proportional to the particle mass, the larger particles require higher magnetic intensity than for the finer ones (Vijayendra, 2001). In magnetic separation of fine particles, magnetic forces must exceed that of the hydrodynamic drag forces. But, higher magnetic

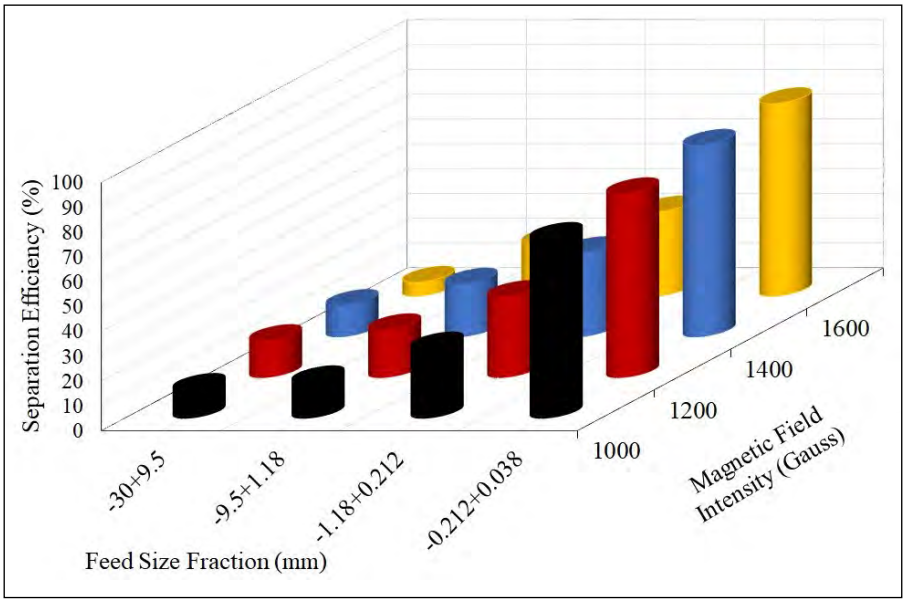

Figure 6- Separation efficiency of magnetic separation.

forces than gravity forces are required for the coarse mineral particles (Arol and Aydoğan, 2004). Hence, as the particle size increases, the gravity force will be further increased and it may be also greater than the magnetic force. This can lead to a decrease in the recovery of coarse magnetic particles and accordingly a decrease in separation efficiency of the same liberation level.

As the magnetic field intensity increases, magnetic minerals are normally captured efficiently by magnetic separators, resulting in an increase of magnetic particles, hence to a marginal increase in SE values. SE of coarsest size fraction (-30+9.5) are similar for all magnetic fields. It can be concluded that the effect of gravity forces on the coarse particles are higher as mentioned above. In addition, poor liberation of coarser size fractions can negatively affect the separation efficiency. The SE increases with the increasing field intensity for other size fractions. Highest separation efficiencies can be obtained at finest feed size. Therefore, the degree of liberation of the size fractions can be inferred as the main reason behind this effect. It should be noted that sufficient liberation is required for the separation efficiency to increase with magnetic field intensity.

SE values of jigging are presented in Figure 7.

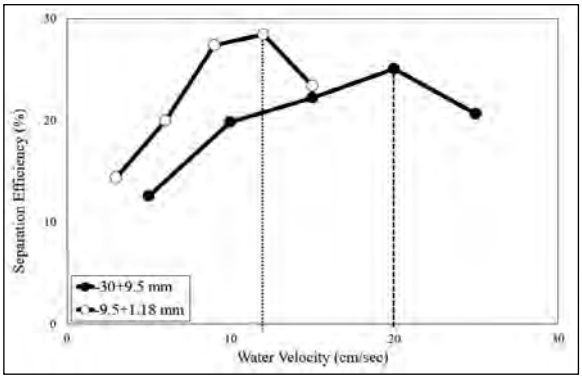

Figure 7- Separation efficiency of jigging.

It is visible from the Figure 7 that the SE is related with feed size and water velocity. Figure 7 shows that -9.5+1.18 mm size fraction has a higher SE. Higher SE value of this size fraction indicates the significant effect of better liberation. To increase the SE of both fractions, water velocity should be increased. A higher amount of water is required to increase SE of coarse size fraction. A water velocity of 12 cm/sec is necessary for the optimum separation of the magnetite mineral from the gangues at -9.5+1.18 mm size fraction. An increase in water velocity above 12 cm/sec has negative effect on SE. Similarly, the 20 cm/sec water velocity is acceptable for the optimum separation at -30+9.5 mm size fraction.

In literature, certain studies in detail can be found on the jigging process. The authors of such studies report two important finding about SE of jigging in these studies (Mukherjee et al., 2005*a, b*; Mukherjee et al., 2006; Mukherjee and Mishra, 2006; Mukherjee, 2009). According to their results the SE increases with increase in water velocity, achieves a maximum point and then decreases. In addition, coarse size feed material needs a higher maximum water velocity for optimum efficiency (Mukherjee and Mishra, 2006). Maximum water velocity term as an important term and parameter in defining optimum SE value of the jigging method is reported by Mukherjee. According to author, the efficiency of jigging is related to the water velocity (Mukherjee et al., 2006). Figure 7 clearly indicates that maximum water velocity values were also observed in this study.

According to Das et al. (2008), the SE of jigging is higher at finer sizes and the 4-5 cm/sec water velocity is sufficient to concentrate the iron particles from the gangues at a size fraction of -5+1 mm. A water velocity value above these values did not result in much positive effect on SE. In the present study, similar results to those of previous studies were obtained. According to results, maximum water velocity of -30+9.5 mm can be given as 20 cm/sec, and maximum water velocity of -9.5+1.18 mm can be given as 12 cm/sec for studied low grade iron ore. The results of all studies show that maximum water velocity term is valid and important for jigging process. However, the maximum water velocities to treat different types of iron ore should be determined to obtain optimum SE. SE values can vary according to the feed size.

Separation efficiency of the coarser size fraction suggests poor liberation characteristics. This inference was verified through optical analysis. The heavy liquid tests revealed that a concentrate grade of maximum

54% Fe is attainable for -30+1.18 mm fraction with an overall recovery of 82%. The concentrate grade obtained during jigging tests nearly met the analysis grade while the recovery was around 66% of the analysis value.

Separation efficiency of shaking table is figured in Figure 8.

It can be observed from Figure 8 that shaking table performed best especially at finer particle sizes and at an angle of 2°. The SE of both size fractions increases significantly with decreasing the tilt angle. It is observed from the test results that table tilt angle effects the SE significantly. So it is clear that feed size, liberation degree and deck tilt angle have a major influence on SE of the shaking table process.

Lower separation efficiencies of -1.18+0.212 mm size fraction can be explained with insufficient liberation obtained from liberation analyses. The average liberation degrees of -1.18+0.212 mm size fraction and -0.212 mm size fraction are calculated as 64% and 89.05% respectively.

It is observed from shaking table test results the lowest angle should be used to obtain highest SE. Above 2°, separation efficiency of shaking table decreases significantly. The decrease of SE can be explained by residence time of particles. Residence time of particles in the flowing film decrease with increasing angle. In this short period of time, transportation of the very fine magnetite particles to middling and tailing can decrease the selectivity. In addition, it can be concluded that desliming (removing of -38 μm) has positive effects on overall efficiencies. Relationship between iron recovery and separation efficiency values of separation methods is shown in Figure 9.

It can be revealed from Figure 9 that an increase in recovery increases the SE of magnetic separation. The SE of jigging and shaking table increases with increasing recovery up to a certain value. Then, SE of gravity concentration methods decreases significantly. This can be explained with the limited effect of gravity forces on the magnetic particles. In addition, higher iron recoveries can be obtained with sufficient liberation of magnetite particles. The poor liberation characteristic of +1 mm can negatively affect the SE of jigging and DLIMS. In contrast, liberation of magnetite increases below 1 mm. An increase in SE of shaking table and WLIMS can be the result of this better liberation. Figure 9 clearly shows that SE of wet magnetic separation is significantly higher than shaking table and jigging approximately 80% iron recovery. It can be concluded from Figure 9 that SE of WLIMS is better than various gravity separation techniques for iron ore beneficiation. The lower efficiency of DLIMS can be described with the effect

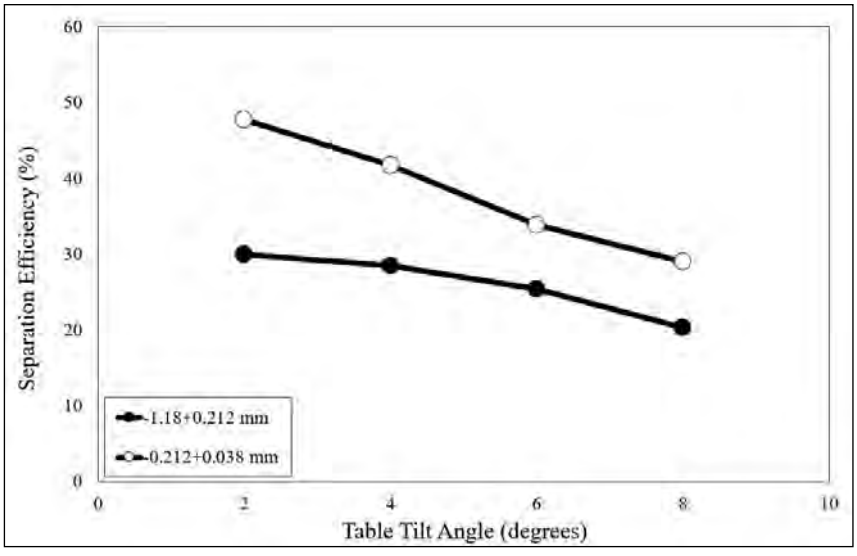

Figure 8- Separation efficiency of shaking table.

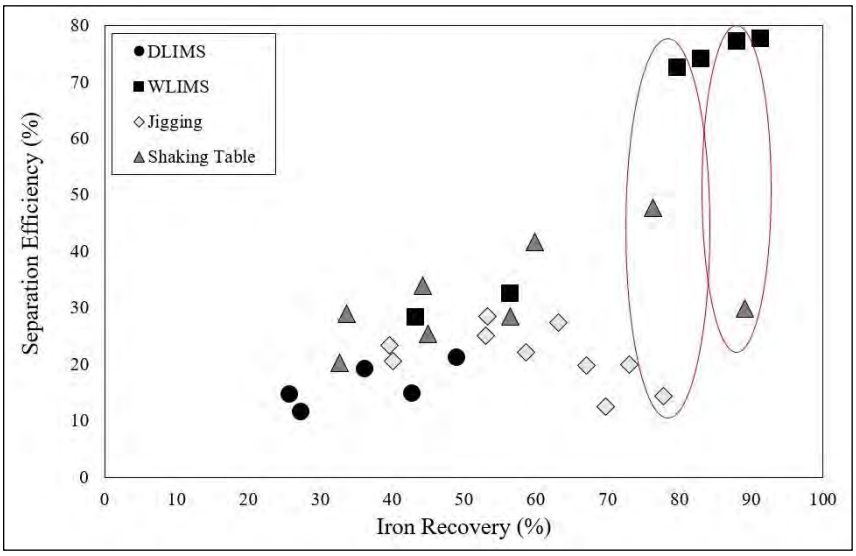

Figure 9- Relationship between iron recovery and separation efficiency.

of gravity forces on coarser particles and mainly with poor liberation.

Average separation efficiencies of gravity concentration and magnetic separation were calculated for average feed sizes by using statistical analysis. The results of gravity concentration and magnetic separation are tabulated in Table 7 and 8, respectively. The mean separation efficiencies of gravity concentration and magnetic separation are shown in Figure 10.

It can be revealed from Figure 10 that separation efficiency values of magnetic separation vary between 11.19% to 75.34%. Similarly, separation efficiency values of gravity concentration vary between 20.05% to 38.07%. A decrease in average particle size increases the separation efficiency of both methods. Separation efficiencies of gravity concentration and magnetic separation takes similar values above 1 mm, however, separation efficiency of magnetic separation is significantly higher than gravity concentration below 1 mm.

Table 7- Average separation efficiencies (SE) of gravity concentration.

Feed Size Fraction (mm),	Mean Feed Size (mm)	Mean SE (%)	Median	Standard Deviation	Standard Error
-30+9.5	19.75	20.05	20.62	4.65	2.08
-9.5+1.18	5.34	22.68	23.39	5.76	2.57
-1.18+0.212	0.70	26.03	26.94	4.26	2.13
-0.212+0.038	0.13	38.07	37.80	8.27	4.13

Table 8- Average separation efficiencies (SE) of magnetic separation.

Feed Size Fraction (mm)	Mean Feed Size (mm)	Mean SE (%)	Median	Standard Deviation	Standard Error
-30+9.5	19.75	11.19	12.13	3.95	1.98
-9.5+1.18	5.34	19.17	20.26	3.14	1.57
-1.18+0.212	0.70	32.21	33.27	2.67	1.34
-0.212+0.038	0.13	75.34	75.34	2.48	1.24

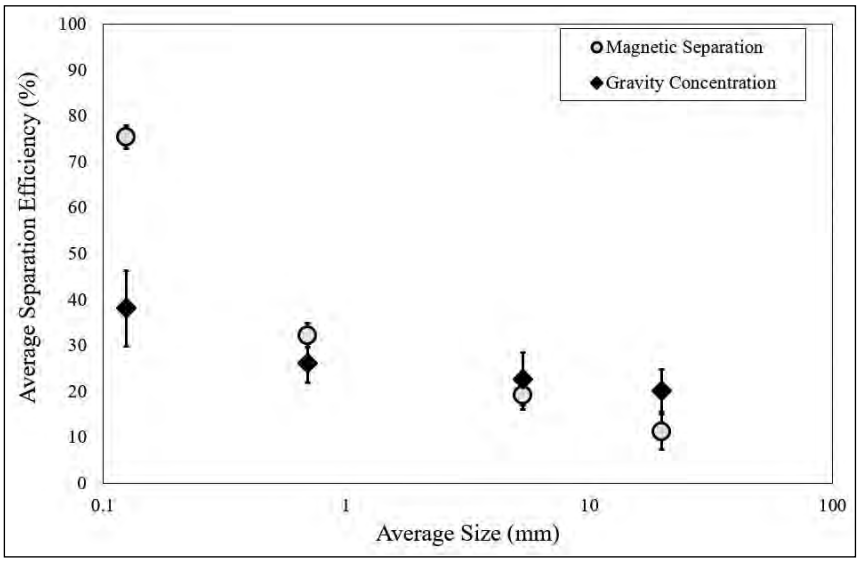

Figure 10- Separation efficiency (SE) of magnetic separation and gravity separation.

6. Results

An iron ore sample which is low grade in nature from the Eastern Anatolian, Turkey, has been subjected to detailed material characterization and various concentration methods with the objective to evaluate grade/recovery relationships and the SE of different physical beneficiation methods. Detailed beneficiation tests including dry and wet low intensity magnetic separation, jigging, and shaking table were performed to coarser, intermediate and finer size fractions of the ore. The effect of most significant operational parameters which are, magnetic field intensity, water velocity and table tilt angle on the separation efficiency values were evaluated and discussed.

Performance evaluation of beneficiation methods have been performed by calculating SE. Calculated separation efficiencies revealed that operational parameters significantly affect the separation efficiencies of all methods. According to results decrease in feed size fraction increases the separation efficiency irrespective of the beneficiation method. This result clearly shows that better liberation in finer size fraction positively affects SE. The strict relationship between size dependent iron recovery and SE can be beneficial finding potential reasons of lower SE values at higher recoveries for iron ore concentration.

Mean SE of different size fractions showed that separation efficiencies of gravity concentration and magnetic separation takes similar values above 1 mm, however, separation efficiency of magnetic separation is significantly higher than gravity concentration below 1 mm for studied iron ore sample.

According to SE calculations it can be concluded that Test 16 gives the best efficiency value (77.61%). In this test wet magnetic separation has been applied to -212+38 μm size fraction. According to test results a magnetic concentrate can be obtained with 64.01 %Fe and 91.27% total iron recovery. However, the presented results are independent of economic considerations, and can only compare the technical efficiency of different beneficiation methods. It is difficult to know whether a lower separation efficiency of any beneficiation method is related to operational conditions or a result of insufficient liberation. In the present study a strictly controlled test program was performed. The variation of the SE values can be explained according to nature of the beneficiation methods and material properties.

For low grade ores; especially for iron ores, it is very crucial to develop a flow sheet to achieve the optimum grade and recovery while decreasing the cost likely by using optimum method. Therefore, the grade/recovery curves and separation efficiency calculations used in this research can be used as a qualitative method to compare the efficiency of different beneficiation

methods and choose the best technically. Both grade/recovery curves and separation efficiency methods have advantages as they are fast and basic methods for the efficiency evaluation by using experimental results. To apply these techniques to DLIMS, WLIMS, jigging, and shaking table and other potential methods can help in acquiring a good comprehension of the plant dynamics and the optimization.

To technically determine the best process condition with respect to operational parameters and beneficiation methods these basic calculations can be useful and give advantages to researchers. One of the advantages of this method is the determination of the best process among several ones. The presented results are one of the strategical methods for any separation process evaluation in no economic terms but process performance. The grade/recovery curves and relationship between recovery and SE will separately present useful results based on the needs of the users.

References

Amikiya, C. A. 2014. Characterisation of iron ore - a case study of Mount Tokadeh, Western Nimba Area, Liberia. Master of Philosophy in Chemical Engineering, Kwame Nkrumah University of Science and Technology, 119.

Amiri, S. H. 2019. Investigation of efficiency of magnetic separation methods for processing of low-grade iron pigments ore (RED Ochre). International Journal of Mineral Processing and Extractive Metallurgy 4(1), 18-25.

Arol, A. I., Aydoğan, A. 2004. Recovery enhancement of magnetite fines in magnetic separation. Colloids and Surfaces A: Physicochemical and Engineering Aspects 232, 151-154.

Barari, H. B., Sen, P., Sengupta, P. 1979. Generalized approach for multi-component multi-stage separation efficiency. Society of Mining Engineers AIME 266, 1901–1904.

Chatterjee, A. 1998. Role of particle size in mineral processing at Tata Steel. International Journal of Mineral Processing 53, 1-14.

Das, B., Prakash, S., Das, S. K., Reddy, P. S. R. 2008. Effective beneficiation of low grade iron ore through jigging operation. Journal of Minerals and Materials Characterization and Engineering 7, 27-37.

Dobbins, M., Dunn, P., Sherell, I. 2009. Recent advances in magnetic separator designs and applications. The 7th International Heavy Minerals Conference What next, The Southern African Institute of Mining and Metallurgy, 63-70.

Drzymala, J. 2006. Atlas of upgrading curves used in separation and mineral science and technology. Physicochemical Problems of Mineral Processing 40, 19-29.

Drzymala, J. 2007. Atlas of upgrading curves used in separation and in mineral science and technology. Physicochemical Problems of Mineral Processing 41, 27-35.

Drzymala, J. 2008. Atlas of upgrading curves used in separation and mineral science and technology. Physicochemical Problems of Mineral Processing 42, 75-84.

Dworzanowski, M. 2012. Maximizing the recovery of fine iron ore using magnetic separation. Journal of the Southern African Institute of Mining and Metallurgy 112, 197-202.

Hearn, S. 2002. The use of hindered settlers to improve iron ore gravity concentration circuits. Mineral processing plant design, practice, and control, Colorado. Society for Mining, Metallurgy and Exploration Incorporation.

Irannajad, M., Salmani Nuri, O., Allahkarami, E. 2018. A new approach in separation process evaluation. Efficiency ratio and upgrading curves. Physicochemical Problems of Mineral Processing 54, 847-57.

Lin, I. J., Knish-Bram, M., Rosenhouse, G. 1997. The beneficiation of minerals by magnetic jigging, Part 1. Theoretical aspects. International Journal of Mineral Processing 50, 143-59.

Mahmoud, M. A. 2010. Statistical design application and analysis of separation efficiency in Davis Tube tester. Journal of Engineering Sciences, Assiut University 38, 1047-1058.

Makhija, D., Mukherjee, A. K., Ghosh, T. K. 2013. Preconcentration feasibility of gravity and magnetic techniques for banded hematite Jasper. International Journal of Mining Engineering and Mineral Processing 2, 8-15.

Mukherjee, A. K. 2009. New method for evaluation of gravity separation processes. Mineral Processing and Extractive Metallurgy Review 30, 191-210.

Mukherjee, A. K., Mishra, B. K. 2006. An integral assessment of the role of critical process parameters on jigging. International Journal of Mineral Processing 81, 187-200.

Mukherjee, A. K., Dwivedi, V. K., Mishra, B. K. 2005*a*. Analysis of a laboratory jigging system for improved performance. Minerals Engineering 18, 1037-1044.

Mukherjee, A. K., China, M., Rai, S. K., Sinha, M. 2005*b*. Flowsheet development for Joda classifier fines. R and D Reports 60(4), 8.

Mukherjee, A. K., Bhattacharjee, D., Mishra B. K. 2006. Role of water velocity for efficient jigging of iron ore. Minerals Engineering 19, 952-59.

Özcan, Ö., Aghlmandı Harzanagh, A., Orhan, E., Ergün, Ş. 2021. Beneficiation and flowsheet development of a low grade iron ore: a case study. Bulletin of the Mineral Research and Exploration 165, 235-251.

Rayner, J. G., Napier-Munn, T. J. 2000. The mechanism of magnetics capture in the wet drum magnetic separator. Minerals Engineering 13, 277-285.

Schulz, N. F. 1979. Separation efficiency. Transactions of the Society of Mining Engineers. The American Institute of Mining, Metallurgical, and Petroleum Engineers 247, 81–87.

Seifelnassr, A., Moslim, E., Abouzeid, A. Z. 2012. Effective processing of low-grade iron ore through gravity and magnetic separation techniques. Physicochemical Problems of Mineral Processing 48, 567-578.

Shivakumar, I. A., Chinthapudi, E., Ho-Seok, J., Barada, K. M,, Jan, D. M. 2017. Selection of gravity separators for the Beneficiation of the Uljin Tin Ore. Mineral Processing and Extractive Metallurgy Review 38, 54-61.

Sousa, R. J. C. 2020. Assessment of separation efficiency in mineral processing using the ultimate upgrading concept-a holistic window to integrate mineral liberation data. PhD Dissertation, Department of Mining Engineering, Faculty of Engineering of University of Porto.

Suthers, S. P., Nunna, V., Tripathi, A., Douglas, J., Hapugoda, S. 2014. Experimental study on the beneficiation of low-grade iron ore fines using hydrocyclone desliming, reduction roasting and magnetic separation. Mineral Processing and Extractive Metallurgy 123(4), 212-227.

Vijayendra, H. G. 2001. A Handbook on Mineral Dressing. Vikas Publishing House, New Delhi, 271–279.

Wills, B. A., Napier-Munn, T. J. 2006. Mineral Processing Technology, 6th Edition Australia. Elsevier Science and Technology Books.

Wills, B. A., Finch, J. A. 2016. Wills' Mineral Processing Technology: An Introduction to the Practical Aspects of Ore Treatment and Mineral Recovery, 8th Edition, Elsevier.

Xiong, D., Liming, L., Holmes, R. 2015. Developments in the physical separation of iron ore: magnetic separation. iron ore. Mineralogy, Processing and Environmental Sustainability 66, 283-307.

Bulletin of the Mineral Research and Exploration

http://bulletin.mta.gov.tr

Modeling of the complex hydrocarbon traps by the shot domain acoustic finite difference method and data-processing

Şerife BOĞAZKESEN[a*] and Hakan KARSLI[b]

[a]*Atatürk University, Faculty of Engineering, Department of Civil Engineering, Erzurum, Türkiye*
[b]*Karadeniz Technical University, Faculty of Engineering, Department of Geophysics, Trabzon, Türkiye*

Research Article

Keywords:
Finite Difference Method, Data Processing, Hydrocarbon Traps, Seismic Modeling, Synthetic Shot.

ABSTRACT

Numerical modeling studies have a widespread application in exploration seismology in order to understand the seismic reflection responses of hydrocarbon traps formed in relation to tectonic structure, lithological changes and unconformities in complex geological environments and to develop effective data processing strategies. In this study, the seismic modeling of two important hydrocarbon trap models (Granite Wash and Normal Fault Trap) was performed by the Finite Difference Method (FDM), which provides the solution of the acoustic wave equation. Seismic data models were carried out in the pre-stack shot environment, and the obtained shot data were passed through appropriate data-processing stages to obtain stack and migration (zero offset) sections. By converting the obtained migration sections to depth, the spatial location and dimensions of hydrocarbon traps on the section were determined and it has been observed that they are compatible by comparing with the initial geological models. Thus, the seismic responses of hydrocarbon trap structures were learned, the importance of data processing was understood, and zero offset cross-sections were obtained by processing of the generated synthetic shot records. Accordingly, it was observed that it is appropriate to make more and frequent shots in the investigation of granite wash type traps which are thin and short-width, whereas it is useful to make relatively less frequent shots in order to reduce the scattering intensity caused by the discontinuities of the fault type structures. Consequently, it is thought that before the field study for the hydrocarbon exploration, the modeling of the pre-stack shot instead of the post-stack modeling (zero offset) will contribute to the development of the data processing stages and the testing of the seismic section interpretation. In the future, such synthetic models and data processing will be developed for different complex trap structures and real data.

Received Date: 15.03.2021
Accepted Date: 20.08.2021

1. Introduction

Hydrocarbon (petroleum, natural gas, and coal) resources account for 86% of the world's energy consumption. In Türkiye, this rate reaches 92% (TPAO, 2022). Therefore, investments and interest in the exploration and discovery of hydrocarbon traps still remain more important. As a result, great deals of effort are put in towards further developing onshore and offshore activities both in Türkiye and in the globe through the usage of advanced technology and effective methods.

A hydrocarbon trap is defined as a porous and permeable rock with any geometric shape that contains structurally or stratigraphically formed oil and natural

Citation Info: Boğazkesen, Ş., Karslı, H. 2022. Modeling of the complex hydrocarbon traps by the shot domain acoustic finite difference method and data-processing. Bulletin of the Mineral Research and Exploration 168, 93-109. https://doi.org/10.19111/bulletinofmre.985502.

**Corresponding author: Şerife BOĞAZKESEN, serifebogazkesen@atauni.edu.tr*

gas, or both. As is known, the most powerful method for detecting the location of hydrocarbon traps of different scales at different depths of the Earth is the seismic reflection. Studies of hydrocarbon traps by seismic reflection method include data collection from the field with multi-source system, multi-receiver systems, processing and interpretation of collected data with up-to-date software suitable for the purpose. The interpretation allows the determination of structures and hydrocarbon traps by taking into account the structural and stratigraphic principles. At the same time, to know how the seismic responses of structural and stratigraphic hydrocarbon traps will be in general provides important contributions to the interpreter for the interpretation of seismic sections. Also, complexity of the geological structures in which the traps are located and omissions in data processing processes or the deficiencies and errors in the parameter selection will adversely affect the quality of the seismic sections to be interpreted.

Seismic reflection response of hydrocarbon traps is performed by numerical modeling of acoustic or elastic seismic wave propagation within the designated ground model and referred to as seismic modeling. The seismic modeling is commonly used to plan for collecting good quality seismic data (Gjøystdal et al., 2007; Robertson et al., 2015) and to improve seismic data processing workflow on complex geological structures (Aminzadeh et al., 1997; Gjøystdal et al., 2007; Huang et al., 2010; Özbek et al., 2010) and they are also extremely useful for associating an interpreted geological model with real data. An important application on this field is the experimentation of different geological models to study structural and stratigraphic problems encountered during seismic interpretation (Sayers and Chopra, 2009). Under the circumstances, seismic modeling is especially used and especially the use of seismic modeling to check the validity of interpretation in complex geological situations. Thus, seismic modeling is one of the most reliable way to investigate the validity of models representing different types of structural traps and to find the best fit with real seismic data (Lingrey, 1991; Morse et al., 1991; Alaei, 2006; Alaei and Petersen, 2007).

Geological models are constructed from lithological units containing one-dimensional (1D), two-dimensional (2D), or three-dimensional (3D) P, S-wave velocities and intensities. Geological ground models can include simple structures with horizontal and inclined plane decals, and also complex structures with discontinuities in the lateral and vertical directions. Just the same, hydrocarbon-containing geological structure models usually consist of the complexities of their structural and sedimentary conditions. Geological modeling of wave propagation in such environments and the actual terrain data with different advantages and disadvantages in comparison with ray tracing, discrete wave number, finite differences, finite elements, etc although many methods are employed, such as numerical, Finite Difference Method (FDM) can provide successful results in very complex environments. FDM, the most well-known method that provides a high-precision and complete numerical solution of partial differential equations, is widely used in seismic modeling studies FDM, the most well-known method that provides a high-precision and complete numerical solution of partial differential equations, is widely used in seismic modeling studies (Kelly et al., 1976; Virieux, 1986; Igel et al., 1995; Etgen and O'Brien, 2007; Bansal and Sen, 2008; Liu and Sen, 2009; Robertson et al., 2015; Talukdar and Behera, 2018). The process of wave propagation modeling with FDM started in parallel with the development of computer technologies in the 1960s, and the fact that it began to be used in wave propagation problems attracted a lot of attention (Alterman and Karal, 1968; Boore, 1970; Ottaviani, 1971). These methods provide a full-wave field solution and include all wave fields such as reflection, scattering, repetition and surface wave. So far, this method has solved many problems such as accuracy, stability and high-order operator arrangement for calculating numerical derivatives (Zhang and Zhang, 2007; Liu and Sen, 2009). For this reason, FDM has become the preferred modeling method for highly complex geological models, especially since it provides accurate amplitude information. Geiger and Daley (2003) used Acoustic Finite Difference (AFD) equations to simulate acoustic fields in variable density and velocity environments and numerical solutions of these equations were performed in MatLab (Matrix Laboratory) environment. In the solution, the researchers generated the first Marmousi data set using the 5-point central finite difference

algorithm. However, Nejati and Hashemi (2012) made zero-expansion seismic modeling of four different geological models with FDM in their study and to test the accuracy of the obtained section, they compared it with the interpreted sections. With this approach Many researchers who study complex geological and bedrock environments have adopted this method (Blake et al., 1999; Bohlen et al., 2003; Jinhua et al., 2009; Ahmadi et al., 2013). After the FDM, the scattering is brought to their real position by applying stack migration, and the real underground image is obtained correctly. Talukdar and Behere (2018) used the FDM to obtain the artificial shooting data of complex geological underground structures under uneven thick basaltic rocks, by applying Kirchhoff pre aggregation time migration and post aggregation depth migration to these model data, they successfully visualized the changes of inclined faults and lithology.

Seismic reflection modeling is usually carried out on the aggregation and / or migration profile (zero expansion profile) obtained after a series of data processing on the field from collected data. The most important reason for this is to save computing time and computer storage capacity, and also avoid intensive data processing to create zero extension segments (stacking and migration segments) starting from shot point data. However, with the developments leading to increasing computer speed, power and enhanced data processing software, and studies on shot point record modeling has been increasing in recent years. Considering that the seismic data are collected from the field with shot point receiver array in a certain order, modeling the shot point records, and then processing the shot point records to obtain stacking and / or migration profiles is a more realistic method of seismic data interpretation.

In this study, it was aimed to model the shot records of geological ground models (granite wash and normal fault trap) that may be complex hydrocarbon traps with FDM and to obtain zero-opening sections with data processing applications. To this end, Matlab based software developed by Youzwishen and Margrave (1999) is used to calculate manual artificial shooting data and arrange it according to the purpose. The calculated shot model data were processed with ProMax software and Kirchhoff time migration cross sections were obtained after stacking. The indication of hydrocarbon trap was examined on the zero expansion section thus obtained. In addition, the compatibility between reflection levels and geological model was also compared.

2. Material and Method

2.1. Acoustic Finite Difference Method (AFDM)

FDM is a numerical solution of differential wave equation used to calculate seismic wave propagation in any geological model. When this method is applied to acoustic wave equation, it is called AFDM, and when it is applied to elastic wave equation, it is called Elastic Finite Differences Method (EFDM). In this article, the acoustic equation given in Equation 1 is solved and modeled by FDM. The seismic wave field is calculated at each grid point shown in Figure 1 by providing an approximation with finite difference formulas that are derivatives of the wave equation and solving the resulting difference equation recursively. However, the number of (analytical) solutions of the wave equation is rare, and usually approximate numerical solutions are preferred for wave field modeling. Under this background, FDM has developed into a numerical technique in artificial seismic data calculation and has been widely used (Marfurt, 1984; Krebes and Lee, 1994; Manning and Margrave, 1998; Youzwishen and Margrave, 1999; Carcione et al., 2002; Margrave, 2003; Moczo et al., 2007).

AFDM provides the direct solution of the partial differential acoustic wave equation given by Equation 1 under certain initial and boundary conditions. The method provides for the possibility of obtaining the propagation of acoustic waves in complex geological models from simple to complex. The 2D scalar (numerical) wave equation (x, z) of the method can be written in Cartesian (perpendicular) coordinates as follows (Lines et al., 1999).

$$\frac{\partial^2 \emptyset(x,z,t)}{\partial t^2} = v^2(x,z)\nabla^2 \emptyset(x,z,t) \quad (1)$$

In Equation 1, x and z are the horizontal and vertical distances (meter-m), respectively, on the grid network, t is two-way travel times (second-s), $\nabla^2$is the velocity of the medium in which the wave propagates (meters/second-m/s), Laplace; $\emptyset(x, z, t)$ and wave

potential or represents the acoustic wave field. The Laplace processor 2B ∇^2 is given by the Equation 2.

$$\nabla^2\emptyset = \frac{\partial^2\emptyset}{\partial x^2} + \frac{\partial^2\emptyset}{\partial z^2} \quad (2)$$

The Laplace operator can be calculated approximately using second-and fourth-degree derivative approximations with central difference operators. These approaches are using 5 and 9 grid points, respectively. In this study, Equation 3, a 9 grid-point fourth-degree Laplace operator approximation, was used by Youzwishen and Margrave (1999) because it provides accuracy and broadband solution, although it increases the calculation time.

$$\nabla^2\emptyset = \frac{-\emptyset(x+2,z)+16\emptyset(x+1,z)-30\emptyset(x,z)+16\emptyset(x-1,z)-\emptyset(x-2,z)}{12\Delta x^2} + \frac{-\emptyset(x,z+2)+16\emptyset(x,z+1)-30\emptyset(x,z)+16\emptyset(x,z-1)-\emptyset(x,z-2)}{12\Delta z^2} \quad (3)$$

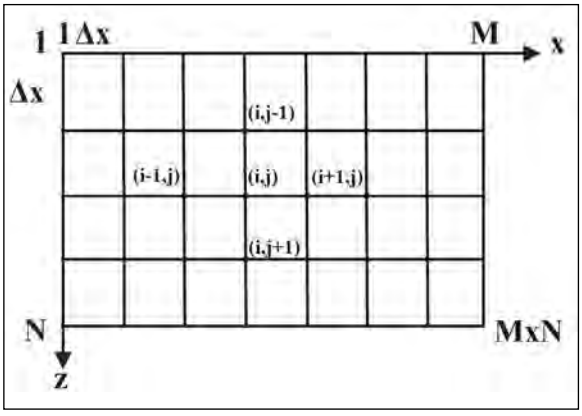

Figure 1- Grid mesh suitable for central finite difference derivative approach. Here, Δx: the grid spacing in the x direction, M: the number of grids in the x direction, Δz: grid spacing in the z direction, N: number of grids in the z direction, i: coordinate x and j: it represents the z coordinate.

As shown in Figure 1, any point (i, j) on the grid network is called a network point. According to this point, the points (i +1, j) and (i-1, j) are located to the right and left, while the points (i, j +1) and (i, j-1) represent the points located above and below. If the network used is a regular network, network points can be easily expressed. For example, for a network such as in Figure 1, the network points are as follows

$x_i = i.\Delta x_i$ i = 0,1,2,……, M

$z_i = j.\Delta z_i$ j = 0,1,2,……., N

In such solutions, if an insufficient number of grid points per wavelength is used, an artificial grid dispersion (scattering) is formed (Holberg, 1987), and this is an important numerical problem. The practical solution to overcome this problem is to choose the grid spacing as small as possible. However, this may increase the calculation time (Youzwishen and Margrave, 1999). In practice, the grid ranges can be different, as they will be taken equal horizontally and vertically (Δx=Δz). However, the stability condition for the fourth-degree approximation, which includes the ambient speed, sampling time, and grid spacing, is as shown in Equation 4.

$$\frac{V_{max}\Delta t}{\Delta x} \leq \sqrt{\frac{3}{8}} \quad (4)$$

Here; V_{max} is the maximum velocity (meters/second-m/s), Δt is the temporal sampling interval (sec-s), and Δx is the spatial sampling interval (meter-m) (Δx=Δz). Calculation of the time derivative on the left side of Equation 1 using the quadratic central differences approach is given in Equation 5.

$$\frac{\partial^2\emptyset}{\partial t^2} = \frac{\emptyset(t+\Delta t)-2\emptyset(t)+\emptyset(t-\Delta t)}{\Delta t^2} \quad (5)$$

If Equations 3 and 5 are substituted into the numerical wave equation in Equation 1, the wave field at time t+Δt can be solved iteratively in Equation 6 given below.

$$\emptyset(x,z,t+\Delta t) \approx (2+\Delta t^2 V(x,z)^2\nabla^2)\emptyset(x,z,t) - \emptyset(x,z,t-\Delta t) \quad (6)$$

In Equation 6, ϕ is the P-wave potential. Equation 6 shows that if the wave field is known at time t and t-Δt, the wave field at time t+Δt can be calculated. This process is called time stepping and snapshot of the wave propagation at each time. Paying close attention, the wave field is simply removed at time t-Δt, while the Laplace processor is applied to the wave field at time T. In order for Equation 6 to be used in each time step, it must be defined in advance at times t=0 and t=Δt. This usually requires simply defining a source function or wavelet. In this study, a zero-phase Ricker waveguide was used as the source.

3. Geological Models Used

In the conducted researches, many types of traps have been found, which are formed in the form of structural, stratigraphic and their composition. A classification of all three types of traps was made by Hyne (1984). Of these, a stratigraphic (granite

wash) and a structural (normal fault) trap sample were selected, and modeling of shot records and data processing were performed using by FDM. The ground models of the selected trap types are multilayer structures and contain multiple topographic interfaces.

The information about the source function, spatial and temporal calculation parameters used in granite wash and normal fault trap modeling is given in Table 1 below. Reflective decals for modeling were digitized and depth, distance and velocity information were introduced into the modeling software. Attention has been paid to the fact that ground models represent real complex environments. The change in the density values of the layers was taken as constant ($p=2.0$ g/cm^3), since it was very small compared to the seismic wave velocity.

Table 1- Parameters used for modelling.

Granite Wash/Normal Fault Trap Model	
Profile length (m)	2000
Maximum depth (m)	1000
Receiver interval (m)	10
Shot interval (m)	40
Number of shots	46/25
Number of receivers	201
Max. velocity (m/s)	4000
Min. velocity (m/s)	2000
Max. offset (m)	2000
Min. offset (m)	100
Calculation time step (ms)	0.02
Sampling time (ms)	4
Record lenght (ms)	1000
Minimum Phase Ricker Source Wavelet (Hz)	30

3.1. Granit Wash Trap Model

The Granite Wash trap model, which is a type of stratigraphic trap, has been the target of petroleum research and development studies along with the discovery of oil (Sproule, 1956). A significant amount of hydrocarbons in Granite Wash traps accumulates in low-permeable traps, unlike conventional medium-high-permeable oil traps. These hydrocarbon sources are called unconventional sources and according to the classification of Hyne (1984), they are known as non-traditional stratigraphic tight gas-sand traps. The traps of this type shown in Figure 2 are sandstones associated with decomposed granite rock and are deep structures (Dec et al., 1996). Underground geological structures containing such hydrocarbon traps are quite complex and do not have similar characteristics to, so it can be quite difficult to identify and define them by seismic surveys.

Figure 2 shows a model of a granite wash trap in a multilayer medium. The model underlying the granite rocks cover to 2700 m/s velocity unit (porous and permeable sandstone, limestone, dolomite, or fractured rock may be) for the peak point on each side from the velocity of 1200 m/s on both sides from the apex is designed to contain (turquoise blue color). However, these trap velocities 2650 m/s (between brown 70-850 m units), 2500 m/s (light color open between 500-600 m units) and 2580 m/s (600-750 m and yellow colored between 400-500 units; non-permeable marl, shale, salt, or mikritik limestone) rocks that covered and locked away. Other units reached the surface by deposited conformably in accordance with the overburden rock (the yellow-colored unit between 400-500 m) with an anticline structure towards the surface. The velocity of the surface layer is 1000 m/s, thickness is 150 m on the left side, 50 m in the middle and 125 m on the right side. In addition, source receiver intervals are shown on veolocity-depth models.

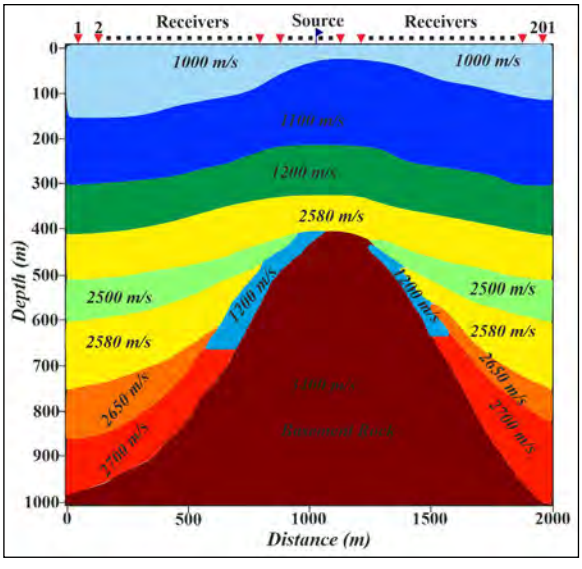

Figure 2- Granite wash trap model. 201 receivers were used. The source receiver (red triangles) layout is shown, with the shot position (dark blue flag) right in the middle of the line.

Examples of 46 shot records calculated according to the parameters in Table 1 for the geological model in Figure 2 are (1., 10., 19., 28., 37., and 46th.). Automatic Gain Control (OGC) is applied and shown in Figure 3. The main reflections can be identified on the shot records, but the reflections from under and above the trap are quite difficult to recognize due to interference. This can be attributed to reasons such as the trap structure is not thick enough, the wavelet used is low frequency, and the grid spacing of the finite difference scheme is wide. Since the main goal of this study is to determine the trap structure by processing data of this complexity, no further improvement has been made in modeling.

3.2. Normal Fault Trap Model

Normal fault type traps are structural traps that are curved, formed as a result of the intersection of two faults or the intersection of many faults. Normal fault trap formations occur when the blocks of the fault move in such a way as to prevent the migration of oil. For example, an impermeable and sealed formation on one side of the fault may move in the opposite direction to the oil-field formation on the other side; In this case, the impermeable layer blocks the flow of oil and an oil pool forms against the fault (Biddle and Wielchowsky, 1994). An exemplary normal fault trap is shown in Figure 4. In this model, oil is placed inside the trap structures (1500 m/sec - turquoise blue color) and covered with overburden rock (2580 m/sec - light green color). However, source receiver intervals are shown on velocity-depth models. In general, although frequent shots provide more common midpoint reflection (folding), it has been observed that frequent interval shots in areas close to discontinuity zones also increase the scattering intensity and deteriorate

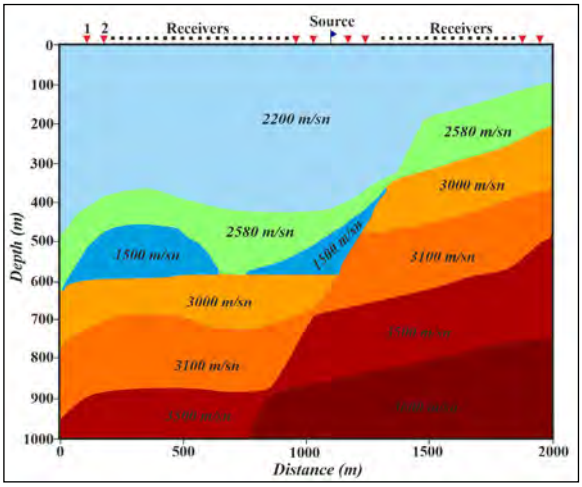

Figure 4- Normal fault trap model 201 receivers were used. The source receiver (red triangles) layout is shown, with the shot position (dark blue flag) right in the middle of the line.

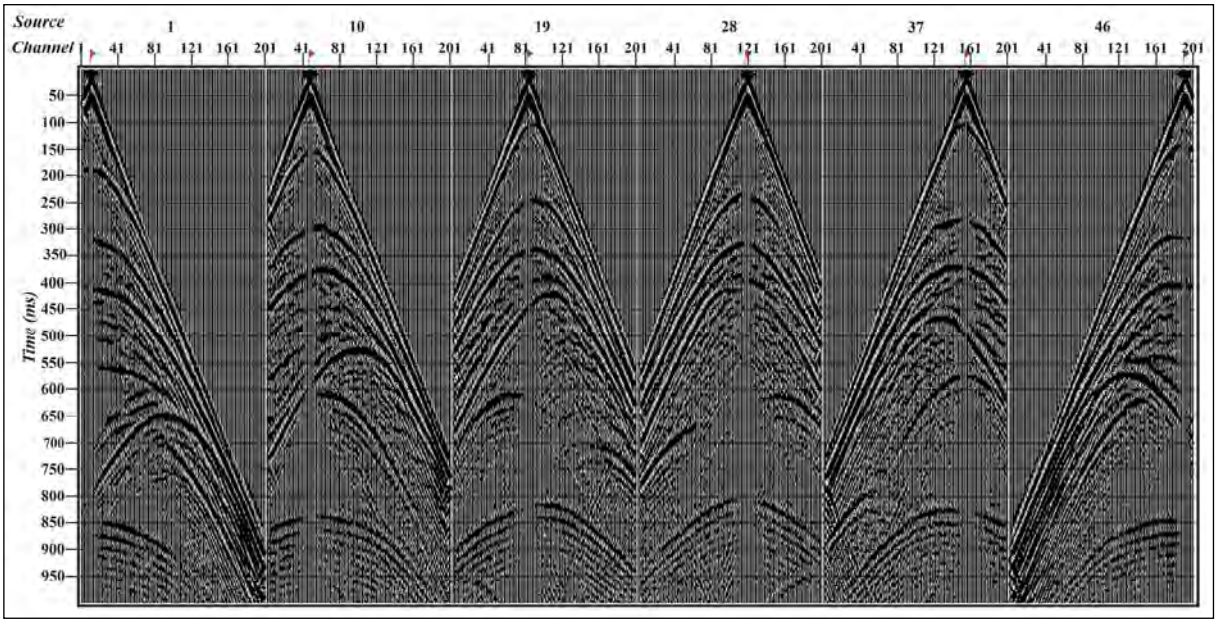

Figure 3- Raw shot groups loaded with 1st, 10th, 19th, 28th, 37th and 46th geometry calculated for the granite wash model. The red flag indicates the seismic source (shot point).

the data quality. For this reason, the number of throws has been reduced to 25, unlike granite wash modeling in the modeling of seismic throw records of a normal fault. Therefore, the number of throws has been reduced to 25, unlike granite wash modeling in the modeling of seismic throw records of a normal fault. Examples of 25 shot records calculated for the normal fault trap model in Figure 4 are presented in Figure 5.

4. Data Processing

The processing of the calculated shot records was carried out using ProMax software.

In this context, the data-processing workflow aimed at obtaining a zero-offset seismic cross-section by suppressing the noise contained in the shot recordings and regulating the reflections, as well as strengthening

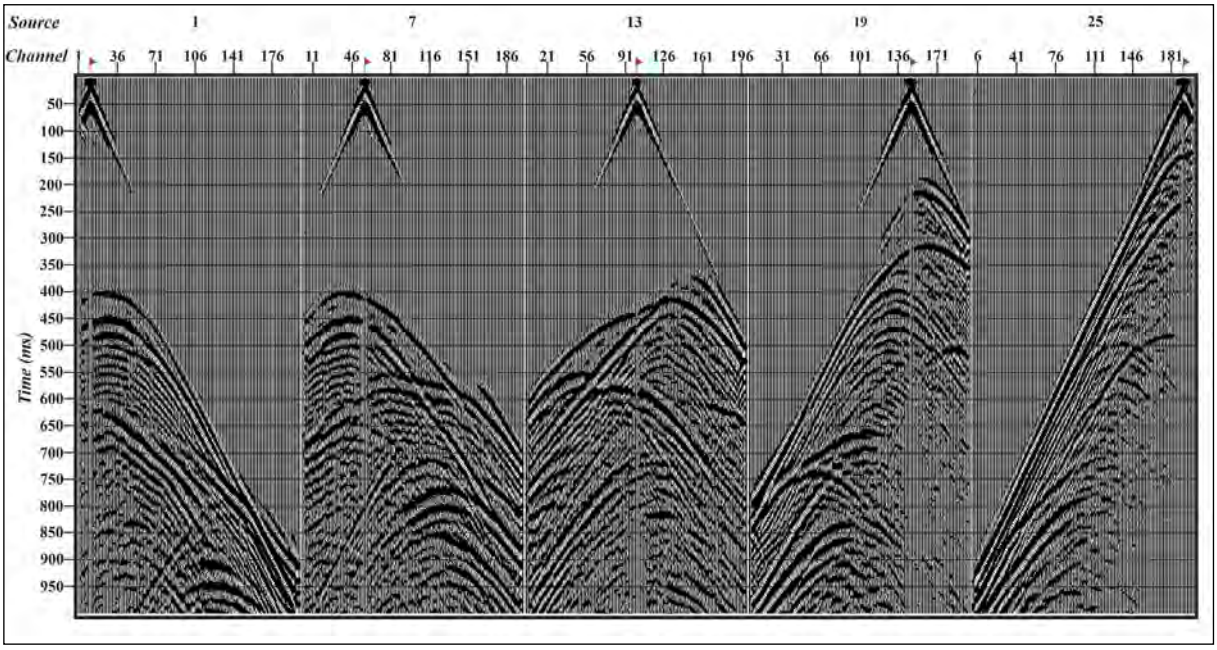

Figure 5- Raw shot groups loaded with 1st, 7th, 13th, 19th and 25th geometry for the normal fault trap model. The red flag indicates the seismic source (shot point).

Table 2- Processes that can be implemented in the data-processing workflow and the reasons for their implementation.

Applied Process	Reasons for Application
Data Loading	Data Reading
Geometry Set Up	Introducing Source and Receiver Positions to the Program
Top Mute	Muting Arrival of Direct Waves
Bandpass Filter (Ormsby Filter)	Filtering Low and High Frequency Noises
Predictive Deconvolution	Suppressing Multiple Reflections/Increasing Temporal Resolution
Bandpass Filter (Ormsby Filter)	Attenuation of High Frequency Noises Strengthened After Deconvolution
Common Midpoint (CMP) Sorting	Creating Common Midpoint Trace Gather
Velocity Analysis	Obtaining RMS (Root Mean Square) Velocity Functions at Each CMP Point for The Best Quality Stacking.
Normal Moveout (NMO) Correction	Moving Pre-Stacking Reflections to Zero Offset Time
Stacking	Overlap of NMO Applied CMP Data
Kirchhoff Time Migration	Elimination of Scattering, Moving Reflections from Curved Interfaces to their Correct Geometric Location
Depth Conversion	Converting Time Axis to Depth
Imaging - Automatic Gain Control (AGC) has been implemented.	Equivalent Amplitudes for Display Purposes

the primary reflections from the reflective surfaces, is given in Table 2. Primary reflections are extremely affected both by scattering and by interference from leaking edge reflections despite the absorbing condition. Therefore, the data-processing stages were applied by selecting the most appropriate parameters.

4.1. Processing Granite Wash Artificial Data

The 46 synthetic data obtained in the granite wash modeling were processed according to the workflow specified in Table 2. After reading the data and the geometric information was defined, the first arrival wave fields (direct ingoing waves and refraction waves) were tried to be cleaned by cutting from the top. However, as can be seen from the shot records in Figure 3, these initial arrivals are quite intertwined with shallow reflections. Therefore, deleting the first destinations from such data requires a lot of attention, otherwise shallow reflections can be damaged. If these initial arrivals are not sufficiently removed, they prevent the focus of speed contours at shallow levels, especially in speed analysis, and can create quite a problem.

However, although the model shot data does not contain low-frequency surface waves and high-frequency noise, processing noise (artifact) may occur due to data modeling. A band-pass filter with cut-off frequencies of [10 16 60 80] Hz was applied to filter these noises and preserve the useful spectral band of the data (Figure 6). The cut-off frequencies were determined by examining the spectral content of the data and determining which frequency range the useful spectral information was. For this purpose, the pre-band pass filter (Figures 7a and 7b) and post-filter (Figures 7c and 7d) of shot recording No. 1 were compared. The determined filter cut-off frequencies are shown on the Fourier average amplitude spectrum in Figure 7b. Frankly small-amplitude high-frequency noise in the post-filter shot data (Figure 7c) is attenuated, and therefore the signal-to-noise ratio of the data in general increases, and in particular the reflection are strengthened (Figure 7b).

After filtering the shot records, a predictive deconvolution with a first estimation length of 6 ms and an operator length of 80 ms was applied to dampen the repeated reflections (Figure 8). Since the noise amplitudes especially in the high frequency limits outside the useful band of the data increase after the predictive deconvolution, a band pass filter was applied to the data at cut-off frequencies of [8,10,70,90] Hz after deconvolution (Figures 9a and 9b). Thus, with the application of deconvolution (Figures 9c and 9d), the multiples were weakened and the vertical

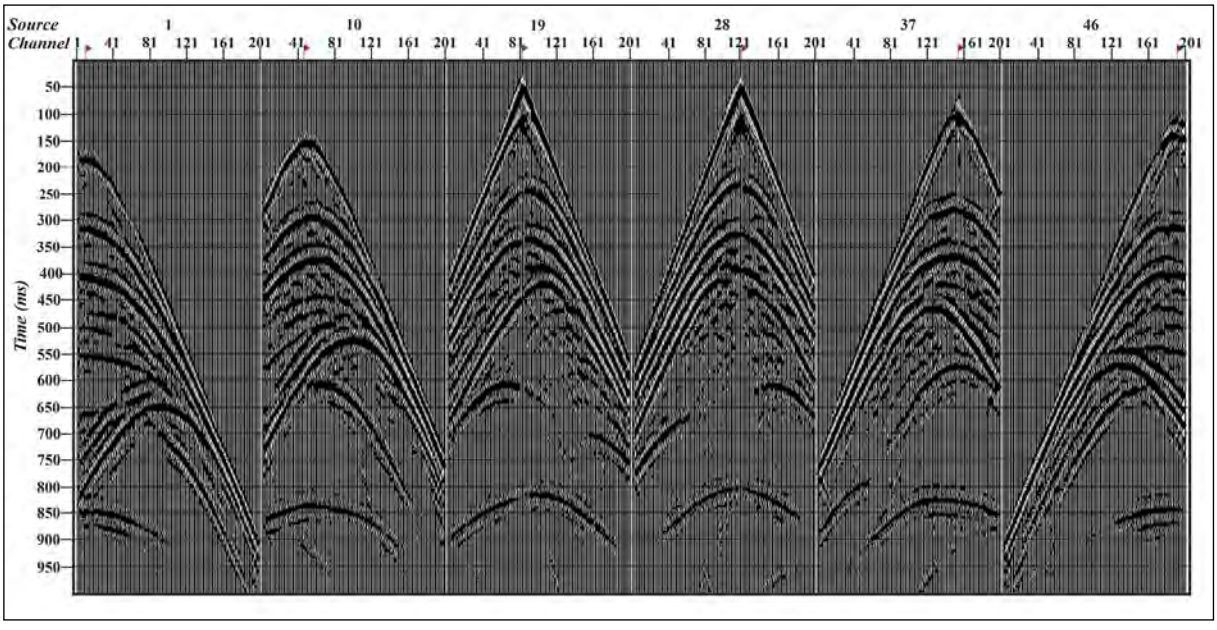

Figure 6- The 1st, 10th, 19th, 28th, 37th and 46th shot groups in which the top cutting process and then band pass filter processes are applied to discard the first arrivals of the granite wash model. The red flag indicates the seismic source (shot point).

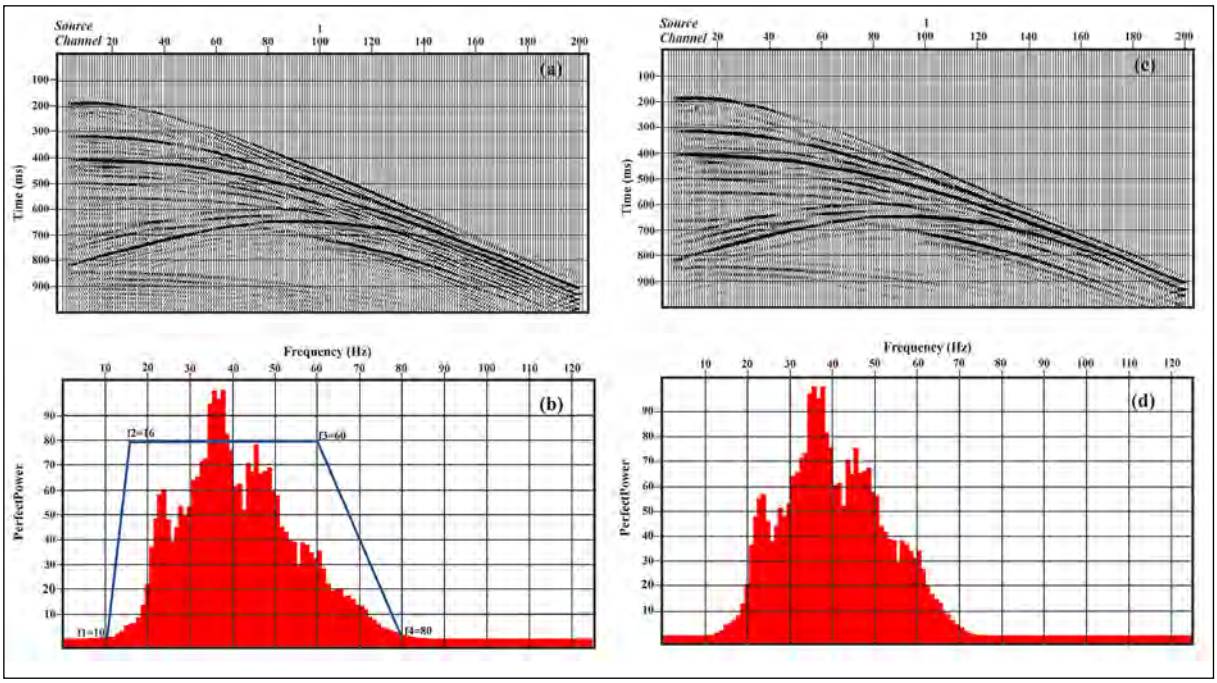

Figure 7- Comparison of the 1st shot recording from granite wash modeling before and after band pass filter. a), b) unfiltered and filtered, and c), d) shot records and Fourier mean amplitude spectra, respectively.

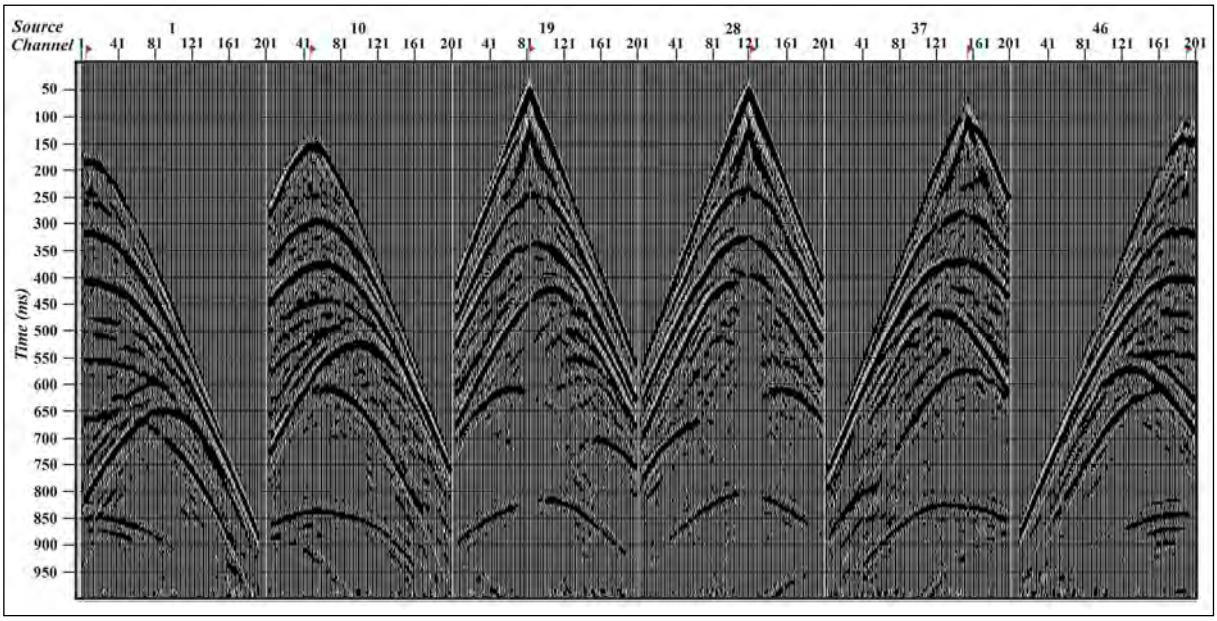

Figure 8- Predictive deconvolution results for the 1st, 10th, 19th, 28th, 37th and 46th artificial shot groups passed through the preliminary data processing stages.

resolution was increased. However, with the help of a band-pass filter, noise is reduced, which is amplified in the high-frequency zone and exerts a distorting effect. In Figure 10, velocity spectrums plots with and without predictive deconvolution applied (left) and applied (right) are given. The velocity spectrum calculation was performed every 20 CMP. Since deep reflections become especially noticeable after deconvolution and their amplitude becomes stronger, the corresponding amplitudes of the speed spectrum

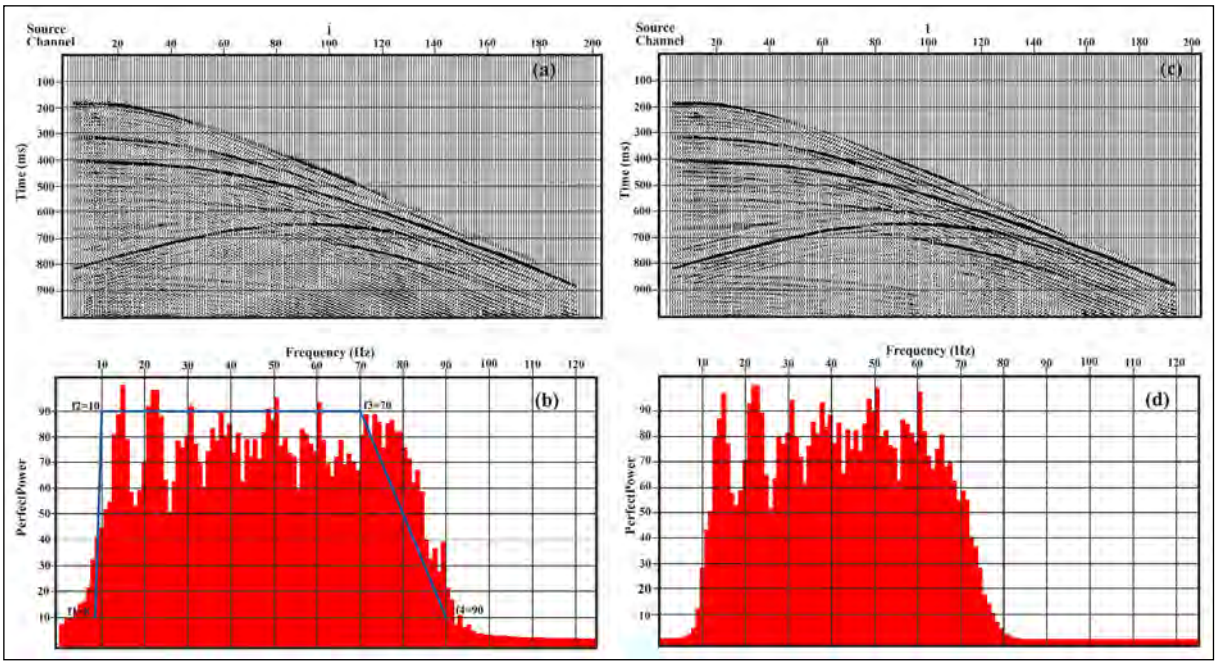

Figure 9- After the predictive deconvolution of the 1st shot recording from the granite wash modeling, the band-pass filter; a) unapplied, b) applied and, c), d) shot records and the amplitude spectra to the Fourier medium.

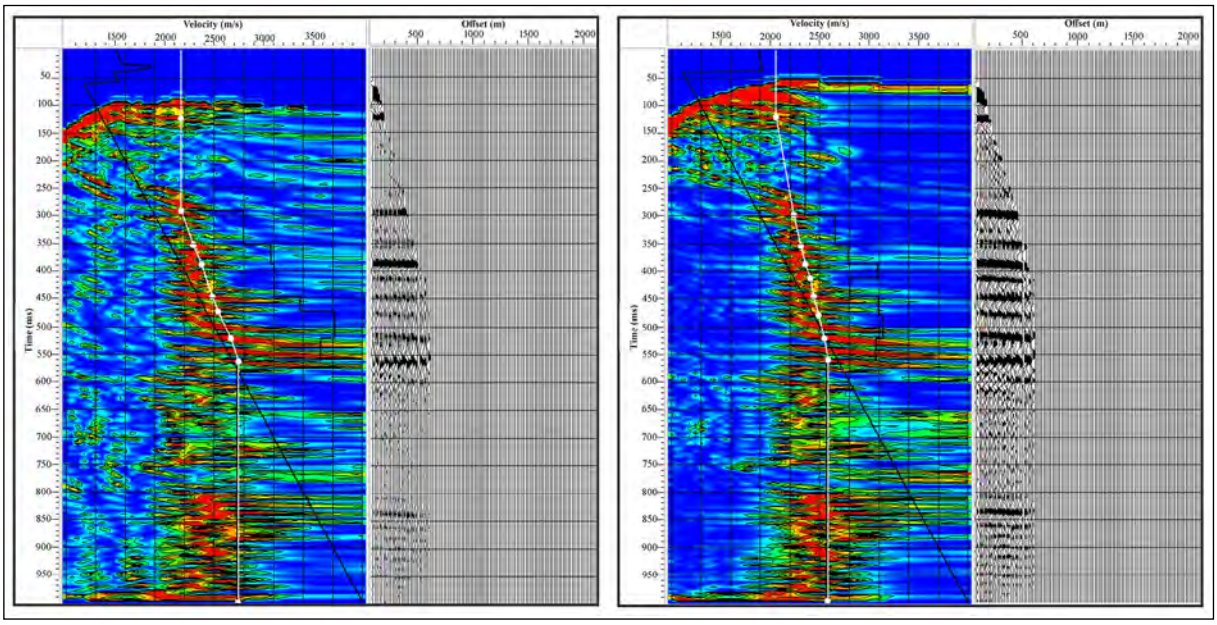

Figure 10- 340. velocity spectrum application on CMP group; a) velocity spectrum images with no predictive deconvolution and, b) applied. The white solid line shows the marked RMS.

are also strengthened at that rate, and therefore the velocity estimation is also made more confidently.

When we look at the CMP section after deconvolution (Figure 10b), it is noteworthy that many reflections in the 300-600 ms range can be seen differently than those in the CMP cross section in Figure 10a, and especially the presence of reflections in the range of 800-1000 ms. This situation can actually be traced in the velocity spectrum as well. While the velocity picking (white line in Figures 10a and b) was similar on both spectra up to 550 ms, after

that, in the post-deconvolution velocity spectrum, the contours were shifted to higher veolocities. Therefore, the predictive deconvolution provided both an increase in the stacking quality and a more accurate determination of the velocity field. Thus, velocity estimates were improved by the deconvolution process, and the determined RMS velocities were applied to the CMP groups, and the NMO corrected CMP groups were obtained. At this stage, the rate function of each CMP is combined to create a speed field for the migration process that will be applied at the next stage. However, in order to remove the stress fields originating from the NMO from the data, a 60% NMO top-cutting process was applied and a masonry section was obtained.

4.2. Processing of Normal Fault Trap Model Data

In normal fault trap modeling, 25 synthetic shot records were obtained and processed according to the workflow specified in Table 2. First, primarily waves were tried to be cleaned by cutting from the top (Figure 11). In the shots on the upper block side of the fault (19 in Figure 5 and 25th. 3) since the reflectors are close to the surface, the reflections are highly interferential with the first arrivals, therefore, direct arrivals could not be completely deleted in these shots, especially in the sections after 100ms. At the next stage, a band-pass filter with cut-off frequencies of [12, 18, 55, 70] Hz was applied to suppress low-and high-frequency process noise (Figure 11). The results of the time and spectral window of shot data 1 as an example for comparison before and after the filter are shown in Figure 12. According to the Fourier average amplitude spectrum of the input data in Figure 12a (Figure 12b), the useful spectral band of the data is between 18-55 Hz. Accordingly, the filter cut-off frequencies are set to [12 18 55 70] Hz so as not to change this part of the data and are shown in the figure (with a blue line). The time section of the filter result is shown in Figure 12c and the Fourier average amplitude spectrum is shown in Figure 12d. Although both time sections and spectral results do not show a significant difference in comparison, in fact, especially high-frequency small-amplitude vibrations outside the band (see it can be observed that it decays from 500 to 600 ms).

Figure 13 shows the result of applying predictive deconvolution, the operator length of which is 80.0 ms and the prediction distance is 7 ms, to the shot data applied during the preliminary data processing stages. Thus, by attenuating the multiple reflections that are likely to occur, a contribution was made to the velocity

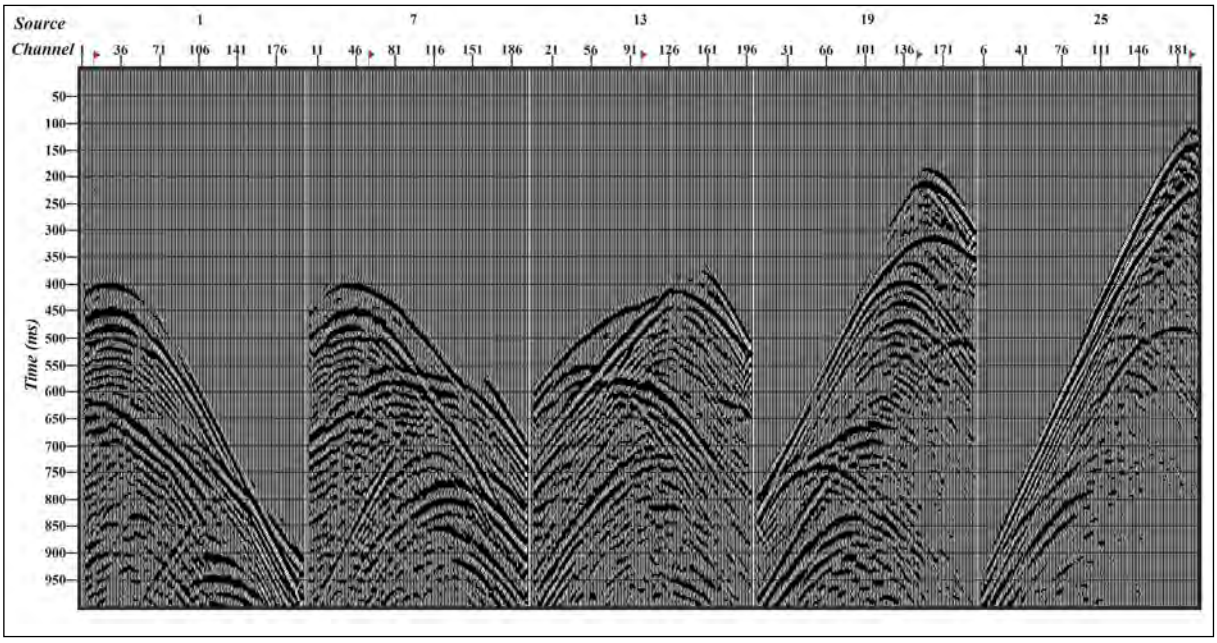

Figure 11- The 1st, 7th, 13th, 19th and 25th shot groups, in which the top shear process is applied to discard the first arrivals from the artificial data of the normal fault trap model, and the band pass filter processes are applied in the following stage. The red flag symbol represents the seismic source (shot point).

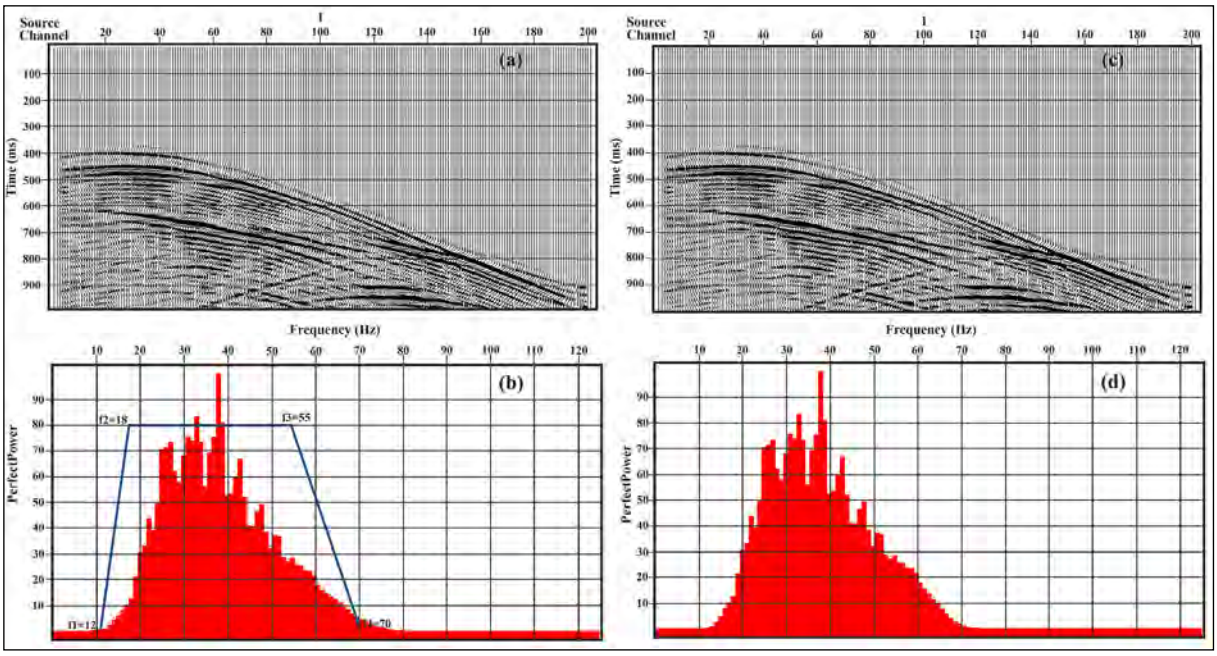

Figure 12- Comparison of the 1st shot recording before and after the bandpass filter; a), b) unfiltered and c), d) filtered shot records and Fourier mean amplitude spectra, respectively.

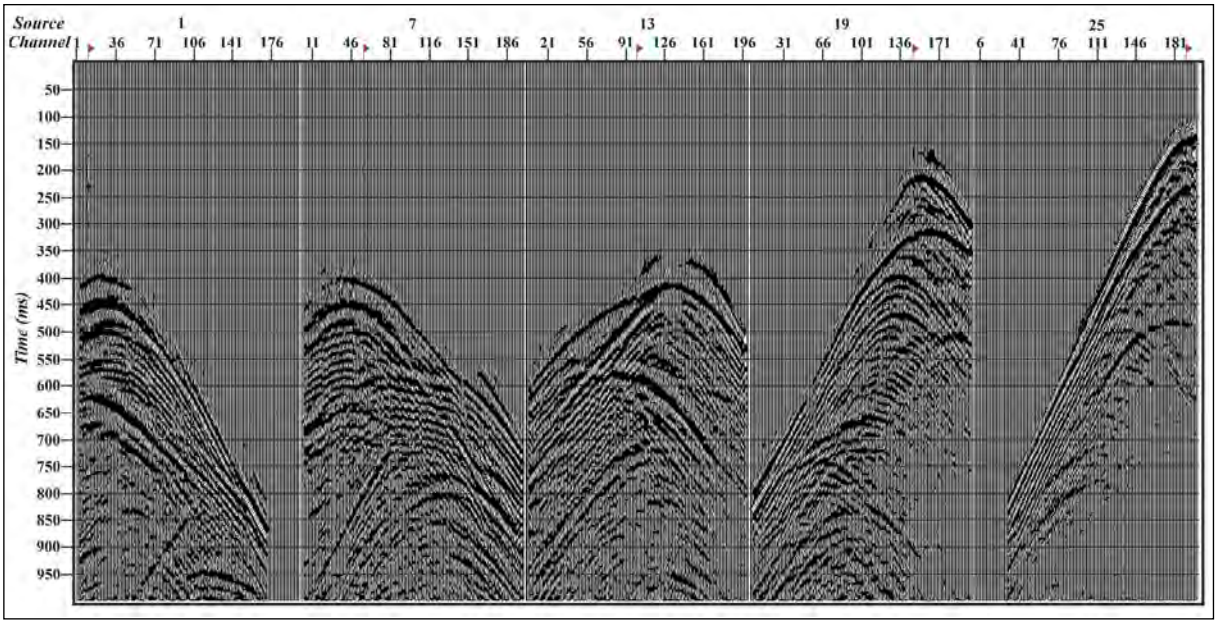

Figure 13- Predictive deconvolution application with operator length of 80.0 ms and prediction distance of 7 ms for the 1st, 7th, 13th, 19th and 25th artificial shot groups passed through the preliminary data processing stages.

estimation and recognition of primary reflections in the velocity spectrum.

In the next processing step, the data was transferred from the shooting environment to the common midpoint environment by the sorting process. At this stage, it was preferred to use the expression common midpoint (CMP) instead of the common depth point (CDP) for the trace families that will be formed by the traces that are considered to be reflected from the common point. Because the common point traces are made according to the midpoint of the source-receiver

distance on the surface by sorting process. Also, if the reflector is inclined, the common depth point rule does not occur, and reflections occur from the upslope. Thus, velocity analysis was applied to these groups by creating CMP trace groups and 330 at about 1750 m of the normal fault trap model, the CMP trace group is shown in Figure 14. The resulting image is actually an input-output energy ratio-based velocity spectrum (semblance) process, and the most accurate velocity selection (RMS values) over this spectrum is performed visually interactively and the stacking process is performed. The correct choice of speed will ensure the success of the NMO. However, due to the complexity of the data, the stressed areas from NMO were deleted prior to stacking (Figure 14 - right). By combining the obtained velocity functions for each CMP group, the velocity field is obtained, and this velocity field was used in the post-accretion migration stage. A post-accretion Kirchhoff time migration was applied to the obtained accretion data and the time axis of the cross-section was converted to depth using RMS velocities to compare the main reflection levels in the obtained migration cross section. AGC (automatic gain control) was applied by selecting the window length up to a quarter (1/4) of the data recording time for display purposes.

5. Findings

The main purpose of the study was to compare the compatibility of the initial geological model with the migration cross section that will be obtained by calculating the artificial seismic shot records of a complex geological structure containing hydrocarbons and processing these shots with data processing applications, so the findings are given in this context. For the granite wash model ground structure, a Kirchhoff time migration was applied to the stack section produced by the processing steps in Table 2, and then the migration cross section in depth obtained by applying a depth conversion is also given in

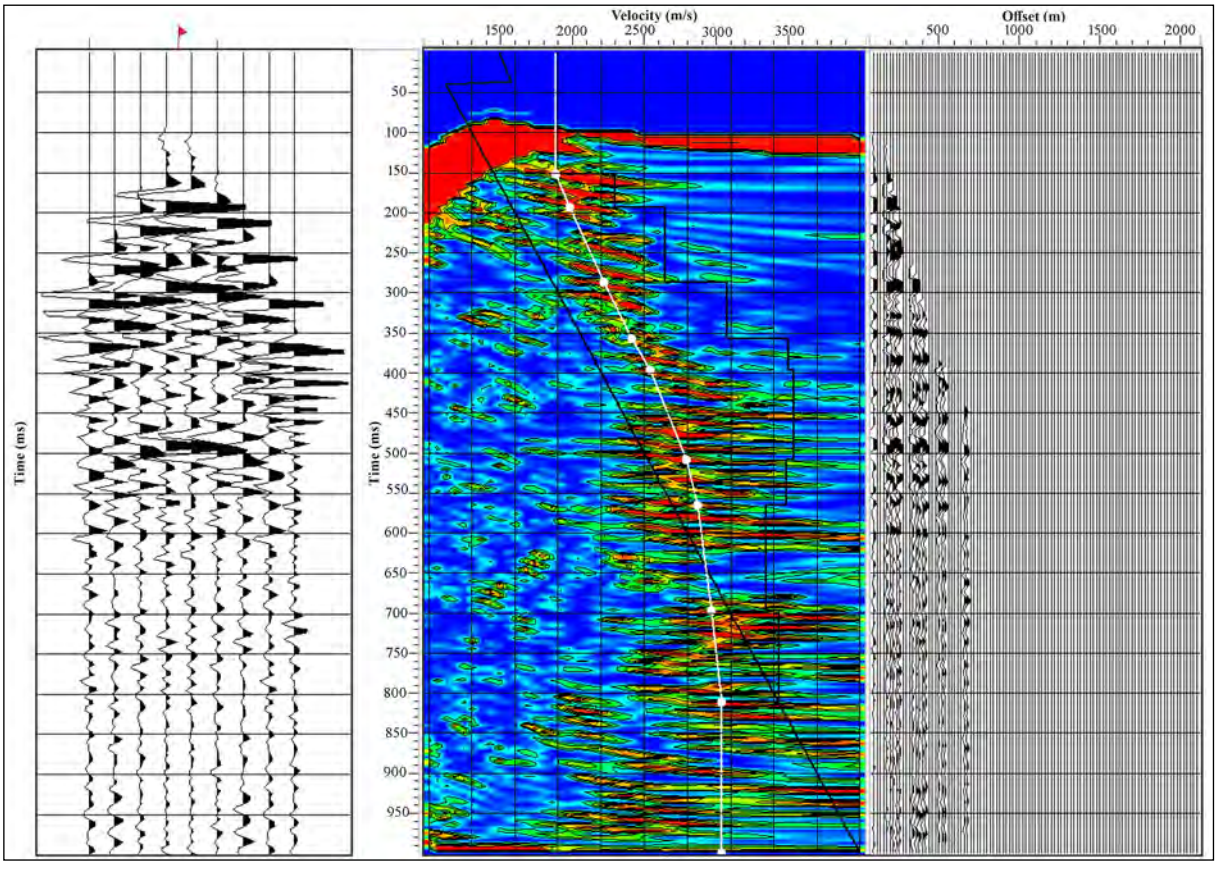

Figure 14- Velocity analysis application on the 330 - CMP group after deconvolution. 330 - CMP traces (left), velocity spectrum image (middle), and view of the CMP group with NMO correction applied (right).

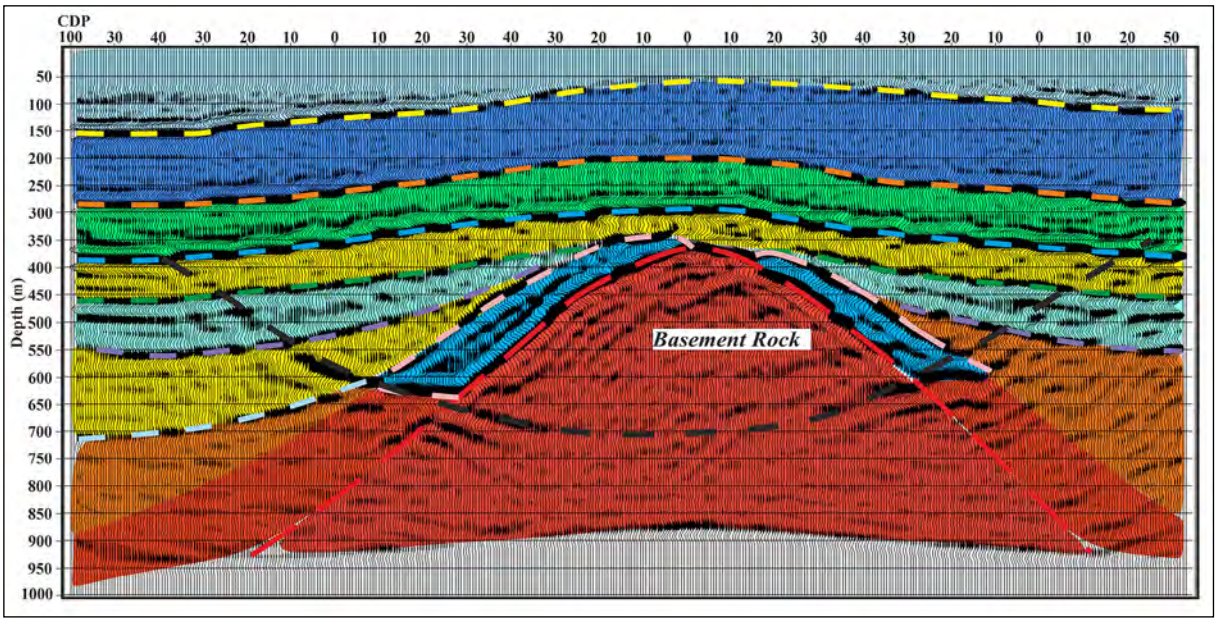

Figure 15- Migration section obtained by applying Kirchhoff time migration and seismic depth conversion after stacking. The main layers are indicated by dashed lines on the section.

Figure 15. The migration step is a process in which scattering and reflections are moved to their real places and almost a real ground model is produced when applied with the correct velocity values and with the appropriate technique. The reflected layers on the migration cross section given in Figure 15 are defined and shown with dashed lines. It can be seen that there is generally a good similarity between the seismic migration section and the ground model in Figure 2. When the migration cross section in Figure 15 was examined, the upper reflectors between 150-400 m depth were continuous, and the granite wash structure between 450 m and 1000 m depth and the trap structures on the right and left sides of the granite wash structure between 450-650 m depth could be determined positional. When evaluated in this context, it was seen that the initial geological model containing the interpreted section and the hydrocarbon trap was in very good harmony. However, the thinning of the thickness of the units towards the top of the granite creates a problem of both vertical and lateral separation in these parts. From a different view point, although there is no negative effect on the interpretation, the event (black dashed line) seen with a convex hyperbolic shape at the bottom of the section has been evaluated as an excessive migration error (high velocity condition) that is often encountered in relation to the velocities used in the migration process. However, the fact that the boundaries of the geometrically closed structure could be determined almost immediately showed the success of data processing applications and the suitability of the processing parameters used.

Similarly, the migration cross-section obtained by processing the shot data calculated for the normal fault trap model according to the workflow in Table 2 is shown in Figure 16. In general, the migration cross section obtained with the initial ground model has a good relationship each other and the trap structures and layers are able to determined. However, migration effects have been observed along the fault plane in relation to the fact that the normal fault trap model has produced more scattering (in circles with yellow dots). In addition, the continuity of reflections is interrupted due to the fault in general. In particular, the reflections under the traps located in the lower block of the fault have both their amplitude weakened and the reflection continuity from the upper block has been significantly interrupted. Therefore, whether the reflected levels have a lateral continuity or not may require an interpretation related to the interpreter's experience.

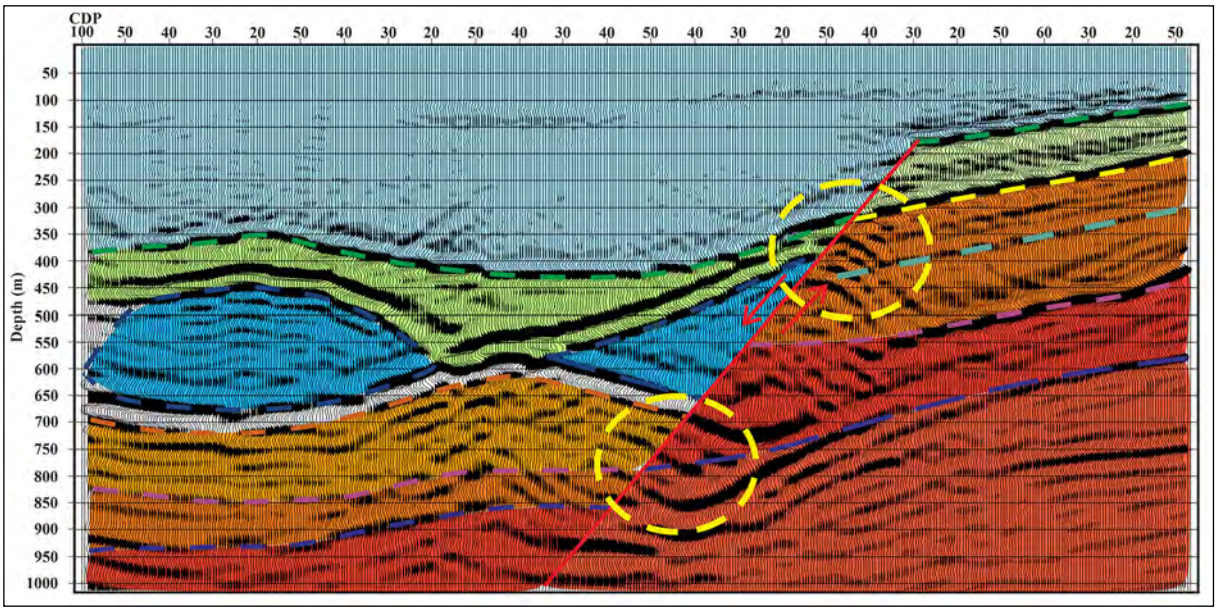

Figure 16- Migration section obtained by applying Kirchhoff time migration and depth conversion after stacking. The main levels are indicated on the section.

6. Results

In this article, the seismic reflection reactions of the firing medium of two hydrocarbon traps of the granite wash and normal fault trap types formed in complex geological environments were calculated using the FDM technique, which provides a full-wave field solution. By processing the shot data, the initial ground model and hydrocarbon traps were tried to be displayed. According to modeling studies, i) in the search of thinner and shorter hydrocarbon traps, such as in the granite wash structure, more frequent intermittent shots should be done for reflection record, which will further sample the trap, ii) on the contrary, if the traps associated with faults with a high potential for producing scattering are to be uncovered, a smaller number of shots should be done to reduce the scattering intensity caused to discontinuities. It has been shown that in this way, data collection will be more useful in improving the success of data processing applications and therefore, the image quality of migration sections. However, although artificial data has been used, as is often encountered in the processes of processing real land data, the negative effects of artificial processing noise (in modeling and migration application) (misleading reflection level, reflection migration, reflection distortion, etc.) have been observed on migration cross sections.

However, with the help of data processing applications, the approximate real spatial positions of the layered structure, reflective topographies and trap structures in the initial ground model could be determined on the migration sections obtained in accordance with the obtained migration sections. Therefore, it is proved that the calculation and processing of artificial seismic data on the shot domain for complex underground geological models contributes to the interpretation process. Most especially this modeling approach will be extremely valuable when the interpreter makes estimates of the subsurface geological model and compares the obtained artificial seismic data with seismic data recorded on the terrain. Thus, it is believed that pre-stack shot data modeling, rather than post-stack (zero distance), especially before a decarbon exploration field study, will make a positive contribution to the development of data processing stages and testing of seismic cross-sectio interpretations.

Acknowledgements

The authors, one of the judges, contributed to the development of the article with his constructive criticism and suggestions, Prof. Dr. Derman DONDURUR, Prof. Dr. Serkan ÖZTÜRK and another referee who did not reveal his name. In this

study, Matlab code for Finite Difference Modeling of CREWES project is used for free access http://www.crewes.ucalgary.ca/).In order to process the calculated shot records, the Department of Geophysical Engineering of Karadeniz University of technology carried out academic research and use. Promax software of Landmark Graphics Co. donated by Halliburton company is used.

References

Ahmadi, O., Juhlin, C., Malehmir, A., Munck, M. 2013. High-resolution 2D seismic imaging and forward modeling of a polymetallic sulfide deposit at Garpenberg, Central Sweden. Geophysics 78, 339–350.

Alaei, B. 2006. Seismic Depth Imaging of Complex Structures, an example from Zagros fold thrust belt, Iran. PhD Thesis, University of Bergen.

Alaei, B., Petersen, S. A. 2007. Geological modeling and finite difference forward realization of a regional section from the Zagros fold-and-thrust belt. Petroleum Geoscience 13, 241–251.

Alterman, Z., Karal, F. C. 1968. Propagation of elastic waves in layered media by finite- difference methods. Bulletin of the Seismological Society of America 58, 367-398.

Aminzadeh, F., Brac, J., Kunz, T. 1997. SEG/EAGE 3D Modeling Series No 1. Society of Exploration Geophysicists and the European Association of Geoscientists and Engineers.

Bansal, R., Sen, M. K. 2008. Finite-difference modelling of S-wave splitting in anisotropic media. Geophysical Prospecting 56, 293-312.

Biddle, K. T., Wielchowsky, C. C. 1994. Hydrocarbon Traps, Magoon, L. B., Dow, W. G. (Eds.). The Petroleum system- from source to traps. AAPG Memoir 60, 217-234.

Blake, B., Figueroa, D., Manceda, R., Oller J., Hofland, G. 1999. 3D forward ray trace seismic modeling of strike lines in complex geology. SEG Technical Program Expanded Abstracts, 1871-1874.

Bohlen, T., Müller, C. F., Milkereit, B. 2003. Elastic wave scattering from massive sulfide orebodies: on the role of composition and shape. In: Eaton, D., Milkereit, B., Salisbury, M. (Ed.), Hardrock Seismic Exploration, SEG Developments in Geophysics Series 10.

Boore, D. M. 1970. Finite-difference solutions to the equations of elastic wave propagation, with application to Love waves over dipping interfaces. PhD Thesis, M.I.T., Claerbout, 1985.

Carcione, J. M., Herman, G. C., Kroode, A. P. E. 2002. Seismic modeling. Geophysics 67, 1304–1325.

Dec, T., Hein, F. J., Trotter, R. J. 1996. Granite wash alluvial fans, fan-deltas and tidal environments, northwestern Alberta: implications for controls on distribution of Devonian clastic wedges associated with the Peace River Arch. Bulletin of Canadian Petroleum Geology 44 (3), 541-565.

Etgen, J. T., O'Brien, M. J. 2007. Computational methods for large-scale 3D acoustic finite-difference modeling: a tutorial. Geophysics 72, 223–230.

Geiger, H. D., Daley, P. F. 2003. Finite difference modelling of the full acoustic wave equation in Matlab. CREWES Research Report 15.

Gjøystdal, H., Iversen, E., Lecomte, I., Kaschwich, T., Drottning, A., Mispel, J. 2007. Improved applicability of ray tracing in seismic acquisition, imaging, and interpretation. Geophysics 75, 261–271.

Holberg, O. 1987. Computational aspects of the choice of operator and sampling interval for numerical differentiation in large-scale simulation of wave phenomena. Geophysical Prospecting 35, 629-655.

Huang, Y., Lin, D., Bai, B., Roby, S., Ricardez, C. 2010. Challenges in presalt depth imaging of the deepwater Santos Basin, Brazil. The Leading Edge 29, 820–825.

Hyne, N. J. 1984. Oil and Gas Field Classifier, Second edition. PennWell Maps Puslishing Company.

Igel, H., Mora, P., Riollet, B. 1995. Anistotropic wave propagation through finite-difference grids. Geophysics 60, 1203–1216.

Jinhua, Y., Tao, L., Tianyue, H. 2009. Modeling seismic wave propagation within complex structures, Applied Geophysics 6, 30-41.

Kelly, K. R., Ward, R. W., Treitel, S., Alford, R. M. 1976. Synthetic seismograms: a finite-difference approach. Geophysics 41, 2–27.

Krebes, E. S., Lee, L. H. T. 1994. Inhomogeneous plane waves and cylindrical waves in anisotropic anelastic media. Journal of Geophysical Research 99(23), 899-919.

Lines, L. R., Slawinski, R., Bording, R. P. 1999. Short note: a recipe for stability of finite-difference wave-equation computations. Geophysics 64, 967-969.

Lingrey, S. 1991. Seismic modeling of an imbricate thrust structure from the foothills of the Canadian Rocky Mountains. Fagin, S. W. (Ed.). Seismic Modeling of Geologic Structures Applications to exploration Problems. Society of Exploration Geophysicists 111-125.

Liu, Y., Sen, M. K. 2009. Advanced finite-difference methods for seismic modeling. Geohorizons, 5-16.

Manning, P. M., Margrave, G. F. 1998. Elastic wave finite difference modelling as a practical exploration tool. CREWES Research Report. 10, 16.

Marfurt, J. K. 1984. Accuracy of Finite-Difference and Finite Element Modeling of the Scalar and Elastic Wave Equations, Society of Exploration Geophysicists.

Margrave, G. 2003. Numerical methods of exploration seismology with algorithms in Matlab. http://www.crewes.org/ResearchLinks/FreeSoftware/.

Moczo, P., Robertsson, O. J. A., Eisner, L. 2007. The finite-difference time-domain method for modeling of seismic wave propagation. Advances in Geophysics 48, 421-516.

Morse, P. F., Purnell, G. W. Medwedeff, D. A. 1991. Seismic modeling of fault-related folds. Fagin, S. W. (Ed.). Seismic Modeling of Geologic Structures: Applications to Exploration Problems. Society of Exploration Geophysicists, 127–152.

Nejati, M., Hashemi, H. 2012. Migrated Exploding Reflectors in Evaluation of Finite Difference Solution for Inhomogeneous Seismic Models. Engineering 4, 950-957.

Ottaviani, M. 1971. Elastic wave propagation in two evenly welded quarter-spaces. Bulletin of the Seismological Society of America 61, 1119-1152.

Özbek, A., Vassallo, M., Özdemir, K., Van Manen, D. J., Eggenberger, K. 2010. Crossline wavefield reconstruction from multicomponent streamer data: part 2 - joint interpolation and 3D up/down separation by generalized matching pursuit. Geophysics 75, WB69–WB85.

Robertson, J. O. A., Van Manen, D. J., Schmelzbach, C., Renterghem, C. V., Amudsen, L. 2015. Finite-difference modeling of wavefield constitutes. Geophysical Journal International 203, 1334-1342.

Sayers, C., Chopra, S. 2009. Introduction to special section: Seismic modeling. The Leading Edge 28, 528-529.

Sproule, J. C. 1956. Granite wash of Northern Alberta. Journal of the Alberta Society of Petroleum Geologists 4(9), 197-203.

Talukdar, K., Behere, L. 2018. Sub-basalt imaging of hydrocarbon-bearing Mesozoic sediments using ray-trace inversion of first-arrival seismic data and elastic finite-difference full-wave modeling along Sino r– Valod profile of Deccan Syneclise, India. Pure and Applied Geophysics 175, 2931–2954.

TPAO (Türkiye Petrolleri Anonim Ortaklığı). http://www.tpao.gov.tr/?mod=sektore-dair&contID=97. 25 April 2022.

Virieux, J. 1986. P-SV wave propagation in heterogeneous media: Velocity stress finite difference method: Geophysics 51, 889–901.

Youzwishen, C. F., Margrave, G. F. 1999. Finite difference modelling of acoustic waves in Matlab. CREWES Research, Report No: 11.

Zhang, H., Zhang, Y. 2007. Implicit splitting finite difference scheme for multi-dimensional wave simulation. 75th Annual International Meeting, SEG, Expanded Abstracts, 2011-2014.

Bulletin of the Mineral Research and Exploration

http://bulletin.mta.gov.tr

Interpretation of satellite gravity anomalies with pseudo-depth slicing method filter in Türkiye

İlkin ÖZSÖZ[a*] and Ceyhan Ertan TOKER[a]

[a]*General Directorate of Mineral Research and Exploration, Ankara, Türkiye*

Research Article

Keywords:
Satellite Gravity Data, Spectral Methods, Pseudo - Depth Slicing Method, Radial Average Power Spectrum, Qualitative Interpretation.

ABSTRACT

In this study, discontinuities and major tectonic boundaries are interpreted in and around Türkiye by Bouguer gravity anomaly. The World Gravity Map 2012 is used for the interpretation of major tectonic features in the Anatolia Region. Radial average power spectrum (RAPS) and band-pass filter are used for long and short wavelength separation. For the whole study area, four depth segments are detected. Moreover, the radial average depths of these depth segments are 54.9 km, 32.2 km, 21.9 km and 8.0 km. In order to conduct better interpretation, the study area was divided into three subareas from the west to the east (area 1 to area 3). In area 1 (41.4 km, 21.2 km and 7.8 km) and area 2 (48.1 km, 20.0 km and 6.6 km), three depth sources are detected. Furthermore, four various depth segments are analysed in area 3 (54.3 km, 29.8 km, 20.8 km and 8.6 km). The interpretation of the whole study area, area 1, area 2 and area 3 showed that depth of the sediment accumulation in the Western Anatolia is estimated as 7.8 km.

Received Date: 26.03.2021
Accepted Date: 26.07.2021

1. Introduction

The gravity anomalies can be considered as the sum of the long and short-wavelength components. In general, the short-wavelength components can be associated with the near-surface geological structures while the long-wavelength components likely to indicate the deep-seated structures. The anomalous body can be estimated from short or long-wavelength components concerning its depth and size (Arfaoui et al., 2011).

The short and long wavelength components can be identified by interpreting the regional or residual part of the observed data. There are various methods for regional-residual separation, which can be applied via least-squares fitting of polynomial surfaces (Simpson, 1954), spectral factorization (Gupta and Ramani, 1980), frequency domain operations, Wiener filters (Pawlowski and Hansen, 1990), finite element method (Mallick and Sharma, 1999) and matrix smoothing method by average weighting process (Arfaoui et al., 2011).

In this study, the gravity anomaly, obtained from World Gravity Map 2012 (WGM 2012) (Bonvalot et al., 2012) is analysed. WGM 2012 includes land, marine, airborne and satellite gravity data as well as satellite altimetry data. Geophysical and geodetic characteristics of gravity anomaly are taken into account during computing WGM 2012 (Bonvalot et al., 2012). Bouguer and terrain correction is computed by 1'*1' resolution topography and bathymetry ETOPO1 (Amante and Eakins, 2009) grid. Additionally, the

Citation Info: Özsöz, İ., Toker, C. E. 2022. Interpretation of satellite gravity anomalies with pseudo-depth slicing method filter in Türkiye. Bulletin of the Mineral Research and Exploration 168, 111-130. https://doi.org/10.19111/bulletinofmre.974936

**Corresponding author: İlkin ÖZSÖZ, ilkin.ozsoz@mta.gov.tr*

atmospheric mass effect is removed from the observed data (Bonvalot et al., 2012).

There were many previous studies (Ateş et al., 1999, 2012; Arslan, 2016) about gravity and magnetic interpretation in Türkiye. Western Anatolia is investigated by Sari et al. (2002), Tirel et al. (2004), Doğru et al. (2017) and Kahveci et al. (2019). Additionally, Büyüksaraç et al. (2005), Onal et al. (2008), Oruç (2011), Bilim (2017*a*) and Bilim et al. (2017*b*) interpreted the Central Anatolia region via gravity and magnetic data. Finally, tectonic and crustal structures in the Eastern Anatolia are evaluated by Pamukçu et al. (2007), Büyüksaraç (2007), Maden et al. (2009) and Pamukçu et al. (2015).

The aim of this paper is to decompose superimposed geological structures in terms of their wavenumber component and interpret the regional tectonic boundaries and discontinuities between 22° E and 45° E, 35° N and 42°N. In order to improve the interpretation phase, the study area is divided into three particular subareas (area 1, area 2, and area 3). The whole study area and the sub-areas are interpreted by the spectral analysis method which was proposed by Spector and Grant (1970). The average depth of causative bodies is estimated by this method.

Throughout this paper, variations of the tectonic structures with depth and wavenumber will be interpreted. The combination of the RAPS and band-pass filter provides characteristics of the tectonic elements for the certain wavenumber interval. Although a variety of papers were previously published, interpreting the geological structures of Türkiye, none of which had taken into account the variations of these structures with respect to depth. This paper was undertaken to explain the spatial distribution of the tectonic elements within the different wavenumber intervals via the pseudo-depth slicing method, which was proposed by Arfaoui et al. (2011).

2. Tectonic Settings

The study area is located in the seismically active zone and it comprises various tectonic regimes. Figure 1 illustrates the boundaries of the study area. Although the study area comprises many different countries, Türkiye is the major target of this paper. The tectonic activity in the study area initiated with the continental collision of the Eurasian and African plates (Şengör and Kidd, 1979; Şengör and Yılmaz, 1981; Okay and Tüysüz, 1999; Bozkurt and Mittwede, 2001; Moix et al., 2008; Göncüoğlu, 2010).

Historically, the location of the study area corresponds to the boundary between two mega-continents, Laurasia and Gondwana (Durand et al., 1999; Bozkurt and Mittwede, 2001). These mega-continents provided distinctive lithospheric fragments which amalgamated when the Arabian plate collided with the Anatolian plate (Bozkurt and Mittwede, 2001). The development of the Tethyan oceans might be related to the spatial characteristics of the mega-continents (Bozkurt and Mittwede, 2001; Robertson, 2004; Robertson et al., 2009).

The existence of two Tethyan oceans, Paleotethys and Neotethys, can be tracked back by age and distribution characteristics of subduction complexes and ophiolites (Şengör, 1979, 1987; Şengör and Yılmaz, 1981; Okay and Tüysüz, 1999; Stampfli, 2000; Bozkurt and Mittwede, 2001). The southern Neotethys, Intra-Pontide, and the northern Neotethys are the oceanic basins that are related to the Neotethys (Bozkurt and Mittwede, 2001). The latter two no longer exist but the southern Neothethys can be observed in the Eastern Mediterranean Sea (Robertson and Shallo, 2000).

It is worth noting that there are different models that explain evolution of Tetyhs oceans in Türkiye (Şengör and Yılmaz, 1981; Okay and Tüysüz, 1999; Ustaömer and Robertson, 1999; Göncüoğlu et al., 2000; Stampfli, 2000; Elmas and Yiğitbaş, 2001).

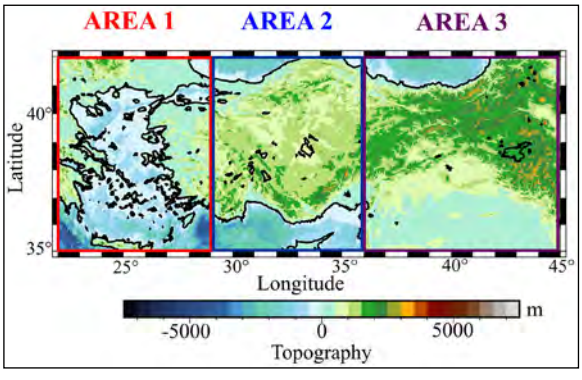

Figure 1- Location map of the study area and subareas (areas 1, 2 and 3).

Okay and Tüysüz (1999) suggested that Türkiye can be divided into five major suture zones which are Intra-Pontide, Southeast Anatolian, Inner Tauride, Antalya, and İzmir-Ankara-Erzincan. According to Ketin (1966), Pontides, Anatolides, Taurides, and bounding faults are subdivisions of Anatolia.

Pontides (Triassic age) located in the northern part of the study (Bozkurt and Mittwede, 2001). The tectonic patchwork of Pontides includes three major zones (Okay, 1989) which are Strandja Zone (Okay et al., 2001), İstanbul Zone (Aydın et al., 1986; Görür et al., 1997; Dean et al., 2000) and Sakarya Zone (Bingöl et al., 1975; Şengör et al., 1980; Şengör and Yılmaz, 1981; Tekeli, 1981; Koçyiğit, 1987, 1991; Altıner et al., 1991; Altıner and Koçyiğit, 1993; Genç and Yılmaz, 1995; Okay and Monie, 1997; Rojay and Altiner, 1998; Kozur et al., 2000).

In the southern part, Anatolides and Taurides are treated together (Tauride-Anatolide platform) by Şengör and Yılmaz (1981). Bornova flysch zone (Erdoğan, 1990), Tavsanli zone (Harris et al., 1994; Sherlock et al., 1999), Afyon zone (Özcan et al., 1988), Menderes Massiff and Central Anatolian Crystalline Complex are comprised by Anatolide platform. Furthermore, the Tauride platform includes unmetamorphosed nappes, comprised of carbonates, turbidites, and clastic rocks (Özgül, 1976, 1985).

The southeastern part of the study area is characterized by the juxtaposition of Arab and Tauride-Anatolide platforms (Ketin, 1966; Yılmaz, 1993; Yılmaz and Yıldırım, 1996). Additionally, the Arabian platform might have a major contribution to potential hydrocarbon production in Türkiye.

Paleozoic sedimentary rocks and nappe structures are observed in the Anatolide-Tauride block (Bozkurt and Mittwede, 2001). Unlike Taurides, ubiquitous regional metamorphism is noted in the Anatolide block (Okay et al., 2001). Nappe structures are common in the Taurides whereas deformed, sliced and metamorphosed rocks are characteristics of the Anatolide block (Bozkurt and Mittwede, 2001).

In the Late Miocene-Pliocene, intra-continental convergence was initiated between the Tauride-Anatolide platform and Pontides (Bozkurt and Mittwede, 2001). Consequently, N-S shortening was initiated in the study area. At the present time, N-S compression continues in the only eastern part of Türkiye (Dewey et al., 1986; Şaroğlu and Yılmaz, 1986; Bozkurt and Mittwede, 2001; Faccenna et al., 2006; Keskin, 2007; Göğüş and Psyklywec, 2008).

The Miocene sedimentation is ubiquitous in the study area. In western Anatolia, there are many E-W trending grabens. Furthermore, foreland basins are noted in the Tauride platform (Legeay et al., 2016). In Pontides and Anatolides, Miocene sedimentation developed as collision-related basins (Görür et al., 1998; Kaymakçı et al., 2000; Ocakoğlu et al., 2001; Catto et al., 2018; Gülyüz et al., 2019). In addition, Görür et al., (2000) indicated that marine carbonates and clastic sediments in the Pontides are associated with the Paratethys.

In the eastern part of the study area between Eurasia and the Arabian platform, Miocene sedimentation is characterized by reefal limestones, turbidites, and marine carbonates (Bozkurt and Mittwede, 2001). The closure of the Bitlis Ocean was initiated by the convergence between the Arabian and Anatolian Plate in the Late Miocene (Bozkurt and Mittwede, 2001). This intracontinental convergence results in uplift and crustal thickening in the eastern part of the study area. Consequently, the Southeast Anatolian Suture occurred. The tectonic regime of Eastern Anatolia converted from a compressional-contractional regime to a new compressional regime in the neotectonic period (Bozkurt and Mittwede, 2001).

Türkiye can be divided into three major structures in terms of neotectonic framework: North Anatolian Fault Zone (Ketin, 1969), East Anatolian Fault Zone, and Aegean Cyprian Arc (Figure 2). Firstly, the dextral North Anatolian Fault Zone and the sinistral East Anatolian Fault Zone are intracontinental transform faults. Secondly, Aegean Cyprian Arc is the convergent plate boundary. Another fault that has an impact on the neotectonics of Türkiye is the sinistral Dead Sea Fault. In northeast Türkiye, a continental triple junction formed where two strike-slip faults coincided (Karig and Kozlu, 1990).

Rotstein (1984) suggested that the amalgamated crustal fragment is moving to the west. Hence, the westward extrusion results in a counter-clockwise

Figure 2- Simplified tectonic map of the study area (modified from Şengör et. al., 1985; Bozkurt and Mittwede, 2001. NAFZ= North Anatolian Fault Zone, EAFZ= East Anatolian Fault Zone, DSFZ= Dead Sea Fault Zone).

rotation of Anatolia. The internal deformation of Anatolia stems from the NAFZ, EAFZ and the westward movement of Anatolia (Bozkurt and Mittwede, 2001). Şengör et al. (1985) divided Anatolia into four Neotectonic provinces; the East Anatolian contractional, West Anatolian extensional, the Central Anatolian and the North Anatolian provinces. Major structures and continental blocks of the study area is illustrated in Figure 3.

3. Method

3.1. Radially Averaged Power Spectrum (RAPS)

Bhattacharyya (1966) mentioned the fundamentals of spectral analysis in terms of magnetic sources. The power spectrum is generally based on the geometry of sources instead of the source parameter (Maus and Dimri, 1995).

Spector and Grant (1970) introduced the RAPS. Radial (or Azimuthal) variation of the power spectrum can be expressed as

$$S^2(k) = [e^{(-4\pi k)}](1 - e^{(-4\pi k)^2}\left(A^2(k\phi)\right)) \quad (1)$$

where $S^2(k)$ is the radial power spectrum and k is the wavenumber. The term $[e^{(-4\pi k)}]$ represents radial

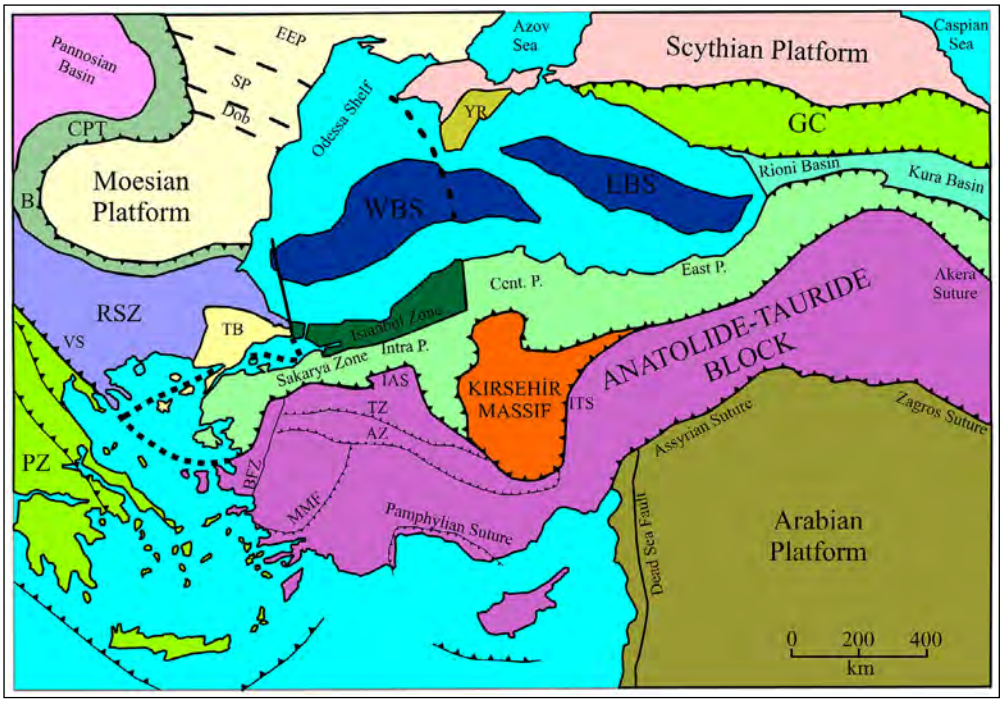

Figure 3- Continental blocks and major structures of northeast Mediterranean (modified from Şengör, 1984; Okay, 1989; Okay et. al., 1994; Okay and Tüysüz, 1999. PZ= Pelagonian Zone, VS= Vardar Suture, RSZ= Rhodope-Strandja Zone, B= Balkanides, CPT= Carpathians, Dob= Dobrudja, SP= Scythian Platform, EEP= East European Platform, YR= Yayla Range, WBS=West Black Sea Basin, EBS= East Black Sea Basin, GC= Greater Caucasus, Intra P.= Intra Pontide Suture, Cent. P.= Central Pontides, East P.= Eastern Pontides, IAS= İzmir - Ankara Suture, TZ= Tavşanlı Zone, AZ= Afyon Zone, MMF= Menderes Massif, BFZ= Bornove Flysch Zone).

averaging. A^2 (kϕ) denote the dimensions of prisms along the horizontal plane. Hence Equation 1 can be written as

$$S^2(k) = f(\phi) * f(t) * f(\phi) \quad (2)$$

where f(h) is depth, f(t) is depth extent, and f(ϕ) is the size factor. The major contribution comes from depth (Fairhead, 2016).

The prominent advantage of this method is depth estimation can be applied to the observed data (Fairhead, 2016). Regional and residual separation is not required. Furthermore, Spector and Grant (1970) mentioned that each linear segment represents an average depth. On the other hand, the apparent drawback of the RAPS is powers, which are averaged, is not fitting the same wavenumber (Maus and Dimri, 1995).

RAPS may detect more than one source. In this case, the anomaly can be separated by using appropriate filters.

3.2. Filter Design

Saramaeki et al. (1993) mentioned the fundamentals of filter design. Filter design is an iterative process. If the designed filter does not provide the desired response, filter properties (cut-off frequency, filter degree, etc.) should be adjusted. Error in the observed data is the other contributor that affects the response of the filter.

The primary drawback of the steep filters is the Gibbs phenomenon. The Gibbs phenomenon results in side-lobes which may seriously affect the interpretation of the data (Gottlieb and Shu, 1997).

Therefore, fixed window functions are used for reducing the effect of the Gibbs phenomenon. The window function tapers the designed filter smoothly. In this study, the Gaussian window is used for tapering the filter. Figure 4 shows the schematic illustration of the designed filter and its windowed version by Gaussian window.

3.3. Pseudo Depth Slicing

Depth estimation and source estimation can be estimated from the log-log plot of the squared amplitude spectrum. Fairhead (2016) suggested that it can be a powerful tool in terms of regional-residual separation.

The gravity anomaly grid can be considered as the sum of anomalies from various depth segments. The anomaly grid can be represented via RAPS (Spector and Grant, 1970).

Generally, the long-wavelength anomalies in the RAPS are associated with the deeper regional structures. However, Fairhead (2016) emphasizes that shallow structures may have long-wavelength components. This phenomenon should be taken into account during regional-residual separation.

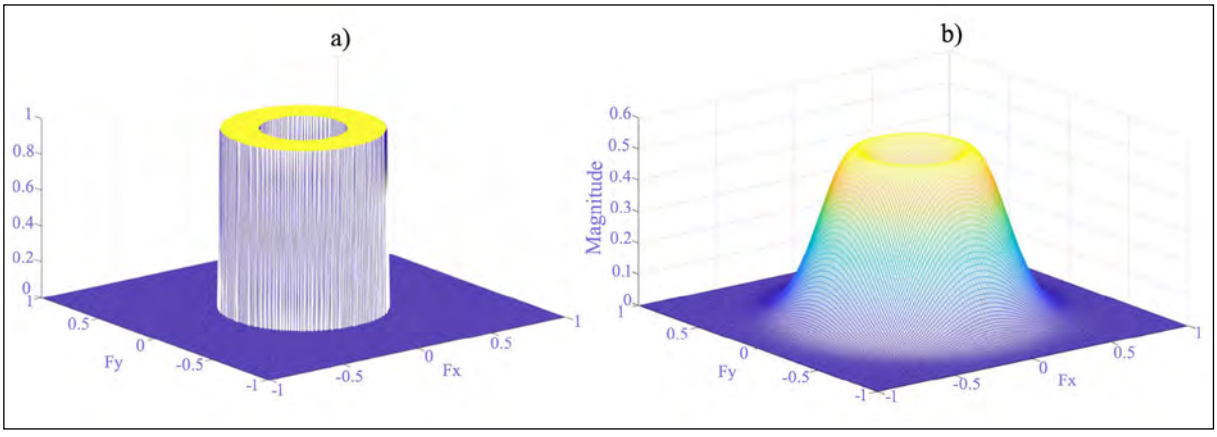

Figure 4- Schematic demonstration of desired and applied filters; a) the desired filter that is susceptible to the Gibbs phenomenon, b) applied filter, windowed by Gaussian window. It has more gentle slopes.

Desired wavelength components can be filtered with the help of the power spectrum. If only the long-wavelength components of the power spectrum are targeted, the swing-tail filter can be used. According to Cordell and Grauch (1985), the swing-tail filter suppresses a high-frequency tail that follows the linear segment. In general, near-surface anomalies and noise are removed from data. Fairhead (2016) recommended that after the swing-tail filter, Euler deconvolution or the other automated depth estimation technique can be used.

On the other hand, the swing-head filter is exactly the opposite of the swing-tail filter. It suppresses long-wavelength components. Consequently, shorter wavelength components can be interpreted clearly. It should be noted that if there is one linear segment on the RAPS, this filter cannot be applied.

Swing-tail and swing-head filters provide deep and shallow sources respectively. However, if the desired depth is an intermediate depth, a band-pass filter ought to be used. The result will contain short and long-wavelength components of data. Moreover, two depth slices were filtered. For obtaining the depth slice of intermediate depths, at least three linear segments are required on the power spectrum.

Figure 5 briefly explains the pseudo-depth slicing method. For instance, depth slices with shorter wavelength (or higher wavenumber) components can be obtained by swing head filter.

The obvious advantage of the pseudo depth slicing method is separating anomalies from various depths. Moreover, it isolates anomalies between desired wavelengths.

3.4. Edge Detection Process

Geosoft Oasis Montaj's Centre for exploration (CET) extension was used as an edge detection method which was proposed by Lam et al. (1992), Kovesi (1997, 1999), Holden et al. (2008), and Holden et al. (2010). In this context, we used a quantitative method that includes three stages:

1) Specifying local neighborhood by the standard deviation (SD). The equation for SD is provided as:

$$SD = \sqrt{\frac{1}{N}\sum \quad (x_i - \mu)} \tag{3}$$

where N is the number of data and π is the mean value of data within the window.

2) Quantitatively detecting lateral continuities or line-like features by frequency-based approach. If

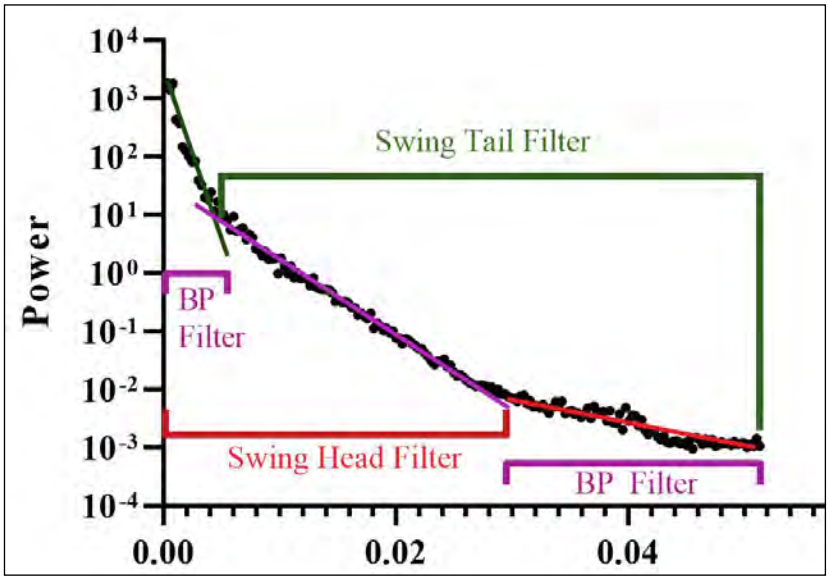

Figure 5- Brief explanation of swing-tail, swing-head, and a band-pass filter (BP filter) on the RAPS.

$r_i(x)$ and $i_i(x)$ considered as real and imaginary parts of the signal and $A_n(x)=\sqrt{r_i(x)^2 + i_i(x)^2}$, symmetry can be computed as:

$$Sym(x) = \frac{\sum_{i=1}^{n} \quad (|r_i(x)| - |i_i(x)| - T)}{\sum_{i=1}^{n} \quad A_n(x) + \varepsilon} \qquad (4)$$

where T is a term for noise suppression and $\mathcal{E}$ is used as a constant to prevent division by zero.

3) Skeletonising the discontinuities. First of all, connected edge sets should be constructed. Line segments are fitted to the connected edges. Then, the threshold value is determined. The maximum deviation between the fitted line segment and edge ought to be calculated. If the deviation exceeds the threshold value, the edge is split into two components approximate location of the maximum deviation. This is an iterative process, the maximum deviation is divided into two components until the maximum deviation keeps within the threshold.

4. Findings

RAPS, band-pass filtering, and depth slicing method are applied to the whole study area, western part (area 1), central part (area 2), and eastern part (area 3) of the study area (Figure 1).

The radially averaged depths for the study area, area 1, area 2, and area 3 are estimated by the RAPS. These depths can be considered as approximate depths of the major tectonic sequences. Figure 6 demonstrates the RAPS of the whole study area. Additionally, the RAPS results of area 1, area 2, and area 3 are presented in Figure 7.

As it can be seen from Figure 6, four different primary depth sources are detected. In order to design the appropriate filter, the wavenumber range of

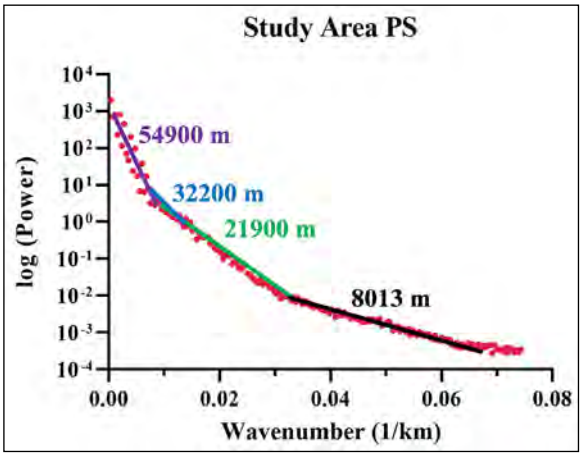

Figure 6- Radially averaged depth values of the whole study area.

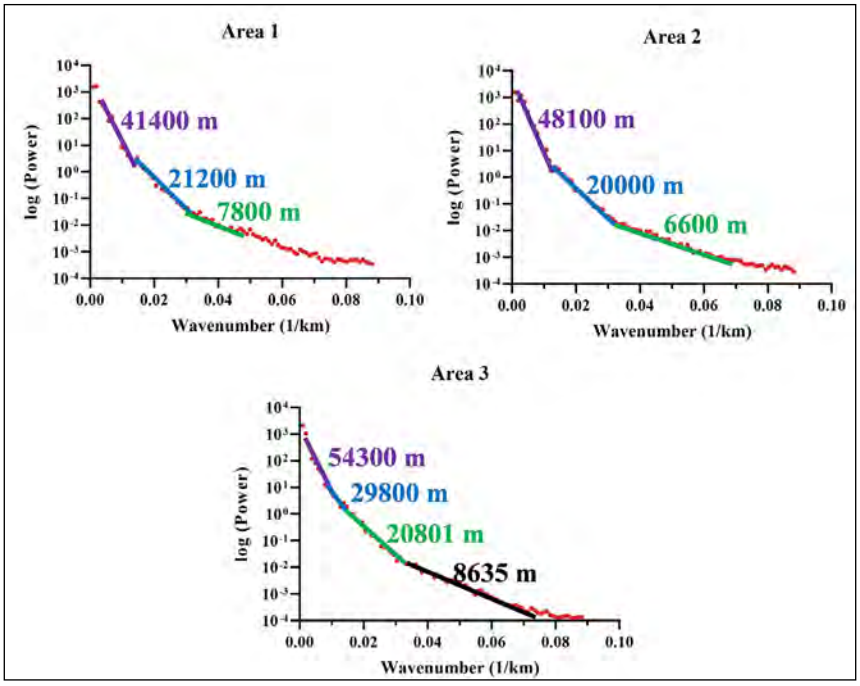

Figure 7- Radially averaged depth values of area 1 (western part), area 2 (central part), and area 3 (eastern part).

each depth source should be detected. The detected approximate wavenumber ranges for the detected depth sources are 0.000-0.010 1/km for 54.9 km, 0.010- 0.012 1/km for 32.2 km, 0.012-0.025 1/km for 21.9 km and 0.025-0.061 1/km for 8 km.

For the area 1, the wavenumber ranges are roughly 0.003-0.013 1/km for 41.4 km, 0.013-0.029 1/km for 21.2 km, 0.029-0.065 1/km for 7.8 km. In the area 2, approximate wavenumber intervals are 0.002-0.013 1/km for 48.1 km, 0.013-0.026 1/km for 20.0 km, 0.026-0.068 1/km for 6.6 km. The selected wavenumber intervals for the area 3 are about 0.001-0.011 1/km for 54.3 km, 0.008-0.011 1/km for 29.8 km, 0.011-0.032 1/km for 20.8 km, 0.032-0.070 1/km for 8.6 km.

The gravity anomaly for the corresponding average depth is obtained after the filtering desired wavenumber intervals. The filtered gravity anomaly for the whole study area, area 1, area 2, and area 3 are shown in Figures 8, 9, 10, and 11.

The computed edge detection map of the entire study area is demonstrated in Figure 17. Tectonic features and quantitatively interpreted discontinuities are overlaid to the SD map.

5. Qualitative and Quantitative Interpretation

Tectonic boundaries, faults, lineaments overlaid on gravity anomalies. Furthermore, their variations with different radial average depths are interpreted. Firstly, the name and position of the emphasized tectonic features are presented in the study area (Figure 12). Then, the geological structures are overlaid on the whole study area (Figure 13), area 1 (Figure 14),

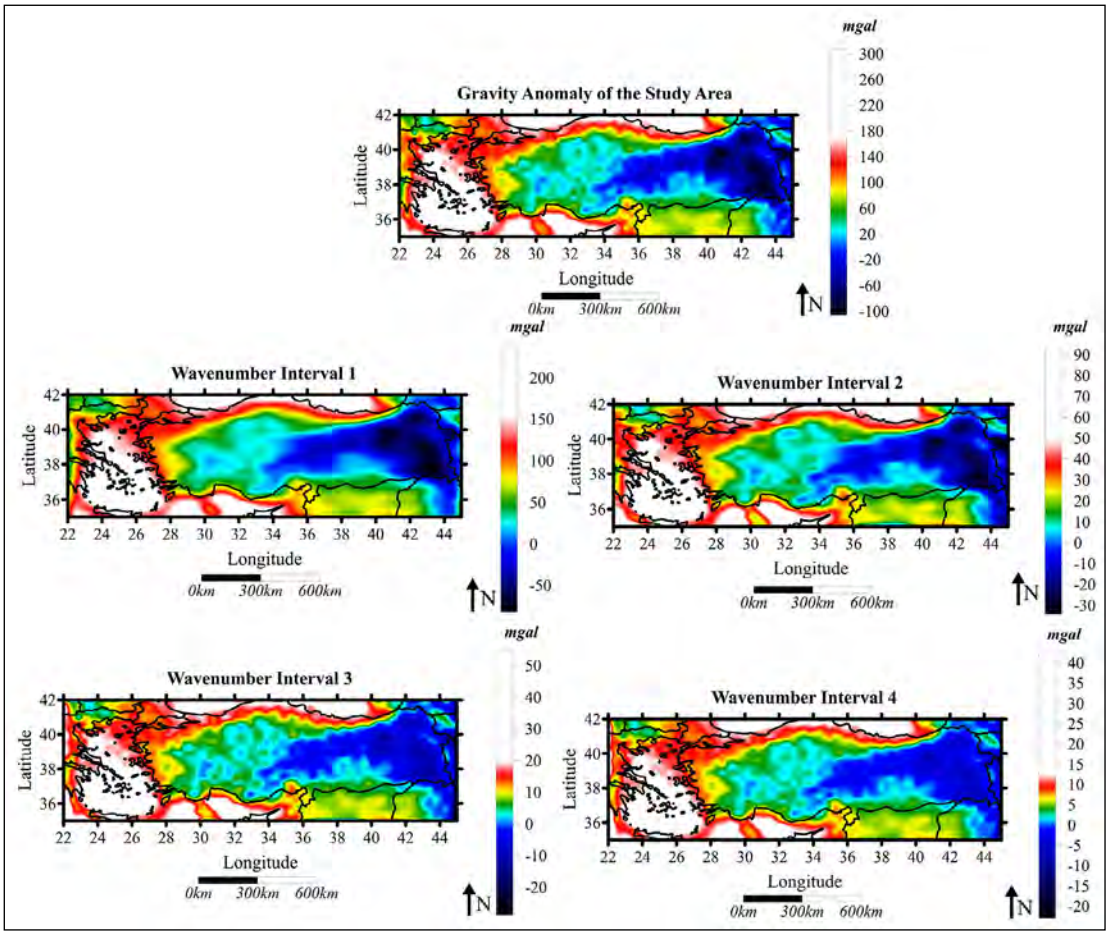

Figure 8- The gravity anomaly of the study area and its filtered components. Wavenumber interval 1 (54.9 km) = 0.000 - 0.010 1/km, wavenumber interval 2 (32.2 km) = 0.010 - 0.012 1/km, wavenumber interval 3 (21.9 km) = 0.012 - 0.025 1/km and wavenumber interval 4 (8 km) = 0.025 - 0.061 1/km.

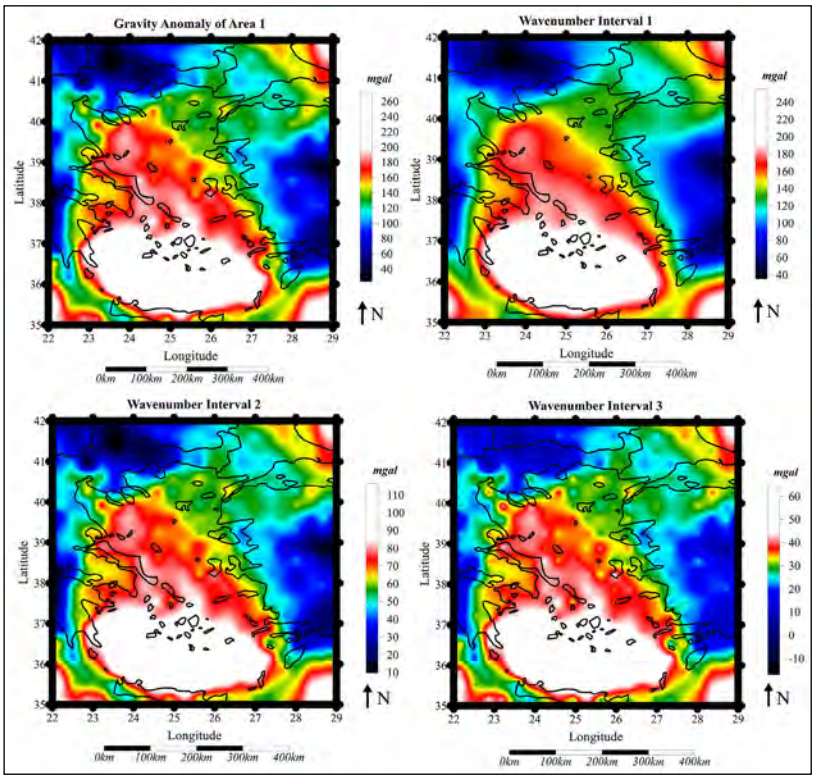

Figure 9- The gravity anomaly of area 1 and its filtered components. wavenumber interval 1 (41.4 km) = 0.003 -0.013 1/km, wavenumber interval 2 (21.2 km) = 0.013 - 0.029 1/km, wavenumber interval 3 (7.8 km) = 0.029 - 0.065 1/km.

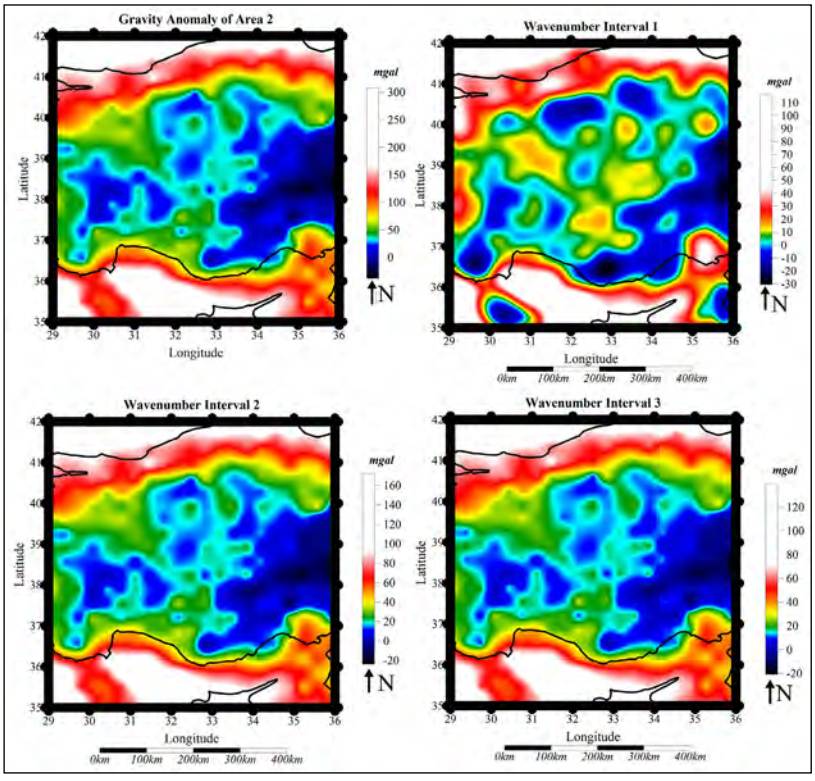

Figure 10- The gravity anomaly of area 3 and its filtered components. Wavenumber interval 1 (48.1 km) = 0.002 - 0.013 1/km, wavenumber interval 2 (20.0 km) =0.013 - 0.026 1/km, wavenumber interval 3 (6.6 km) = 0.026 - 0.068 1/km.

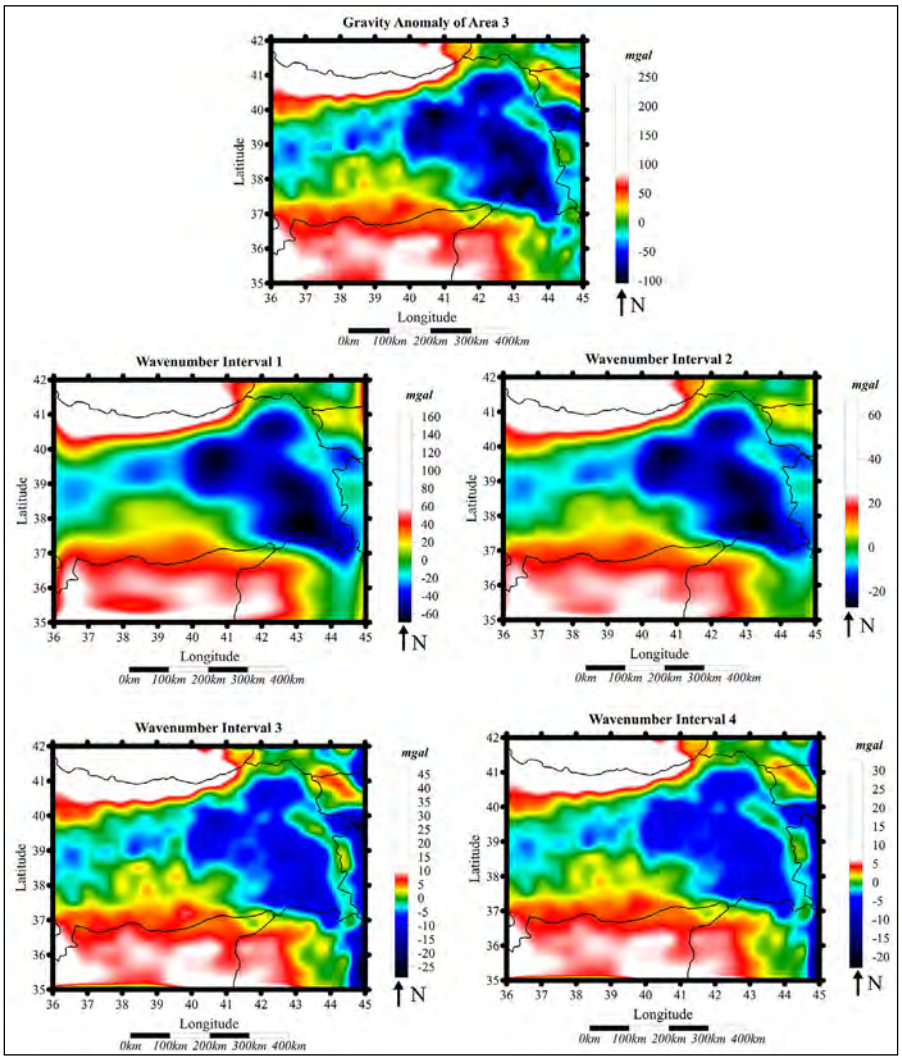

Figure 11- The gravity anomaly of area 3 and its filtered components. Wavenumber interval 1 (54.3 km) = 0.001 - 0.011 1/km, wavenumber interval 2 (29.8 km) =0.008 - 0.011 1/km, wavenumber interval 3 (20.8 km) =0.011 - 0.032 1/km, wavenumber interval 4 (8.6 km) = 0.032 - 0.070 1/km.

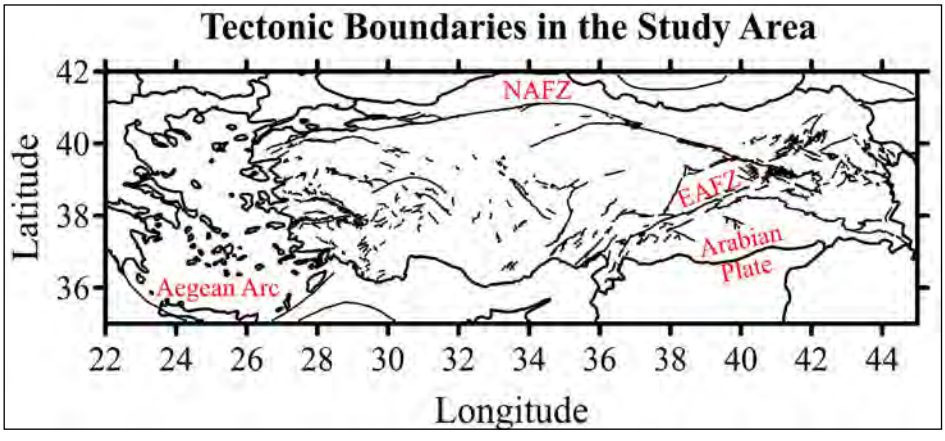

Figure 12- The major tectonic boundaries which are used in the interpretation phase.

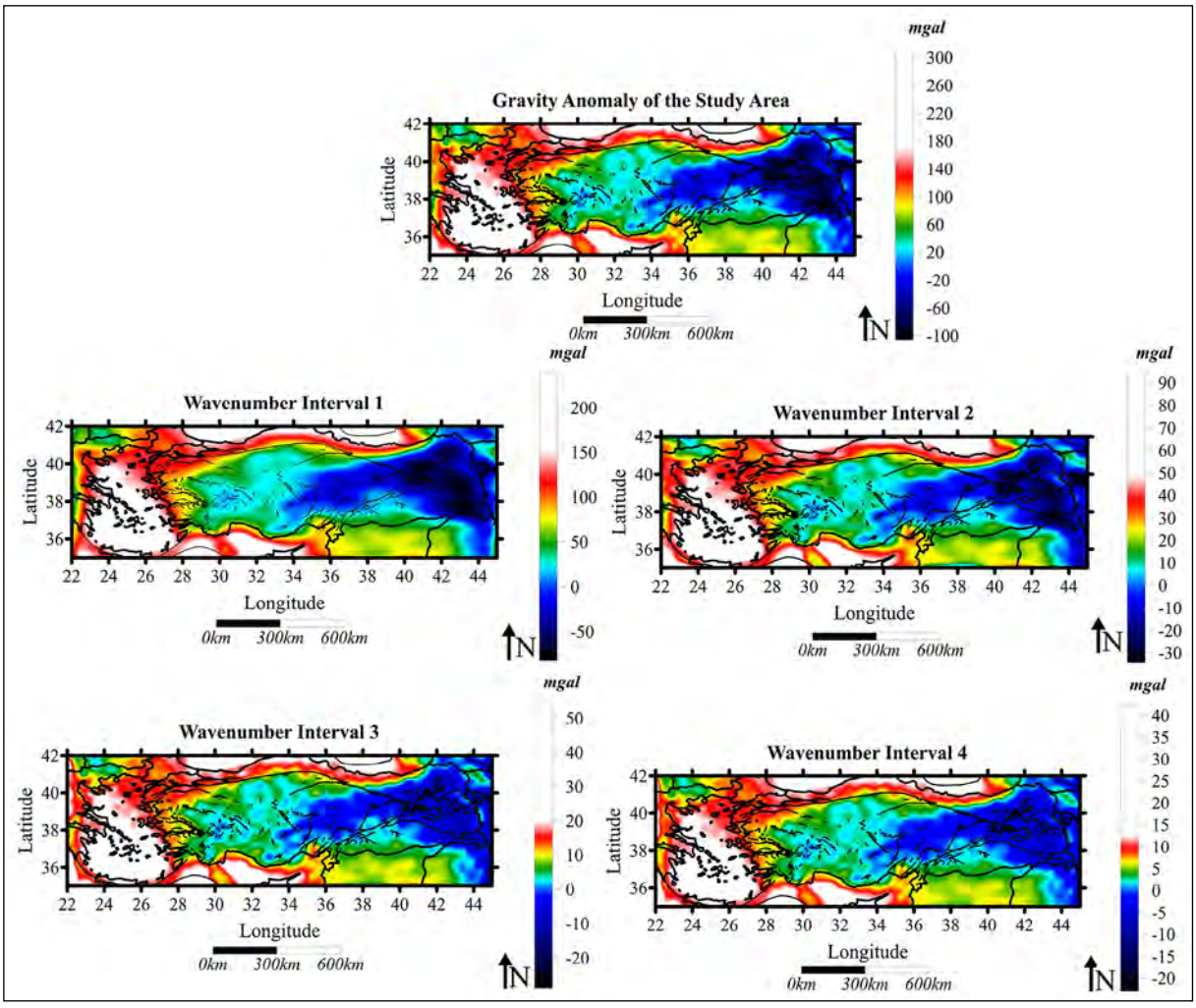

Figure 13- Qualitative interpretation of the whole study area. Wavenumber interval 1 (54.9 km) = 0.000 - 0.010 1/km, wavenumber interval 2 (32.2 km) = 0.010 - 0.012 1/km, wavenumber interval 3 (21.9 km) = 0.012 - 0.025 1/km and wavenumber interval 4 (8 km) = 0.025 - 0.061 1/km.

area 2 (Figure 15), and area 3 (Figure 16) for the detailed analysis.

In Figure 13, the wavenumber interval 1, containing the longest wavelengths, smoothly reflects the deeper geological variations in the study area. On the other hand, wavelength interval 4, which includes the shortest wavelength components, generally presents the shallower tectonic characteristics.

Broadly speaking, the geodynamics of the eastern part is controlled by the deeper mechanisms since the notable decrease in gravity anomaly occurs only for the long-wavelength components (wavenumber interval 1 and wavenumber interval 2). Conversely, the gravity anomaly of the western part is quite stable for each wavelength component. The central part of the study can be barely interpreted from the regional study area as tectonic structures are quite small with respect to the resolution of data.

Extensional tectonics along the N-S direction dominates Western Anatolia Region. The extensional mechanism results in E-W grabens. Moreover, the subduction zone between the Eurasia Plate and the African Plate formed Aegean Arc.

As it can be seen from Figure 14, the western part of the study area, area 1, is demonstrated. The location of the Aegean Arc is fairly obvious in each

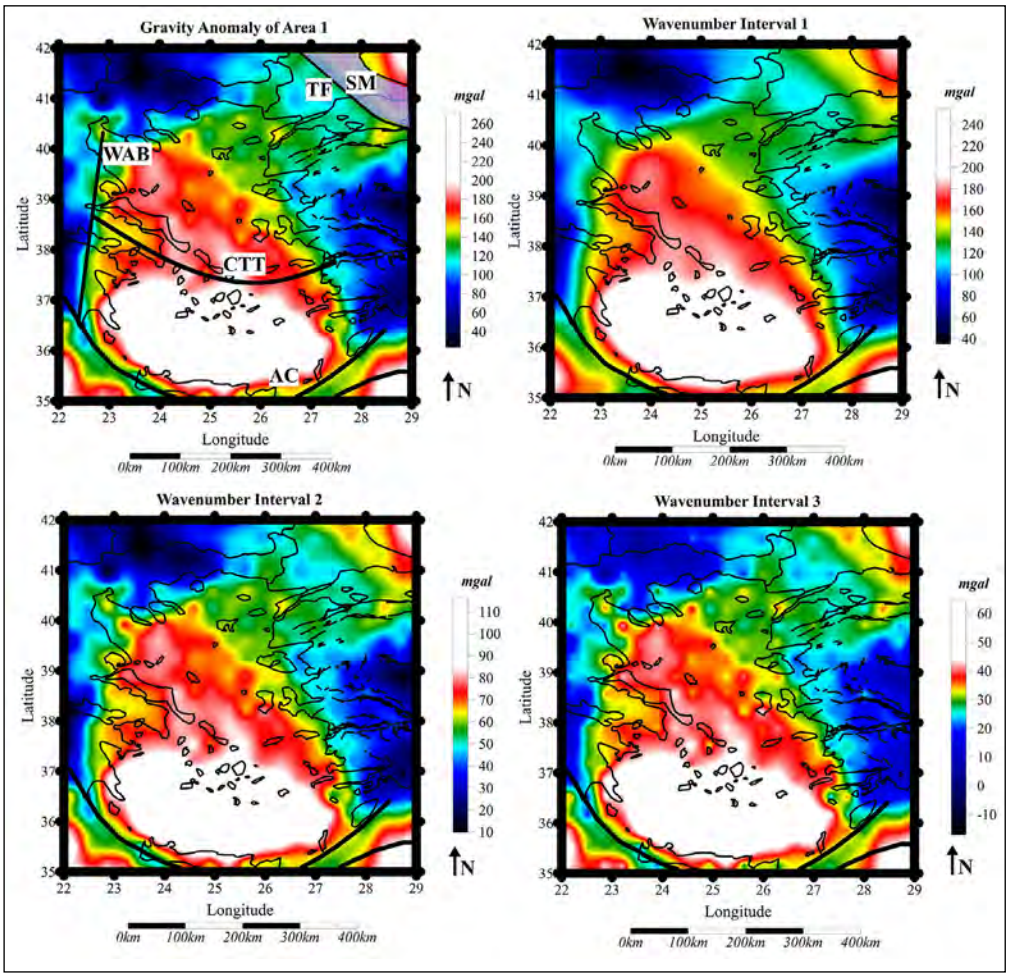

Figure 14- Qualitative interpretation of area 1. Wavenumber interval 1 (41.4 km) = 0.003 - 0.013 1/km, wavenumber interval 2 (21.2 km) = 0.013 - 0.029 1/km, wavenumber interval 3 (7.8 km) = 0.029 -0.065 1/km. Interpreted tectonic structures are WAB= West Aegean Boundary, TF= Thrace Fault, CTT= Cycladic Tectonic Trend, SM= Strandja Massif.

wavelength interval. This subduction zone, related to the Aegean Arc, is specified by a higher gravity anomaly. Furthermore, it can be said that the Aegean Arc dominates the tectonic mechanism of area 1 for each depth segment.

It is known that accumulated sediments in grabens are generally characterised by a decreasing gravity anomaly. The effect of sedimentation in Western Anatolia can be tracked from the wavenumber interval 3, whose radial average depth is roughly 8 km. In addition, minor faults indicate boundaries of grabens in area 1. Unlike the Aegean Arc, grabens can be associated with the shallow tectonic regime of Western Anatolia.

Thrace Fault can be observed in each depth interval (depth intervals 1, 2, and 3) and its strike is NW-SE. Southwest of the Thrace Fault is characterised by lower gravity anomalies while higher gravity anomalies are observed in the northeast part (Strandja Massif) of the fault. It might be said that the northern Aegean Region and the southern Thrace have fairly similar tectonic characteristics. There is a major boundary that initiated from the southern Aegean plate to the northwestern part of the Aegean Plate where the Thrace fault is discontinuous in the Peloponnesus. This major boundary is the crustal-scale and it can be interpreted from each depth interval.

Notably high gravity anomaly zone is bounded by Crete Island in the south and Cyclades Massif in the

north. Moreover, subduction of the African plate to the Aegean Plate formed fore-arc structures which are characterized by lower gravity anomalies.

In general, the shallow and extensional tectonic regime in the Western Anatolia demonstrates credible similarities with previous studies (Sarı et al., 2002; Tirel et al., 2004; Pamukçu and Yurdakul, 2008; Doğru et al., 2017, 2018; Kahveci et al., 2019; Doğru and Pamukçu, 2019).

In Figure 15, Aegean Arc and NAFZ are the major tectonic structures. The edge of the Aegean Arc cannot be clearly observed in the deepest depth slice (wavenumber interval 1 (48.1 km)) whereas its boundaries are more obvious in wavenumber interval 2 (20.0 km) and wavenumber interval 3 (6.6 km). The position of the NAFZ is considerably obvious in each pseudo-depth segment. Therefore, it can be said that NAFZ has an impact at each radial average depth, 48.1 km, 20 km, and 6.6 km. Overall, gravity anomalies in each depth segment are quite stable from deeper to shallower in Central Anatolia.

Even though NAFZ adversely correlated to the plate boundaries in the East, it is quite concordant with the boundary of the western Pontides. In this case, it might be said that NAFZ becomes deeper from the East to the West. Salt Lake fault is not corresponding to the gravity anomalies. Therefore, it can be said that this fault formed in shallow depths.

In the Antalya region, there is an anomaly along the NW direction, which is possibly associated with boundary transition. Both sides of the Antalya-Samsun lineament (wavenumber intervals 1, 2, and 3) can be characterised by different crustal thicknesses. The change in crustal thickness formed three tectonic sub-regions.

Thrace-Eskişehir fault zone along NW direction is correlated with gravity anomalies in-depth interval 1.

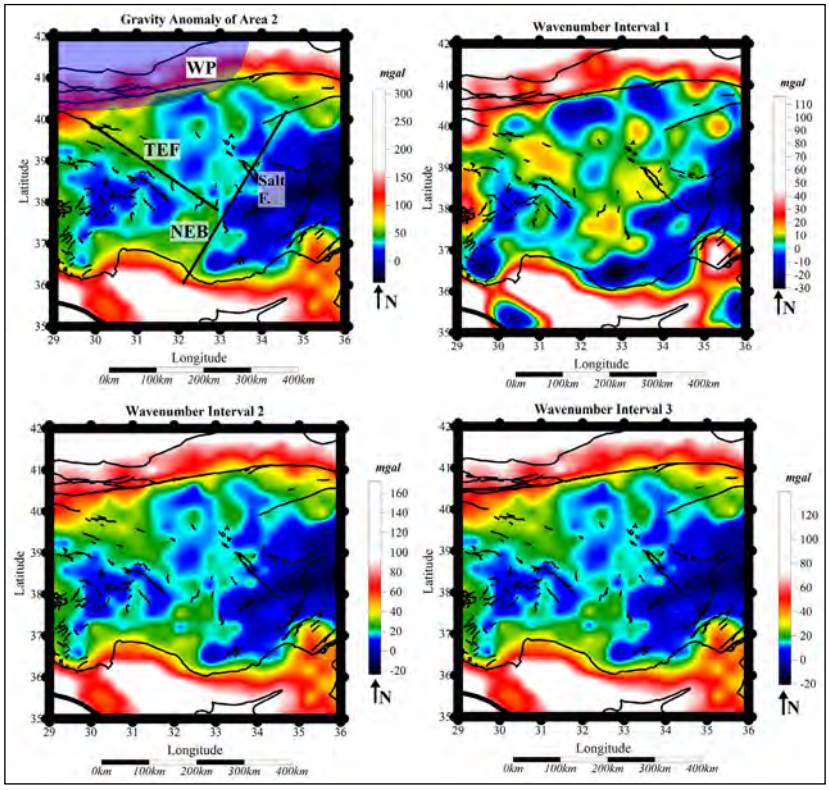

Figure 15- Qualitative interpretation of area 2. Wavenumber interval 1 (48.1 km) = 0.002-0.013 1/km, wavenumber interval 2 (20.0 km) = 0.013-0.026 1/km, wavenumber interval 3 (6.6 km) = 0.026-0.068 1/km. Interpreted tectonic structures are WP= Western Pontides, TEF= Thrace-Eskişehir Fault, NEB= Northeast Boundary, Salt F.= Salt Lake Fault.

Plate shortening initiated from the southern Cyprus region can be tracked to the Mersin-Anamur shoreline while it cannot be observed across the Antalya-İskenderun shoreline.

The interpreted tectonic structures and discontinuities in Central Anatolia is somewhat correlated with regional scale gravity anomalies (Büyüksaraç et al., 2005; Önal et al., 2008; Oruç, 2011, Bilim et al., 2017, Bilim, 2017 and Oruç et al., 2019).

The dominant tectonic mechanism in Eastern Anatolia is the compressional regime. Minor faults in Eastern Anatolia are related to the continental collision. The lower gravity anomaly in area 3 can be associated with the regions with crustal thickening (Figure 16). Lower gravity anomalies were observed where NAFZ and EAFZ coincided. There is no significant variation on the gravity anomaly within the Arab Platform due to the stable tectonic characteristics of this platform.

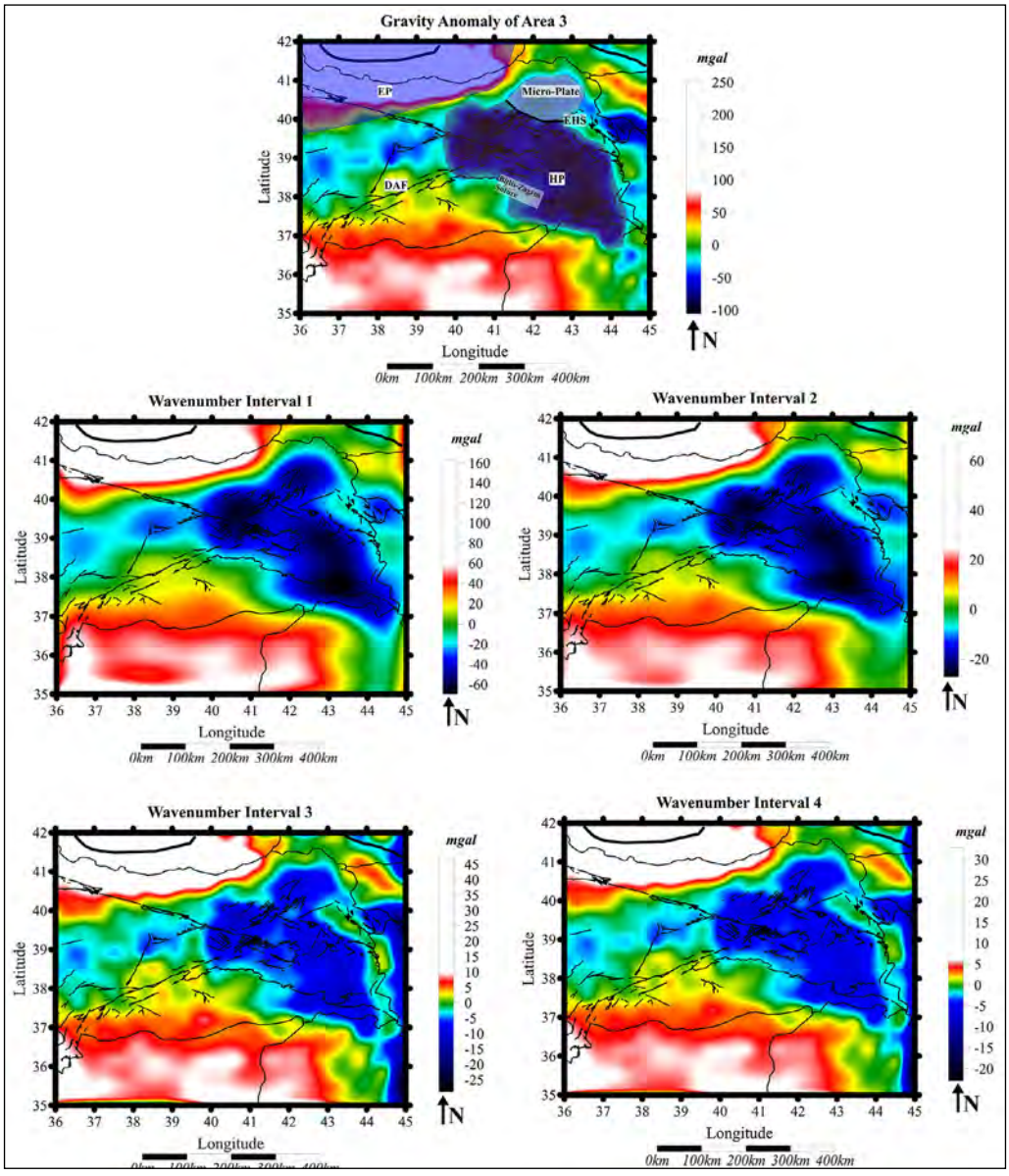

Figure 16- Qualitative interpretation of area 3. Wavenumber interval 1 (54.3 km) = 0.001 - 0.011 1/km, wavenumber interval 2 (29.8 km) = 0.008 - 0.011 1/km, wavenumber interval 3 (20.8 km) = 0.011 -0.032 1/km, wavenumber interval 4 (8.6 km) = 0.032 - 0.070 1/km. Interpreted tectonic structures are; EP= Eastern Pontides, DAF= East Anatolian Fault, HP= Hakkari Plate, EHS= Erzurum -Horasan Subsidence.

If gravity anomalies in Figure 16 are analyzed in terms of various depth segments, the effect of crustal thickening, minor faults, and boundaries of the Arabian Platform are becoming uncertain with decreasing radial average depth. Interpretation of the minor fault zone can be conducted by the longer wavelength components, wavenumber interval 1 (54.3 km) and wavenumber interval 2 (29.8 km). The minor fault zone was barely detected from the shorter wavelength components, wavenumber interval 3 (20.8 km) and wavenumber interval 4 (8.6 km), owing to the fact that this zone occurred at deeper parts of the subsurface.

Eastern Pontide, Eastern Anatolia, and the northern part of the Eastern Anatolia (microplate) are three major plate boundaries in area 3. The microplate (area 3) is bounded by Erzurum-Horasan subsidence in the Southwest and the national border of Türkiye in the east. Furthermore, the boundaries of the Hakkari plate are; southern part of the Türkiye-Iraq national border in the south, the Türkiye-Iran national border in the east, the Erzurum-Horasan subsidence in the north, and the Arabian plate in the west. The EAFZ and the Arabian Plate can be interpreted in all depth intervals and the gravity anomaly. EAFZ is concordant with tectonic structures in each depth interval whereas NAFZ cannot be correlated with deeper tectonic structures. This concordance might be tracked from the following previous studies: Pamukçu et al. (2007), Büyüksaraç (2007), Maden et al. (2009) and Pamukçu et al. (2015). The tectonic boundaries in Eastern Anatolia resulted from the northward movement of the Arabian plate.

The interpreted tectonic boundaries and discontinuities for the whole study area are somewhat compatible with Ateş et al., (2012). The major difference between Ateş et al., (2012) and this study is the resolution of the gravity data. Since WGM 2012 resolution is not as high as interpreted gravity data in Ateş et al. (2012), minor discontinuities are unlikely to be interpreted.

For the purpose of obtaining an unbiased interpretation of the study area, a quantitative edge detection method is used. The detected discontinuities are compared to the tectonic features in the study area (Figure 17). Initially, it is worth saying that the land-marine transition zones generated dramatically high contrast in the SD map. Therefore, the edge detection technique assigned linear features to these zones.

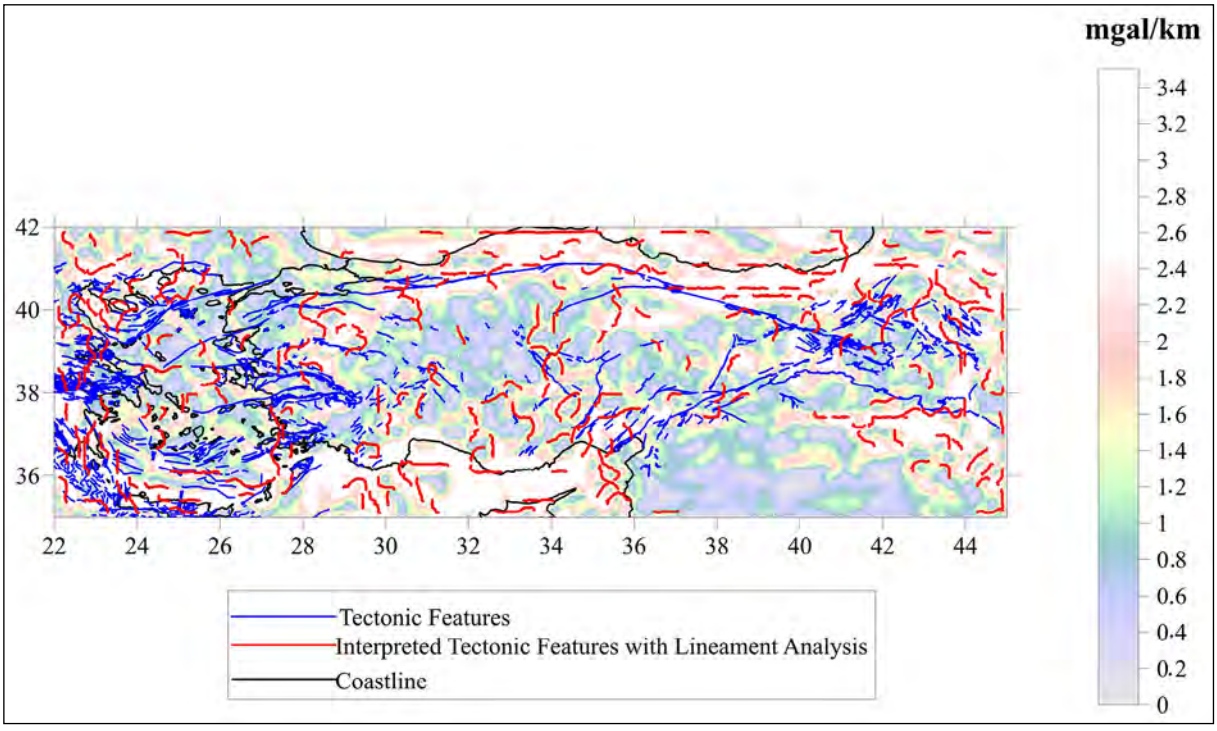

Figure 17- Standard deviation map which is overlaid by tectonic features (blue) and interpreted lineaments (red).

In the western part of the study area, lineaments are more or less correlated with geological structures except for Western Anatolia. The graben structures in Western Anatolia produce non-symmetrical anomalies and edge detection methods unable to detect these structures. However, this problem might be overcome using data with higher resolution. Furthermore, the detected linear features and geological discontinuities are compatible in Central Anatolia. It is fair to say that NAFZ is credibly interpreted by the quantitative approach. In Eastern Anatolia, the Arabian platform is barely detected due to the lower contrast and symmetry in the SD anomaly. Nevertheless, the tectonic features in Northeast Anatolia somewhat reliably correspond to the estimated linear segments.

6. Results

Interpretation of the study area for different pseudo-depth segments described variation of tectonic elements with depth. The method combined the results of the radial average power spectrum and band-pass filter. This study provided a different perspective of interpretation which takes into account depth dimension simultaneously.

From the West to the East, dominant tectonic events occurred shallower to deeper subsurface. Grabens have a quite clear gravity anomaly at only the shallowest depth (≈8 km) in Western Anatolia. In addition, the crustal thickening effect can be observed at deeper parts (≈54.3 and ≈29.8 km) of the subsurface in Eastern Anatolia. NAFZ is the major structure that is interpretable at each pseudo-depth segment.

The qualitatively interpreted discontinuities are compared to the line segments obtained from the quantitative edge detection method. The comparison results are not presenting a perfect correlation but credible interpretation might be achieved. Although quantitative and automated edge detection methods provide notably precise findings, the accuracy of these approaches is not as high as the precision. As a consequence, the combination of qualitative and quantitative techniques would yield better interpretation.

Regarding the limitations of this study, it is apparent that WGM 2012 gravity anomaly is dominated by the longer wavelength components. Shorter wavelength components cannot be analyzed due to the dominant high-altitude measurements. Therefore, the RAPS results barely detect shorter wavelength components. The second limitation is that the determination of the pseudo-depth segments from RAPS is quite subjective.

Acknowledgements

We would like to express our sincere thanks to anonymous reviewers for their constructive comments.

References

Altıner, D., Koçyiğit, A. 1993. Third remark on the geology of Karakaya basin. An Anisian mega block in northern Central Anatolia: micropaleontologic, stratigraphic and tectonic implications for the rifting stage of Karakaya basin, Turkey. Revue De Paléobiologie 12(1), 1-17.

Altıner, D., Koçyiğit, A., Farinacci, A., Nicosia, U., Conti, M. A. 1991. Jurassic, lower Cretaceous stratigraphy and paleogeographic evolution of the southern part of north-western Anatolia. Geologica Romana 28, 13-80.

Amante, C., Eakins, B. W. 2009. ETOPO1 1 arc - minute global relief model: procedures, data sources, and analysis. National Oceanic and Atmospheric Administration Technical Memorandum, NESDIS NGDC-24.

Arfaoui, M., Inoubli, M. H., Tlig, S., Alouani, R. 2011. Gravity analysis of salt structures: an example from the El Kef - Ouargha region (northern Tunisia). Geophysical Prospecting 59(3), 576-591.

Arslan, S. 2016. Geophysical regional gravity map of Turkey and its general assessment. Bulletin of the Mineral Research and Exploration 153, 185-202.

Ateş, A., Kearey, P., Tufan, S. 1999. New gravity and magnetic anomaly maps of Turkey. Geophysical Journal International 136(2), 499-502.

Ateş, A., Bilim, F., Büyüksaraç, A., Aydemir, A., Bektaş, O., Aslan, Y. 2012. Crustal structure of Turkey from aeromagnetic, gravity and deep seismic reflection data. Surveys in Geophysics 33(5), 869-885.

Aydın, M., Şahintürk, Ö., Serdar, H. S., Özçelik, Y., Akarsu, I., Üngör, A., Çokuğraş, R., Kasar, S. 1986. Ballıdağ - Çangaldağ (Kastamonu) arasındaki bölgenin jeolojisi. Geological Society of Turkey Bulletin 29, 1-16.

Bhattacharyya, B. K. 1966. Continuous spectrum of the total - magnetic - field anomaly due to a rectangular prismatic body. Geophysics 31(1), 97-121.

Bilim, F. 2017. Investigating Moho depth, Curie point, and heat flow variations of the Yozgat Batholith and its surrounding area, north-central Anatolia, Turkey, using gravity and magnetic anomalies. Turkish Journal of Earth Sciences 26(6), 410-420.

Bilim, F., Koşaroglu, S., Aydemir, A., Büyüksaraç, A. 2017. Thermal investigation in the Cappadocia Region, central Anatolia - Turkey, analyzing Curie point depth, geothermal gradient, and heat-flow maps from the aeromagnetic data. Pure and Applied Geophysics 174(12), 4445-4458.

Bingöl, E., Akyürek, B., Korkmazer, B. 1975. Geology of the Biga Peninsula and some characteristics of the Karakaya Formation. Congress of Earth Sciences on the Occasion of the 50th Anniversary of the Turkish Republic. Maden Teknik Arama Genel Müdürlüğü, Ankara, 71-77.

Bonvalot, S., Balmino, G., Briais, A., Kuhn, M., Peyrefitte, A., Vales, N., Biancale, R., Gabalda, G., Reinquin, F. 2012. World gravity map: a set of global complete spherical Bouguer and isostatic anomaly maps and grids. European Geosciences Union General Assembly, 11091.

Bozkurt, E., Mittwede, S. K. 2001. Introduction to the geology of Turkey - a synthesis. International Geology Review 43(7), 578-594.

Büyüksaraç, A. 2007. Investigation into the regional wrench tectonics of inner East Anatolia (Türkiye) using potential field data. Physics of the Earth and Planetary Interiors 160(1), 86-95.

Büyüksaraç, A., Jordanova, D., Ateş, A., Karloukovski, V. 2005. Interpretation of the gravity and magnetic anomalies of the Cappadocia region, central Turkey. Pure and Applied Geophysics 162(11), 2197-2213.

Cattò, S., Cavazza, W., Zattin, M., Okay, A. I. 2018. No significant Alpine tectonic overprint on the Cimmerian Strandja Massif (SE Bulgaria and NW Turkey). International Geology Review 60(4), 513-529.

Cordell, L., Grauch, V. J. S. 1985. Mapping basement magnetization zones from aeromagnetic data in the San Juan Basin, New Mexico in the utility of regional gravity and magnetic anomaly maps. Society of Exploration Geophysicists, 181-197.

Dean, W. T., Monod, O., Rickards, R. B., Demir, O., Bultynck, P. 2000. Lower Palaeozoic stratigraphy and palaeontology, Karadere – Zirze area, Pontus mountains, northern Turkey. Geological Magazine 137(5), 555-582.

Dewey, J. F., Hempton, M. R., Kidd, W. S. F., Saroğlu, F., Şengör, A. M. C. 1986. Shortening of continental lithosphere: the neotectonics of Eastern Anatolia - a young collision zone. Geological Society Special Publication 19(1), 1-36.

Doğru, F., Pamukçu, O. 2019. Analysis of gravity disturbance for boundary structures in the Aegean Sea and western Anatolia. Geofizika 36(1), 53-76.

Doğru, F., Pamukçu, O., Özsöz, I. 2017. Application of tilt angle method to the Bouguer gravity data of western Anatolia. Bulletin of the Mineral Research and Exploration 2017(155), 213-222.

Doğru, F., Pamukçu, O., Gönenç, T., Yıldız, H. 2018. Lithospheric structure of western Anatolia and the Aegean Sea using GOCE - based gravity field models. Bollettino Di Geofisica Teorica Ed Applicata 59(2), 135-160.

Durand, B., Jolivet, L., Horvath, F., Seranne, M. 1999. The Mediterranean Basins: Tertiary extension within the Alpine Orogen. Geological Society of London 156.

Elmas, A., Yiğitbaş, E. 2001. Ophiolite emplacement by strike-slip tectonics between the Pontide Zone and the Sakarya Zone in northwestern Anatolia, Turkey. International Journal of Earth Sciences 90(2), 257-269.

Erdoğan, B. 1990. Stratigraphy and tectonic evolution of the İzmir - Ankara Zone between İzmir - Seferihisar. Turkish Association Petroleum Geology 2, 1-20.

Fairhead, J. D. 2016. Advances in Gravity and Magnetic Processing and Interpretation. European Association of Geoscientists and Engineers Publications.

Faccenna, C., Bellier, O., Martinod, J., Piromallo, C., Regard, V. 2006. Slab detachment beneath eastern Anatolia: a possible cause for the formation of the North Anatolian Fault. Earth and Planetary Science Letters 242(1–2), 85–97.

Genç, Ş. C., Yılmaz, Y. 1995. Evolution of the Triassic continental margin, Northwest Anatolia. Tectonophysics 243(2), 193-207.

Göğüş, O. H., Psyklywec, R. N. 2008. Mantle lithosphere delamination driving plateau uplift and syn-convergent extension in eastern Anatolia. Geology 36(9), 723-726.

Gottlieb, D., Shu, C. W. 1997. On the Gibbs phenomenon and its resolution. Society for Industrial and Applied Mathematics Review 39(4), 644-668.

Göncüoğlu, M. C. 2010. Introduction to the geology of Turkey: geodynamic evolution of the Pre - Alpine and Alpine terranes. Mineral Research and Exploration Monography Series 5, 1-69.

Göncüoğlu, M. C., Turhan, N., Şentürk, K., Özcan, A., Uysal, Ş., Yaliniz, M. K. 2000. A geotraverse across northwestern Turkey: tectonic units of the central Sakarya region and their tectonic evolution. Geological Society of London. Special Publications 173(1), 139-161.

Görür, N., Monod, O., Okay, A.I., Şengör, A. M. C., Tüysüz, O., Yiğitbaş, E., Sakınç, M., Akkök, R. 1997. Palaeogeographic and tectonic position of the Carboniferous rocks of the western Pontides (Turkey) in the frame of the Variscan belt. Bulletin De La Société Géologique de France 168(2), 197-205.

Görür, N., Tüysüz, O., Şengör, A. M. C. 1998. Tectonic evolution of the central Anatolian basins. International Geology Review 40(9), 831-850.

Görür, N., Çağatay, N., Sakinç, M., Akkök, R., Tchapalyga, A., Natalin, B. 2000. Neogene Paratethyan succession in Turkey and its implications for the paleogeography of the Eastern Paratethys. Geological Society of London. Special Publications 173(1), 251-269.

Gülyüz, E., Özkaptan, M., Kaymakçı, N., Persano, C., Stuart, F. M. 2019. Kinematic and thermal evolution of the Haymana basin, a fore-arc to a foreland basin in central Anatolia (Turkey). Tectonophysics 766, 326-339.

Gupta, V. K., Ramani, N. 1980. Some aspects of regional - residual separation of gravity anomalies in a Precambrian terrain. Geophysics 45(9), 1412-1426.

Harris, N. B., Kelley, S., Okay, A. I. 1994. Post-collision magmatism and tectonics in northwest Anatolia. Contributions to Mineralogy and Petrology 117(3), 241-252.

Holden, E. J., Dentith, M., Kovesi, P. 2008. Towards the automated analysis of regional aeromagnetic data to identify regions prospective for gold deposits. Computers and Geosciences 34(11), 1505–1513.

Holden, E. J., Kovesi, P., Dentith, M. C., Wedge, D., Wong, J. C., Fu, S. C. 2010. Detection of regions of structural complexity within aeromagnetic data using image analysis. International Conference Image and Vision Computing New Zealand, 1-8.

Kahveci, M., Çırmık, A., Doğru, F., Pamukçu, O., Gönenç, T. 2019. Subdividing the tectonic elements of Aegean and Eastern Mediterranean with gravity and GPS data. Acta Geophysica 67(2), 491-500.

Karig, D. E., Kozlu, H. 1990. Late Palaeogene - Neogene evolution of the triple junction region near Maraş, south - central Turkey. Journal of the Geological Society 147(6), 1023-1034.

Kaymakçı, N., White, S. H., Van Dijk, P. M. 2000. Palaeostress inversion in a multiphase deformed area: kinematic and structural evolution of the Çankırı Basin (Central Türkiye), part 1– northern area. Geological Society of London. Special Publications 173(1), 295-323.

Keskin, M. 2007. Eastern Anatolia: a hotspot in a collision zone without a mantle plume. Special Paper of the Geological Society of America 430, 693–722.

Ketin, İ. 1966. Tectonic units of Anatolia (Asia minor). Bulletin of the Mineral Research and Exploration 66, 66.

Ketin, I. 1969. About the North Anatolian Fault. Bulletin Mineral Research and Exploration Institute Turkey 72, 1-29.

Koçyiğit, A. 1987. Tectono-stratigraphy of the Hasanoğlan (Ankara) region: evolution of the Karakaya orogen. Yerbilimleri 14, 269-293.

Koçyiğit, A. 1991. First remarks on the geology of the Karakaya Basin: Karakaya orogen and Pre-Jurassic nappes in eastern Pontides, Turkey. Geologica Romana 27, 3-11.

Kovesi, P. 1997. Symmetry and asymmetry from the local phase. In Tenth Australian Joint Conference on Artificial Intelligence 190, 2-4.

Kovesi, P. 1999. Image features from phase congruency. Journal of Computer Vision Research 1(3), 1-26.

Kozur, H. W., Aydın, M., Demir, O., Yakar, H., Göncüoglu, M. C., Kuru, F. 2000. New stratigraphic and palaeogeographic results from the Palaeozoic and early Mesozoic of the Middle Pontides (northern Turkey) in the Azdavay, Devrekani, Küre, and Inebolu areas: implications for the Carboniferous - Early Cretaceous geodynamic evolution and some related remarks to the Karakaya oceanic rift basin. Geologia Croatica 53(2), 209-268.

Lam, L., Lee, S. W., Suen, C. Y. 1992. Thinning methodologies - a comprehensive survey. Institute

of Electrical and Electronics Engineers 14(9), 869-885.

Legeay, E., Ringenbach, J. C., Kergaravat, C., Callot, J. P., Mohn, G., Kavak, K. 2016. Geodynamics of the Sivas Basin (Turkey): from a forearc basin to a retro arc foreland basin. European Geosciences Union General Assembly, EPSC2016, 14961.

Maden, N., Gelisli, K., Eyüboğlu, Y., Bektaş, O. 2009. Determination of the tectonic and crustal structure of the eastern pontide orogenic belt (NE Turkey) using gravity and magnetic data. Pure and Applied Geophysics 166(12), 1987-2006.

Mallick, K., Sharma, K. K. 1999. A finite element method for computation of the regional gravity anomaly. Geophysics 64(2), 461-469.

Maus, S., Dimri, V. 1995. Potential field power spectrum inversion for scaling geology. Journal of Geophysical Research: Solid Earth 100(B7), 12605-12616.

Moix, P., Beccaletto, L., Kozur, H. W., Hochard, C., Rosselet, F., Stampfli, G. M. 2008. A new classification of the Turkish terranes and sutures and its implication for the paleotectonic history of the region. Tectonophysics 451(1-4), 7-39.

Ocakoğlu, F. 2001. Repetitive subtidal - to - coastal sabkha cycles from a Lower - Middle Miocene marine sequence, eastern Sivas Basin. Turkish Journal of Earth Sciences 10(1), 17-34.

Okay, A. I. 1989. Tectonic units and sutures in the Pontides, northern Turkey. In tectonic evolution of the Tethyan region. Springer, Dordrecht, 109-116.

Okay, A. I., Monié, P. 1997. Early Mesozoic subduction in the eastern Mediterranean: evidence from Triassic eclogite in northwest Turkey. Geology 25(7), 595-598.

Okay, A. I. Tüysüz, O. 1999. Tethyan sutures of northern Turkey. Geological Society of London. Special Publications 156(1), 475-515.

Okay, A. I., Şengör, A. C. M., Görür, N. 1994. Kinematic history of the opening of the Black Sea and its effect on the surrounding regions. Geology 22(3), 267-270.

Okay, A. I., Tansel, I., Tüysüz, O. 2001. Obduction, subduction, and collision as reflected in the Upper Cretaceous - Lower Eocene sedimentary record of western Turkey. Geological Magazine 138(2), 117-142.

Oruç, B. 2011. Edge detection and depth estimation using a tilt angle map from gravity gradient data of the Kozaklı - central Anatolia region, Turkey. Pure and Applied Geophysics 168(10), 1769-1780.

Oruç, B., Ulutaş, E., Pamukçu, O., Selim, H. H., Sönmez, T. 2019. Rheological stratification and spatial variations in the effective elastic thickness of the lithosphere underneath the central Anatolian region, Turkey. Journal of Asian Earth Sciences 176, 1-7.

Önal, K. M., Büyüksaraç, A., Aydemir, A., Ateş, A. 2008. Investigation of the deep structure of the Sivas Basin (inner east Anatolia, Turkey) with geophysical methods. Tectonophysics 460(1-4), 186-197.

Özcan, A., Göncüoğlu, M. C., Turan, N., Uysal, S., Şentürk, K., Isik, A. 1988. Late Palaeozoic evolution of the Kütahya - Bolkardağ belt: Turkey. Middle East Technical University 21, 211-220.

Özgül, N. 1976. Toroslar'ın bazı temel jeoloji özellikleri. Bulletin of the Geological Society of Turkey 19, 65-78.

Özgül, N. 1985. Geology of the Alanya region. International Ketin Symposium, Geological Society of Turkey Publication, Ankara, 97-120.

Pamukçu, O. A., Akçığ, Z., Demirbaş, Ş., Zor, E. 2007. Investigation of crustal thickness in eastern Anatolia using gravity, magnetic and topographic data. Pure and Applied Geophysics 164(11), 2345-2358.

Pamukçu, O., Yurdakul, A. 2008. Isostatic compensation in Western Anatolia with an estimate of the effective elastic thickness. Turkish Journal of Earth Sciences 17(3), 545-557.

Pamukçu, O., Gönenç, T., Yurdakul Çırmık, A., Demirbaş, Ş., Tosun, S. 2015. Vertical and horizontal analysis of crustal structure in Eastern Anatolia region. Bulletin of the Mineral Research and Exploration 151, 217-229.

Pawlowski, R. S., Hansen, R. O. 1990. Gravity anomaly separation by Wiener filtering. Geophysics 55(5), 539-548.

Robertson, A. 2004. Development of concepts concerning the genesis and emplacement of Tethyan ophiolites in the Eastern Mediterranean and Oman regions. Earth-Science Reviews 66(4), 331-387.

Robertson, A., Shallo, M. 2000. Mesozoic – Tertiary tectonic evolution of Albania in its regional eastern Mediterranean context. Tectonophysics 316(4), 197-254.

Robertson, A., Karamata, S., Šarić, K. 2009. Overview of ophiolites and related units in the Late Palaeozoic – Early Cenozoic magmatic and tectonic development of Tethys in the northern part of the Balkan region. Lithos 108(4), 1-36.

Rojay, B., Altıner, D. 1998. Middle Jurassic - Lower Cretaceous biostratigraphy in the Central Pontides (Turkey): remarks on paleogeography and tectonic evolution. Rivista Italiana di Paleontologia e Stratigrafia 104(2).

Rotstein, Y. 1984. Counterclockwise rotation of the Anatolian block. Tectonophysics 108(2), 71-91.

Saramaeki, T., Mitra, S. K., Kaiser, J. F. 1993. Finite impulse response filter design. Handbook for digital signal processing 4, 155-277.

Sarı, C., Şalk, M. 2002. Analysis of gravity anomalies with hyperbolic density contrast: An application to the gravity data of western Anatolia disaster-resilient cities view project analysis of gravity anomalies with hyperbolic density contrast: an application to the gravity data of Western Anatolia. International Journal of the Balkan Geophysical Society 5, 3.

Şaroğlu, F., Yilmaz, Y. 1986. Geological evolution and basin models during a neotectonic episodes in Eastern Anatolia. Bulletin of the Mineral Research and Exploration 107, 107.

Şengör, A. M. C. 1979. Mid - Mesozoic closure of Permo - Triassic Tethys and its implications. Nature 279, 590-593.

Şengör, A. M. C. 1984. The Cimmeride orogenic system and the tectonics of Eurasia. Geological Society of America Special 195, 82.

Şengör, A. M. C. 1987. Tectonics of the Tethysides: orogenic collage development in a collisional setting. Annual Review of Earth and Planetary Sciences 15(1), 213-244.

Şengör, A. M. C., Yılmaz, Y. 1981. Tethyan evolution of Turkey: a plate tectonic approach. Tectonophysics 75(4), 181-241.

Şengör, A. M. C., Kidd, W. S. F. 1979. Post-collisional tectonics of the Turkish - Iranian plateau and a comparison with Tibet. Tectonophysics 55(3–4), 361–376.

Şengör, A. M. C., Yılmaz, Y., Ketin, I. 1980. Remnants of a pre–Late Jurassic ocean in northern Turkey: fragments of Permian-Triassic Paleo-Tethys. Geological Society of America Bulletin 91(10), 599-609.

Şengör, A. M. C., Görür, N., Şaroğlu, F., Biddle, K. T., Christie Blick, N. 1985. Strike-slip deformation, basin formation, and sedimentation. Society of Economic Palaeontologists and Mineralogists. Special Publication 37, 227-264.

Sherlock, S., Kelley, S., Inger, S., Harris, N., Okay, A. 1999. ^{40}Ar - ^{39}Ar and Rb - Sr geochronology of high-pressure metamorphism and exhumation history of the Tavşanlı Zone, NW Turkey. Contributions to Mineralogy and Petrology 137(2), 46-58.

Simpson Jr, S. M. 1954. Least-squares polynomial fitting to gravitational data and density plotting by digital computers. Geophysics 19(2), 255-269.

Spector, A., Grant, F. S. 1970. Statistical models for interpreting aeromagnetic data. Geophysics 35(2), 293-302.

Stampfli, G. M. 2000. Tethyan oceans. Geological Society of London. Special Publications 173(1), 23.

Tekeli, O. 1981. Subduction complex of pre - Jurassic age, northern Anatolia, Turkey. Geology 9(2), 68-72.

Tirel, C., Gueydan, F., Tiberi, C., Brun, J. P. 2004. Aegean crustal thickness is inferred from gravity inversion. Geodynamical implications. Earth and Planetary Science Letters 228(3-4), 267–280.

Ustaömer, T., Robertson, A. H. 1999. Geochemical evidence used to test alternative plate tectonic models for pre-Upper Jurassic (Palaeotethyan) units in the central Pontides, N Turkey. Geological Journal 34(2), 25-53.

Yılmaz, Y. 1993. New evidence and model on the evolution of the southeast Anatolian orogen. Geological Society of America Bulletin 105(2), 251-271.

Yılmaz, Y., Yıldırım, M. 1996. Geology and evaluation of the nap region (the metamorphic massifs) of the Southeast Anatolian Orogenic Belt. Turkish Journal of Earth Sciences 5(3), 21-38.

Bulletin of the Mineral Research and Exploration

http://bulletin.mta.gov.tr

Extraction of rubidium from Malatya - Kuluncak area complex ore

Ayşe ERDEM[a*], Hüseyin Eren OBUZ[a], Haydar GÜNEŞ[a], Şölen DİKTEPE[a], Buse ÖZEN İLİK[a], Çiğdem KARA[a], Hasan AKÇAY[a], Akan GÜLMEZ[a] and Zümrüt ALKAN[a]

[a]*General Directorate of Mineral Research and Exploration, Department of Mineral Analysis and Technology, 06800, Ankara, Türkiye*

Research Article

Keywords:
Leaching, Roasting, Rubidium.

ABSTRACT

In this study, studies were carried out to take rubidium (Rb), which is in a complex form of Na +K feldspar, pyroxene, and alumina silicate into solution in an environmentally sensitive manner with high recovery. Malatya - Kuluncak complex ore was used in this study. In the first stage of the study, the roasting method was tried to obtain rubidium chloride (RbCl) or rubidium sulphate (Rb_2SO_4) structures, which are the water-soluble forms of rubidium in the sodium-potassium feldspar minerals. Roasting was carried out using different additives and calcium chloride was identified as the most suitable additive material for this ore structure. In studies investigating the effect of roasting temperature and time, the evaporation amount of RbCl was calculated. After deciding on the additives, the additive amount, solid/liquid ratio in the leaching stage, and leach time were optimized. The optimum conditions were determined as a leaching time of 120 minutes at 1/3 solid/liquid ratio after roasting for 60 minutes at the roasting temperature of 900 °C at 70% calcium chloride ($CaCl_2$) addition. the solution efficiency of rubidium was calculated as 96%. Taking Rb into solution from primary sources was first achieved with this study in Türkiye.

Received Date: 24.04.2021
Accepted Date: 16.09.2021

1. Introduction

Rubidium (Rb) was first discovered by German chemists Bunsen, R. W. and Kirchhoff, G. R. in 1861. As a member of the alkali metals, the element Rubidium was described as a having low fusing point (39 °C), high plasticity, soft, and silvery-white in color. (Patnaik, 2003; Zhou et al., 2015). Although it is the most commonly found 16th element in nature, no minerals of rubidium are found. Therefore, the total production of the element varies between 2 to 4 tons annually (Butterman and Reese Jr, 2003). Rb is obtained as a by-product of potassium [(K,Rb) $Li_2AlSi_4O_{10}F_2$] production from the lepidolite mineral and cesium production from ($Cs_2Al_2Si_4O_{12}$) the pollucite mineral. (Patnaik, 2003; Shan et al., 2013; Tavakoli et al., 2015; Xing et al., 2018; Zeng et al., 2019; Liu et al., 2019).

Rubidium and its compounds are popular in space, nuclear, advanced technology and energy industries. Since Rb ionizes easily, it was considered to be used in ion engines, yet cesium is known to be more efficient in this field. Rubidium-87 is used in atomic clocks due to its electron structure. It was used to locate brain tumors since it does not accumulate on normal tissue, and its radioactive properties. (Butterman and Reese Jr, 2003; Wagner, 2011; Heynes et al.,2016; Ertan and Erdoğan, 2017).

Citation Info: Erdem, A., Obuz, E. H., Güneş, H., Diktepe, Ş., İlik Özen, B., Kara, Ç., Akçay, H., Gülmez, A., Alkan, Z. 2022. Extraction of rubidium from Malatya - Kuluncak area complex ore. Bulletin of the Mineral Research and Exploration 168, 131-140. https://doi.org/10.19111/bulletinofmre.997306

**Corresponding author: Ayşe ERDEM, ayse.erdem@mta.gov.tr*

The roasting method is described as processing elements in relatively high temperatures without excessing the melting temperature under suitable atmospheric conditions to induce chemical changes in their structures.Chlorination roasting, on the other hand, is commonly used for taking insoluble metal compounds into the solution by transforming them into soluble metal chlorides. Alkali metals sodium, potassium and Rb are highly soluble in water in their chloride salt forms. Through the process of chlorination roasting of the alkali elements, water soluble alkali metal chloride salts are obtainable. Rubidium chloride (RbCl) can have evaporation behavior above its melting temperature of 718 °C. An alternative method for this process is the sulphation roasting. To achieve the formation of Rb_2SO_4 and its dissolution, insoluble alkali compounds must be heated to the formation heat of the salt, the presence of sulphate. Upon the heating process, highly water-soluble alkali sulphate salts are obtained. Using these methods together may result in more efficient solubility (Gupta, 2003; Yan et al., 2012; Tavakoli et al., 2015; Zheng et al., 2016; Xing et al., 2018; Zeng et al., 2019; Wang et al., 2020).

Studies are carried out on the production of rubidium element from both primary and secondary sources. For the production from secondary sources, the wastes of gold, kaolin clay and boron clay were used. Direct leaching and chlorination roasting – water leaching methods were used in these studies. Obtaining Rb from kaolin clay wastes (0.21% Rb) by acid leaching and chlorination roasting – water leaching is studied by Zhou et al. (2015). In both methods, the efficiency of taking Rb into solution was evaluated. The methods were compared based on the metal recoveries. Zhou et al. (2015) determined the chlorination roasting – water leaching method to be more suitable for kaolin clay wastes when compared to acid leaching method. Rb that is contained in the ore was taken into solution with 90.6% recovery. Another study about waste was carried out by Ertan and Erdoğan (2017) for Rb recovery from boron wastes. They used HF in their chlorination roasting and acid extraction process. Although HF was more efficient in the destruction of silicate structures, they decide that this is not the preferred method due to its hazardous nature to humans and the environment. Another study was carried out with waste of Mouteh which is one of the largest gold processing plant. These wastes contain 120 ppm Rb. The mentioned study consists of three main stages: In the first stage, nitric acid leaching is used to remove unwanted elements from the wastes. In the second stage, salt mixtures are used for roasting. In the third and the final stage, Rb is taken into the solution using with water leaching. For the process of roasting, a mixture of sodium sulphate and calcium chloride was used. The Rb conversion rate was calculated as 90.95%. In the water leaching stage 90.95% percent of the Rubidium sulphate and 97.14% of rubidium chloride was taken into solution (Tavakoli et al., 2015; Zhou et al., 2015; Ertan and Erdoğan, 2017).

For the production of Rb from primary sources, rocks and minerals which contain Rb such as granite, biotite and zinnwaldite etc. are generally used in literature. In recent studies, roasting – water leaching, acid leaching and reaction with sulphuric acid methods were used. For production of Rb from biotite, Zeng et al. (2019) used chlorination roasting – water leaching and direct acid leaching as two distinct methods. The recovery of metal from source was calculated as 96.25% with direct acid leaching while it was improved to 97.15% with roasting-water leaching. Ultimately, chlorination roasting – water leaching method provides a higher efficiency in taking Rb into solutions, as compared to sulphuric acid leaching.

Possible reactions of ores containing rubidium in chlorination roasting are presented in Equations 1, 2 and 3 (Zeng et al., 2016, 2019)

$$CaCl_2+2SiO_2+Al_2O_3+Rb_2O = CaAl_2Si_2O_8+2RbCl \quad (1)$$

$$CaCl_2+2SiO_2+Rb_2O = CaSiO_3+2RbCl \quad (2)$$

$$CaCl_2+Al_2O_3+3Rb_2O = Ca_3Al_2O_6+6RbCl \quad (3)$$

However, in chlorination roasting – water leaching method, more K is taken into solution with a higher amount of Rb, as compared to sulphuric acid leaching method. More K in solution together with Rb complicates downstream process to extract Rb. Taking into solution process of Rb-containing granitic rocks with alkaline leaching is studied by Xing et al. (2018). In this study, a sodium hydroxide solution was used at 230 °C, to break the structure that Rb is attached, which allows for the uptake of Rb into the solution with a very high

level of efficiency (95%). To remove the silica from the solution, precipitation with calcium oxide technique is utilized. Subsequently, tert-Butyl-2-(α-Methylbenzyl) Pheno (t-BAMBP) is used to separate K and Rb from each other. Finally end-product rubidium chloride and potassium chloride (KCl) were obtained. Another study was carried out by Vu et al. (2013) to produce lithium and Rb from zinnwaldite mineral. In that study, $CaCO_3$ is used for sintering, followed by water leaching and alkaline leaching methods. The efficiency rates of elements taking into solution were determined to be 84% for lithium and 91% for rubidium. Studies on Rb production based on the ore and wastes vary depending on the structure of the ore and the type of waste. (Zeng et al., 2019).

In this study, experiments were conducted to take Rb element that is contained in complex ore structures into solution with a high rate of efficiency in an eco-sensitive motivation. The effects of using different substances in roasting on the Rb conversion and passing into solution rates are examined and the process is optimized. This study is the first of its kind in Türkiye, in taking Rb into solution with a high degree of efficiency from primary sources. Additionally, analysis methods such as SEM, XRF and XRD were used to examine the extraction mechanisms in detail. The ore used within the framework of the study being complex; consists of ~45% Na + K feldspar (Na - K - $AlSi_3O_8$) as main mineral, ~%20 pyroxene (Ca, Na, Fe, Mg, Mn – Si_2O_6), ~11-12% alumina silicate (clay, mica) and 6% calcite minerals. The RbO_2 content of the ore was calculated to be 0.05% by weight.

2. Experimental Studies

2.1. Raw Material and Experiment Equipment

The ore used in the study was provided by Malatya-Kuluncak prospect area belonging to the General Directorate of Mineral Research and Exploration (Öztürk et al., 2019; Pulat et al., 2022). It contains 0.05% RbO_2. Calcium chloride ($CaCl_2.2H_2O$ 99% pure), sodium chloride (NaCl 99.5% pure) and sodium sulphate ($Na_2SO_4.10H_2O$ 97% pure) were provided by ISOLAB.

For the process of chlorination roasting, box furnace (Nevola Reis 120/18) was used. The concentrations of elements in the solution were measured with Agilent 725 Series Inductively Coupled Plasma Atomic Emission Spectroscopy (ICP-OES) device. Metal compositions in the input and output samples were determined with Thermo Scientific ARL Perform's X-Ray Fluorescence Spectroscopy device. For the determination of ore structure in the input sample, Panalytical X'pert Pro was used. Electron microscope imaging and EDS analyses were performed with the FEI inspect F50 Scanning Electron Microscope (SEM-EDS) device.

2.2. Method

The entire ore was firstly ground to 53 microns and homogeneously mixed with calcium chloride solid at predetermined proportions. This homogeneous mixture was then placed into alumina-silica crucibles. Structural water was taken into consideration while calculating additives. Crucibles were put into the box furnace at room temperature and were roasted at desired temperature and for certain duration. Upon roasting, the crucibles were taken out of the box furnace and left out to cool down in desiccator for 24 hours at room temperature. In the preliminary roasting experiments, the effects of additives ($CaCl_2$, NaCl and Na_2SO_4) were examined. For the experiments to determine the roasting temperature, the effects of different temperatures (800, 850 and 900 °C) and different additive proportions (10%, 30%, 50%, 70% and 90%) were evaluated.

After the roasting process, samples were ground homogeneously. The ground samples were weighed on Precisa XB 320M. Then, water leaching experiments were performed with 250 mL beakers using magnetic stirrers (Heidolph, MR Hei-Standard). In the water leaching process, the solid sample on the beaker was mixed with pure water at predetermined proportions. Subsequently, as the water leaching process was finalized, solid/liquid separation was performed using blue ribbon filter papers. During the optimization of leaching process, different solid/liquid ratios (1/2, 1/3, 1/4) and leaching durations (60, 120, 180 minutes) were observed. All experiments were conducted with 100 grams of ore. Solids were analyzed with XRF and XRD spectrometers while for the liquids ICP-OES analysis was performed. Flow chart of the method is given in Figure 1.

2.3. Data Processing

In processing of the experimental data, Equations 4-6 were used.

$$\tau_1 = \frac{c_1 \times V_1}{m_0 \times c_0} \quad (4)$$

$$\tau_2 = \frac{m_r \times c_r}{m_0 \times c} \quad (5)$$

$$\tau_3 = 1 - \tau_2 - \tau_1 \quad (6)$$

τ_1, τ_2 and τ_3 represent Rb leaching efficiency, the amount of Rb left in solid after the leaching process, and the ratio of evaporated Rb, respectively. The c_1 in Equation 4 represents the amount of Rb that is inside the solution while the c_0 is the amount of Rb in the solid part. The c_r in Equation 5 is the amount of Rb in solid after the leaching process. The V_1 in Equation 4 represents the volume after liquid leaching.

3. Findings

3.1. Preliminary Roasting Experiments

In the preliminary roasting experiments, the effects of the addition of calcium chloride and sodium sulphate-sodium chloride salts on the efficiency of taking Rb into the solution were examined.

Within the context of preliminary roasting experiments, parameters such as roasting temperature (900 °C), roasting duration (60 min), water leaching (60 min), and the solid/liquid ratio (1/3) were held fixed in order to evaluate only the effect of additives. Reactions were observed when chlorination and sulphatization roasting were done at 800-900 °C and 700 – 900 °C, respectively. (Alonso et al., 2012; Zheng et al., 2016). Therefore, the temperature was selected as 900°C for the preliminary experiments. The effects of the additives on the efficiency of taking Rb into the solution in this study are presented in Table 1.

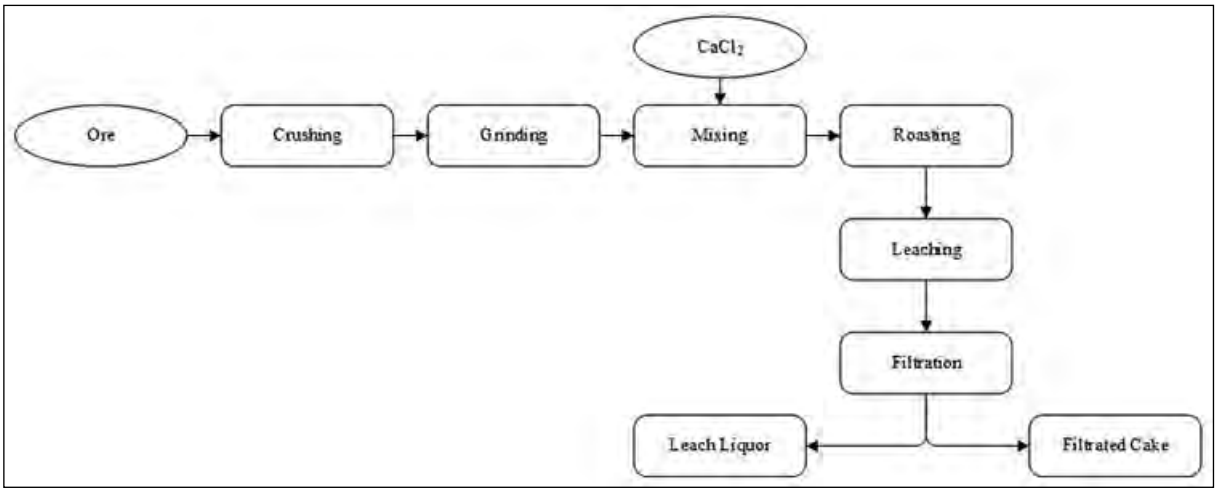

Figure 1- Flow chart of the method.

Table 1- The effects of the ratio of roasting additives on the efficiency of taking Rb into the solution.

Roasting Conditions				Efficiency of Taking Rb into Solution (%)
Unit (Ore)	Unit ($CaCl_2$)	Unit (NaCl)	Unit (Na_2SO_4)	
100	50	-	-	78.3
100	50	20	-	38.5
100	40	30	-	36.6
100	30	40	-	35.2
100	50	-	20	33.4
100	40	-	30	24.5
100	30	-	40	18.2

The experimental results at roasting conditions show that the highest rate of efficiency is obtained when only calcium chloride is used for taking Rb into the solution. In this ore structure, especially the sodium is observed to have a negative effect in taking Rb into the solution. In an instance where sodium chloride is accompanied with calcium chloride, the ratio of the negative effects of sodium chloride on the efficiency seems to be almost the same even if its amount is increased. Calcium chloride seems to be the most effective roasting additive for this ore structure. Thus, only calcium chloride was used for the optimization processes.

3.1.1. Effect of Roasting Time and the Temperature

Firstly, the entire ore size was ground to 53 µm and mixed with a predetermined amount of calcium chloride. Then, roasting was carried out at temperatures of 800, 850, 900 °C. While examining the effects of duration and temperature of roasting; parameters such as leaching duration (60 min), $CaCl_2$ additive amount (50%) and solid/liquid ratio (1/3) were held fixed. The effects of duration for each roasting temperature were also examined. The schematic display of the analyses' results are given in Figure 2. For the 60-minute roasting process, it is seen that changing the roasting temperature from 800°C to 850°C increases the efficiency of taking Rb into the solution by 37% and 5% when the temperature is increased to 900 °C. This increase in the roasting temperature correlates with the experimental result of Zeng et al. (2019) on the roasting temperature. When the temperature approaches 900 °C, solution efficiency decreases.

As the effect of 120-minute roasting time, 1% increase in efficiency is observed when the temperature is increased from 800 °C to 850 °C and 5% increase in efficiency is observed when the temperature is increased from 850 °C to 900°C. While the roasting

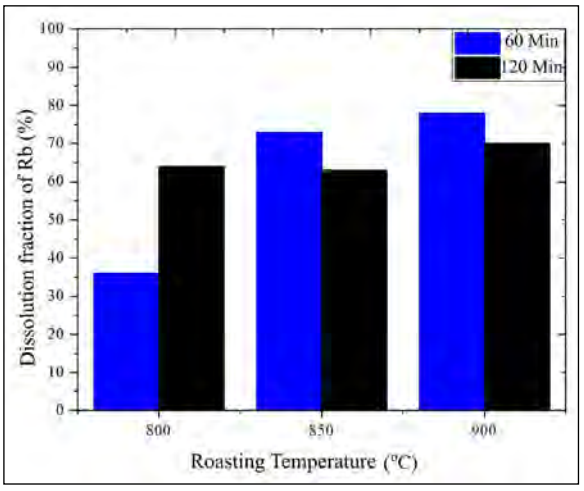

Figure 2- The effects of roasting temperature and duration on Rb dissolution.

duration experiments conducted at 800 °C result in a positive effect for the conversion of Rb into RbCl, for the temperatures of 850 °C and 900 °C an increase in roasting duration affected negatively. This is caused by the RbCl vaporization at high temperatures. The effects of roasting duration and temperature on the efficiency of taking Rb into solution and RbCl vaporization is given in Table 2. When the data in Table 2 is examined, the optimum roasting temperature is determined to be 900 °C with 60 minutes of roasting duration.

3.2. The Effect of Calcium Chloride Amount

After the optimization of roasting temperature and duration, the effects of $CaCl_2$ additive amount on the recovery of taking Rb into the solution were examined. Parameters of the leaching duration (60 minutes) and the leaching solid/liquid ratio as (1/3) were kept fixed. Experiments were conducted by using the additives of $CaCl_2$ at 10 - 30 - 50 - 70 and 90% ratios.

In Figure 3, the efficiency of $CaCl_2$ on taking Rb into solution is given. In this study, a change in the

Table 2- Effects of roasting temperature and duration on efficiency.

Roasting Temperature (°C)	Roasting Duration (min.)	τ_1(%)	τ_2 (%)	τ_3(%)
800	60	35.8	63.2	0.0
800	120	63.8	36.0	0.0
850	60	73.0	24.2	2.8
850	120	64.2	21.4	14.4
900	60	82.5	13.3	4.2
900	120	69.7	12.2	18.1

amount of $CaCl_2$ from 10% to 30% results in a 39% increase in efficiency of taking Rb into solution. A change in $CaCl_2$ amount from 30% to 50% yields 29% increase in efficiency whereas a respective change in $CaCl_2$ amount from 50% to 70% results in a 5% increase in efficiency. A change in the calcium chloride by more than 70% does not affect the conversion rate. This phenomenon is a result of the reaction ending as all Rb atoms found in feldspar convert into RbCl. The lack of increase in the efficiency of taking Rb into the solution despite the end of reaction is related with the solid/liquid and duration parameters during the leaching process. When the effects of $CaCl_2$ additive on the efficiency of taking Rb into the solution are examined, similar results are obtained as compared to the results of the studies of Zheng et al. (2016) carried out with kaolin. Their studies, as similar to our study, show an increase in efficiency as the calcium chloride amount is increased until a point is reached where the efficiency remains constant.

3.3. The Effect of Solid/Liquid Ratio

Leaching duration (60 min.) in the solid/liquid ratio optimization stage, and the amount of $CaCl_2$ additive (70%) were kept fixed. For the examination of the effects of solid/liquid, ratios of 1/2 – 1/3 and 1/4 were used. The effects of parameters on the efficiency of taking Rb into solution is given in Figure 4.

In this study, a change in solid/liquid ratio from 1/2 to 1/3 results in 9% increase in efficiency of taking Rb into solution while the respective efficiency remains constant at a solid/liquid ratio change from 1/3 to 1/4. This is attributed to taking the entire Rb that is converted into solution. Therefore, 1/3 solid/liquid ratio is specified as the optimum parameter.

3.4. The Effect of Leaching Duration

In this study, the durations of 60, 120 and 180 minutes were tested while the parameters of solid/liquid (1/3) and $CaCl_2$ (70%) were kept fixed. The respective results are given in Figure 5. The results show that a change in the duration of leaching from 60 to 120 minutes results in a 9% increase in efficiency of taking Rb into solution. On the other hand, a change in the duration of leaching to 180 minutes lowers the efficiency by 1%. Hence, a duration longer than 120 minutes does not affect the efficiency of taking Rb into solution.

Figure 6a shows the SEM image of the input sample whereas Figure 6b shows the SEM image of the sample after roasting with 70% $CaCl_2$, a duration of 60 minutes at 900°C. As observed in Figure 6a, feldspar crystal is clearly visible. Figure 6b shows that the crystal structure of feldspar is alterated and new structures are formed. These new structures

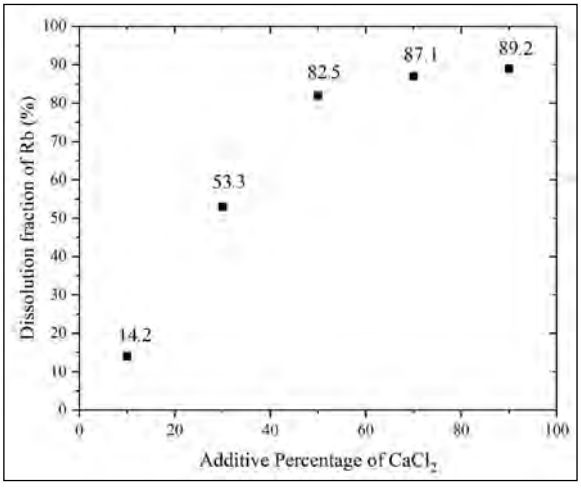

Figure 3- The effects of the amount of $CaCl_2$ Additive on the efficiency of taking Rb into solution.

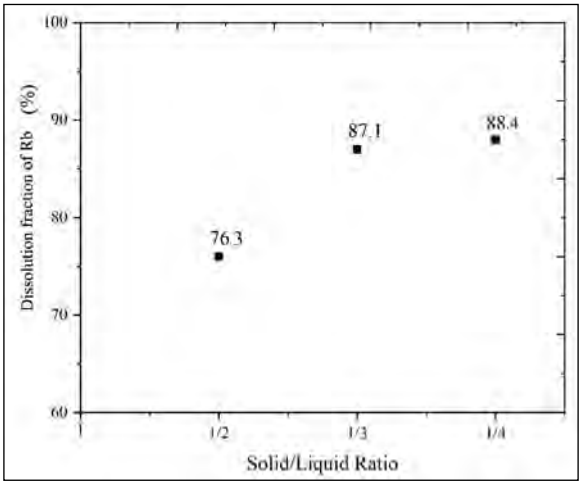

Figure 4- The effects of solid/liquid ratio on the efficiency of taking Rb into solution.

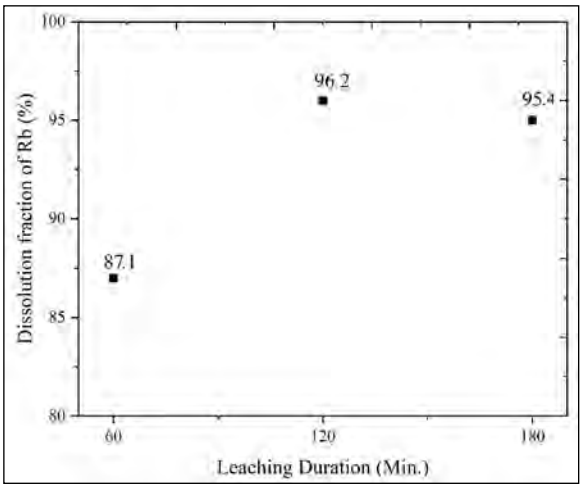

Figure 5- The effects of leaching duration on the efficiency of taking Rb into solution.

were analyzed with XRD analyses. Pre-roasting chlorination, post-roasting and post-extraction structures are given in Figure 7.

XRF analyses' results of the output solid from the roasting – water leaching on the input ore are given in Table 3. When the analyses' results are examined, it is seen that 96% of Rb is taken into solution with 4% evaporation. Additionally, the efficiency of potassium and sodium elements in taking into solution are determined as 92.6% and 59.0% respectively.

According to the Table 3, calcium oxide amount in the input ore increases from 1.41% to 13.13% after roasting – leaching process. The increase in the calcium oxide is the result of reactions given in Equation 1 – 3. In the reaction between calcium fluoride and feldspar, chloride ion bonds with rubidium, sodium and potassium, which creates rubidium chloride. Meanwhile, calcium, aluminum and silicon create a triple bond, resulting in a calcium alumina silicate structure. Therefore, in the XRF analysis, an increase in calcium oxide at the solid is observed after the leaching.

XRD analyses of the input sample (Figure 7a), chlorination roasting (Figure 7b) and leaching (Figure 7c) were performed for this study. When Figure 7a is examined, feldspar and albite are determined in the input sample. After roasting with calcium chloride (Figure 7b), an alterated of K-feldspar to rubidium chloride, sodium chloride, potassium chloride, silica (SiO_2) and andesine [$(Ca,Na)(Al,Si)_4O_8$] mineral is observed. Also, the salts from alkali K, Na and Rb metals contained in K-feldspar are obtained. When the next step, the extraction process (Figure 7c), is examined, alkali metal salts are dissolved and the minerals such as albite [(Na,Ca)AlSi3O8] and hibschite [Ca3Al2(SiO4)2(OH)4] remain undissolved. Reactions during roasting are given in Equations 1 – 3.

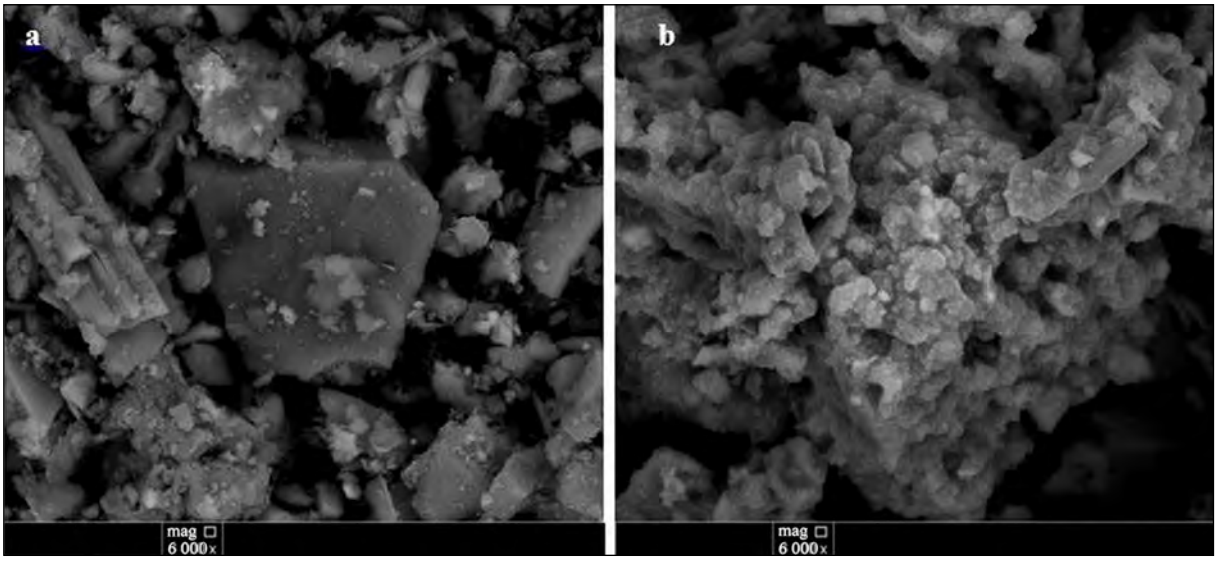

Figure 6- a) Input sample and, b) SEM imaging after roasting.

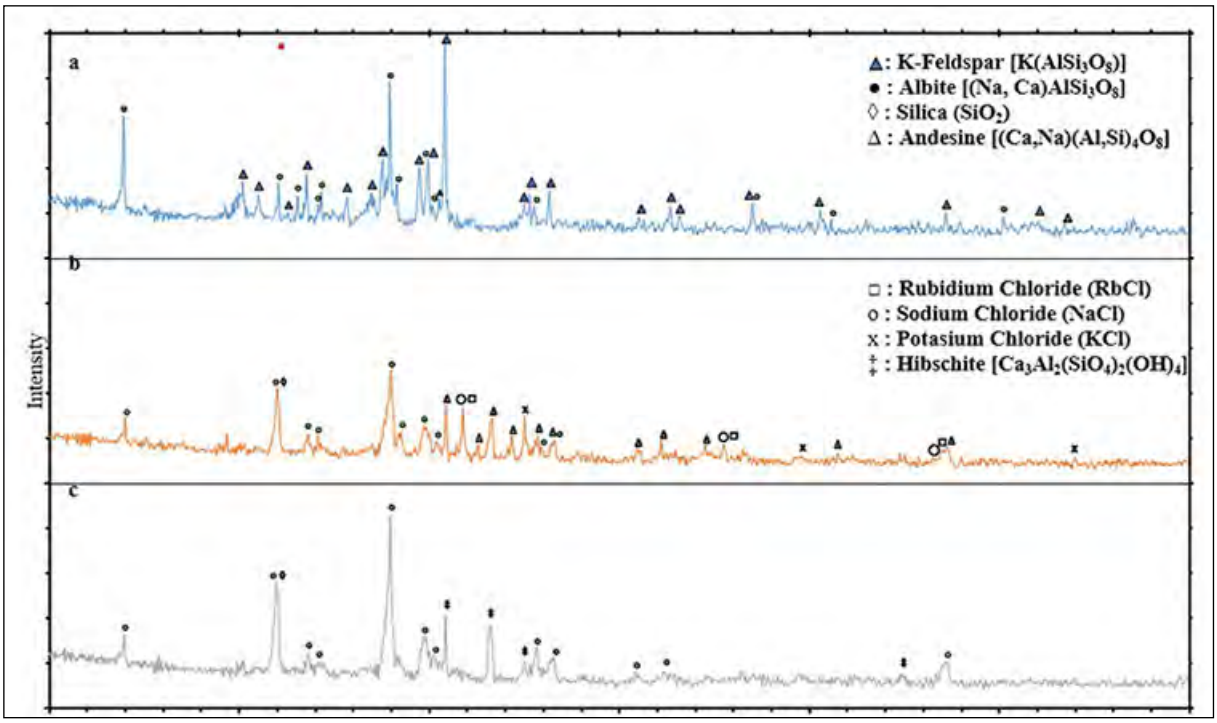

Figure 7- XRD powder sample results in order; a) before roasting, b) after chlorination roasting and c) after leaching.

Table 3- Before and after leaching XRF results of the solid.

Compound	Al_2O_3	CaO	Fe_2O_3	K_2O	MgO	Na_2O	Rb_2O	SiO_2	A.ZA	Other
Ore input (%)	15.8	1.4	8.4	4.7	1.8	4.1	0.05	56.7	4.1	3.7
After leaching (%)	14.4	13.2	7.8	0.6	1.2	1.7	0.00	56.4	1.4	3.3

As the amount of Rb in the sample after roasting is very low, the determination of the element is not expected at the XRD analysis. However, it is possible to determine the salts, such as NaCl and RbCl, in solid as these compounds peak at the same angles (2θ: 31.8, 45.7, 56.7).

4. Discussion

In the literature, maximum efficiency was achieved by taking Rb into solution when calcium chloride is added only. Sodium sulphate affects negatively whereas sodium chloride has no negative or positive effect. Therefore, calcium chloride was selected as additive material for the experiments.

After the decision of using calcium chloride as a roasting additive, experiments were conducted at different roasting temperatures. In this context, RbCl vaporization was also taken into account for the calculations. The effects of vaporization were presented with analyses and calculations. Especially, 120-minute experiments were conducting at increasing roasting temperatures and durations. Within this experimental framework, optimum parameters were determined.

Subsequently, the effects of additives were examined after the effects of roasting temperatures. During this examination, the effects of additive increase at taking Rb into solution were calculated and it is given in the Table 1. Certain amount of chloride ions are necessary in the environment to take the entire Rb in feldspar to solution. Therefore, an increase in the efficiency is observed when the amount of calcium chloride increases. In contrast, no increase in efficiency is observed for $CaCl_2$ level above 70% due to the fact that conversion is finalized. Lack of higher increase in efficiency after the end of reaction

is related to solid/liquid ratio and duration parameters during the leaching process.

An overlook of the solid/liquid ratio parameter points out the requirement of sufficient amount of water present in the environment to take Rb fully into solution. An increase in the solid/liquid ratio to 1/3 ratio results in a positive effect while the efficiency remains constant at higher ratios. This is due to $CaCl_2$, NaCl and KCl salts accompanying RbCl in solid. As these salts have a high solubility rate, an increase in efficiency is observed until the environment reaches a sufficient level of water.

Another important parameter during the leaching process is the duration. An increase in the duration of leaching process causes an increase in the efficiency of taking Rb into solution. However, the efficiency remains stable even if the duration increases. This is speculated to be caused by the entire structure of RbCl being taken into solution with water. It is not possible to achieve higher levels of efficiency due to RbCl vaporization, as previously mentioned.

5. Results

In this study, roasting process is used as the beginning stage of taking Rb element into the solution containing feldspar mineral within the complex ore structure. RbCl is obtained in the roasting stage, and taken into solution with water leaching.

Calcium chloride was observed to be the most effective additive compound. Subsequently, the effects of roasting temperature and duration were examined.

In the stages of examining the effects of different roasting temperatures and durations, the evaporation amount of RbCl was determined. It is observed that an increase in roasting temperature and duration results in more evaporation. Evaporation factor was taken into account in determining temperature and duration of roasting. In this study, the optimum roasting temperature and duration were determined as 900 °C and 60 minutes, respectively.

Upon determining the roasting duration, the temperature and the additive, experiments were conducted on the additive amount. The optimum additive amount needed to achieve the highest efficiency was determined as 70% in experiments using $CaCl_2$ at different proportions ranging from 10% to 90%.

After the optimum roasting parameters were determined, solid/liquid ratio and leaching durations were examined. The highest efficiency was achieved at 1/3 solid/liquid ratio.

Following that, the effects of leaching duration on the efficiency of taking Rb into solution were examined. In these examinations, the optimum duration was determined as 120 minutes. However, longer durations do not increase the efficiency.

In the studies carried out, optimum parameters were determined as 70% $CaCl_2$ additive amount, 900 °C roasting temperature, 60 minutes of roasting duration, 1/3 solid/liquid ratio, 120 minutes of water leaching. The efficiency of taking Rb into solution was determined to be 96.2% in these conditions.

Acknowledgements

This study was carried out within the scope of the Scientific Research project coded 35-16-01-03 of the General Directorate of Mineral Research and Explorations. We take this opportunity to thank Research Assistant Dr. Erkan İLİK of Eskişehir Osmangazi University for his generous support, Ebru KAVUÇU of the General Directorate of Mineral Research and Exploration, Ufuk KİBAR for SEM imaging and Ayşe KOYUNCU for the XRF analyses.

References

Alonso, E., Sherman, A. M., Wallington, T. J., Everson, M. P., Field, F. R., Roth, R., Kirchain, R. E. 2012. Evaluating rare earth element availability: a case with revolutionary demand from clean technologies. Environmental Science and Technology 46(6), 3406–3414.

Butterman, W., Reese Jr., R. 2003. Mineral commodity profiles-rubidium. United States Geological Survey, Report No: 45.

Ertan, B., Erdoğan, Y. 2017. Two methods on rubidium extraction from boron clays. Advances in Ecological and Environmental Research, 281–291.

Gupta, C. K. 2003. Chemical Metallurgy: Principles and Practice. Chemical Metallurgy, Wiley.

Heynes, W. M., Lide, D. R., Bruno, T. J. 2016. Handbook of Chemistry and Physics. CRC Press, Florida.

Liu, J., Yin, Z., Li, X., Hu, Q., Liu, W. 2019. A novel process for the selective precipitation of valuable metals from lepidolite. Minerals Engineering 135, 29-36.

Öztürk, H., Hanilçi, N., Altuncu, S., Kasapçı, C. 2019. Rare earth element (REE) resources of Turkey: An overview of their characteristics and origin. Bulletin of the Mineral Research and Exploration 159, 129–143.

Patnaik, P. 2003. Handbook of inorganic chemicals. Choice Reviews Online 40(11), 40–6428.

Pulat, O., Karakaş, M., Yastı, M. A. 2022. Relationship of ore properties and alteration of the Büyük Kuluncak (Malatya) Nb - U - NTE - Zr - Li deposit. Bulletin of the Mineral Research and Exploration 167, 127-148.

Shan, Z. Q., Shu, X. Q., Feng, J. F., Zhou, W. N. 2013. Modified calcination conditions of rare alkali metal Rb-containing muscovite ($KA_{l2}[AlSi_3O_{10}](OH)_2$). Rare Metals 32(6), 632–635.

Tavakoli, M. M. R., Javad Koleini, S. M., Javanshir, S., Abolghasemi, H., Abdollahy, M. 2015. Extraction of rubidium from gold waste: process optimization. Hydrometallurgy 151, 25–32.

Vu, H., Bernardi, J., Jandova, J., Vaculikova, L., Golias, V. 2013. Lithium and rubidium extraction from zinnwaldite by alkali digestion process: sintering mechanism and leaching kinetics. International Journal of Mineral Processing 123,9-17.

Wagner, F. S. 2011. Rubidium and Rubidium Compounds. Kirk-Othmer Encyclopedia of Chemical Technology, John Wiley and Sons, Inc.

Wang, J., Hu, H., Wu, K. 2020. Extraction of lithium, rubidium and cesium from lithium porcelain stone. Hydrometallurgy, 191.

Xing, P., Wang, C., Ma, B., Wang, L., Zhang, W., Chen, Y. 2018. Rubidium and potassium extraction from granitic rubidium ore: process optimization and mechanism study. ACS Sustainable Chemistry and Engineering 6(4), 4922–4930.

Yan, Q. X., Li, X. H., Wang, Z. X., Wang, J. X., Guo, H. J., Hu, Q. Y., Peng, W. J., Wu, X. F. 2012. Extraction of lithium from lepidolite using chlorination roasting-water leaching process. Transactions of Nonferrous Metals Society of China 22(7), 1753–1759.

Zeng, Q., Huang, L., Ouyang, D., Hu, Y., Zhong, H., He, Z. 2019. Process optimization on the extraction of rubidium from rubidium-bearing biotite. Minerals Engineering 137, 87–93.

Zheng, S., Li, P., Tian, L., Cao, Z., Zhang, T., Chen, Y., Zhang, Y. 2016. A chlorination roasting process to extract rubidium from distinctive kaolin ore with alternative chlorinating reagent. International Journal of Mineral Processing 157, 21–27.

Zhou, L., Yuan, T., Li, R., Zhong, Y., Lei, X. 2015. Extraction of rubidium from kaolin clay waste: process study. Hydrometallurgy 158, 61–67.

Bulletin of the Mineral Research and Exploration

http://bulletin.mta.gov.tr

Coulomb stress changes and magnitude-frequency distribution for Lake Van region

Hamdi ALKAN[a*] and Erdem BAYRAK[b]

[a]*Van Yüzüncü Yıl University, Faculty of Engineering, Department of Geophysics, Van, Türkiye*
[a]*Atatürk University, Earthquake Research Centre, Erzurum, Türkiye*

Research Article

Keywords:
Eastern Türkiye, Van Lake Region, Coulomb Stress, b-value, Seismotectonic.

ABSTRACT

The tectonic structure of Türkiye is under the influence of Arabian, Eurasian, African, and Anatolian plates. Lake Van region, located in eastern Türkiye, has been exposed to many devastating earthquakes in historical and instrumental periods. In this paper, using regional earthquakes, the tectonic stress variation of Lake Van region was investigated using the Coulomb stress change and the b-value distribution. 83 earthquakes that occurred between 2000 and 2020 are used to calculate the Coulomb stress change, while 17815 earthquakes that occurred between 1903 and 2021 are used to calculate the b-value distribution. Coulomb stress change gives an idea about the transfer of energy to nearby faults. Coulomb stress change and b-value distribution maps were created at different depths to model the variation of stress. The low b-values and positive Coulomb stress values were especially observed around the Van and Yeniköşk faults. On the contrary, no significant variation in stress change was observed around Süphan and Nemrut volcanoes, and high b-values were calculated in this region. Coulomb stress change and earthquake epicentral distribution are compatible and most events occurred in positive stress regions. In conclusion, stress change and b-value distribution were interpreted together and positive stress regions were revealed in the region.

Received Date: 02.07.2021
Accepted Date: 01.09.2021

1. Introduction

The Eastern Anatolian Plateau is a region located on the Alpine-Himalayan Orogenic Belt and is very active in terms of its seismicity. The active tectonics of the region are generally affected by the active collision belt that occurs as a result of the ~15 mm/year movement of the Arabian Plate to the north and the ~5 mm/year movement of the Eurasian Plate to the south (Şengör et al., 2003; Reilinger et al., 2006; Keskin, 2007; Irmak et al., 2012; Toker et al., 2017*a*, *b*). This collision starts approximately 11 million years ago and the boundary associated with the collision is defined as the Bitlis-Zagros Suture Zone (BZKK) (Doğan and Karakaş, 2013). The magmatic activity starts simultaneously with a new tectonic regime that develops following the collision (Alan et al., 2011). As a result of the compression deformation caused by the Eurasian and Arabian Plates, the Anatolian Plate tends to rotate counterclockwise and escape to the west. This deformation is especially dominant along the North Anatolian Fault Zone (NAFZ) and East Anatolian Fault Zone (EAFZ), which shows strike-slip fault characteristics (Keskin, 2003; Şengör et al., 2003; Bayrak et al., 2013; Reilinger et al., 2006). Right-lateral NAFZ and left-lateral EAFZ overlap at the Karlıova triple junction (Toker, 2014). To the east of the Karlıova triple junction, there are diffuse zones of deformation associated with the collision. This deformation accumulates along the NW-SE

Citation Info: Alkan, H., Bayrak, E. 2022. Coulomb stress changes and magnitude - frequency distribution for Lake Van region. Bulletin of the Mineral Research and Exploration 168, 141-156. https://doi.org/10.19111/bulletinofmre.990666

**Corresponding author: Hamdi ALKAN, hamdialkan@yyu.edu.tr*

trending dextral faults and NE-SW trending left directional faults, which represent escape tectonics in the Eastern Anatolian Block and continental lithospheric shortening along the Caucasian Thrust Zone (Toker, 2014). In the period following the continent-continental collision, active deformation caused the crustal shortening and thickening, and thus the elevation of the region (Şaroğlu and Yılmaz, 1986; Yılmaz et al., 1987; Alan et al., 2011). Lake Van Basin is located north of the BZKK, and southeast of the Karlıova triple junction (Bayrak et al., 2013).

The Van Lake Basin is a dome-shaped basin formed as a result of the tectonic activity of normal, reverse and strike-slip faults in the Eastern Anatolian compression regime. This faulting causes hydrothermal activity, intense seismicity and regional volcanism (Toker et al., 2017*a*, *b*). Lake Van Basin is approximately 1650 m above sea level and has a maximum water depth of 450 m. Süphan Volcano with an altitude of ~4400 m is located just north of Lake Van, and Nemrut Volcano with an altitude of ~3500 m is located just to the west of the lake. These volcanoes are young geological structures that were active during the Holocene time (Figure 1). Also, the metamorphic rocks and Palaeozoic aged ophiolitic units in the Bitlis Massif crop out in the south of Lake Van, and volcanic rocks and ophiolite components, young-current fluvial and lacustrine fragments and carbonates belong to the Yüksekova Complex in the east (Alan et al., 2011; Akıncı et al., 2014; Çukur et al., 2017). Volcanic and volcano-clastic rocks in the west and north of Lake Van, and Pliocene deposits and Quaternary lake sediments are settled around the city center of Van (Sumita and Schmincke, 2013; Mackenzie et al., 2016).

Lake Van consists of three deep basins, namely the Northern, Tatvan and Deveboynu basins, which are separated from each other by several ridge structures on the lake bottom (Çukur et al., 2017). Regarding the formation of the Van Lake Basin and its exact age of formation, Lahn (1948) and Degens et al. (1984) suggested that the lava flow from the Nemrut Volcano acted as a dam along the Muş Basin and was formed due to the interruption caused by the drainage of the Murat River. However, recent studies show that this is not a lava flow, but potentially a kind of pyroclastic flow, and the outlet of Lake Van was blocked much earlier than assumed (about 600.000 years ago) (Çukur et al., 2014).

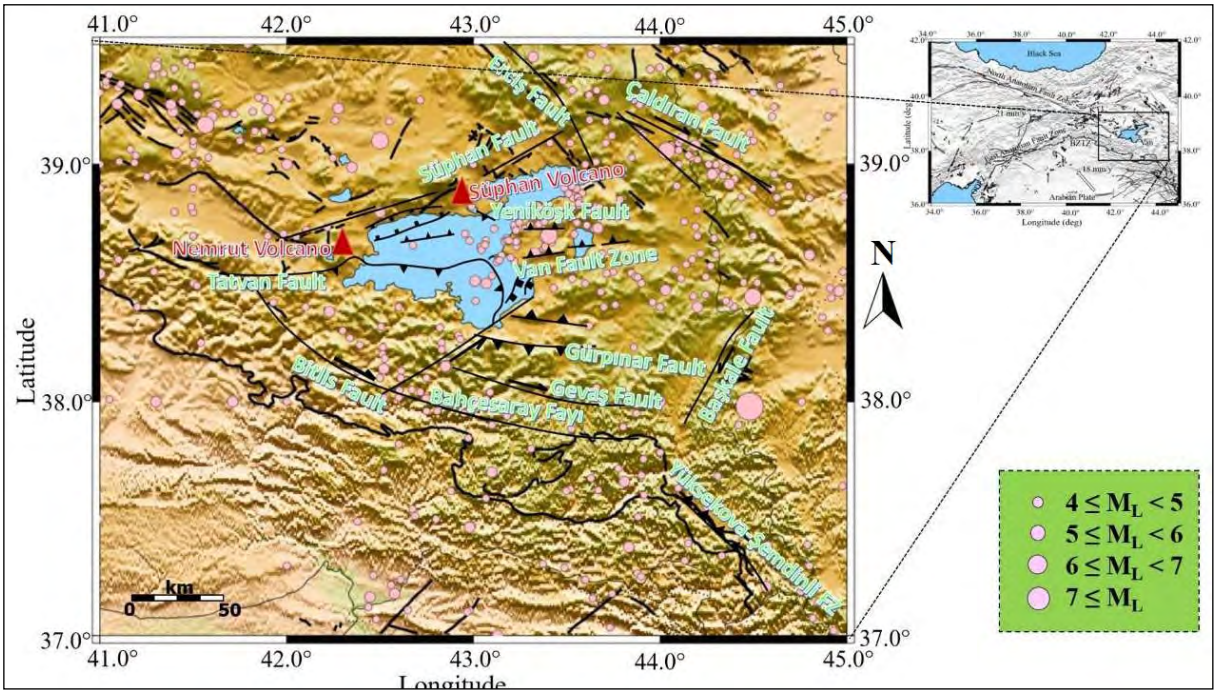

Figure 1- Seismotectonic map of the Van Lake Basin (modified from Selçuk, 2016; Emre et al., 2018 and Alkan et al., 2020). Holocone volcanoes are shown with red triangles.

The Van Lake Basin is under the influence of several active tectonic structures (Figure 1, Görür et al., 2015) Gevaş Fault and Süphan Fault located between Gevaş and Gürpınar towns, and the Çaldıran Fault and Erciş Fault located in the northeast of the lake have right-lateral strike-slip fault characteristic (Bayrak et al., 2013). The Van Fault Zone and Yeniköşk Fault, which are very close to the city center of Van, show an east-west direction reverse fault mechanism (Emre et al., 2013). Gürpınar Fault is a fault located in the south of Van and consists of three different segments. This fault is seismically active and has an east-west direction reverse and strike-slip fault mechanism (Selçuk, 2016). The Başkale Fault and Yüksekova-Şemdinli Fault Zone located in the southeast of the region are important tectonic structures. These active faults, which show a strike-slip faulting mechanism, have caused significant earthquakes (Akkaya, 2015).

The Van Lake Basin and its surroundings have been exposed to many destructive earthquakes in the historical and instrumental periods. In the historical period, the locations of 24 earthquakes with a magnitude greater than 5 and varying between V-IX have been determined (Alan et al., 2011). According to the instrumental period data, a large number of earthquakes with magnitudes between 3 and 7.3 occurred in the Van Lake Basin and its surroundings. The most important of them are; Başkale Earthquake (M=6.0) in 1908, Erciş Earthquake (Ms=5.9) in 1941, Çaldıran Earthquake in 1976 (Ms=7.3), Sütlüce Earthquake in 2005 (Ms=5.9) and the Van Earthquake that occurred in 2011 (Mw=7.2) (Akkaya, 2015; Özer, 2019; Alkan et al., 2020). 2011 Van earthquake resulted in 600 mortalities and the destruction of hundreds of buildings, rendering them unusable (Işık et al., 2017). Just after the Van Earthquake, the focal mechanism solution of which was a reverse fault, another earthquake with Ml=5.6 occurred southwest of Van Lake on 09.11.2011. It has been determined that this earthquake is independent of the Van Fault Zone, where the first earthquake occurred, and has a left-sided strike-slip mechanism on the Edremit Fault (Akıncı et al., 2014; Işık et al., 2017; Öztürk, 2017). In addition, 6284 aftershocks with magnitudes ranging from 1.7 to 5.8 occurred in the region between 23.10.2011 and 09.12.2011 (AFAD, 2011). On 23.02.2020, an earthquake (Mw=5.9) with the epicenter of Hoy (Iran) occurred at the northeastern end of the Başkale Fault. On the same day, another earthquake (Mw=5.9) occurred in the same region (AFAD, 2020*a*). Finally, an earthquake (Mw=5.4) the epicenter of which was Saray (Van) occurred on 25.06.2020 and was felt strongly in the surrounding settlements (AFAD, 2020*b*).

Coulomb stress change is very important in earthquake interactions, interpretation of future earthquakes, and assessment of seismic hazard. Also, the *b*-value calculated from the Gutenberg-Richter relationship is frequently used to display the state of the stress occurring along any fault zone (Ansari, 2016). In this study; Coulomb stress change is modeled by using focal mechanism solutions of earthquakes greater than 4.5 (Table 1) in and around the Van Lake Basin, and *b*-values are calculated using the highest probability method. Using these maps, it is aimed to determine the regional tectonic stress variation and determine the regions with the potential to produce earthquakes in the future.

2. Data

For the Coulomb stress changes, the focal mechanism results of 83 earthquakes that occurred between 2000 and 2020 in the study region were used. Table 1 shows the date, magnitude, depth, strike, rake, and dip values. According to the focal mechanism results, it is seen that strike-slip and reverse faults are active (Figure 2).

2.1. Data Used for the Gutenberg - Richter Method

The *b-value* is calculated using the AFAD DDA earthquake catalog. The catalog includes 31976 earthquakes with magnitudes (M_L) ranging from 0.7 to 7.0 that occurred between 28.04.1903 and 09.06.2021. The catalog used to calculate the *b-value* should be homogeneous, that is, of the same magnitude type (Bayrak et al., 2009; Öztürk and Bayrak, 2012; Öztürk, 2015, 2018). The AFAD catalog describes it as M_L and therefore no magnitude conversion has been done.

Another important issue in making the catalog ready for calculation is the removal of foreshocks and aftershocks from the catalog. The process of removing the foreshocks and aftershocks from an

Table 1- Focal mechanism results for earthquakes occurring in the study region (37.0°-42.0°N Latitude and 41.5°-47.0°E Longitude). The focal mechanism results of earthquakes are compiled from the AFAD website (https://deprem.afad.gov.tr/ddakatalogu).

No	Date (dd mm yy)	Latitude (°N)	Longitude (°E)	Magnitude (Mw)	Depth (km)	Strike (°)	Dip (°)	Rake (°)
1	14/12/2020 21:58:45	38.901	43.487	4.7	9.20	212.0	82.0	8.0
2	03/12/2020 05:45:19	37.999	41.712	5.0	14.02	155.0	88.0	166.0
3	16/09/2020 14:48:19	38.705	41.981	4.7	17.08	231.0	64.0	40.0
4	07/08/2020 19:20:13	38.131	42.613	4.6	6.99	331.0	83.0	171.0
5	25/06/2020 10:03:29	38.472	44.028	5.4	7.48	167.0	49.0	-85.0
6	03/04/2020 05:44:24	38.909	43.529	4.7	12.99	175.0	85.0	3.0
7	23/02/2020 16:00:29	38.450	44.502	5.9	8.10	120.0	83.0	-160.0
8	23/02/2020 05:52:57	38.436	44.489	5.9	14.90	187.0	50.0	-61.0
9	21/07/2018 06:15:13	39.038	44.153	4.5	7.52	75.0	85.0	-148.0
10	23/06/2018 03:50:03	38.623	44.300	4.7	8.48	201.0	77.0	-7.0
11	14/06/2018 15:42:21	38.941	43.555	4.5	13.66	187.0	45.0	36.0
12	01/05/2017 16:30:40	38.265	42.928	4.5	12.44	308.0	88.0	177.0
13	23/11/2016 12:14:36	38.539	43.870	4.6	9.97	305.0	76.0	167.0
14	23/01/2016 07:53:44	38.049	42.670	4.5	15.21	279.0	42.0	163.0
15	29/10/2015 09:46:39	39.119	43.743	4.8	4.90	119.0	61.0	-167.0
16	23/06/2015 22:35:20	38.681	43.179	4.5	30.45	268.0	44.0	97.0
17	18/02/2014 21:51:35	38.836	43.563	4.6	11.67	224.0	81.0	34.0
18	21/09/2013 02:15:44	38.673	43.418	4.5	17.03	252.0	42.0	50.0
19	12/06/2013 19:02:51	38.624	43.690	4.6	15.91	232.0	23.0	87.0
20	24/11/2012 16:04:28	38.833	43.572	4.5	17.53	93.0	66.0	145.0
21	05/08/2012 20:37:21	37.463	42.979	5.3	12.94	326.0	58.0	154.0
22	24/06/2012 20:07:21	38.733	43.667	5.0	23.62	96.0	42.0	89.0
23	14/06/2012 05:52:51	37.157	42.443	5.5	11.68	329.0	44.0	79.0
24	26/03/2012 10:35:33	39.234	42.276	5.0	16.96	116.0	67.0	168.0
25	24/02/2012 13:07:10	38.827	43.565	4.5	22.09	22.0	82.0	-10.0
26	17/02/2012 09:32:57	38.743	43.216	4.6	7.02	258.0	50.0	56.0

Table 1- Continued.

27	20/01/2012 09:57:37	38.703	43.497	4.5	21.32	244.0	37.0	62.0
28	06/12/2011 15:46:25	37.263	43.876	4.6	3.19	312.0	83.0	-166.0
29	06/12/2011 02:55:59	38.833	43.616	4.7	15.36	119.0	58.0	172.0
30	04/12/2011 22:15:03	38.481	43.299	4.9	12.22	32.0	86.0	2.0
31	30/11/2011 00:47:21	38.470	43.290	5.0	19.79	166.0	56.0	-58.0
32	24/11/2011 00:48:07	38.633	43.028	4.5	15.90	253.0	53.0	47.0
33	22/11/2011 03:30:35	38.609	43.207	4.5	22.95	55.0	88.0	6.0
34	21/11/2011 21:00:35	38.691	43.139	4.6	1.91	238.0	90.0	4.0
35	21/11/2011 20:55:56	38.669	43.205	4.6	22.74	82.0	42.0	97.0
36	18/11/2011 17:39:39	38.802	43.852	5.2	8.00	201.0	90.0	20.0
37	17/11/2011 12:38:31	38.867	43.569	4.5	17.10	92.0	78.0	-166.0
38	14/11/2011 22:08:14	38.703	43.083	5.1	23.32	256.0	41.0	66.0
39	14/11/2011 16:47:16	38.624	43.075	4.7	18.98	103.0	49.0	105.0
40	14/11/2011 16:31:31	38.621	43.040	4.5	19.21	95.0	45.0	90.0
41	12/11/2011 18:20:01	38.632	43.173	4.6	19.15	71.0	47.0	73.0
42	09/11/2011 20:45:38	38.464	43.253	4.5	17.74	39.0	77.0	-9.0
43	09/11/2011 19:23:34	38.438	43.282	5.6	21.47	163.0	52.0	-44.0
44	08/11/2011 22:05:50	38.719	43.077	5.4	8.36	255.0	43.0	59.0
45	07/11/2011 22:14:12	38.935	43.483	4.5	14.63	156.0	69.0	-14.0
46	07/11/2011 15:54:48	38.663	43.632	4.8	4.43	31.0	69.0	5.0
47	06/11/2011 02:43:12	38.939	43.554	4.6	11.66	9.0	81.0	30.0
48	05/11/2011 19:19:15	38.814	43.513	4.6	22.03	191.0	74.0	17.0
49	02/11/2011 11:43:02	37.253	43.900	4.8	7.78	156.0	80.0	-179.0
50	02/11/2011 04:34:21	38.884	43.590	4.8	18.03	25.0	84.0	0.0
51	01/11/2011 21:10:44	38.846	43.609	4.5	5.06	237.0	54.0	56.0
52	30/10/2011 01:55:04	38.729	43.612	4.6	22.36	31.0	73.0	-23.0
53	29/10/2011 22:24:22	38.924	43.543	4.8	16.67	199.0	90.0	-18.0
54	29/10/2011 18:45:49	38.622	43.152	4.6	13.97	80.0	42.0	110.0

Table 1- Continued.

55	28/10/2011 16:34:10	38.897	43.583	4.5	12.44	198.0	86.0	-18.0
56	27/10/2011 08:04:22	37.380	43.834	5.6	21.61	267.0	48.0	110.0
57	26/10/2011 16:19:44	38.659	43.285	4.5	1.45	35.0	89.0	-3.0
58	26/10/2011 03:16:18	38.692	43.200	4.8	20.62	222.0	57.0	70.0
59	26/10/2011 02:59:05	38.828	43.506	4.6	14.81	58.0	75.0	22.0
60	25/10/2011 15:27:13	38.826	43.566	4.5	16.01	55.0	83.0	21.0
61	25/10/2011 14:55:06	38.823	43.585	5.4	17.44	36.0	89.0	-9.0
62	24/10/2011 23:55:15	38.787	43.390	4.6	26.37	21.0	89.0	-22.0
63	24/10/2011 22:13:30	38.713	43.097	4.5	19.24	239.0	52.0	65.0
64	24/10/2011 15:28:06	38.693	43.147	4.8	18.71	215.0	70.0	25.0
65	24/10/2011 08:49:19	38.706	43.582	5.0	17.27	231.0	43.0	73.0
66	24/10/2011 04:18:45	38.680	43.310	4.5	12.58	145.0	57.0	141.0
67	23/10/2011 20:45:34	38.644	43.127	5.8	6.79	137.0	55.0	147.0
68	23/10/2011 19:43:24	38.697	43.150	4.5	7.55	228.0	52.0	-119.0
69	23/10/2011 19:06:05	38.735	43.328	5.0	22.09	252.0	34.0	65.0
70	23/10/2011 18:53:47	38.724	43.302	4.8	6.08	129.0	74.0	124.0
71	23/10/2011 18:10:44	38.629	43.192	5.0	19.81	106.0	30.0	102.0
72	23/10/2011 16:05:10	38.751	43.508	4.8	20.85	175.0	43.0	57.0
73	23/10/2011 15:57:59	38.717	43.326	4.6	21.78	63.0	43.0	100.0
74	23/10/2011 15:24:29	38.590	43.149	4.7	21.55	77.0	22.0	153.0
75	23/10/2011 13:17:03	38.811	43.467	4.7	15.41	140.0	68.0	128.0
76	23/10/2011 11:32:40	38.777	43.394	5.5	22.61	213.0	51.0	99.0
77	23/10/2011 10:56:48	38.782	43.363	5.8	19.92	305.0	71.0	-140.0
78	23/10/2011 10:41:20	38.689	43.465	6.7	19.02	98.0	66.0	88.0
79	29/05/2011 11:02:29	37.216	42.560	4.6	11.25	58.0	78.0	4.0
80	30/04/2011 15:26:03	38.183	42.525	4.5	5.00	125.0	86.0	-176.0
81	14/03/2011 18:57:09	38.601	44.171	4.7	12.47	225.0	74.0	-30.0
82	25/01/2005 16:44:16	37.622	43.703	5.9	41.2	301.0	78.0	-169.0
83	15/11/2000 15:05:37	38.410	42.950	5.2	18.0	100.0	64.0	111.0

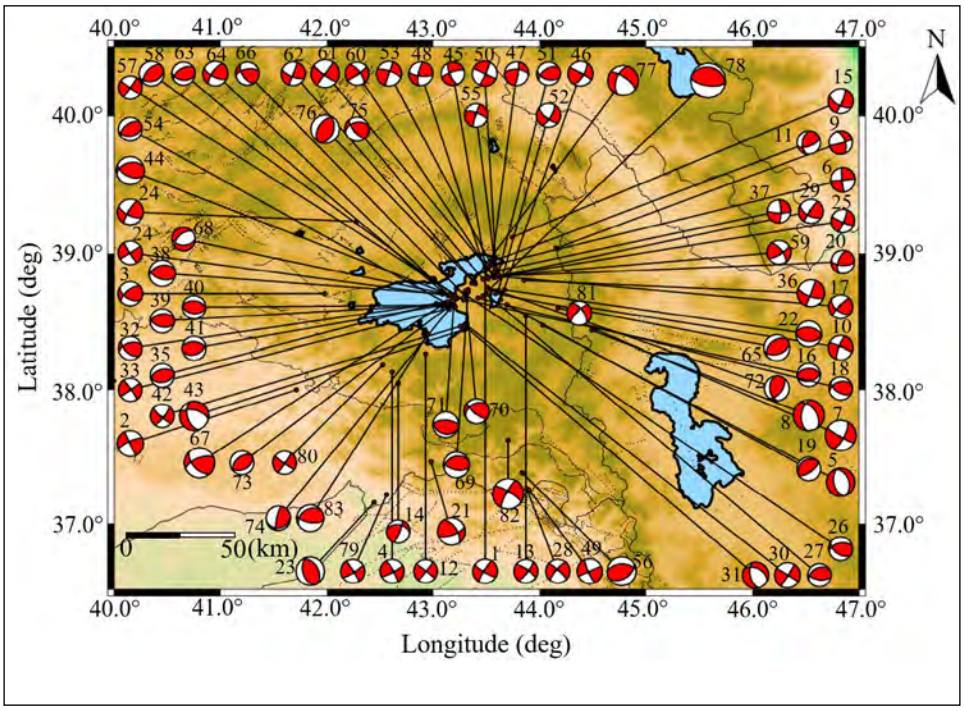

Figure 2- Fault mechanism results from major earthquakes affecting Lake Van and its surroundings. The parameters of the focal mechanism solution are given in Table 1.

earthquake catalog is known as decluster analysis. In this analysis, clustering is performed by determining a space window and a time window. There are different methods for reclustering, and the Reasenberg (1985) method, which is one of the most frequently used methods, is applied in this study. With the Reasenberg method, 14161 foreshocks and aftershocks are removed from the catalog and the final catalog consists of a total of 17815 earthquakes (Figure 3). The epicentral distribution of these earthquakes is shown in Figure 1. In Figure 3, the graph of the primary catalog and the year-earthquake number of the last catalog are shown. When this graph is examined, it is seen that there has been a significant increase in the number of earthquakes, especially after 2000, and it is thought that this is due to the increase in the number of earthquakes recorded together with the increase in earthquake stations in the region.

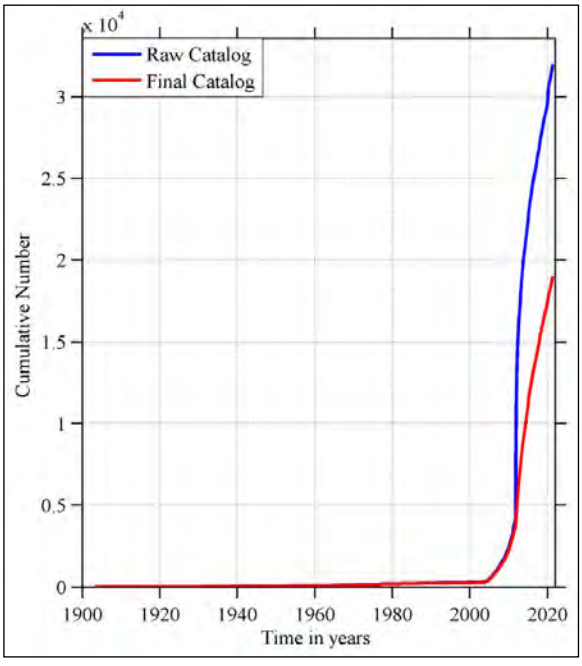

Figure 3- Cumulative number of earthquakes before and after foreshocks and aftershocks are removed from the catalog.

When the magnitude - earthquake number histogram graph of the final catalog is examined (Figure 4), it is seen that the magnitude of the majority of the earthquakes in the study region is less than 4.0. The largest earthquake that occurred in the study region was the M_L= 7.0 earthquake that occurred in 1930.

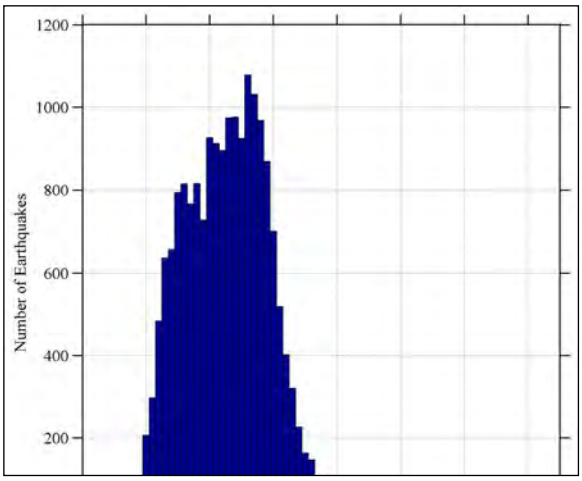

Figure 4- Magnitude histogram of the final catalog.

3. Method

3.1. Coulomb Stress Changes

The static stress change is due to the displacement of a point source or a fault, and it is necessary to multiply by the elastic stiffness to obtain the stress variation. A fault plane is a plane with a specified strike, dip, and rake in which the stress provided by a source is resolved. In the calculation of the Coulomb stress change, the shear stress component, which depends on the geometry of the fault, and the normal stress component, which depends on the subduction of the fault, are taken into account (Toda et al., 2011). Coulomb stress change depends on the geometry and sliding of an earthquake and the effective friction coefficient (Ansari, 2016; Çirmik et al., 2017). The Coulomb failure criterion is considered for the situation where the stress change is positive and is expressed by Equation 1:

$$\Delta\sigma_{cfc}=\Delta\tau_s+\mu'\Delta\sigma_{n'} \quad (1)$$

$\Delta\sigma_{cfc}$: variation of failure stress caused by shear in the source fault, $\Delta\tau_s$ variation of shear stress, $\Delta\sigma_{n'}$ normal stress variation and π: coefficient of friction on the fault. The coefficient of friction is dimensionless, ranging from 0 to 1. Poisson's ratio was chosen as 0.25, Young's modulus was 8x105 (bar) and the friction coefficient was 0.4. Positive values of the Coulomb failure criterion correspond to an increase in the probability of rupture during an earthquake, while negative values correspond to a decrease in stress (Mogi, 1962). It is assumed that Coulomb stress changes between -0.1 and +0.1 bar are sufficient to predict future earthquakes (Yadav et al., 2012). Earthquake stress changes can be used to interpret seismic hazard maps (Ahadov and Jin, 2019). In this study, Coulomb 3.3 software was used for Coulomb stress change calculations (Toda et al., 2011).

3.2. Maximum Likelihood Method

Gutenberg - Richter (1944) law, also known as the magnitude-frequency relationship, is represented by Equation 2. It has been stated that this equation is directly related to the physics of earthquake abundance (Mogi, 1962) and

$$LogN=a-bM \quad (2)$$

here, M: earthquake magnitude, N shows the cumulative number of earthquakes, a and b constant regression coefficients.

Studies have shown that the *b-value* varies depending on many different parameters. The main ones are; that the *b-value* is inversely proportional to the stress (Scholz, 1968; Wyss, 1973), directly proportional to the heterogeneity of the fault (Mogi, 1962), and directly proportional to the heat flow (Warren and Latham, 1970). It has been reported that there is an inverse proportionality between the P-wave velocity (Ogata et al., 1991) and high *b-values* are observed in aftershocks, while low *b-values* are observed in foreshocks (Suyehiro, 1964). As a result, it can be said that a low *b-value* is associated with high stress and strain, high P-wave velocity, and low heterogeneity.

There are different methods for calculating the *b-value* described by Gutenberg and Richter (1944). The most prominent of these are the least-squares and the maximum likelihood methods. With the maximum likelihood method, which is one of the most frequently used methods around the world, the *b-value* is calculated with the following formula (Aki, 1965):

$$b=\frac{1}{\log_{10}[\bar{M}-(M_{min}-\Delta m/2)]} \quad (3)$$

M_{min} is the minimum magnitude of completeness, $\bar{M}$ is the mean magnitude of earthquakes and Δm is the

magnitude resolution. The ZMAP program (Wiemer, 2001) was used to determine the Gutenberg - Richter relationship.

4. Discussion

In Figure 5, the Coulomb stress changes in the first 30 km are modeled. In especially, the positive Coulomb stress changes are shown in the region between the Van and Yenişehir Faults. In addition, positive stress values can be realized in the region between Hoy and Başkale. Negative Coulomb stress values are calculated around the Çaldıran Fault Zone. Earthquakes with $M_L \geq 4.0$ are also shown on the map to investigate the relationship between the Coulomb stress changes and the epicenters of the earthquakes. The regions of earthquake intensity usually coincide with positive Coulomb stress changes.

Figure 6 shows the Coulomb stress change results for different depths (7.5, 15, 22.5, and 30 km). Positive Coulomb stress indicates increased stress, while negative values indicate decreased stress (Olsson, 1999). Considering the stress changes at all depths, firstly positive Coulomb stress variations are observed especially around Erciş and Adilcevaz located in the north of Lake Van. This region is located in Süphan Fault and Erciş Fault. Recently, a destructive earthquake has not occurred on these faults. On the contrary, negative stress values are observed around Muradiye and Çaldıran, which are located to the east of this region. Because the Çaldıran Fault Zone has hosted destructive earthquakes in the past, the reason for the negative stress values is explained. Another important region shown in Figure 3 is the location of Van city center, which is east of Lake Van. For this region, while positive stress changes are observed at 7.5 and 15 km depths, negative stress values can be observed at increasing depths. According to these findings, it is reasonable to expect seismic activity at shallow depths in the Yeniköşk Fault and Van Fault Zone. However, the opposite situation can be mentioned for the region between Van and Hoy. Whilst negative stress values are observed at 7.5 and 15 km depths, the positive stress values are observed at 22.5 and 30 km depths.

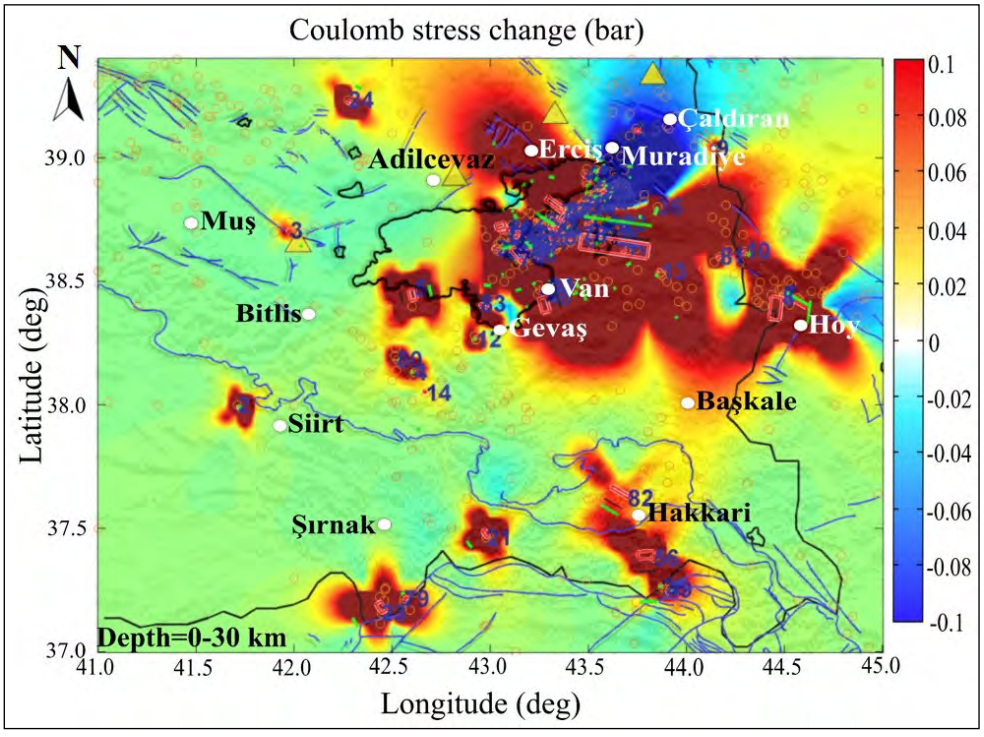

Figure 5- Coulomb stress changes calculated for a depth of 0 - 30 km (orange circles indicate the location of earthquakes greater than 4.0). The focal mechanism solutions of earthquakes were taken from the website of Kandilli Observatory and Earthquake Research Institute (KOERI, http://www.koeri.boun.edu.tr/scripts/lst0.asp).

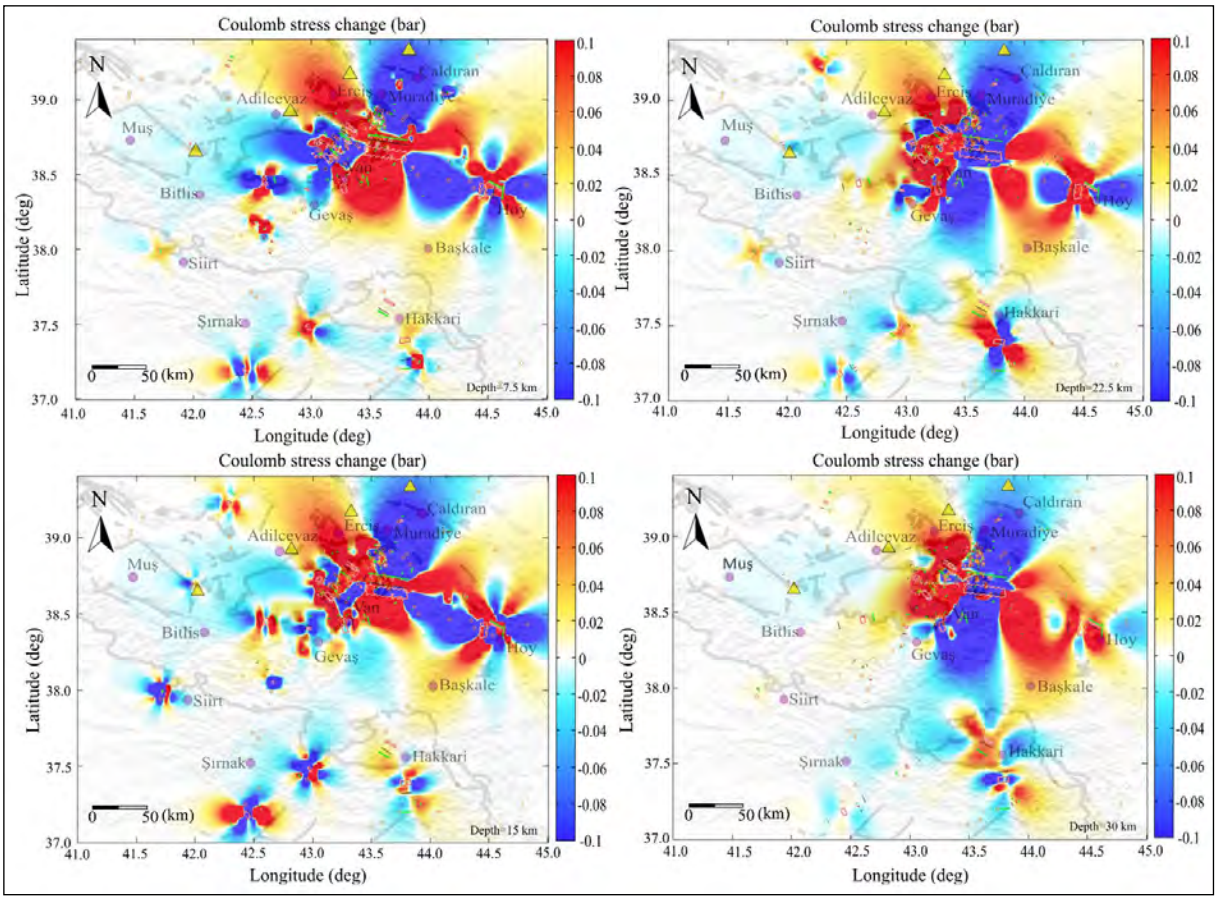

Figure 6- Coulomb stress change maps calculated for different depths. The yellow triangles represent volcanoes that are active during the Holocene.

Two earthquakes of the same magnitude (M_w= 5.9) occurred on 23.02.2020 to the northeast of the Başkale Fault. The epicentral depths of these earthquakes are 14.9 km and 8.1 km (AFAD, 2020*a*). The west of Lake Van generally has negative anomalies for each depth interval. In this region where Tatvan Fault and Bitlis Fault are located, an earthquake with a magnitude of M_w= 4.7 occurred (Table 1, Number: 3). In addition to this, when looking at the focal mechanism solutions in Figure 2, it can be seen that the potential earthquake of these faults is low. In the vicinity of Şırnak and Hakkari, located in the south of the study region, small-scale positive and negative stress anomalies are observed for all depth intervals. This stress variation shows that the Coulomb stress value is related to the small and medium earthquakes occurring in the Yüksekova - Şemdinli Fault Zone and the Southeast Anatolian Suture Zone.

Using the 0.1° × 0.1° grid interval, the regional change of the *b-value* is mapped and the closest 300 earthquakes are selected for each grid, and the minimum number of earthquakes is calculated as 20. One of the most important issues in calculating the *b-value* is the correct determination of the completeness magnitude (M_c). The method proposed by Wiemer and Wyss (2002) is used to calculate the M_c value. According to this algorithm, the number of earthquakes corresponding to the magnitude values is obtained and the magnitude value of the highest number of earthquakes is determined as M_c (Wiemer and Wyss, 2002).

The *b-value* is generally close to 1.0 in active seismic zones in different parts of the world (Frohlich and Davis, 1993). It has been stated that the *b-value* varies between 0.5 and 1.5 in different parts of the world (Wiemer and Wyss, 1997; Olsson, 1999; Öztürk and Bayrak, 2012; Öztürk, 2015, 2018).

The *b-values* obtained in this study vary between 0.5 and 1.5 (Figure 7). Figure 8 shows the standard deviations of the b-values calculated to the Maximum likelihood method. As can be clearly seen in Figure 8, standard deviation values less than 0.1 are obtained for most of the study region. This indicates that the obtained *b-values* are statistically significant. Standard deviation values greater than 1.0 are obtained for the region in the southwest of the study region. It is thought that this may be due to the low intensity of earthquakes in the region.

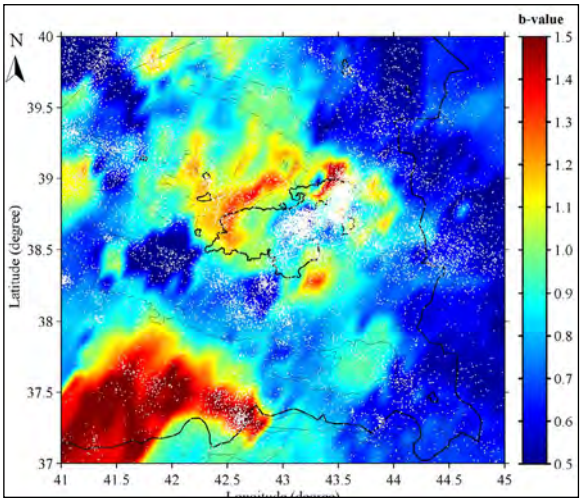

Figure 7- The *b-values* variation map calculated for the study region [white dots show the epicentral distribution of earthquakes in the catalog used in the study (URL-2)].

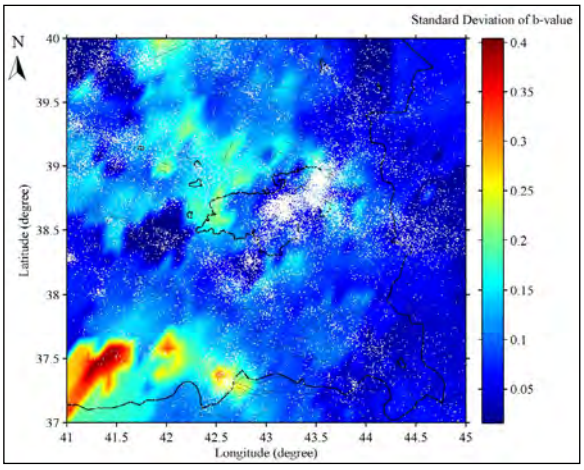

Figure 8- The standard deviation values obtained from the *b-values* [white dots depict the epicentral distribution of earthquakes in the catalog used in the study (URL-2)].

It can be seen that the *b-value* for the study region a is generally obtained as less than 1.0. Also, the highest b-values (~1.5) are obtained in the southwest of the study region. However, considering the earthquake epicenter distribution and the standard deviation map of the *b-value*, it should be said that the values obtained are not within the confidence interval since there are few earthquakes in the southwest of the study region. Relatively high *b-values* are obtained around the Süphan and Nemrut volcanoes in the NNE region of Lake Van. Cirmik (2018) calculated high heat flow values for this region. Maden and Öztürk (2015) stated that there were high negative gravity values in regions with low *b-values*. Mahatsente et al. (2018) mapped gravity anomaly values for the Eastern Anatolia region. In their study, they calculated high positive gravity anomalies for this region and these anomalies agreed with the high *b-values* in this region. As a result, it can be said that this region has a low-stress level.

Low *b-values* are also striking around the Çaldıran, Başkale, and Yüksekova-Şemdinli Faults in the east of the study region. Mahatsente et al. (2018) observed high negative gravity anomalies in this region, which is consistent with low *b-values*. Aydemir et al. (2014) obtained negative high gravity anomalies for this region in their study. It can be said that this region has a high-stress level according to the *b-value* change. Aydemir et al. (2014) determined an east-west trending discontinuity starting from the vicinity of Nemrut volcano and extending to the east of Lake Van. Lower *b-values* are obtained in the eastern section of this discontinuity compared to the western section. Büyüksaraç et al. (2021) conducted a probabilistic seismic hazard analysis in and around the Van city. They determined that the highest ground acceleration values varied between 0.24 and 0.43 g and stated that the highest danger was in the Çaldıran district, and the lowest danger was in the Gürpınar district.

Low *b-values* are striking in the vicinity of the Van Fault Zone and Yeniköşk Fault, located to the east of Lake Van. Cirmik (2018) obtained relatively high P-wave velocity values and low heat flow values for this region. Alkan et al. (2020) calculated that the depth of Moho varies between approximately 41-47 km in the Lake Van and its surroundings. They observed that the Moho discontinuity is shallower around the

Van Fault Zone and Yeniköşk Fault. The shallower Moho and low *b-values* in this region indicate a high Coulomb stress value.

Low b-values are obtained between the Bitlis Thrust Zone and Lake Van. Çırmık (2018) obtained relatively low P-wave velocities with low heat flow values for this region. While the b-values obtained in this region are compatible with the heat flow, the b-values do not show a close agreement with the P-wave velocities. Mahatsente et al. (2018) observed negative high gravity values for this region.

The relationship between the *b-value* depending on the tectonic compression and the Coulomb stress variation is very important. For this purpose, the Coulomb stress changes are calculated for the 0-30 km depth interval using the focal mechanisms shown in Table 1 (Figure 5). Positive stress changes and small *b-values* are calculated especially around the Van Fault Zone and Yeniköşk Fault. This shows that the region has a high-stress level. In addition, positive stress values and small *b-values* are calculated between the Başkale and Çaldıran Faults. No significant change in Coulomb stress change is observed around the Süphan and Nemrut Volcanoes, and high *b-values* (>1.2) are obtained in this region. These findings show the low-stress variation.

The 3-dimensional *b-value* map in the study region is created using ZMAP software. For each grid, at least 20 and the closest 200 events are selected, and a map is obtained for the 0.1° × 0.1° × 5 km grid interval. The 3-dimensional *b-value* map shown in Figure 9 is calculated using the Maximum Likelihood method. Five horizontal maps are drawn at depths of 0, 7, 5, 15, 22.5, and 30 km to examine the variation of the *b-value*. The *b-values* range from 0.5 to 1.5. According to Figure 9, the *b-value* generally decreases with increasing depth.

The *b-value* increases up to a depth of 7.5 km around the Van Fault Zone and Yeniköşk Fault. However, the *b-value* decreases after this depth. The *b-value* is obtained as 1.5 in the region where the Nemrut and Süphan volcanoes have located the northwest of Lake Van. However, the *b-value* is calculated as 1.0 at 30 km depth. Özacar et al. (2010) pointed out the existence of partial melting consisting

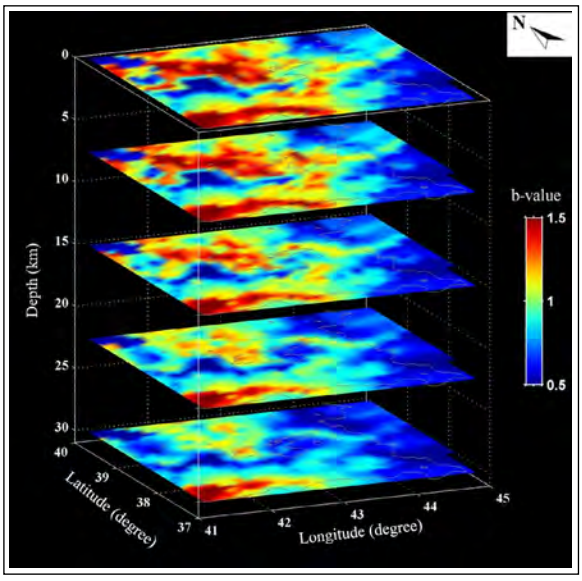

Figure 9- 3D variation of the *b-value* (maps correspond to depths of 0, 7.5, 15, 22.5, and 30 km, respectively, from top to bottom).

of young volcanic units in this region. Cirmik (2018) stated that the seismicity in this region is low and the crustal rigidity is low. According to all these results, it can be said that the stress variation of this region is low.

In the region between the Bitlis Thrust Zone and Lake Van, the *b-value* generally remains constant at 0.6 up to 15 km, and it is observed that it decreases to 0.5 after this depth. Alkan et al. (2020) determined that the P-wave velocity for this region partially increases with a depth of 30 km depth. It can be said that the high P-wave velocities are compatible with the low *b-values*.

The small *b-values* (<0.9) are founded in and around the Çaldıran Fault, Başkale Fault, and Yüksekova-Şemdinli Fault in the east of the study region. Zhu (2018) expressed this region as the Eastern Anatolia volcanic region. Zhu (2018) showed that the Vp/Vs value for this region increases with depth. On the other hand, the 1930 earthquake (M_L= 7.0), the 1976 earthquake (M_L= 6.1), and the 2020 earthquake (M_L=6.2) are reported in this region, and these earthquakes indicate that the stress values in this region are high.

The behavior of Coulomb stress changes and *b-value* at different depths are also compared in this work. Coulomb stress values generally change from negative to positive values with increasing depth. Smaller *b-values* are observed at increasing depths in the study region. In other words, it can be said that the stress level increases with increasing depths according to both values. However, positive Coulomb stress values are observed in the first 15 km around the Yeniköşk Fault located just east of Lake Van, while the negative values are obtained after this depth level. Even though this negative value, the *b-value* decreases with depth for this region. It may be useful to determine and compare the stress changes for these faults using different methods.

5. Results

Many earthquakes that caused loss of life and property in and around the Lake Van region have been reported in historical and instrumental periods. The static stress change caused by an earthquake will be useful in predicting another future earthquake on nearby faults. Coulomb stress changes are important for earthquake interactions and seismic hazard assessment. In this study, Coulomb stress changes of 83 earthquakes that occurred in and around the Lake Van region are analyzed. According to the findings of the Coulomb stress changes, it is observed that the Coulomb stress values increase around the Van, Yenişehir, Başkale, and Çaldıran Faults and it is concluded that the potential of these faults to produce earthquakes in the future is higher than the other faults in the region. In addition, the *b-value* change associated with compatibility with tectonic stress is also revealed within the scope of this study. The regions with positive Coulomb stress values show the low *b-values* and faults with high stress are revealed. In other words, the high *b-values* reflecting low-stress values are conformably obtained with negative Coulomb stress values. Finally, these parameters are calculated for different depths to model the stress change with depth and the maps of these parameters are created. It is observed that the stress generally increased with depth and these two parameters are compatible with each other. As a result, it has been shown that the positive Coulomb stress determined as a result of this study and the low *b-values* are in harmony and that these parameters can be used successfully in revealing the regions with the potential to produce earthquakes in the future.

Acknowledgements

The authors thank Republic of Türkiye Prime Ministry Disaster Emergency Management Authority Presidential of Earthquake Department (AFAD) for providing data for this study. Figures 1 and 2 were prepared using the GMT software (Wessel et al., 2013). The fault information used in the figures was digitized from the MTA drawing editor (Emre et al., 2018).

References

AFAD (T.C. İçişleri Bakanlığı, Afet ve Acil Durum Yönetimi Başkanlığı, Deprem Dairesi Başkanlığı). 2011. Van Depremi (23 Ekim 2011) raporu, Ankara.

AFAD (T.C. İçişleri Bakanlığı, Afet ve Acil Durum Yönetimi Başkanlığı, Deprem Dairesi Başkanlığı). 2020*a*. 23 Şubat 2020 Hoy (İran) Mw 5.9 depremlerine ilişkin ön değerlendirme raporu, Ankara.

AFAD (T.C. İçişleri Bakanlığı, Afet ve Acil Durum Yönetimi Başkanlığı, Deprem Dairesi Başkanlığı). 2020*b*. 25 Haziran 2020 Saray (İran) Mw 5.4 depremlerine ilişkin ön değerlendirme raporu, Ankara.

AFAD (T.C. İçişleri Bakanlığı, Afet ve Acil Durum Yönetimi Başkanlığı). https://deprem.afad.gov.tr/ddakatalogu. 01 June 2021.

Ahadov, B., Jin, S. 2019. Effects of Coulomb stress change on Mw> 6 earthquakes in the Caucasus region. Physics of the Earth and Planetary Interiors 297-106326.

Akıncı, A., Malagnini, L., Herrmann, B., Kalafat, D. 2014. High-frequency attenuation in the Lake Van region, Eastern Turkey. Bulletin of the Seismological Society of America 104(3), 1400-1409.

Aki, K. 1965. A note on the use of microseisms in determining the shallow structures of the Earth's crust. Geophysics 30, 665-666.

Akkaya, I. 2015. The application of HVSR microtremor survey method in Yüksekova (Hakkari) region, Eastern Turkey. Journal of African Earth Sciences 109, 87-95.

Alan, H., Bozkurt, E., Çağlan, D., Dirik, K., Özkaymak, Ç., Sözbilir, H., Topal, T. 2011. Van Depremleri (Tabanlı-Edremit) Raporları. Türk Mühendis

ve Mimar Odalar Birliği, Jeoloji Mühendisleri Odası, 110.

Alkan, H., Çınar, H., Oreshin, S. 2020. Lake Van (Southeastern Turkey) experiment: receiver function analyses of lithospheric structure from teleseismic observations. Pure and Applied Geophysics 177, 3891-3909.

Ansari, S. 2016. Co-seismic stress transfer and magnitude-frequency distribution due to the 2012 Varzaqan-Ahar earthquake doublets (Mw 6.5 and 6.4), NW Iran. Journal of Asian Earth Sciences 132, 129-137.

Aydemir, A., Ateş, A., Bilim, F., Büyüksaraç, A., Bektaş, O. 2014. Evaluation of gravity and aeromagnetic anomalies for the deep structure and possibility of hydrocarbon potential of the region surrounding Lake Van, Eastern Anatolia, Turkey. Surveys in Geophysics 35(2), 431-448.

Bayrak, Y., Öztürk, S., Çınar, H., Kalafat, D., Tsapanos T.M., Koravos, G.C, Leventakis, A. 2009. Estimating earthquake hazard parameters from instrumental data for different regions in and around Turkey. Engineering Geology 105(3-4), 200-210.

Bayrak, Y., Yadav, R.B.S., Kalafat, D., Tsapanos, T.M., Çınar, H., Singh, A. P., Bayrak, E., Yılmaz, Ş., Öcal, F., Koravos, G. 2013. Seismogenesis and earthquake triggering during the Van (Turkey) 2011 seismic sequence. Tectonophysics 601, 163–176.

Büyüksaraç, A., Işık, E., Harirchian, E. 2021. A case study for determination of seismic risk priorities in Van (Eastern Turkey). Earthquakes and Structures 20(4), 445–455.

Çırmık, A. 2018. Examining the crustal structures of eastern Anatolia, using thermal gradient, heat flow, radiogenic heat production and seismic velocities. Bollettino di Geofisica Teorica ed Applicata 59, 2, 117-134.

Çırmık, A., Doğru, F., Gönenç, T., Pamukçu, O. 2017. The stress/strain analysis of kinematic structure at Gülbahçe Fault and Uzunkuyu Intrusive (İzmir, Turkey). Pure and Applied Geophysics 174(3), 1425-1440.

Çukur, D., Krastel, S., Schmincke, H. U., Sumita, M., Tomonaga, Y., Çağatay, M. N. 2014. Water level changes in Lake Van, Turkey, during the past ca. 600 ka: climatic, volcanic and tectonic controls. Journal of Paleolimnology 52, 201-214.

Çukur, D., Krastel, S., Tomonaga, Y., Schmincke, H. U., Sumita, M., Meydan, A. F., Çağatay, M. N., Toker, M., Kim, S. P., Kong, G. S., Horozal, S. 2017. Structural characteristics of the Lake Van Basin, eastern Turkey, from high-resolution seismic reflection profiles and multibeam echosounder data: geologic and tectonic implications. International Journal of Earth Sciences 106, 239-253.

Degens, E. T., Wong, H. K., Kempe, S. 1984. A geological Study of Lake Van, Eastern Turkey. Geologische Rundschau 73, 701-734.

Doğan, B., Karakaş, A. 2013. Geometry of co-seismic surface ruptures and tectonic meaning of the 23 October 2011 Mw 7.1 Van earthquake (East Anatolian Region, Turkey). Journal of Structural Geology 46, 99-114.

Emre, Ö., Duman, T. Y., Özalp, S., Elmacı, H., Olgun, S., Şaroglu, F. 2013. 1/1.250.000 scale Turkey Active Fault Map. General Directorate of Mineral Research and Exploration Special Publication.

Emre, Ö., Duman, T. Y., Özalp, S., Saroglu, F., Olgun, S., Elmacı, H., Can, T. 2018. Active fault database of Turkey. Bulletin of Earthquake Engineering 16(8), 3229-3275.

Frohlich, C., Davis, S. D. 1993. Teleseismic b values; or, much ado about 1.0. Journal of Geophysical Research: Solid Earth 98(B1), 631-644.

Görür, N., Çağatay, M., Zabcı, C., Sakınç, M., Akkök, R., Şile, H., Örçen, S. 2015. The late Quaternary tectono-stratigraphic evolution of the Lake Van, Turkey. Bulletin of the Mineral Research and Exploration 151, 1-46.

Gutenberg, B., Richter, C. F. 1944. Frequency of earthquakes in California. Bulletin of the Seismological Society of America 34(4), 185-188.

Irmak, T. S., Doğan, B., Karakaş, A. 2012. Source mechanism of the 23 October 2011, Van (Turkey) earthquake (M= 7.1) and aftershocks with its tectonic implications. Earth Planets Space 64, 991-1003.

Işık, S. E., Konca, A. Ö., Karabulut, H. 2017. The seismic interactions and spatiotemporal evolution of seismicity following the October 23, 2011 M 7.1 Van, Eastern Anatolia, earthquake. Tectonophysics 702, 8-18.

Keskin, M. 2003. Magma generation by slab steepening and breakoff beneath a subduction–accretion complex: an alternative model for collision-related volcanism in Eastern Anatolia, Turkey. Geophysical Research Letters 30, 9-4.

Keskin, M. 2007. Eastern Anatolia: A hotspot in a collision zone without a mantle plume. Geological Society of America Special Paper 430, 693–722.

KOERI (Kandilli Observatory and Earthquake Research Institute). http://www.koeri.boun.edu.tr/sismo/zeqdb/. 01 June 2021.

Lahn, E. 1948. Türkiye göllerinin jeolojisi ve jeomorfolojisi hakkında bir etüd. MTA Yayınları, B(12).

Mackenzie, D., Elliott, J. R., Altunel, E., Walker, R. T., Kurban, Y.C., Schwenninger, J. L., Parsons, B. 2016. Seismotectonics and rupture process of the M 7.1 2011 Van reverse-faulting earthquake, eastern Turkey, and implications for hazard in regions of distributed shortening. Geophysical Journal International 206, 501–524.

Maden, N., Öztürk, S. 2015. Seismic b-values, bouguer gravity and heat flow data beneath Eastern Anatolia, Turkey: tectonic implications. Surveys in Geophysics 36(4), 549-570.

Mahatsente, R., Önal, G., Çemen, I. 2018. Lithospheric structure and the isostatic state of Eastern Anatolia: Insight from gravity data modelling. Lithosphere 10(2), 279-290.

Mogi, K. 1962. Study of elastic shocks caused by the fracture of heterogeneous materials and its relations to earthquake phenomena. Bulletin of the Earthquake Research Institute University of Tokyo 40(1), 125-173.

Ogata, Y., Imoto, M., Katsura, K. 1991. 3-D spatial variation of b-values of magnitude-frequency distribution beneath the Kanto District, Japan. Geophysical Journal International 104, 135-146.

Olsson, R. 1999. An estimation of the maximum b-value in the Gutenberg-Richter relation. Geodynamics 27, 547-552.

Özacar, A. A., Zandt, G., Gilbert, H., Beck, S. L. 2010. Seismic images of crustal variations beneath the East Anatolian Plateau (Turkey) from teleseismic receiver functions. Geological Society of London, Special Publications 340(1), 485-496.

Özer, Ç. 2019. Investigation of Soil Amplification in Lake Van Basin. Research Reviews in Engineering. Gece Kitaplığı, Türkiye.

Öztürk, S. 2015. Depremselliğin fraktal boyutu ve beklenen güçlü depremlerin orta vadede bölgesel olarak tahmini üzerine bir modelleme Doğu Anadolu Bölgesi, Türkiye. Gümüşhane Üniversitesi, Fen Bilimleri Enstitüsü Dergisi 5(1), 1-23.

Öztürk, S. 2017. Space-time assessing of the earthquake potential in recent years in the Eastern Anatolia region of Turkey. Earth Sciences Research Journal 21(2), 67-75.

Öztürk, S. 2018. Earthquake hazard potential in the Eastern Anatolian Region of Turkey: seismotectonic *b* and *Dc*-values and precursory quiescence *Z*-value. Frontiers of Earth Science 12(1), 215-236.

Öztürk, S., Bayrak, Y. 2012. Spatial variations of precursory seismic quiescence observed in recent years in the Eastern part of Turkey. Acta Geophysica 60(1), 92-118.

Reasenberg, P. 1985. Second-order moment of central California seismicity, 1969–1982. Journal of Geophysical Research: Solid Earth 90(B7), 5479-5495.

Reilinger, R., McClusky, S., Vernant, P., Lawrence, S., Ergintav, S., Cakmak, R., Ozener, H., Kadirov, F., Guliev, I., Stepanyan, R., Nadariya, M., Hahubia, G., Mahmoud, S., Sakr, K., ArRajehi, A., Paradissis, D., Al-Aydurs, A., Prilepin, M., Guseva, T., Evren, E., Dmitrotsa, A., Filikov, S.V., Gomez, F., Al-Ghazzi, R., Karam, G. 2006. GPS constraints on continental deformation in the Africa-Arabia-Eurasia continental collision zone and implications for the dynamics of plate interactions. Journal of Geophysical Research Solid Earth 111(B5), B05411.

Scholz, C. H. 1968. The frequency-magnitude relation of microfracturing in rock and its relation to earthquakes. Bulletin of the Seismological Society of America 58(1), 399-415.

Selçuk, A. S. 2016. Evaluation of the relative tectonic activity in the eastern Lake Van basin, East Turkey. Geomorphology 270, 9-21.

Sumita, M., Schmincke, H. U. 2013. Impact of volcanism on the evolution of Lake Van II: temporal evolution of explosive volcanism of Nemrut Volcano (eastern Anatolia) during the past ca. 0.4 Ma. Journal of Volcanology and Geothermal Research 253, 15–34.

Suyehiro, S. 1964. Foreshocks and aftershocks accompanying a perceptible earthquake in central Japan. Papers in Meteorology and Geophysics 15, 71-88.

Şaroğlu, F., Yılmaz, Y. 1986. Doğu Anadolu'da Neotektonik Dönemdeki Jeolojik Evrim ve Havza Modelleri. Maden Tetkik ve Arama Genel Müdürlüğü, Jeoloji Etütleri Dairesi, Ankara.

Şengör, A. M. C., Özeren, S., Genç, T., Zor, E. 2003. East Anatolian high plateau as a mantle-supported, north-south shortened domal structure. Geophysical Research Letters 30, 4.

Toda, S., Stein, R. S., Sevilgen, V., Lin, J. 2011. Coulomb 3.3 graphic-rich deformation and stress-change software for earthquake, tectonic, and volcano research and teaching-user guide. United State Geological Survey, Open-File Report, 1060.

Toker, M. 2014. Discrete characteristics of the aftershock sequence of the 2011 Van Earthquake. Journal of Asian Earth Sciences 92, 168-186.

Toker, M., Şengör, A. M. C., Schluter, F. D., Demirbağ, E., Çukur, D., Imren, C., Niessen, F., PaleoVan-working Group. 2017*a*. The structural elements and tectonics of the Lake Van basin (Eastern Anatolia) from multi-channel seismic reflection profiles. Journal of African Earth Sciences 129, 165-178.

Toker, M., Pınar, A., Tur, H. 2017*b*. Source mechanisms and faulting analysis of the aftershocks in the Lake Erçek area (Eastern Anatolia, Turkey) during the 2011 Van event (Mw 7.1): implications for the regional stress field and ongoing deformation processes. Journal of Asian Earth Sciences 150, 73–86.

Warren, N. W., Latham, G. V. 1970. An experimental study of thermally induced microfracturing and its relation to volcanic seismicity. Journal of Geophysical Research 75(23), 4455-4464.

Wessel, P., Smith, W. H. F., Scharroo, R., Luis, J. F., Wobbe, F. 2013. Generic Mapping Tools: Improved version released. EOS, Transactions American Geophysical Union 94, 409-410.

Wiemer, S. 2001. A software package to analyze seismicity: ZMAP. Seismological Research Letters 72(3), 373-382.

Wiemer, S., Wyss, M. 1997. Mapping the frequency-magnitude distribution in asperities: An improved technique to calculate recurrence times?. Journal of Geophysical Research: Solid Earth 102(B7), 15115-15128.

Wiemer, S., Wyss, M. 2002. Mapping spatial variability of the frequency-magnitude distribution of earthquakes. In Advances in Geophysics 45, 259.

Wyss, M. 1973. Towards a physical understanding of the earthquake frequency distribution. Geophysical Journal of the Royal Astronomical Society 31(4), 341-359.

Yadav, R. B. S., Gahalaut, V. K., Chopra, S., Shan, B. 2012. Tectonic implications and seismicity triggering during the 2008 Baluchistan, Pakistan earthquake sequence. Journal of Asian Earth Sciences 45, 167–178.

Yılmaz, Y., Şaroğlu, F., Güner, Y. 1987. Initiation of the Neomagmatism in East Anatolia. Tectonophysics 134, 177-199.

Zhu, H. 2018. High Vp/Vs ratio in the crust and uppermost mantle beneath volcanoes in the Central and Eastern Anatolia. Geophysical Journal International 214(3), 2151-2163.

Bulletin of the Mineral Research and Exploration

http://bulletin.mta.gov.tr

Accurate whole-rock geochemistry analysis by combined ICP-OES and LA-ICP-MS instruments

Gönenç GÖÇMENGİL[a*], Fatma ŞİŞMAN TÜKEL[b], Fulya UZUN[c], Marcel GUILLONG[d], İsak YILMAZ[b], Namık AYSAL[b] and Nurullah HANİLÇİ[b]

[a]*İstanbul University-Cerrahpaşa, Geochronology and Geochemistry Laboratory, İstanbul, Türkiye*
[b]*İstanbul University-Cerrahpaşa, Geological Engineering Department, İstanbul, Türkiye*
[c]*İstanbul University-Cerrahpaşa, Geological Engineering Department, Institute of Graduate Studies, İstanbul, Türkiye*
[d]*Swiss Federal Institute of Technology in Zürich (ETH), Department of Earth Sciences, Zurich, Switzerland*

Short Note

Keywords:
Copper-Rich Gold Ore, Gold Adsorption, Activated Carbon, Resin, Selectivity.

ABSTRACT

ICP-OES and LA-ICP-MS instruments routinely used to assess the geochemical properties of the various natural and synthetic materials. In this contribution, the analytical routines and method development procedures of the ICP-OES and LA-ICP-MS facilities installed at the İstanbul University-Cerrahpaşa Geological Engineering Department, Geochronology and Geochemistry Laboratory have been evaluated using well-known international rock standards. Sample preparation techniques, method development, experimental setup and measurement conditions for the both ICP-OES and LA-ICP-MS instruments were discussed and specific analyze results of NIST SRM 614, BCR-2, AGV-2, BCR-2G and AGV-2G were evaluated. Flux-free USGS glass standards were produced by in-house techniques and flux-bearing glasses were produced by fusion of sample with the mixture of ultra-pure lithium-tetraborate, lithium metaborate and lithiumbromide were evaluated and compared with the well-known reference values in the literature. Relative standard deviation (RSD) values for the major oxide measurements for standards given range of 0.0 wt. % to 1.5 wt. %. RSD values for the trace and rare-earth-elements values were mainly lower than 10 wt. %. The results confirm that the both flux-bearing and flux-free glasses reasonably match with the world-wide inter-laboratory values for international standards samples. The combination of these two instruments can be used to conduct geochemistry of various solid earth materials.

Received Date: 08.02.2021
Accepted Date: 03.06.2021

1. Introduction

Whole-rock geochemical data is the benchmark of the petrological studies and different aspects of the geological research. From the beginning of the 1970s large compilation and datasets from the various parts of the world have been created for igneous, metamorphic and sedimentary petrology studies by using whole-rock geochemistry (Pearce et al., 1984). Majority of these data have been determined successively by instruments of X-ray Fluorescence (XRF, Potts and Webb, 1992), Inductively Coupled Plasma-Mass Spectrometry (ICP-MS; Jenner et al., 1990), Inductively Coupled Plasma Atomic Emission Spectroscopy (ICP-AES) or Inductively Coupled Plasma - Optical Emission Spectrometry (ICP-OES; Dahlquist and Knoll, 1978) and many different techniques outlined in Jochum et al., (2011).

Citation Info: Göçmengil, G., Şişman Tükel, F., Uzun, F., Guillong, M., Yılmaz, İ., Aysal, N., Hanilçi, N. 2022. Accurate whole - rock geochemistry analysis by combined ICP - OES and LA - ICP - MS instruments.Bulletin of the Mineral Research and Exploration 168, 157-165. https://doi.org/10.19111/bulletinofmre.947703

**Corresponding author: Gönenç GÖÇMENGİL, gonencgocmengil@gmail.com*

Together with the XRF techniques, ICP-OES also frequently used to assess the whole-rock geochemical or specific element contents of the desired samples (Jarvis and Jarvis, 1992; Navarro et al., 2002; Alomary and Belhadj, 2007). ICP-OES is a spectrometric technique to assess the elemental content of the aqueous solutions. Sample preparation techniques, dilution factors, element infiltration and interpretation of the output data significantly affect the results of the ICP-OES instrumentation. However, ICP-OES routinely used to analyze for the major oxide elements and high concentration (>100 ppm) element ratios (Elburg et al., 2012; Shao et al., 2017).

By the development of the combined analysis of Laser Ablation (LA) and ICP-MS, these combined instruments became also a powerful and routine tool to detect the whole rock geochemistry of the geological samples (Longerich et al., 1996; Norman et al., 1996; Günther et al., 2001; Petrelli et al., 2008; Tamura et al., 2015). Apart from the spot analysis of the actual samples such as minerals, glass or rock powder pellets; sample preparation techniques such as powdering (Imai, 1990), flux-free fusion (Fedorowich et al., 1993; Norman et al., 1996), Pt-crucible flux-free fusion (Chen et al., 2000), Pt-capsule flux-free fusion (Kurosawa et al., 2006) and lithium borate ($Li_2B_4O_7$) fusion (Günther et al., 2001; Eggins, 2003) are frequently used to create samples that are suitable for LA-ICP-MS measurements.

In this contribution, we will explore the analytical capabilities of the ICP-OES and LA-ICP-MS instruments installed at the Geochronology and Geochemistry Laboratory of İstanbul University-Cerrahpaşa, Faculty of Engineering, Department of Geological Engineering. Developed methods to measure the whole rock geochemistry of the natural rock associations for combined ICP-OES and LA-ICP-MS and evaluated experimental scheme of the analysis will be checked by measuring the international reference samples of BCR-2 (and BCR-2G- flux free), AGV-2 (and AGV-2G flux free) by USGS (United States Geological Survey) and SRM NIST 614. In the following chapter, we first give the general outlines of the experimental setup of the ICP-OES and LA-ICP-MS for the whole rock geochemistry analysis; we will explain the samples preparation techniques, then we further discuss the data acquisition, data interpretation and subsequent results.

2. Instrumentation

We use Perkin Elmer AVIO 200 ICP-OES together with Perkin Elmer NexION 2000 ICP-MS combined with ESI NWR213 solid state laser for the whole rock analytical measurements. First we present the general configuration, sample preparation and experimental conditions of the ICP-OES instrument, and then we will evaluate the general characteristics of the LA-ICP-MS configuration.

2.1. Sample Dissolution Procedures and Experimental Conditions for ICP-OES

Rock powders of the BCR-2 and AGV-2 used for the whole rock measurements. We mainly measure the major oxide elements (analytes) to deduce the desired content of the studied samples with ICP-OES. 0.2 gram of rock powder was fused with 1 gram of ultra-pure lithium-tetraborate ($Li_2B_4O_7$), lithium metaborate ($LiBO_2$) and lithiumbromide (LiBr) (We mention this technique as lithium tetraborate fusion or fusion for the remainder of the text). Mixed powders were poured in the platinum-gold (95 wt. %) Pt + 5 wt. % Au) crucibles and heated at 1050 °C for 20 minutes. Fused rock powders dissolved in 5 wt. % trace metal grade (63.012 %) HNO_3 solution on hot plates with magnetic mixer. The solutions were transferred to falcon tubes of known weight and additional 5 wt. % HNO_3 added up to 50 g total mass of the final solution. Depending on the type of the sample, they were diluted by 1/1000 or 1/2000 dilution factors. Apart from the three different USGS standards, Geological Survey of Japan (GSJ; JR-1, JG1-A), additional USGS standards (BHVO-1; GSP-2; and reagent blanks) were also prepared for calibration and internal standardization.

Perkin Elmer AVIO 200 ICP-OES has very low argon consumption rate (8 L/min) and generates matrix-tolerant plasma during the measurement stage. Attenuated radial, attenuated axial, radial and axial modes of plasma views using for the specific elements. All the tables for the manuscript stored in Mendeley Database. Plasma operating conditions for ICP-OES given in Mendeley Database, 2021. More common major oxides were mainly measured with radial modes while the scarcer elements have been measured

by axial modes. Sample measurement takes place 100 seconds and sample washout cleaning sessions between samples also taken as 60 seconds. Limit of detection with spectral wavelengths for the major oxide analytes are given in Mendeley Database, 2021. Coefficient of correlation for the ICP-OES analysis always calibrated for greater values than 0.9995 (>r).

2.2. Sample Dissolution Procedures and Experimental Conditions for ICP-OES

Perkin Elmer NexION 2000 ICP-MS combined with ESI NWR213 laser system have been used to measure the specific analyte content of the desired samples. We use BCR-2, AGV-2, BCR-2G and AGV-2G USGS glass standards and NIST 614 standard to show to how accurate the geochemistry analysis done by LA-ICP-MS measurements. Besides, during analysis, a reagent blank glass that only contain 1 gram of ultra-pure $Li_2B_4O_7$, $LiBO_2$ and LiBr added to the analyze section to allow correction during data interpretation.

BCR-2 and AGV-2 glass discs were created by using lithium tetraborate fusion procedure that were explained in the section above. Contrary to dissolving processes that we have conducted before the ICP-OES analysis, the fused glass discs were left in the crucibles and cooled. The cooled discs were ripped-off from the crucibles. These fused glass discs were embedded in the epoxy then polished it acquire a flat surface for analysis. We also produced flux-free BCR-2 and AVG-2 glass discs (without adding a lithium-tetraborate) by the scheme given in Wilson (2017). We also embedded these flux-free glasses of BCR-2G and AGV-2G in epoxy and polished the embedded surface (Figure 1).

The surface of the different samples were cleaned with methanol, 2 wt. % HNO_3 trace metal grade nitric acid and 18 MΩ ultrapure water before the analysis. We use NIST glasses 610 and 612 for initial instrument calibration and within session measurements. Helium was used as a carrier gas for ablated aerosol. LA-ICP-MS operating conditions were outlined in the Mendeley Database, 2021.

LA-ICP-MS measurements were carried out using time resolved analysis operating in a peak jumping mode. The laser repetition rate and the laser energy density are fixed to 10 Hz and ~7 J/cm^2, respectively (Mendeley Database, 2021). Data were collected by runs that consists three standard measurements at the beginning (each on 610 and 612), nine spot measurement three standard measuring on the closing of the measurements with session. The selected measuring scheme were implemented from Petrelli et al., (2008). Internal standards were selected as ^{29}Si or ^{42}Ca which were given by the measurements in ICP-OES for BCR-2 and AGV-2. The internal standard values for NIST 614 were from the GEOREM database. All samples (standards, samples and blanks) were in the same sample holder.

Limits of detections (LODs) values have been evaluated according to outline given in Longerich et al., (1996). In the Figure 2, we plotted the general

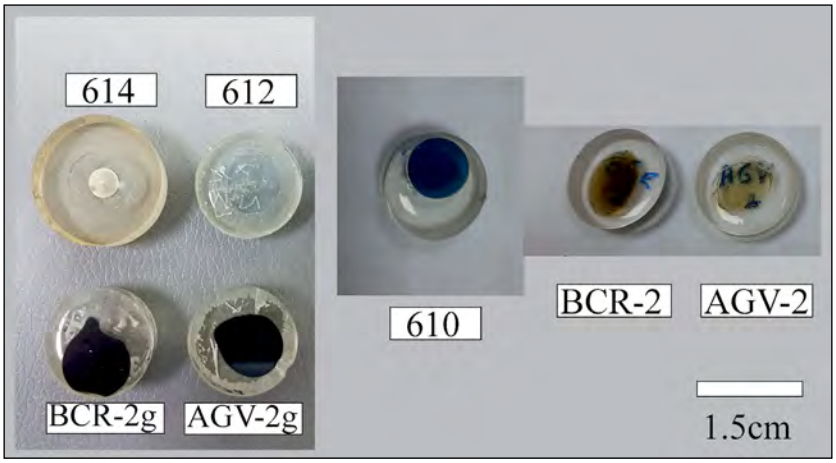

Figure 1- Embedded glass discs prepared for LA-ICP-MS measurements.

LODs values for standard reference material 610. LODs values were dispersed along 4.7 to 0.01 ug/g for 40 µm spot size. Differences in the LODs values were extremely sensitive to spot size, instrument counting power, accuracy, behaviour of the elements and background gas values in the measurement system (Günther et al., 2001). If all other parameters except spot size were fixed, range of the LODs mainly were controlled by increase or decrease of the spot size. If we pick a lower value of spot size such as 20 um, range of LODs reduced but the sampling area by laser might represent a lower fraction of the glass disc and therefore poor representation of the measured samples. Thus, in our attempts, we experienced the most reliable results achieved by using 40 µm even the LODs slightly large range comparing the other spot values.

3. Data Reduction for ICP-OES and LA-ICP-MS

The data reduction of ICP-OES analysis were done by Perkin Elmer SYNGISTIX data reduction software. The measured intensities were directly calculated as weight percent by the algorithms written in the software. For the natural samples, pre-calculated loss of ignition values were added during the calculation. The iron content of the samples were given as total FeO in the results.

Trace element analysis of the selected samples have been conducted by LA-ICP-MS and data reduction was done by the SILLS (Guillong et al., 2008); ICPMSDatCAL (Liu et al, 2010) softwares. SILLS (Guillong et al., 2008); ICPMSDatCAL (Liu et al, 2010) softwares (Figure 3 and 3b).

4. Discussion

In this section, first we will present and discuss the results of ICP-OES measurements on the two USGS standards that were dissolved by nitric acid techniques. Afterwards, we presented the results of the measurements conducted by LA-ICP-MS system and discussed the accuracy and homogeneity of the produced flux-bearing and flux-free glasses of the standard materials.

4.1. Discussion of the ICP-OES Measurements

The results of the major oxide compositions of the BCR-2 and AGV-2 were situated in the reasonable range with the standards values given in the literature for these two well-known samples (Govindaraju, 1994; Jochum et al., 2016). The measured values were compared with the large-scale data set of the Jochum et al., (2016) that contain measurement for BCR-2 and measurement for AGV-2 that were compiled from various techniques. The measured values from our results were compared to the compilation values fits well (Mendeley Database, 2021). The biggest RSD values belong to P_2O_5 and MnO measurements but they remain below 1.5. Accuracy (here expressed

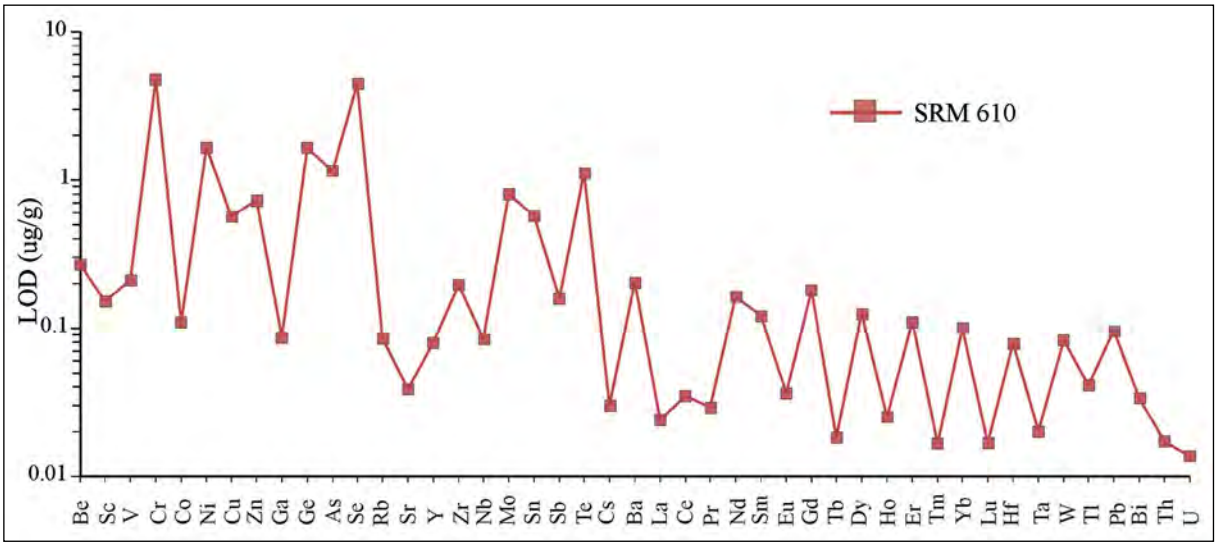

Figure 2- Limits of detection for 40 µm laser spot size on SRM 610.

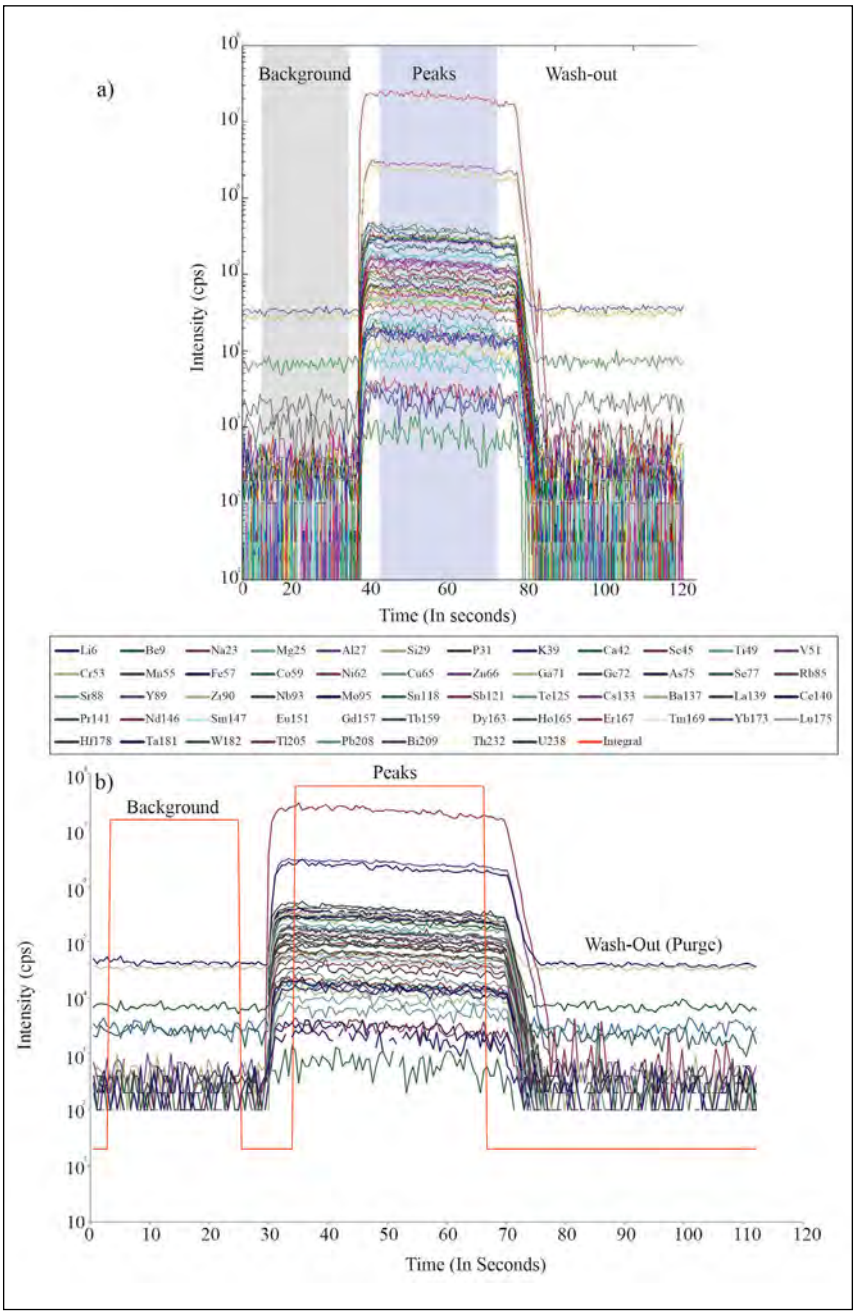

Figure 3- a) Signal selection window of the SILLS software, b) data reduction and signal selection window of the ICPMSDataCal.

as relative deviation from the standard reference material) is 2.5 % better than all the measurements. Thus the measured USGS glasses give accurate results and they can be used to constrain the internal standards for the various natural and synthetic rock and mineral samples that evaluated at the LA-ICP-MS system.

4.2. Discussion of the LA-ICP-MS Measurements

Even though there are many different problems can effect and alter the measurement on LA-ICP-MS systems as outlined in the previous sections, the glass producing techniques and glass homogeneity also significantly affect the measurements (Liu et al., 2013). The contribution of the Jochum et al. (2011)

clearly was indicated core and rim variations of the different elements along the whole scale measurements on NIST SRM 610 to 617. To tackle this problem, we also mainly measure the core regions of the both our in-house produced glass discs with or without-fusion processes.

Results of the measured standards have been given in Mendeley Database. In all measurements, the standards were reasonably matched well with the measurements that have been conducted in different laboratories. Error values were displayed as two sigma (σ) and reasonably low for the majority of the trace element values.

The lithium tetraborate fusion mainly sustains robust sample digestion and creates nearly homogeneous and intact samples that can be easily stored and re-measured after long periods of time (Eggins, 2003). However, in house generation of the flux-free glasses can posses problems since the absence of the fluxing agent and possible case of incomplete homogenization throughout the sample (Petrelli et al., 2008, Jochum et al., 2016). We plot the results of our samples and compare their relative deviation from a standard value (Figure 4). Majority of the plotted samples created by the lithiumtetraborate fusion (BCR-2 and AGV-2) display more minor relative deviation than flux-free glasses (BCR-2g and AGV-2g). The most prominent spikes come from Tb and Lu measurements on flux-free glass samples. Thus it can be postulated that the flux-bearing glasses are more reasonable agents to understand the general trace element chemistry of the desired samples.

Since the rare earth elements are one of the most common geochemical discriminator in the geochemical studies (e.g. Pearce et al., 1984) we specifically show their RSD values in weight percent to show the reliability of our measurement in Figure 5. In these RSD values are mainly calculated lower than the 10 % percent relative to standard reference values for the fused discs, while the flux-free glasses display much higher relative standard distributions as outlined above. Besides, SRM 614 values also display values always lower better than 10 % relative distribution values. Surprisingly, in both AGV-2g and BCR-2g samples, Tb values display high relative deviations. The reason of this defect related with the possible incomplete homogenization during fusion processes. But even so, the case majority of the sample was situated within the reasonable range.

Thus, the results show the good precision levels of both in-house produced flux-free glass standards and flux-bearing fused glass discs during the ICP-OES and LA-ICP-MS measurements.

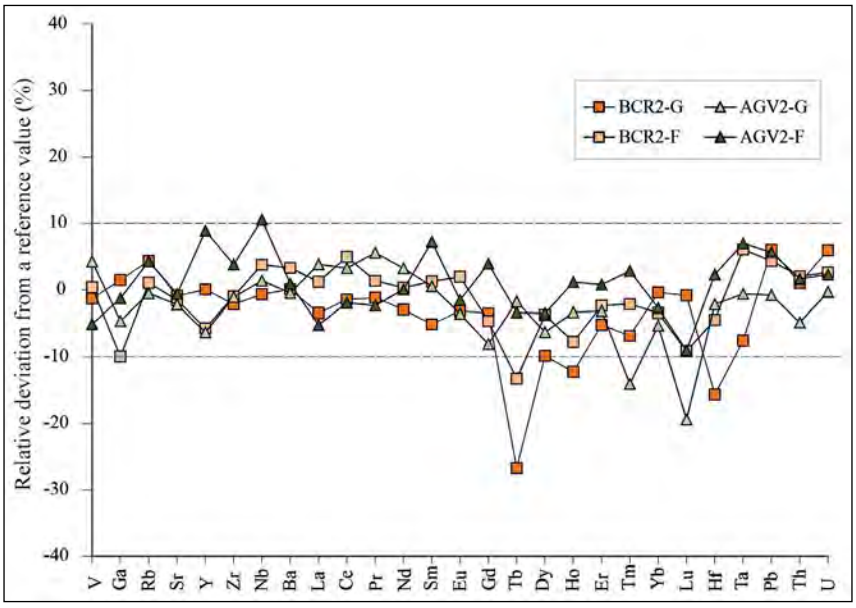

Figure 4- Relative standard deviation from a reference value of the measurements conducted in this study. The reference values taken from Jochum et al. (2016) (BCR-2F and AGV2-F represent samples generated by lithium tetraborate fusion).

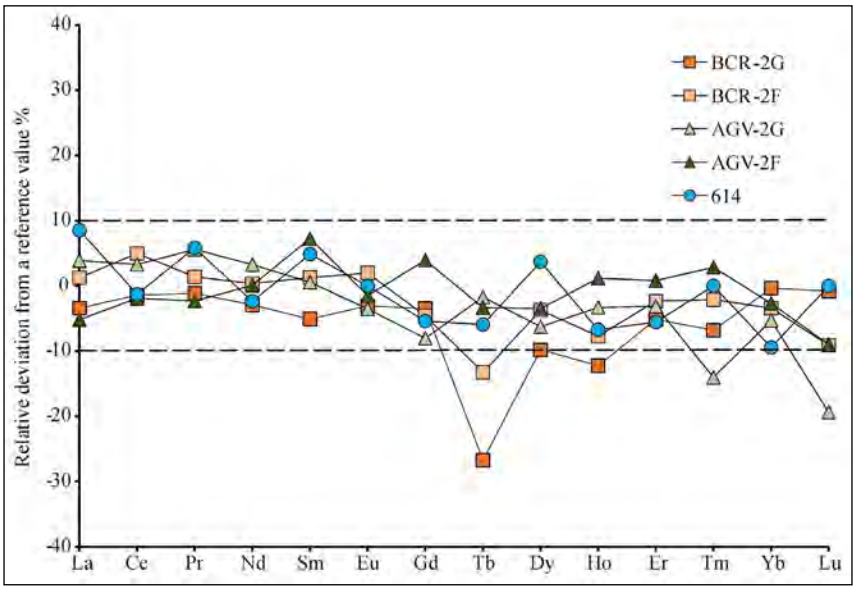

Figure 5- Relative deviation from a reference value for specifically for REE values of the measured samples. Values for SRM 614 taken from Jochum et al. (2011) other values taken from Jochum et al. (2016) (BCR-2F and AGV2-F represent samples generated by lithium tetraborate fusion).

5. Results

ICP-OES and LA-ICP-MS measurements, which are installed at İstanbul University-Cerrahpaşa Geological Engineering Department Geochronology and Geochemistry Laboratory display accurate analysis capabilities have been conducted in international known standard reference materials. ICP-OES analysis of major oxide elements reasonably match with the international standards. Mainly, majority of the samples display better relative deviation values than 10%. The flux-free glasses of BCR-2g and AGV-2g often display much higher relative deviation comparing to standard values as high as 25%. Thus, the lithium tetraborate fusion displays more homogeneous glasses for the LA-ICP-MS measurements. The reason of this situation can be related with the incomplete homogenization of the desired sample. Anyhow, samples reasonably display close values with the international standard values.

Therefore, the combined measurement systems confirm the well resolved capabilities and application potential of this laboratory on various areas of petrology, geochemistry, analysis of natural and synthetic minerals, metals, environmental samples and archaeological - archaeometry samples.

Acknowledgements

This work was supported by the Research Funds of the İstanbul University - Cerrahpaşa, project number: 23384.

References

Alomary, A. A., Belhadj, S. 2007. Determination of heavy metals Cd, Cr, Cu, Fe, Ni, Pb, Zn by ICP-OES and their speciation in Algerian Mediterranean Sea sediments after a five-stage sequential extraction procedure. Environmental Monitoring and Assessment 135, 1-3, 265-280.

Chen, Z., Canil, D., Longerich, H. P. 2000. Automated in situ trace element analysis of silicate materials by laser ablation inductively coupled plasma mass spectrometry. Fresenius' Journal of Analytical Chemistry 368, 73-78.

Dahlquist, R. L, Knoll, J. W. 1978. Inductively coupled plasma-atomic emission spectrometry: analysis of biological materials and soils for major, trace, and ultra-trace elements. Applied Spectroscopy 32, 1-30.

Eggins, S. M. 2003. Laser ablation ICP-MS analysis of geological materials prepared as lithium borate glasses. Geostandards Newsletter 27, 147-162.

Elburg, M. A., Andersen, T., Bons, P. D., Weisheit, A., Simonsen, S. L., Smet, I. 2012. Metasomatism and metallogeny of A-type granites of the Mt

Painter–Mt Babbage Inliers, South Australia. Lithos 151, 83-104.

Fedorowich, J. S., Richards, J. P., Jain, J. C., Kerrich, R., Fan, J. 1993. A rapid method for REE and trace-element analysis using laser sampling ICP-MS on direct fusion whole-rock glasses. Chemical Geology 106(3-4), 229-249.

Georem database. http://georem.mpch-mainz.gwdg.de/start.asp?dataversion=current. 27 Şubat 2021.

Govindaraju, K. 1994. 1994 compilation of working values and sample description for 383 geostandards. Geostandards Newsletter 18, 1-158.

Guillong, M., Meier, D. L., Allan, M. M., Heinrich, C. A., Yardley, B. W. 2008. A Matlab-based program for the reduction of laser ablation ICP-MS data of homogeneous materials and inclusions. Mineralogical Association of Canada Short Course 40, 328-333.

Günther, D., Quadt, A. V., Wirz, R., Cousin, H., Dietrich, V. J. 2001. Elemental analyses using laser ablation-inductively coupled plasma-mass spectrometry LA-ICP-MS of geological samples fused with $Li_2B_4O_7$ and calibrated without matrix-matched standards. Microchimica Acta 136(3-4), 101-107.

Imai, N. 1990. Quantitative analysis of original and powdered rocks and mineral inclusions by laser ablation inductively coupled plasma mass spectrometry. Analytica Chimica Acta 235, 381-391.

Jarvis, I., Jarvis, K. E. 1992. Inductively coupled plasma-atomic emission spectrometry in exploration geochemistry. Journal of Geochemical Exploration 44(1-3), 139-200.

Jenner, G. A., Longerich, H. P., Jackson, S. E., Fryer, B. J. 1990. ICP-MS—a powerful tool for high-precision trace-element analysis in Earth sciences: Evidence from analysis of selected USGS reference samples. Chemical Geology 83(1-2), 133-148.

Jochum, K. P., Weis, U., Stoll, B., Kuzmin, D., Yang, Q., Raczek, I., Enzweiler, J. 2011. Determination of reference values for NIST SRM 610–617 glasses following ISO guidelines. Geostandards and Geoanalytical Research 35(4), 397-429.

Jochum, K. P., Weis, U., Schwager, B., Stoll, B., Wilson, S. A., Haug, G. H., Enzweiler, J. 2016 . Reference values following ISO guidelines for frequently requested rock reference materials. Geostandards and Geoanalytical Research 40(3), 333-350.

Kurosawa, M., Shima, K., Ishii, S., Sasa, K. 2006. Trace element analysis of fused whole-rock glasses by laser ablation-ICP-MS and PIXE. Geostandards and Geoanalytical Research 30(1), 17-30.

Liu, Y., Hu, Z., Zong, K., Gao, C., Gao, S., Xu, J., Chen, H. 2010. Reappraisement and refinement of zircon U-Pb isotope and trace element analyses by LA-ICP-MS. Chinese Science Bulletin 55(15), 1535-1546.

Liu, Y., Hu, Z., Li, M., Gao, S. 2013. Applications of LA-ICP-MS in the elemental analyses of geological samples. Chinese Science Bulletin 58(32), 3863-3878.

Longerich, H. P., Jackson, S. E., Günther, D. 1996. Inter-laboratory note. Laser ablation inductively coupled plasma mass spectrometric transient signal data acquisition and analyte concentration calculation. Journal of Analytical Atomic Spectrometry 11(9), 899-904.

Mendeley Database. https://data.mendeley.com/datasets/tfxzf3v44s/draft?a=d0b2dfde-46dd-4c6b-b024-ea27310b85e1. 27 Şubat 2021.

Navarro, M. S., Ulbrich, H. H. G. J., Andrade, S., Janasi, V. A. 2002. Adaptation of ICP–OES routine determination techniques for the analysis of rare earth elements by chromatographic separation in geologic materials: tests with reference materials and granitic rocks. Journal of Alloys and Compounds 344(1-2), 40-45.

Norman, M. D., Pearson, N. J., Sharma, A., Griffin, W. L. 1996. Quantitative analysis of trace elements in geological materials by laser ablation ICPMS: instrumental operating conditions and calibration values of NIST glasses. Geostandards Newsletter 20(2), 247-261.

Pearce, J. A., Harris, N. B., Tindle, A. G. 1984. Trace element discrimination diagrams for the tectonic interpretation of granitic rocks. Journal of Petrology 25(4), 956-983.

Perkin Elmer Syngistix Software. https://www.perkinelmer.com/ lab-solutions/resources/docs/PRD_Syngistix-Atomic-Spec- Software-Family_011968_01.pdf . 27 Şubat 2021.

Petrelli, M., Perugini, D., Alagna, K. E., Poli, G., Peccerillo, A. 2008. Spatially resolved and bulk trace element analysis by laser ablation-inductively coupled plasma-mass spectrometry LA-ICP-MS . Periodico di Mineralogia 77(3), 3-21.

Potts, P. J., Webb, P. C. 1992. X-ray fluorescence spectrometry. Journal of Geochemical Exploration 44(1-3), 251-296.

Shao, F., Niu, Y., Liu, Y., Chen, S., Kong, J., Duan, M. 2017. Petrogenesis of Triassic granitoids in the East Kunlun Orogenic Belt, northern Tibetan Plateau and their tectonic implications. Lithos 282, 33-44.

Tamura, A., Akizawa, N., Otsuka, R., Kanayama, K., Python, M., Morishita, T., Arai, S. 2015. Measurement of whole-rock trace-element composition by flux-free fused glass and LA-ICP-MS: evaluation of simple and rapid routine work. Geochemical Journal 49(3), 243-258.

Wilson, S. 2017. USGS microanalytical reference materials MRMS development. Microscopy and Microanalysis 23, 492-493.

Publication Rules for the "Bulletin of the Mineral Research and Exploration"

1. Purposes

• To contribute to the establishment of scientific communication issues in earth sciences both in Türkiye and internationally.

• To contribute to economic (mining, oil and gas, geothermal etc.), environmental and social (geoheritage etc.) studies in Türkiye and in the World.

• To make the earth science scientific research and applications made by the MTA on publicly known,

• To use the bulletin as an effective tool in the international publication exchange by keeping it at a high level in terms of quality, scope and format,

• To contribute to the efforts of developing Turkish as a language of science and removing foreign words.

2. Scope-Attribute

In order for manuscripts to be published in the Bulletin of the Mineral Research and Exploration, they must have at least one of the following qualifications:

2.1. Research Articles and Reviews

2.1.1. Original Scientific Researches

• Such articles cover original scientific research and its results that contribute to the fundamental issues of earth sciences, research and evaluation of underground resources, and examine the environmental problems in terms of earth sciences,

• It covers research that apply new approaches and methods in solving problems related to earth sciences.

2.1.2. Review Articles

• They cover studies that compile previous research on subjects of earth sciences with a critical approach and put forward a new opinion on that subject.

2.2. Criticism and Response Articles

• Articles that criticize all or part of an article of the bulletin in the latest issue are published in the following first issue, if submitted within six months at the latest from the date of publication digitally.

• Before the publication, review articles are sent to the responsible author of the criticized article to make a response.

• If the criticism is not responded within foreseen time, the criticism letter is published alone, subsequent replies are not published. Replies are not allowed to be re-criticized.

• In criticizing and replying, scientific discussion and ethical rules should be followed. Criticism and response manuscripts should not exceed four pages, including figures, if available.

2.3. Brief Notes

• In "Brief Notes" section of the Bulletin of the Mineral Research and Exploration, the brief, objective and concise articles reflecting the data obtained from scientific researches and applications carried out in the area of earth sciences or new findings related to previously unknown geosciences in Türkiye are given place.

• The articles arranged in the "Brief Notes" section are published without waiting in the first or in the second issue the latest, after the date they are sent to the Chair of the Editorial Board in order to ensure rapid communication.

• Articles requested to be published in the "Brief Notes" section should not exceed four pages, including all figures and tables.

3. Submission and Acceptance for Manuscripts

• The manuscripts submitted to be published in the Bulletin of the Mineral Research and Exploration should be prepared in TURKISH and / or ENGLISH in accordance with the Publishing Rules of the Bulletin of the Mineral Research and Exploration, and submitted via electronic application at http://dergi.mta.gov.tr/index.php.

• The manuscript must not have been previously published partially or completely elsewhere (except in abstract form).

• Manuscripts submitted with the request for publication in the Bulletin of the Mineral Research and Exploration should not exceed 30 pages, including all illustrations. The articles exceeding 30 pages can be published if deemed appropriate by referees and editors.

• In the submitted manuscript, the number of figures and tables should be given in proportion to the main text in a ratio of 1/3.

• Corresponding author is asked to suggest at least three referees for the evaluation of the manuscript. (The proposed referees and the authors should not have any joint work within the last two years).

• Manuscripts that do not comply with the Publishing Rules for the Bulletin of the Mineral Research and Exploration in terms of quality and form are directly returned without being examined in terms of content.

• Manuscripts deemed appropriate in terms of format are sent to at least two expert referees for review by the Editorial Board of the Bulletin of the Mineral Research and Exploration.

• Authors should make the referee corrections and suggestions sent to them within 20 days and upload to the system.

• Comments from referees are evaluated by the Editors and associated editors. Manuscripts deemed necessary to be corrected are sent back to the authors with a request for correction. Whether the suggested corrections have been made or not is checked by the Editorial Board.

• In the revision proposals given by the editors and referees, if there are suggestions that are not accepted by the author and have not been corrected, a report explaining the reason for rejecting these suggestions by the author should be sent to the Editorial Board together with the corrected copies.

• After the last control at the printing stage, the pre-print of the manuscript is sent to the authors in pdf format and the printing control is requested.

• Articles, not accepted for publication are not returned to the authors, for the unpublished articles, a letter is written to the responsible author indicating the reason for rejection.

4. Language and Period of Publication

• The Bulletin of the Mineral Research and Exploration is published three times a year, each issue as being in Turkish and the other in English languages.

• The spelling rules of the Turkish Language Association are valid for the spelling rules for the Turkish issue. However, in spelling of the words related to earth sciences, the spelling forms of technical terms are used in accordance with the decision of the Editorial Board (For example; underground, ground, earth's crust, etc.).

5. Spelling Draft

• The text of the manuscripts to be sent for the first review with the request to be published in the Bulletin of the Mineral Research and Exploration should be written in A4 (29.7 x 21 cm) size, word format, Times New Roman 10 pt., normal with 2.0 line spacing.

• At the bottom, top, left and right of the page 2.5 cm indent must be left. Formulas that require the use of special letters and symbols should be presented in computer media.

• In all subtitles, the initials of all words must be capital. First degree headings to be used in the article should be written in Times New Roman, 10 pt., bold and left aligned by giving numbers. Secondary headings should be written in Times New Roman, 10 pt., normal font and left aligned by giving numbers. Third-degree headings should be written in Times New Roman, 10 pt., italic font and left-aligned by giving numbers. Fourth-order headings should be written in Times New Roman, 10 pt., italic, aligned to the left, without giving numbers, and the text should continue after the title without a colon and a paragraph (see example article: www.dergi.mta.gov.tr).

• One blank line should be left after paragraphs in the text.

• Paragraph headings should be written 0.5 mm indentation.

• One article should respectively contain;

-Title

-Author's Name and Surname and * sign

- Abstract

- Key words

- Introduction

- Main Text

- Discussion

- Results

- Acknowledgements

- Reference sections.

• Line and page numbers must be added to the article text.

5.1. Title of the Article

• The title should reflect the subject of the article as briefly, clearly and adequately as possible. Subjects that are not sufficiently covered in the article should not be included in the title. The first letter of the title should be capitalized and the other words should be in lowercase letters (except for proper names) in Times New Roman, 10 pt. and bolded.

5.2. Author Name, Address and E-Mail Address

• The first name of the authors should be in lowercase (except the first letter), and the surname should be in capital letter and without any title.

• Only the name of the organization should be specified in the occupational address after the name and surname of the authors (position should not be specified).

• ORCID number should be taken from www.orcid.org and placed under the address.

• In articles written by more than one author, numbers should be placed on surnames of the authors, the address information should be included in the bottom line with a single line spacing. In this section, the corresponding author of the article should be indicated by using an asterisk (*) and the corresponding author's e-mail, telephone and other contact information must be provided.

• Abbreviations should not be used in writing the author's name and address. Addresses should be given in Turkish in Turkish publication and in English in English publication.

5.3. Abstract

• Abstract should be written at a level that can be understood without referring to the other parts of the article.

• The abstract should be organized as a brief presentation of the sections in the article, reflect the purpose of the article, be informative, and should be written in a way to emphasize new data and results on the subject.

• Short and simple sentences should be used in writing the abstract.

• In the abstract, there should not be any reference to other parts and illustrations of the article or to other articles.

• Information not mentioned in the main text should not be included in the abstract.

• The abstract should not exceed approximately 200 words and should be written as a single paragraph.

• Abstract should be written in Times New Roman, 10 pt., normal text with single line spacing.

• "ABSTRACT" should not be placed for the articles to be included in "Brief Notes" section.

• The English abstract should be given under the heading "ABSTRACT".

5.4. Key words

In order to facilitate searches, five keywords that will indicate the general content of the article should be selected and specified in this section. Words used in the title should not be repeated.

5.5. Introduction

• In this section, the necessary information for preparatory and facilitative to understand the article such as the purpose of the study, its location, methods of study and previous reviews on the subject should be given.

• If an unusual way is followed in naming, classification and abbreviations within the text of the manuscript, its reason should be stated in this section.

• Each of the topics to be included in this section can create a separate paragraph or a subtitle can be given for each of them when necessary (e.g. method, material, terminology and etc.).

• This section can again be used when reminder information is needed to facilitate the understanding of the article (e.g. statistical information, formulas, experimental or application methods and etc.).

5.6. Main Body of Article

• Constitutes the main body of the article.

• In this section, the data, findings and opinions that are intended to be transferred to the reader on the subject are mentioned.

• The data used in other parts of the article such as "Abstract", "Discussions", "Results" originate from this part.

• Care should be taken not to deviate from the purpose

stressed in the "Introduction" section of the article when dealing the topics. Information that does not contribute to the achievement of the purpose of the article or that is not used to reach the conclusion should not be included.

• All data used in this section and all opinions put forward should be proven by the findings obtained from the studies or based on a source by reference.

• The way and method to be followed in handling the topics vary according to the characteristics of the topics covered.

• Subject headings in necessary numbers with different stages should be used in this section.

5.7. Discussions

• The data and findings objectively conveyed in the "Main Text" section of the article should be discussed by the author in this section. Discussions should be separate from the "Results" section.

5.8. Results

• New data and findings obtained from the review that constitutes the subject of the article should be stated concisely and concretely in this section.

• Subjects that are not adequately addressed and / or covered in the main text should not be included in this section.

• The results can be given as items in order to emphasize the research results and make the expression understandable.

5.9. Acknowledgements

• In this section, important contributions in the realization of the study, which is the subject of the article, are indicated. An attitude that will distract this section from its main purpose should not be taken in the Acknowledgements.

Contribution should be stated as short and concise as possible to the persons and/or organizations that provided assistance (reading, writing, language assistance, etc.) during the research, and should not take an attitude that would distract this section from its main purpose.

5.10. References

• In this section, only the documents mentioned in the article should be included in complete.

• Abbreviations should be avoided in naming the publications and journals.

• The mentioned documents should be written in Times New Roman and 9 pt.

• The first line of the references should be written as justified to the left margin of the page, and the other lines should be written by giving a hanging indent value of 1.25.

• The references should be listed in alphabetical order, taking into account the surnames of the authors.

• If one author has more than one work in the same year, lowercase alphabet letters should be used right after the year of publication and the letters should be italic (e.g. Saklar, 2011*a*, *b*).

• If more than one document of the same author is cited, first his / her single-name publications in chronological order, then double-names according to the second author's surname in chronological order, and then multi-names according to the alphabetical order of the authors' surnames and publication year should be given.

For example:

Corradini, C. 2007. The conodont genus Pseudooneotodus Drygant from the Silurian and Lower Devonian of Sardinia and the Carnic Alps (Italy). Bollettino-Societa Paleontologica Italiana 46 (2/3), 139-148.

Corradini, C., Corriga, M. G. 2010. Silurian and lowermost Devonian conodonts from the Passo Volaia area (Carnic Alps, Italy). Bollettino della Società Paleontologica Italiana 49 (3), 237-253.

Corradini, C., Corriga, M. G. A. 2012. Pridoli – Lochkovian conodont zonation in Sardinia and the Carnic Alps: implications for a global zonation scheme. Bulletin of Geosciences 87 (4), 635-650.

Corradini, C., Serpagli E. 1999. A Silurian conodont biozonation from late Llandovery to end Pridoli in Sardinia (Italy), In Serpagli (Ed.), Studies on conodonts: Proceedings of the 7th European Conodont Symposium. Bollettino della Società Paleontologica Italiana 37 (2-3) (1998), 255-273.

Corradini, C., Corriga, M. G., Männik, P., Schönlaub, H. P. 2015. Revised conodont stratigraphy of the Cellon section (Silurian, Carnic Alps). Lethaia 48 (1), 56-71.

Corradini, C., Leone, F., Loi, A., Serpagli, E. 2001.Conodont Stratigraphy of A Highly Tectonised Silurian-Devonian Section in The San Basilio Area (Se Sardinia, Italy). Bollettino Della Societa Paleontologica Italiana 40 (3), 315-323, 1 Pl.

Corradini, C., Pondrelli, M., Serventi, P., Simonetto, L. 2003. The Silurian cephalopod limestone in the Monte Cocco area (Carnic Alps, Italy): conodont biostratigraphy. Revista Española de Micropaleontologia 35 (3), 285-294.

• If documents of different authors with the same surname are mentioned, they should be written in alphabetical order, considering their first names.

• If the document is in a periodical publication (if it is an article), information about the document is given in the following order: Authors ' surname, first letters of the authors' first names. Year of publication. The name of the article. The name of the publication in which the article was published, volume number and / or issue number with the first letters in capital, the numbers of the first and last page of the document. Punctuation marks like comma and etc. after journal names should not be used.

• In the examples below, the information about the mentioned documents is organized according to different document types, taking into account the punctuation marks.

For example:

Gürsoy, M. 2017. Munzur Dağları Alt Miyosen çökelleri mollusk topluluğu ve paleoekolojisi (Doğu Anadolu, Türkiye). Maden Tetkik ve Arama Dergisi 155, 75-99.

Pamir, H. N. 1953. Türkiye'de kurulacak bir Hidrojeoloji Enstitüsü hakkında rapor. Türkiye Jeoloji Bülteni 4, 1, 63-68.

Robertson, A. H. F. 2002. Overview of the genesis and emplacement of Mesozoic ophiolites in the Eastern Mediterranean Tethyan region. Lithos 65, 1-67.

• If the document is a book: authors' surnames, authors' first names. Year of publication. Title of the book with capital letters. The name of the publishing organization or the name of the publication in which the document was published, the volume and / or issue number, and the total number of pages of the book should be specified, respectively.

For example:

Einsele, G. 1992. Sedimentary Basins. Springer Verlag, 628.

Ketin, İ., Canıtez, N. 1956. Yapısal Jeoloji. İTÜ, 308.

Meriç, E. 1983. Foraminiferler. Maden Tetkik ve Arama Genel Müdürlüğü Eğitim Serisi, 26, 280.

• If the document is published in a book containing the articles of various authors, the usual order for the document included in a periodical publication is followed until the end of the document title. Then the editors' surnames and initials and the abbreviation of the editor word "Ed." is written in parentheses. Then, the title of the book in which the document is located is written with the first letters in capital letters. Name of publishing organization. The place of publication, the volume number of the publication in which the document was published, and the numbers of the first and last pages of the document should be written.

For example:

Anderson, L. 1967. Latest information from seismic observations. Gaskell, T. F. (Ed.). The Earth's Mantle. Academic Press. London, 335-420.

Göncüoğlu, M. C., Turhan, N., Şentürk, K., Özcan, A., Uysal, S., Yalınız, K. 2000. A geotraverse across northwestern Turkey. Bozkurt, E., Winchester, J. A., Piper, J. D. A. (Ed.). Tectonics and Magmatism in Turkey and the Surrounding Area. Geological Society of London. Special Publication, 173, 139-162.

• If it is desired to specify the name of a book in which the writings of various authors are collected as a document; following the surnames and names of the book's editors, in parentheses the "Ed." statement is written. Year of publication. Title of the book with capital letters. The name of the publishing organization or the name of the publication in which the document was published, the volume and / or issue number and the total number of pages of the book should be specified.

For example:

Gaskel, T. F. (Ed.). 1967. The Earth's Mantle. Academic Press, 520.

• If the document is "published abstract", information about the document is given in the following order: Authors' surnames, authors' first names. Year of publication. Name of the document (paper). The name, date and place of the meeting where the paper is published, and the first and last page numbers in the book containing the abstract should be written.

For example:

Öztunalı, Ö., Yeniyol, M. 1980. Yunak (Konya) yöresi kayaçlarının petrojenezi. Türkiye Jeoloji Kurumu 34. Bilim Teknik Kurultayı, Ankara, 36.

Yılmaz, Y. 2001. Some striking features of the Anatolian geology. 4. International Turkish Geology Symposium, 24-28 Eylül 2001, Adana, 13-14.

• If the mentioned document has not been published like report, lecture notes and etc., the word "unpublished" should be written at the end of the information about the document in parentheses after the information about the document is given in the usual order for the document in a periodical publication.

For example:

Akyol, E. 1978. Palinoloji ders notları. EÜ Fen Fakültesi Yerbilimleri Bölümü, 45, İzmir (unpublished).

Özdemir, C., Biçen, C. 1971. Erzincan ili, İliç ilçesi ve civarı demir etütleri raporu. Maden Tetkik Arama Genel Müdürlüğü, Rapor No: 4461, 21, Ankara (unpublished).

• For unpublished courses, seminars and similar notes, the course organizer after document name. The place of the meeting. Title of the book and relevant page numbers should be given.

For example:

Walker, G.R., Mutti, E. 1973. Turbidity facies and facies associations. Society for Sedimentary Geology Pacific Section Short Course. Annaheim. Turbitides and Deep Water Sedimentation, 119-157.

• If the document is a thesis; author's surname, initial of the author's first name. Year of publication. Name of the thesis. The type of the thesis, the university where it was given, the total number of pages, its province and the word "unpublished" are written in parentheses.

For example:

Akıllı, H. 2019. Polatlı-Haymana (Ankara) civarı sıcak sularının izotop jeokimyası (δ18O, δD, 3H, δ13C, δ34S, 87Sr/86Sr) ve ana iz element bileşimleri ile incelenmesi. PhD Thesis, Ankara University, 255, Ankara (unpublished).

Argun Aktan, Ö. 2019. Marmara Denizi Batı Kıta Sahanlığı Yüzeysel Çökellerinde Jeojenik ve Antropojenik Ağır Metal Zenginleşmesine Yönelik Araştırmalar (Şarköy Kanyonu, KB Türkiye). MSc Thesis, Ankara University, 179, Ankara.

• Anonymous works should be arranged according to the publishing institution.

For example:

MTA. 1964. 1/500.000 ölçekli Türkiye Jeoloji Haritası, İstanbul Paftası. Maden Tetkik ve Arama Genel Müdürlüğü, Ankara.

• For the documents that are in print, no date is put after the name of the author, the name of the article and the source to be published should be specified and the word "in print" and / or "in review" should be written at the end (in parentheses).

For example:

Ishihara, S. The granitoid and mineralization. Economic Geology 75th Anniversary (in press).

• Information downloaded from the Internet should be given in the form of the name of the institution, its web address, and the date on which the web address was accessed. Turkish references should be given directly in Turkish and should be written in Turkish characters.

For example:

ERD (Earthquake Research Department of Turkey). http://www.afad.gov.tr. 3 March 2013.

• While citing the source, the original language should be adhered to, and the title of the article should not be translated.

6. Illustrations

• All of the drawings, photographs, plates and tables used in the article are referred to as "illustrating".

• Illustrations should be used when their use is unavoidable or when they make the subject easier to understand.

• In the selection and arrangement of the format and size of the illustrations, an attitude should be made to prevent loss of space as much as possible considering the page length and layout of the bulletin.

• The number of illustrations used should be proportional to the size of the text.

• All illustrations should be submitted in separate files regardless of the text.

• Abbreviations should not be used in illustration explanations in the text and should be numbered in the order of mention within the text.

• Photographs and plates must be submitted as a computer file in which all details can be seen for the examination of the article, with EPS, TIFF or JPEG extension and at least 300 dpi resolution.

6.1. Figures

• Drawings and photographs other than the plate to be included in the article are evaluated together as "Figure" and numbered in the order of mention in the text.

• The figures should be prepared in computer considering the dimensions of a single column width as 7.4 cm or double column width as 15.8 cm. The figure area with its caption should not exceed 15.8x21 cm.

• While preparing the figures, unnecessary details should not be included and care should be taken not to use more space than necessary for the transfer of information.

• In figure descriptions, a space should be left after the word "Figure" is written, and the number is given in the usual sequence number, followed by a hyphen (-) and a space again, and a description of the relevant figure should be written. If the figure legend exceeds the bottom lines, the following lines should to be written after the "Figure 1-" statement alignment. Figure descriptions should be created as follows, without exceeding the edges of the figure and justified on both sides.

For example:

Figure 1- The district of Sandıklı (Afyon); a) geological map of the southwest, b) the general vertical section of the study area (Seymen, 1981), c) Turkey's most important neotectonic structures (modified from Koçyiğit, 1994).

• Drawings should be drawn in computer properly, clean and with care.

• The use of thin lines that may disappear when minimized in figures should be avoided.

• Symbols or letters used in all drawings should not be less than 2 mm (7 pt.) in Times New Roman.

• All standardized symbols used in the drawings should preferably be explained in the drawing, if they are too long then they should be explained in the figure below.

• Bar scale should be used in all drawings and the north direction should be indicated on all maps.

• The name of the author, description of the figure, figure number should not be included in the drawing.

• Photographs should reflect the aims of the subject and should be in adequate numbers.

• Figures should be framed.

6.2. Plates

• Plates should be used in cases where multiple photographs are required to be printed together on a special paper.

• Plate dimensions must be equal to the size of the bulletin's usable area of the page.

• Figure numbers should be written under each of the figures on the plate and bar scale should be used.

• Original plates must be attached to the final copy to be submitted in the case of acceptance of the manuscript.

• Figures and plates should be numbered among themselves and independently. Figures should be numbered with Latin numerals and plates with Roman numerals (eg Figure 1, Plate I).

• There should be no explanation text on the figures inside the plate.

6.3. Tables

• All tables should be arranged in word format and should be prepared in Times New Roman.

• Tables should not exceed the size of 15x8 cm together with the table caption.

• Table explanations should be created without exceeding the edges of the figure and justified as in the example below.

For example:

Table 1- Hydrogeochemical analysis results of geothermal waters in the study area.

7. Nomenclature and Abbreviation

• Abbreviations must be in the accepted international or national form. Unusual nomenclature and abbreviations that are not standardized in the article should be avoided. In cases where it is deemed necessary to use such nomenclature and abbreviations, the way and method followed should be explained.

• There should not be a dot between the words initials used in standard abbreviations (such as MTA, DSİ).

• Abbreviations of geography aspects should be made in English (N, S, E, W, NE and etc.).

The word group to be abbreviated should be written clearly where it is mentioned first time and the abbreviation should be given in parentheses, then only the abbreviated form should be written throughout the article.

• Systems with international validity (m, inch, etc.) should be used as the unit of measure. Decimals should be separated with commas in Turkish articles and with a period in English articles.

• The names of figures, plates and tables in the article should not be abbreviated. For example, "As seen in the generalized stratigraphic section of the region (Figure 1) …….".

7.1. Stratigraphic Nomenclature

• Stratigraphic nomenclature should be done in accordance with the Stratigraphical Classification and Nomenclature Rules prepared by Turkey Stratigraphy Committee (TSC).

(https://www.mta.gov.tr/v3.0/sayfalar/birimler/belgeler/Stratigrafi_adlama_kurallari.pdf)

• Attention should be paid to the use of formation names accepted (formalized) by the TSC. If the formation name used is official, the letter "F" should be capitalized, and if it is informal and plural, the letter "f" should be written in lowercase. For example; Bostancı Formation (formal), Kaynarca formation (unofficial), Baltalimanı, Trakya and Tarlaağızı formations (plural).

7.2. Chronostatigraphic and Geochronologic Nomenclature

• "International Chronostratigraphic Chart" (https://stratigraphy.org/chart), which is updated annually by the International Stratigraphic Committee, should be taken into consideration in chronostratigraphic and geochronological nomenclature.

• Position within a chronostratigraphic unit can be expressed in adjectives indicating the position, for example: lower, middle, upper and etc. When using these adjectives, it should be decided whether the lower, middle and upper distinction is formal / informal in the International Chronostratigraphic Chart.

For example:

lower Miocene, Upper Holocene and etc.

• When stating the time where a geochronological unit is, temporal adjectives such as; early, middle, late and etc. are used. When using these adjectives, the International Chronostratigraphic Chart should be taken into consideration to decide whether the adjectives begin with capital or lowercase letters.

For example:

early Miocene, Late Holocene etc.

7.3. Paleontological Nomenclature and Spelling of Fossil Names

• Original names of fossils should be used.

For example:

Nummulites with limestone

• Fossil genus and species names are written in italics, cf., aff. and gr. etc. expressions are written as normal (perpendicular). When writing fossil names for the first time, the surnames of the people who identify them and the year in which they were first defined should be written. In later uses, the surnames and the year in which they are defined may not be written. The surnames and dates of identifiers coming at the end of the fossil names are not references, they should not be included in the mentioned documents.

For example:

Alveolina aragonensis Hottinger, 1960 not a reference.

Alveolina cf. *aragonensis* Hottinger, 1960 not a reference.

Alveolina aff. *aragonensis* Hottinger, 1960 not a reference.

Alveolina gr. *aragonensis* Hottinger, 1960 not a reference.

• After the first use of the same genus in the text is written clearly, it can be abbreviated as in the example so that it will not be confused with another genus in later use.

For example:

Alveolina aragonensis, A. polathensis, A. ellipsoidalis etc.

• If the date is in parentheses after the person describing it after the name of the fossil in the text, this is a reference and should be included in the mentioned documents.

For example:

Alveolina aragonensis Hottinger (1960) is a reference.

• The following rules should be taken into account when writing the systematic paleontologic section.

a. First of all, genus, species and subspecies to be identified should be written in hierarchical order like the order, upper family, family type species and so on. Later, the species to be described should be written together with the surnames and date of the people who defined the subspecies name. If there is a photograph of the described fossil, the plate or figure with the photograph should be added under the fossil name. The names of the authors listed here are not references, so they are not included in the reference.

For example:

Order: Foraminiferida Eichwald, 1830

Superfamily: Alveolinacea Ehrenberg, 1839

Family: Alveolinidae Ehrenberg, 1839

Type Genus: *Borelis* de Montfort, 1808

Type Species: *Borelis melenoides* de Montfort, 1808
= *Nautilus melo* Fichtel and Moll, 1798

Borelis vonderschmitti (Schweighauser, 1951)

(Plate II, Figure 3-5 or Figure 3A-H).

b. Similar or synonyms (synonym) list should be left-aligned in chronological order. The page and figure number of the synonymous fossil in the relevant study should be included in the synonymous list. Authors in the synonymous list are references and must be included in the references.

For example:

1951 *Neoalveolina vonderschmitti* **Schweighauser**, page 468, figures 1-4.

1974 *Borelis vonderschmitti* (Schweighauser), **Hottinger**, page 67, plate 98, figures 1-7.

c. After the synonymous list is given, the definition, explanations (similarities and differences), dimensions, material, stratigraphic distribution (according to the characteristics of the fossil) should be written.

d. If the fossil is defined for the first time (new species) in the systematic paleontology section, the origin of the name, holotype, type locality, material, description, explanation (similarity and differences), age and geographical distribution, dimensions (according to the features that define the fossil) should be written. Photographs of the fossil identified for the first time by the authors must necessarily be placed in plates or figures.

e. Bar scale indicating the size of fossils must be used definitely in plates / figures.

8. References

• In the references to be made in the Main Text, only the surnames of the authors and the publication year of the mentioned article should be specified. Referencing should be arranged according to one of the following examples:

• Referring to a publication with a single author (in chronological order):

-Altınlı (1972, 1976) defined the Bilecik sandstone in detail.

It is known that the fold axes of the Devonian and Carboniferous units around İstanbul are N-S trending (Ketin, 1953, 1956; Altınlı, 1999).

• Referring to a publication with two authors:

- The upper parts of the unit include Ilerdian fossils (Sirel and Gündüz, 1976; Keskin and Turhan, 1987, 1989).

• Referring to a publication with more than two authors:

- According to Caner et al. (1975), the Alıcı formation reflects the conditions of fluvial environment.

- Unit disappears by wedging towards E (Tokay et al., 1984).

• Referring to a reference in another publication:

It is known that Lebling mentioned about the existence of Liassic around Çakraz (Lebling, 1932; Charles, 1933).

• When referring to the works of the authors with the same surname in the same year, referring the authors' first names by writing their initials:

- Many studies have been done in the field of structural geology in the study area (Gutnic et al., 1979; Yılmaz A., 1983; Yılmaz, İ., 1983; Poisson et al., 1984 etc.).

9. Prints Sent to Authors

Two copies of the relevant issue published in the Bulletin of the Mineral Research and Exploration are sent to the authors.

10. Terms of Publication and Copyrights

• Some or all of the articles to be published in the Bulletin of the Mineral Research and Exploration should not have been published before.

• Authors who submit a publication to the Bulletin of the Mineral Research and Exploration are deemed to have accepted the bulletin's publication rules in advance.

• The copyright of the manuscripts accepted for publication and converted into publications belongs to the General Directorate of Mineral Research and Exploration (MTA).

The authors of the study sign the relevant forms within the scope of the provisions specified in the Regulation of the Editorial Board regarding the transfer of copyright and submit them to the Editorial Board. After the publication of the article, MTA may pay royalty fees to the authors of the article for their declarations within the scope of the "Regulation on the Editorial and Processing Fees to be paid by the Public Organizations and Institutions".

NOTE: Information and forms about Bulletin of the Mineral Research and Exploration can be accessed from the website: http://dergi.mta.gov.tr/index.php.